IPPT Reports on Fundamental Technological Research
1/2018

Zuzanna Poniżnik

Modelling of effective properties and fracture of metal-ceramic interpenetrating phase composites

Rozprawa Doktorska
Promotor: dr hab. inż. Michał Basista, prof. IPPT PAN

Instytut Podstawowych Problemów Techniki
Polska Akademia Nauk

Warszawa 2018

IPPT Reports on Fundamental Technological Research
ISSN 2299-3657
ISBN 978-83-65550-14-9

Rozprawa doktorska obroniona
w IPPT PAN 19 grudnia 2017
wpłynęła do redakcji 27 lutego 2018

Instytut Podstawowych Problemów Techniki Polskiej Akademii Nauk (IPPT-PAN)
Institute of Fundamental Technological Research Polish Academy of Sciences
Pawińskiego 5B, PL 02-106 Warsaw, Poland

Druk/Printed by:
Drukarnia Braci Grodzickich, ul. Geodetów 47A, 05-500 Piaseczno, Poland

Acknowledgements

I would like to express my gratitude to my supervisor Prof. Michał Basista for all his support, encouragement and insightful guidance throughout many years of research leading to this thesis. The presented research would not have been possible without his kindest help, support and belief.

I am thankful to Prof. Barbara Gambin for valuable advice on modelling of the mechanical properties. I would like to thank Prof. Katarzyna Pietrzak for consultations and advice on the experimental part. Consultations on micromechanics with Prof. Katarzyna Kowalczyk-Gajewska are gratefully acknowledged.

I am grateful to Prof. Zdzisław Nowak for his kindest help, advice and consultations on the fracture part of this thesis.

I am grateful to Prof. Dietmar Gross for his advice and scientific guidance during my research stays at the Institute of Mechanics, Darmstadt University of Technology in Germany.

I am thankful to Prof. Jürgen Rödel and to Dr Ludwig Weiler for their scientific guidance during the research stays at the Institute of Materials Science, Darmstadt University of Technology.

I would like to thank Prof. Ralf Müller for his consultations and advice during the research stays at the Institute of Applied Mechanics, University of Kaiserslautern, Germany.

I am grateful to Dr Witold Węglewski for all his cooperation and exceptional help. I am also grateful to Mrs Izabela Dolińska, Ms Monika Milewska, Ms Urszula Czubacka, Ms Agnieszka Sokalska, Dr Jerzy Trębicki, Mr Piotr Putek, Mr Rafał Gawlik and Mr Piotr Matejek for their help and assistance. I owe my sincere thanks to the research teams and staff at the Advanced Composite Materials Division (PZMK), Department of Mechanics of Materials, Institute of Fundamental Technological Research, Darmstadt University of Technology and University of Kaiserslautern, for all help that I have received.

This research has been partially supported by the following projects:

European Union's Sixth Framework Programme project under Grant Agreement NMP-CT-2004-502243 (KMM-NoE)

European Union's Seventh Framework Programme project under Grant Agreement No. 228869 (MATRANS)

Polish National Centre for Research and Development project under contract no. POIG.01.03.01-00-013/08 in the framework of the Innovative Economy Operational Programme (KomCerMet)

Polish National Science Centre project under contract UMO-2014/15/B/ST8/04314 (Influence of Thermal Residual Stresses on Fracture Behaviour and Selected Mechanical Properties of Metal-Ceramic Composites: Experiments and Modeling)

Supplementary calculations for the *J*-integral were performed at High Power Computers Centre of Interdisciplinary Centre for Mathematical and Computational Modelling (ICM KDM) of the University of Warsaw within computational grants G65-8 and G67-21.

This research has been also supported in part by European Social Fund and Polish State Budget in the framework of the Regional Operational Programme ZPORR, Op. 2.6

“Regional Innovative Strategies and Knowledge Transfer” of the Mazovian Voivodship Project “Mazovian Doctoral Grant”.

Modelowanie właściwości efektywnych i pękania w kompozytach o wzajemnie przenikających się fazach metalu i ceramiki

Zuzanna Poniżnik

Instytut Podstawowych Problemów Techniki Polskiej Akademii Nauk

Abstrakt

Tematem rozprawy doktorskiej jest modelowanie makroskopowych (efektywnych) właściwości sprężystych i termicznych oraz procesów deformacji i pękania kompozytów typu *wzajemnie przenikających się faz* (*Interpenetrating Phase Composites, IPC*). W porównaniu z typowymi kompozytami na osnowie metalowej (*metal matrix composites*, MMC), kompozyty IPC wyróżniają się większą jednorodnością mikrostruktury, stabilnością mikrostruktury w podwyższonych temperaturach, podwyższoną przewodnością cieplną, ponadto dzięki sieciowej mikrostrukturze pękanie w IPC nie zachodzi w sposób gwałtowny. Właściwości te powodują, że kompozyty IPC są atrakcyjnymi materiałami konstrukcyjnymi i funkcjonalnymi dla przemysłu transportowego, energetycznego czy elektronicznego, co stanowi silną motywację dla rozwoju technologii wytwarzania, badania mikrostruktury i właściwości oraz modelowania.

W pracy zaproponowano modele analityczne i numeryczne do szacowania efektywnych stałych sprężystości kompozytów IPC. Mechanizmy deformacji i pękania badanych kompozytów pod działaniem obciążeń quasi-statycznych zostały przedstawione w serii modeli numerycznych, z uwzględnieniem rzeczywistej mikrostruktury materiału otrzymanej za pomocą mikrotomografii komputerowej (*computed microtomography*, *micro-CT*). W dodatku do rozprawy zamieszczono wyniki własnych badań doświadczalnych związanych z wytwarzaniem i charakteryzacją materiałów IPC, jako informacji pomocniczych przy konstruowaniu modeli IPC.

Jednym z głównych osiągnięć pracy jest zaproponowanie metodologii wykorzystania danych mikrostrukturalnych z mikrotomografii komputerowej w problemach wyznaczania stałych efektywnych i parametrów pękania materiałów IPC i jej praktyczna numeryczna implementacja w ramach MES.

Modelling of effective properties and fracture of metal-ceramic interpenetrating phase composites

Zuzanna Poniżnik

Institute of Fundamental Technological Research
Polish Academy of Sciences

Abstract

This dissertation is focused on modelling of the effective elastic and thermal properties, deformation and fracture of metal-ceramic *interpenetrating phase composites* (IPCs). Compared to typical *metal matrix composites* (MMC) reinforced with particles or ceramic fibres, the main advantages of IPCs are: improved homogeneity, microstructure stability at elevated temperatures, increased thermal conductivity and, thankful to the interpenetrating microstructure, moderation of cracking with metallic networks. These superior characteristics make the IPCs attractive structural and functional materials for *e.g.* transport, power and electronic industry sectors. The industry push for new materials and technologies provides a strong motivation for research in the fields of processing, characterisation and modelling of IPCs.

Analytical and numerical models are proposed to predict the effective elastic properties of the IPCs. The problems of deformation and fracture of IPCs under quasi-static loading are addressed numerically in a set of models aiming at the determination of the fracture parameters taking into account the crack bridging mechanism. A particular attention is given to creation of numerical models for effective elastic constants and fracture parameters of IPCs based on their real microstructure obtained from computed microtomography (micro-CT) images. Additional information from own experimental research on manufacturing and characterization of IPCs is reported in Appendix as a supporting material used in the modelling.

One of the main contributions of this research to the field of IPCs modelling is the proposed methodology of using micro-CT images of real interpenetrating microstructure in the Finite Element Method approach when calculating the effective elastic constants and the *J*-integral for the interpenetrating phase composites.

List of symbols

Symbol	Meaning
*	effective quantity
$\bar{}$	average quantity
∂	partial differentiation; boundary
$\langle\ \rangle$	Macaulay brackets
$_{i,j}$	partial differentiation of i-th component in direction of j-th component
$\mathbf{1}$	second rank unity tensor
I, II, III	identifiers of sublayers
1, 2, 3	axes of the Cartesian coordinate system; identifiers of layers
A, dA	area; surface, infinitesimal crack surface increase
A, B; Ai	phase identifier; i-th component
a	characteristic dimension of the composite's phase; crack length
Δa, da	infinitesimal increase of crack length
a_1, a_2	crack length at initial state, crack length at final state
$\boldsymbol{a}_i$	vector of the nodal enriched degrees of freedom
a_i	size of a composite's phase in i-th direction
a_α	non-dimensional size parameter of a composite's α-th phase
b, B, B^{slice}	thickness, width; C-T specimen thickness; thickness of a C-T specimen slice

Symbol	Meaning
$\mathbf{b}_i^{\alpha}$	vector of the nodal enriched degrees of freedom
b_i	size of a composite's phase in *i*-th direction
b_α	non-dimensional size parameter of a composite's α-th phase
b, b_{ij}	Eshelby's stress tensor, components of the Eshelby's stress tensor
C, C_{ijkl}	elastic stiffness tensor, components of the elastic stiffness tensor
$\mathbf{C}^*$, C^*_{ijkl}	effective elastic stiffness tensor, components of the effective elastic stiffness tensor
C	contour; open contour surrounding the crack tip
C	corn starch
c	contour; notch depth; crack length
c_i	volume fraction of the *i*-th phase, volume fraction of the *i*-th layer
c_i	size of a composite's phase in *i*-th direction
c_α	non-dimensional size parameter of a composite's α-th phase
c^{layer}	area fraction of the phase *A*
C_{Cu}	amount of copper in the composite
CMC	Ceramic-Matrix Composite
COD	Crack Opening Displacement
C-T	Compact-Tension test
CTE	Coefficient of Thermal Expansion
CZ	Cohesive Zone
D	damage parameter
d	cohesive zone length
E	gradient of deformation
e	Euler number

Symbol	Meaning
E, E_i	Young's modulus; dynamic Young's modulus, Young's modulus of the i-th phase
$E_{Eff}, \bar{E}, E^*$	effective Young's modulus
$E_{\alpha\beta\gamma}$	Young's modulus of the ($\alpha\beta\gamma$) sub-cell
$\bar{E}^{low}, \bar{E}^{up}$	lower bound for the effective Young's modulus, upper bound for the effective Young's modulus
$E^*_{VVR}, E^*_{RVV}, E^*_{VRV}$	effective Young's modulus according to *V-V-R*, *R-V-V*, *V-R-V* sectioning
E_i, E^{layer}	Young's modulus of the i-th phase, effective Young's modulus of a layer
E_m, E_f	Young's modulus of the matrix, Young's modulus of the fibre
E_1, E_2	Young's modulus measured in out-of-plane flexure, Young's modulus measured in in-plane flexure
$-\Delta E_{TCTC}$	reduction of Young's modulus in cooling
$\boldsymbol{e}$, e_n, e_t	unit vector, unit vector normal to the separation plane, unit vector tangential to the separation plane
F	external load
F	yield function
$F_\alpha(x)$	elastic asymptotic crack tip functions
f, f_i, f_α	volume fraction of the phase *B;* volume fraction of the ductile phase; flow potential, volume fraction of the i-th phase, volume fraction of the α-th phase
$\boldsymbol{f}, f$	vector function, scalar function
f_f	fundamental resonant frequency
FEM	Finite Element Method
FFT	Fast Fourier Transform
G, G_i	energy release rate, energy release rate in the i-th mode of cracking

Symbol	Meaning
ΔG, G_m	energy release rate increase, energy release rate of the matrix
ΔG_α	energy release rate increase for an inclined fibre
G, G_i	shear modulus, shear modulus of the i-th phase
$\bar{G}, G^*$	effective shear modulus
$G_{\alpha\beta\gamma}$	shear modulus of the ($\alpha\beta\gamma$) sub-cell
G_{IC} , G_{IIC}	fracture energy (mode *I, II* of cracking)
$G^*_{layer}, G^*_{sublayer}$	effective shear modulus of a layer, effective shear modulus of a sublayer
$G^*_{layer,i}, G^*_{sublayer,i}$	effective shear modulus of the i-th layer, effective shear modulus of the i-th sublayer
$G^*_{VVR}, G^*_{RVV}, G^*_{VRV}$	effective shear modulus according to *V-V-R*, *R-V-V*, *V-R-V* sectioning
G_n, G_s, G_t, G_T	work in the normal direction, work in the shear directions, total work
G_n^C, G_s^C, G_t^C	critical fracture energies in normal and shear directions
H, V	identifier of horizontal sectioning, identifier of vertical sectioning
H	thickness of the specimen
$H(x)$	discontinuous jump function across the crack surfaces
H_{iso}	linear isotropic hardening modulus
h, h_0	half actual length of the bridging part of the fibre, half initial length of the bridging part of the fibre
i	identifier; counter
$\mathbf{I}$, I_{ijkl}	fourth rank unity tensor, components of the fourth rank unity tensor
$\mathbf{I}^S$	symmetric part of a fourth rank unity tensor
$\mathbf{I}_D$, $\mathbf{I}_P$	deviatoric and spherical part of $\mathbf{I}^S$

Symbol	Meaning
IMCE	Integrated Material Control Engineering
IPC	Interpenetrating Phase Composite
J	*J*-integral vector
J, J_i	*J*-integral; component of *J*-integral vector in the *i*-th direction
J_C, J_α	*J*-integral for a monolithic ceramics, *J*-integral for an inclined fibre
K	bulk modulus; bulk modulus of the composite; stress intensity factor
K_i, K_m	bulk modulus of the *i*-th phase, bulk modulus of the matrix
$\overline{K}, K^*, K_{Eff}$	effective bulk modulus
$K^*_{layer}, K^*_{sublayer}$	effective bulk modulus of a layer, effective bulk modulus of a sublayer
$K^*_{layer,i}, K^*_{sublayer,i}$	effective bulk modulus of the *i*-th layer, effective bulk modulus of the *i*-th sublayer
$K^*_{VVR}, K^*_{RVV}, K^*_{VRV}$	effective bulk modulus according to *V-V-R*, *R-V-V*, *V-R-V* sectioning
K_{IC}	plane strain fracture toughness (mode *I* of cracking)
K_{II}, K_{it}	stiffness in shear, bond stiffness in *i*-th shear direction
k_m, k_n	distance between loading pins, distance between supporting pins
L, l	length
l_d, l_d^0	decohesion length, initial spacing
l_0, l_m	protruding length, length of the embedded part of the fibre
M, Mp	corn starch, porous preform based on corn starch PFA
m_i	*i*-th mode mix formulation
m, m_{dry}, m_{H_2O}	mass, mass of the dry specimen, mass of the volume of water equal to the volume of specimen

Symbol	Meaning
m_{satd}, $m_{suspend}$	mass of the specimen infiltrated with water, mass of the specimen suspended in water
micro-CT	X-ray computed microtomography
MMC	Metal-Matrix Composite
n	unit vector; unit vector normal to the contour; unit outward vector normal to the contour
n_i	component of the unit vector in the *i*-th direction
n	specimen width; exponent; counter; number of layers
$N_i(x)$	nodal shape function
P, P	force, maximum recorded load
P	polypropylene wool felt
PFA	Pore Forming Agent
r_f^0, r_f, r_m	radius of the fibre; initial radius of the ligament/fibre, actual radius of the fibre, radius of the matrix
R	rice starch
R_a	roughness
RFDA	Resonant Frequency and Damping Analyser
RVE	Representative Volume Element
R-V-V	way of unit cell division according to Reuss model, then Voigt model, and Voigt model
s	arc element of Γ
dS	area element
$\mathbf{S}^*, S_{ijkl}^*$	effective compliance tensor, components of the effective compliance tensor
SEVNB	Single Edge V-Notched Beam
$SG_{apparent}$	apparent specific gravity
t, t_i	stress vector, components of the stress vector

Symbol	Meaning
$\mathbf{T}$, T_i, t_i	vector of tractions, components of the vector of tractions
$t(x)$, $t(\delta)$	intermolecular cohesive stress, cohesive stress distribution
T_1, T_2	initial temperature; correction factor, final temperature
t	total initial height of the cracking matrix blocks
TC, $-\Delta T_{TCTC}$	max. temperature of the cycle, temperature decrease in cooling
U	strain energy density
$\mathbf{U_0}$	axial displacement
$\mathbf{u}$, u_i	displacement vector, component of the displacement in i-th direction
$\mathbf{u}$, $\mathbf{u}_i$	displacement field, continuous part of the displacement field vector
V, $V_{specimen}$	body volume, volume of the specimen
∂V	closed surface; boundary surface of the body volume
$V_{I\text{-}III}$, V_{II}, $V_{1\text{-}3}$, V_2	volume of the respective layer
$V_{\alpha\beta\gamma}$	volume of the ($\alpha\beta\gamma$) sub-cell
V-V-R	way of unit cell division according to Voigt model, then Voigt model, and Reuss model
V-R-V	way of unit cell division according to Voigt model, then Reuss model, and Voigt model
W	strain energy
W	wool felt
w	scalar
x	coordinate
x_i	i-th axis of the Cartesian coordinate system
XFEM	Extended Finite Element Method
y	coordinate
Y_0	yield stress

Symbol	Meaning
z	coordinate
α	inclination angle; power; counter; serial number of a sub-cell
α, α_i	coefficient of thermal expansion, coefficient of thermal expansion of the i-th phase
α_{Eff}, α^*	effective coefficient of thermal expansion
α^{Voigt}	volume average of the coefficient of thermal expansion according to the Voigt model
$\alpha^*_{RH-Voigt}$, $\alpha^*_{RH-Reuss}$	Rosen-Hashin estimate on effective coefficient of thermal expansion with the Voigt model, Rosen-Hashin estimate on effective coefficient of thermal expansion with the Reuss model
α^*_{RH-VVR}, α^*_{RH-RVV}, α^*_{RH-VRV}	Rosen-Hashin estimate on effective coefficient of thermal expansion with the *V-V-R* model, Rosen-Hashin estimate on effective coefficient of thermal expansion with the *R-V-V* model, Rosen-Hashin estimate on effective coefficient of thermal expansion with the *V-R-V* model
β	serial number of a sub-cell; direction parallel or perpendicular to the crack propagation direction
Γ	contour
γ	serial number of a sub-cell; amount of shear
Δ	increment
$\boldsymbol{\delta}$, δ	displacement vector; opening displacement vector, displacement component; separation of the crack faces
δ_0	displacement associated with ultimate stress
δ_n, δ_t	displacement normal to the separation plane, displacement tangential to the separation plane
δ_c, δ^r	critical displacement at rupture
$\tilde{\delta}_n, \tilde{\delta}_s, \tilde{\delta}_t$	relative displacement conjugate to normal traction, relative displacements conjugate to shear tractions

Symbol	Meaning
δ_{ij}	Kronecker delta
$\boldsymbol{\varepsilon}$, ε_{ij}	strain tensor, components of the strain tensor
$\overline{\boldsymbol{\varepsilon}}, \bar{\varepsilon}_{ij}$	average strain tensor, components of the average strain tensor
$\dot{\boldsymbol{\varepsilon}}$	strain rate tensor
$\dot{\boldsymbol{\varepsilon}}^{\mathbf{e}}, \dot{\boldsymbol{\varepsilon}}^{\mathbf{p}}$	elastic part of the strain rate tensor, plastic part of the strain rate tensor
$\boldsymbol{\varepsilon}^{\mathrm{p}}, \bar{\varepsilon}, \bar{\varepsilon}_0$	plastic strain, equivalent plastic strain, strain corresponding to initial yield stress
$\boldsymbol{\varepsilon}^{\mathbf{T}}$	thermal part of the average strain tensor, components of the average strain tensor
λ	Lamé constant; principal stretch along axis *1*
$\dot{\bar{\lambda}}$	non-negative plastic scalar
μ	Lamé constant; shear modulus; coefficient of friction
μ_{Eff}	effective shear modulus
ν, ν_i	Poisson's ratio; Poisson's ratio of the composite, Poisson's ratio of the *i*-th phase,
$\nu_{Eff}, \bar{\nu}, \nu^*$	effective Poisson's ratio
$\nu_{perpendicular}$, $\nu_{parallel}$	effective Poisson's ratio according to "perpendicular" sectioning, effective Poisson's ratio according to "parallel" sectioning
$\nu^*_{VVR}, \nu^*_{RVV}, \nu^*_{VRV}$	effective Poisson's ratio according to *V-V-R*, *R-V-V*, *V-R-V* sectioning
ν_m, ν_f	Poisson's ratio of the matrix, Poisson's ratio of the fibre
Π	potential energy; potential of internal and external forces
$\Delta\Pi$, $d\Pi$	potential energy increment, potential energy increase
Π^{int}, Π^{ext}	strain energy representing internal energy, potential of the external loads

Symbol	Meaning
Π_1, Π_2	potential energy at the initial state, potential energy at the final state
$\rho, \rho_{dry}, \rho_{H_2O}$	density, density of the dry specimen, density of water
$\boldsymbol{\sigma}$, σ_{ij}	stress tensor, components of the stress tensor
$\overline{\boldsymbol{\sigma}}, \bar{\sigma}_{ij}$	average stress tensor, components of the average stress tensor
σ_0	initial yield stress
σ_C	ultimate stress
$\boldsymbol{\tau}$	shear stress vector, cohesive stress vector
τ_n, τ_s, τ_t	normal traction, shear tractions
τ_n, τ_s, τ_t	cohesive stress component normal to the separation plane, cohesive stress components tangential to the separation plane
$\tau_{max,0}$	failure shear stress
$(\tau_{max,0})_n$, $(\tau_{max,0})_s$, $(\tau_{max,0})_t$	peak nominal stress component normal to the separation plane, peak nominal stress components tangential to the separation plane
v^+, v^-	displacement of upper crack face, displacement of lower crack face
ψ	nondimensional debonding parameter

Contents

1

Introduction

A composite material is usually defined as a man-made material composed of at least two chemically different and clearly separated materials that both are distributed throughout the whole volume of the composite, and for which the properties of the whole composite are different than the properties of its components [1].

Metal-ceramic composites are advanced engineering materials combining mechanical and physical properties of both components aiming to ensure durable and reliable functioning under demanding in-service conditions such as high temperature, high pressure, chemically aggressive environment, complex mechanical loading, or combinations of these factors. They exhibit superior mechanical and service properties compared to conventional structural materials, e.g. high mechanical strength, good wear resistance, resistance to high temperature and thermal shocks, corrosion resistance and low specific weight. They may also be designed as multifunctional materials with specific properties like electric conductivity, heat conductivity, or special magnetic properties. Owing to these unique combinations of properties metal-ceramic composites are being used in automotive, aerospace and rail transport substituting steels or metal alloys in certain structural elements subject to intensive frictional wear, elevated temperature and corrosive environment. Examples of metal-ceramic composites applications in transport sector include brake discs, clutches, valves, nozzles, combustion chambers and exhaust systems. Other applications of metal-ceramic composites can be found in energy, electronics and medical equipment sectors.

The main improvements in material properties of composites compared to the properties of their components can be achieved with the proper choice of the matrix and reinforcement materials, their form, volume fraction and distribution throughout the composite structure, as well as by a proper method of manufacturing [2]. The still unresolved issues in metal-ceramic composites are the relatively high

manufacturing cost and the necessity of using suitable joining techniques to integrate them with other materials in structural components.

One of the main drivers of development of metal-ceramic composites is the inherent brittleness and low fracture toughness of ceramics. The brittleness of ceramics is the origin of their low resistance to crack growth, which limits their potential technological applications as structural materials. Improving fracture toughness of ceramics has been a serious concern for a long time. Additional toughness can be brought to ceramics through the mechanisms like transformation toughening, reinforcing with whiskers, platelets or ceramic fibres, microcrack shielding, ductile particle toughening, and toughening with metallic phase infiltrated into a ceramic porous matrix. In the case of ceramics reinforced with metal particles typical toughening mechanisms are crack trapping, crack bridging and crack deflection. For example, a sixtyfold fracture toughness increase for a glass reinforced with dispersed partly oxidized aluminum particles, four time increase of fracture toughness for Al_2O_3 infiltrated with Ni_3Al intermetallic as compared with monolithic Al_2O_3 (*cf*. [3]), or a twofold fracture toughness increase for a WC/Co composite as compared with pure WC (*cf*. [4]), were reported in the literature.

In general metal-ceramic composites are often divided into metal-matrix composites (MMCs) where ceramic reinforcement is added to a metal matrix, and cermets in which bulk ceramics (*e.g*. oxides, borides, or carbides) are strengthened with metal particles. Depending on the physical structure of the composite cermets can also be considered as metal matrix composites, but their metal content is usually less than 20% by volume. In MMCs the reinforcement may be of different forms (*e.g*. particles, fibres, or porous skeletons) and sizes (*e.g*. continuous or finite). For the sake of completeness it should be added that a subgroup of composite materials called ceramic-matrix composites (CMCs) are not considered as metal-ceramic composites as the reinforcement of ceramic matrices are typically ceramic fibres (*e.g*. carbon, silicon carbide, aluminium oxide, *etc*.).

Interpenetrating phase composites (IPCs), which are the subject of this thesis, are a special type of composites containing no discrete reinforcements but consisting of completely interconnected networks of solid phases, which form almost porosity-free interpenetrating structures. If one phase was removed from the IPC, the other phase would form an open-celled foam with a non-zero rigidity. If the IPC is made of metal and ceramic it is typically the metallic phase that fills out the porous ceramic preform.

In the literature, interpenetrating phase composites (IPCs) are often classified as metal-matrix composites (MMCs) obtained with a specific production technology that is liquid metal infiltration into a porous ceramic preform. In the MMC nomenclature the porous ceramic preform is considered as the reinforcement, while metal filling the pores as the matrix (*e.g.* [5]). Conversely, other authors (*e.g.* [6]) describe IPCs as ceramic-matrix composites (CMCs) reinforced with an interpenetrating ductile metal phase.

The interpenetrating composites form spatially complicated microstructures that are more difficult to describe than those formed by fibres or inclusions in the matrix. Exemplary microstructures of real two-phase interpenetrating Al_2O_3/Cu and Al_2O_3/Al composites are shown in Fig. 1.1. Here, the material microstructure is composed of networks of metallic struts with alumina between them. As both phases form irregular 3D patterns the IPC microstructures can be described as three-dimensional objects only (they do not have their 2D equivalents).

Based on the properties of the constituent phases and geometrical features of the composite, the main characteristics of the IPCs can be determined. The simplest and often used parameter is the volume fraction of phases enabling comparison of composites with different types of microstructures or phase materials, comparison of different methods of modelling, and also comparison of the analytical, numerical and experimental results all together. However, for geometrically complicated microstructures of IPCs more detailed characteristics are necessary. Such geometrical characteristics are phases' shape basis and characteristic dimension of the ligament – its length, diameter, or aspect ratio. If a pore forming agent (PFA) is used to obtain a porous ceramic preform for metal infiltration, the phases' shape basis depends on the traces left in the ceramic's structure by the PFA after burnout. Otherwise, if a liquid phase (metal) is infiltrated into a porous solid phase (ceramic) the phases' shape basis depends on the shape of the solid phase that was formed previously. For example, the solid phase (ceramic) may have the form of a fibrous skeleton made of interconnected ceramic fibres (*e.g.* Saffil fibres), or a porous foam, whose geometrical characteristics are predetermined by the polyurethane foam used.

Elastic properties are important characteristics of IPCs as they can easily be compared with the relevant properties of other materials. The most commonly used are Young's modulus and Poisson's ratio. Bulk and shear moduli are also used, however they are more difficult to measure and, thus, less popular. Typical thermal properties are the coefficient of thermal expansion (CTE), thermal conductivity, and specific heat. Fracture parameters (*e.g.* fracture toughness, *J*-integral, crack opening

displacement) are key mechanical characteristics of interpenetrating phase composites because of brittleness of the ceramic phase.

a)

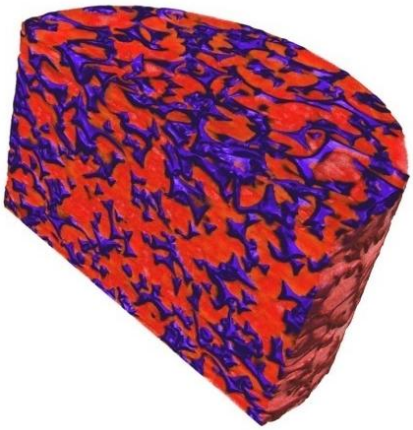

b)

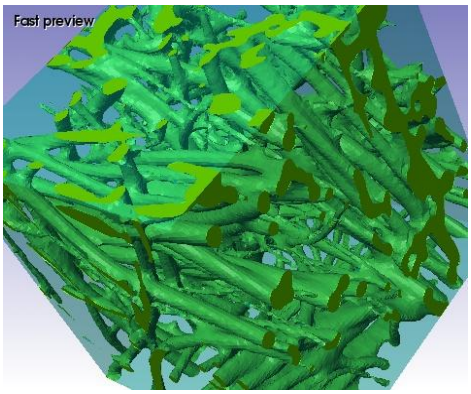

c)

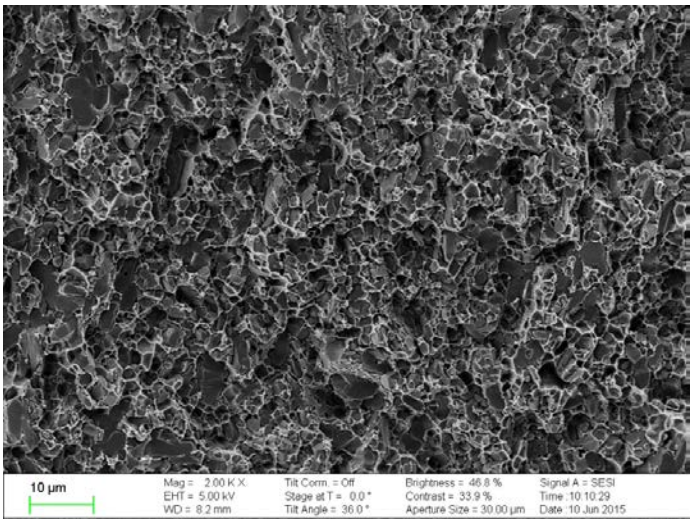

Figure 1.1. Examples of metal-ceramic composite materials with interpenetrating microstructure (IPCs): a) Al_2O_3/Cu composite, red colour - alumina phase, blue - copper phase (courtesy of G. Geier, Leoben; reproduced from [7] with permission of the publisher), b) image of copper phase in Al_2O_3/Cu composite obtained with Simpleware ScanIP [8] software, c) SEM image of fracture surface of Al_2O_3 preform of 34% open porosity pressure infiltrated with Al alloy 44200 (courtesy of Justyna Maj, PZMK IPPT PAN).

In IPCs both phases have more or less equivalent interpenetrating geometry. Therefore, the usual matrix-inclusion terminology is not used as it would be difficult to say which phase is the “matrix” and which serves as the ”inclusions”. A separate terminology has been created instead for these composites. There are different names used in the literature. The term “co-continuous composites” was used by [9–12]. “Composites with interpenetrating phases” was used by Rödel and coworkers (*e.g*. [13–15]). The term “interpenetrating multiphase composites” was used by Torquato *et al.* [16], and Feng *et al.* [17,18]. In the present thesis the term “interpenetrating phase composites”, abbreviated as “IPCs”, will be used throughout.

There are also IPCs made of other materials than metals and ceramics, and also having different properties and purposes than their components. To this end multi-walled carbon nanotubes-polystyrene nanocomposite, alumina-epoxy coatings, or glass-ceramic, metal-metal and ceramic-epoxy resin dental composites can be mentioned. These materials, however, are beyond the scope of the present thesis and will not be described in detail.

A rationale behind designing an IPC is to achieve a highly durable material that would combine the most desirable properties of the constituent phase materials: the high hardness and wear resistance of the ceramic and improved fracture toughness, ductility, and thermal conductivity of the metal. Unlike fibre reinforced composites, which are typically designed to obtain enhanced properties in preferred directions, the interpenetrating spatial networks can improve material properties in all directions, although for specific applications anisotropic IPCs can be designed, too. Also, when compared with particle reinforced composites, IPCs take advantage of the continuous material networks making up the interpenetrating microstructure.

A review of modelling and processing methods of interpenetrating phase composites was published 10 years ago by [3]. At that time there were many works on manufacturing and experimental testing of IPCs but only a few investigations concerning modelling of fracture and crack growth. Mechanical and thermal properties of IPCs, such as fracture strength, fracture toughness, elastic moduli and thermal expansion coefficients were measured by [13-15,19,20]. The obtained results were promising as compared to the respective values for the phase materials. For example, the Al_2O_3/30%Ni_3Al composite manifested the fracture toughness K_{Ic} = 9.2 MPa $m^{1/2}$, which exceeded the fracture toughness of monolithic Al_2O_3 by a factor of 4 [15]. Del Rio *et al*. [12] manufactured Al_2O_3/Al and Al_2O_3/NiAl interpenetrating composites and examined their behaviour in thermal cycles, which proved good applicability of these materials in high-temperature regimes.

Analytical and numerical modelling of interpenetrating phase composites have been given much less attention in the past than the processing techniques and characterization of their properties. A model of a simple interpenetrating network was proposed almost a century ago in a seminal paper by [21] for estimation of the electrical conductivity of binary aggregates. This model was and is still being used by a number of authors dealing with modelling of IPCs. The interpenetrating microstructure considered by [21] had the form of a unit cell with a 3D-cross structure (*cf*. Fig. 2.1). Inspired by the idea of the 3D-cross unit cell, [22] derived a model for bounds for effective elastic constants of an interpenetrating phase composite.

The simple 3D-cross model of interpenetrating networks (Fig. 2.1) was used by [9] in a numerical and experimental study of uniaxial deformation of Al_2O_3/Al IPC. The same 3D-cross structure was employed in numerical modelling of thermal residual stresses in Al_2O_3/Al and Al_2O_3/Cu IPCs by [10]. The models by [21] and [22] were also pivotal for some of the effective properties estimates developed in this PhD thesis and will be discussed in detail in the following sections.

Image analysis and concept of connectivity could be useful in modelling the effective properties of IPCs. Torquato *et al*. [16] discussed the bounds on effective elastic moduli of interpenetrating composites and evaluated bounds involving three-point structural correlation functions, extracting information on microstructure from an image of a sample of B_4C/Al composite. Feng *et al.* [17,18] developed a model for calculating the effective elastic constants of anisotropic multiphase composites, containing both interpenetrating phases and disconnected inclusions. Park *et al*. [11] proposed an RVE of the IPC microstructure to investigate stiffness and nonlinear behaviour of ceramic metal composites and developed new material processing method for improving contiguity at the same level of volume fraction.

It is commonly known that not only the volume fractions of constituent phases, but also their spatial distributions influence the properties of IPCs such as the fracture toughness, mechanical strength, elastic constants, thermal expansion coefficient, etc. Therefore it was necessary to develop models for IPCs that would reflect real spatial distributions of the interpenetrating phases. Since the interpenetrating phases cannot be extracted as disconnected inclusions, methods used previously for matrix-inclusions composites based on the Eshelby tensor of micromechanics (such as effective media and effective field models) were not adequate for calculation of the effective properties of interpenetrating phase composites [17]. Similarly, the rule of mixtures was shown to yield incorrect predictions of the effective coefficients of thermal expansion [19].

In the last decade the research efforts in the field of IPC modelling were put on case studies and specific microstructures by means of the finite element method (FEM), the effect of phase interpenetration being one of the major issues considered. For example, [23] applied object-oriented finite-element method for microstructural modelling of Ni/Al_2O_3 IPC. Agarwal *et al*. [24,25] modelled elastic properties of IPCs with an effective medium approximation approach using mesh-free element-free Galerkin method. Gao and Rayess [26] proposed an FE model of a tetrakaidecahedral unit cell and compared with experimental results. Xie *et al*. [27] used the phase-field method with Cahn-Hilliard equation of pattern evolution to model an IPC. In the paper [28], Galerkin method was applied to three unit cell models of IPCs, namely simple cubic (SC), face-centered cubic (FCC) and body-centred cubic (BCC). The results were compared with FEM results and Voigt-Reuss, Hashin-Shtrikman and Tuchinskii bounds.

Effective material properties are an essential issue in almost any research investigation of advanced composites with complex microstructures. Fracture processes (i.e. crack inception and growth) are of vital importance in practical applications of metal-ceramic composites in various industry sectors, transportation and energy being the most prominent examples. For a relatively novel type of composites like the IPCs these two research topics posed a scientific challenge with potentially wide industrial impact. It can be stated that the inspiration for this thesis was cognitive in nature, but the results may contribute to solving engineering problems. Anticipating further considerations the modelling of effective elastic properties and fracture, besides their individual importance in the field of composites, are interrelated because the material surrounding the growing macrocrack will be assumed to have effective elastic properties.

The structure of the dissertation is as follows. The state of the art in modelling of the effective material properties and fracture of interpenetrating phase composites is presented in Section 2 and Section 3, respectively. The motivation, aim and theses of the dissertation are formulated in Section 4. The original research results obtained by the author are presented in Sections 5 and 6: the proposed analytical and numerical models of the effective elastic and thermal properties of IPCs in Section 5, whereas the numerical models of fracture of IPCs in Section 6. Summary and final conclusions are given in Section 7. References cited in the text are collected in Section 8.

Modelling of the elastic and fracture parameters of interpenetrating metal-ceramic composites is the main theme of the thesis. Nevertheless to give a wider background of the materials investigated essential information on processing

methods and experimental characterization of the IPCs have been added in Appendix A. It includes some original results of experimental work done by the author during her research stays abroad.

2

State of the art in modelling of effective elastic and thermal properties of IPCs

This Section is an overview of available modelling methods of the effective elastic and thermal properties of interpenetrating phase composites. As it was stressed in Sec. 1, composites with interpenetrating microstructure require special approaches when modelling the effective properties. Only the methods that are microstructure independent, or are devised specifically for composites with spatially continuous microstructures can be applicable for the composites investigated in this thesis.

2.1. Analytical modelling of effective elastic and thermal properties of IPCs

The overall properties of composites are typically investigated due to their practical importance. Numerous analytical models have been proposed in the open literature aiming at an estimation of the effective mechanical properties of composites with different types of reinforcement. Nemat-Nasser and Hori [29] discussed the existing models of the overall mechanical properties of inhomogeneous materials. A comprehensive overview of available models including the dilute approximation, the composite spheres model, the self-consistent and generalized self-consistent scheme, the differential scheme, the Mori-Tanaka theory, the Eshelby equivalent inclusion method and the method of cells, is given in [30]. A detailed study on modelling of effective elastic properties of composites with different types of microstructures can also be found in [31]. Many models of the effective elastic properties of composite materials with relatively simple geometry of phases, such as layered, unidirectional fibrous, or particulate composites are already well established and used in applications.

The interpenetrating phases in IPCs cannot be treated as separate inclusions or fibres, hence modelling methods developed for composites of the matrix-inclusion typology are not suitable for IPCs. Consequently, it was necessary to develop new procedures relevant for the particular microstructure of IPCs. However, most researchers kept on using methods that were either developed for microstructures different than interpenetrating, or were modifications of those methods.

Currently, there are different methods available for estimating the effective properties of interpenetrating phase composites. Before presenting the state-of-the art in this field it should be recalled that (i) mechanical properties of the IPC depend on spatial (anisotropic) distributions of the constituent phases, (ii) methods based on the Eshelby tensor shall not be used for IPCs due to substantially different microstructure that cannot be approximated by the matrix/inclusion model underlying the Eshelby elasticity solution [17,18], (iii) there is a need for more suitable methods of estimating thermal expansion coefficients of IPCs than the rule of mixtures [19], (iv) effective properties estimation of IPCs should be supported with the image analysis and concept of connectivity (cf. [17]).

Janus-Michalska and Pęcherski [32] provided a micromechanical model of determination of the macroscopic properties of open-cell foams. The foam microstructure was modelled with a tetragonal unit cell of cubic symmetry, including the set of four identical half-struts forming a diamond-like structure. The effective constitutive matrix, representing the elasticity tensor, was given for the unit cell. Uniaxial extension and pure shear cases of the unit cell were considered. It was concluded that the considered unit cell was elastically isotropic, and thus its elastic behaviour was described by two Kelvin moduli, describing also the macroscopic properties of the foam. The macroscopic elastic properties were derived from the Kelvin eigenmoduli.

Moon *et al*. [33] modelled the effective elastic Young's modulus of Al/Al_2O_3 composites with interpenetrating network structures, manufactured with pressure-assisted liquid metal infiltration, using different analytical models. The Ravichandran, Tuchinskii, Hashin-Shtrikman, and the effective medium approximation (EMA) analytical methods were applied. The results of analytical methods were compared with the results of experimental Young's modulus measurements with resonance frequency technique.

Jhaver [34] presented manufacturing methods, characterization and modelling of the effective elastic properties of aluminium and syntactic polymer foam lightweight interpenetrating polymer composites. The IPCs were produced with a pressureless

infiltration method. The FEM model of the IPC unit cell based on the Kelvin cell was developed to calculate stress-strain response of the composite in the uniaxial compression. For estimation of the effective elastic modulus of the IPC, models of Hashin-Shtrikman, Tuchinskii and Ravichandran were used.

Agarwal *et al*. [24,25] developed two models: the unit cell and the self-consistent model to find the elastic properties of IPCs. Volume fraction and random microstructure were accounted for. The mesh-free, element-free Galerkin method was used. The effective medium approximation approach was adopted to calculate the effective properties of IPCs.

He [35] presented a unit cell based finite element model developed to estimate the effective Young's modulus, Poisson's ratio and the coefficient of thermal expansion of triply periodic IPCs. Five IPCs of different volume fractions of constituents were investigated. ANSYS software was used for FE simulations. The predicted results were compared with existing theoretical and experimental results.

The elastic-plastic behaviour of stainless-steel/bronze interpenetrating phase composites with damage evolution was described in [36]. Tippur [37] studied epoxy based Syntactic Foam (SF) and open-cell aluminum scaffolds IPC foams. The composite specimens were subjected to quasi-static compression tests. A finite element model based on the Kelvin cell was developed to perform an analysis of compression with regard to elastic-plastic large deformations.

2.1.1. Bounds on the effective properties of composites with interpenetrating microstructures

Voigt and Reuss bounds

The Voigt and Reuss models are the most popular methods of estimation of effective mechanical properties of composites irrespective of their microstructure. They provide the widest bounds on the effective elastic properties. Only the elastic properties and volume fractions of the phase materials are taken into account. Thus, these models are universal for all possible structures of composites and enable comparison of different methods.

The Voigt model, often called the *rule of mixtures*, is based on the iso-strain assumption. For an *n*-phase composite with each phase elastic and isotropic, the formulae for the components of the effective stiffness tensor: shear modulus μ_{Eff} and bulk modulus K_{Eff}, take the form

$$\mu_{Eff} = \sum_{i=0}^{n} c_i \mu_i \,, \qquad K_{Eff} = \sum_{i=0}^{n} c_i K_i \,, \tag{2.1}$$

where μ_i is the shear modulus of the i-th phase, K_i – the bulk modulus of the i-th phase, c_i - volume fraction of the i-th phase.

From equations $(2.1)_{1,2}$, using the well-known relations between the elastic constants

$$\begin{aligned} E &= 2\mu(1+\nu), \\ E &= 3K(1-2\nu), \\ E &= \frac{9\mu K}{3K+\mu}, \end{aligned} \tag{2.2}$$

the formulae for the effective Young's modulus and Poisson's ratio for a two-phase composite can be written as

$$\begin{aligned} E_{Eff} &= \frac{9\mu_{Eff}K_{Eff}}{3K_{Eff}+\mu_{Eff}} = \\ &= \frac{[E_A(1-f)(1+\nu_B)+fE_B(1+\nu_A)][E_A(1-f)(1-2\nu_B)+fE_B(1-2\nu_A)]}{E_A(1-f)(1+\nu_B)(1-2\nu_B)+fE_B(1+\nu_A)(1-2\nu_A)}, \\ \nu_{Eff} &= \frac{3K_{Eff}-2\mu_{Eff}}{2\mu_{Eff}+6K_{Eff}} = \\ &= \frac{\nu_A E_A(1-f)(1+\nu_B)(1-2\nu_B)+\nu_B E_B f(1-\nu_A)(1-2\nu_A)}{E_A(1-f)(1+\nu_B)(1-2\nu_B)+E_B f(1+\nu_A)(1-2\nu_A)}, \end{aligned} \tag{2.3}$$

where E denotes Young's modulus, ν - Poisson's ratio, subscripts: $_{A,\,B}$ and $_{Eff}$ denote phase A, phase B and the effective property, respectively, f – is the volume fraction of phase B.

The Reuss model is based on the iso-stress assumption. For an n-phase composite, each phase being elastic and isotropic, the formulae for shear modulus μ_{Eff} and bulk modulus K_{Eff}, have the form

$$\mu_{Eff} = \left(\sum_{i=0}^{n} \frac{c_i}{\mu_i} \right)^{-1}, \tag{2.4}_1$$

$$K_{Eff} = \left(\sum_{i=0}^{n} \frac{c_i}{K_i} \right)^{-1}. \qquad (2.4)_2$$

Using relations $(2.2)_{1,2,3}$, the formulae for the effective Young's modulus and Poisson's ratio for a two-phase composite can be rewritten as

$$E_{Eff} = \frac{9\mu_{Eff} K_{Eff}}{3K_{Eff} + \mu_{Eff}} = \frac{E_A E_B}{E_B(1-f) + E_A f},$$
$$\nu_{Eff} = \frac{3K_{Eff} - 2\mu_{Eff}}{2\mu_{Eff} + 6K_{Eff}} = \frac{fE_A\nu_B + (1-f)E_B\nu_A}{fE_A + (1-f)E_B}. \qquad (2.5)$$

The Voigt and Reuss models are simple and easy to use. However, Aboudi [30] stressed that both the iso-strain and the iso-stress assumption might not be fully accurate. For the Voigt approximation this is due to the lack of equilibrium of tractions at phase boundaries, and for the Reuss approximation this is due to the fact that under implied strains both phases may not remain bonded.

Rosen-Hashin bounds on effective thermal properties

The bounds of Rosen and Hashin [38] for the effective coefficients of thermal expansion are analogous to Hashin-Shtrikman bounds for the effective elastic constants. Levin [39] showed the relationship for a two-phase isotropic composite between coefficients of thermal expansion of the components and the effective bulk moduli. Rosen and Hashin [38] proposed a generalized relation between the effective coefficients of thermal expansion and the effective mechanical properties for a two-phase anisotropic composite. They derived formulae for bounds on the effective coefficient of thermal expansion from the components of the compliance tensors of the effective composite material and its constituents.

For an isotropic composite with isotropic constituent materials, Rosen and Hashin [38] expressed components of the compliance tensor as functions of the bulk moduli. As a result, the effective coefficient of thermal expansion α_{Eff} of such a composite is a function of the bulk moduli of its constituents K_A and K_B, and the effective bulk modulus K_{Eff}, derived according to a relevant model (*e.g.* according to [40]), namely

$$\alpha_{Eff} = \alpha^{Voigt} + (\alpha_A - \alpha_B)\left(\frac{1}{K_A} - \frac{1}{K_B}\right)^{-1}\left[\frac{1}{K_{Eff}} - \left\{\frac{1}{K}\right\}^{Voigt}\right], \qquad (2.6)$$

where the indices denote: $_{A,\ B}$ – composite phases, $_{Eff}$ – effective quantity, ^{Voigt} denotes volume average according to Voigt model, $\alpha^{Voigt} = f_A\alpha_A + f_B\alpha_B$ – Voigt estimate of averaged coefficient of thermal expansion, $\left\{\frac{1}{K}\right\}^{Voigt} = \frac{f_A}{K_A} + \frac{f_B}{K_B}$ – Voigt estimate of averaged inverse of bulk modulus, f_A, f_B – volume fractions of the respective phases.

2.1.2. Models designed specifically for composites with interpenetrating microstructures

The effective elastic properties of composites depend on many parameters. The parameters that are common for all models of the effective elastic properties are material constants and volume fractions of the phases. However, such factors as geometrical shape of particles, presence of discontinuities and damage, or effect of temperature also contribute to the overall material constants. Thus, it was necessary to develop methods suitable for composites with specific microstructures like the interpenetrating phase composites that would account for these factors. For IPCs relevant methods were proposed by *e.g.* [17,18,22] and [41,42]. They are different combinations of the Voigt or Reuss estimates. The works [30,31,43] or [44] should also be mentioned in this context. Since the analytical estimates by Tuchinskii and Feng are essential as the reference solutions in this thesis, they will be outlined in more detail in the following sections.

Models of Frey and Tuchinskii

Due to complex spatial structure of the IPCs, a workable model of effective elastic properties should be straightforward but at the same time capable of accounting for the salient features of the IPC microstructure. The idea of a simple geometrical model for co-continuous networks microstructure may be found in the early paper [21] on modelling of electrical conductivity of binary aggregates. Based on the model of [21], [22] developed a model for calculation of bounds for effective elastic constants of a bimetallic composite. Tuchinskii assumed macroscopically homogeneous and isotropic material. The unit cell was cubic with interpenetrating phases having quadratic cross sections and symmetric within the unit cell. Two division directions of the unit cell using the iso-strain and iso-stress assumptions

were proposed. A detailed discussion of Tuchinskii's derivation methodology is given in [7].

The Tuchinskii's lower bound for the effective Young's modulus is as follows

$$\overline{E}^{low} = a^2 E_B + (1-a)^2 E_A + 2a(1-a)\left(\frac{a}{E_B} + \frac{1-a}{E_A}\right)^{-1}, \tag{2.7}$$

where A, B denote respective phases as in Fig. 2.1 (A for the outer white phase, B for the inner dark phase), a denotes a normalized size parameter of the phase B.

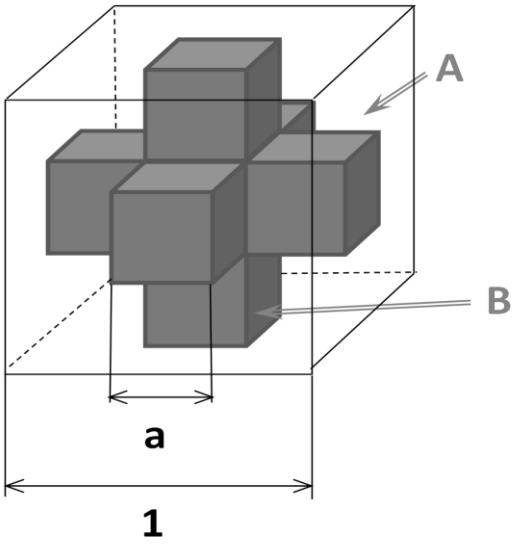

Figure 2.1. Unit cell representing two-phase interpenetrating microstructure, according to [21] and [22].

The Tuchinskii's upper bound for the effective Young's modulus is

$$\overline{E}^{up} = \left[\frac{1-a}{(1-a^2)E_A + a^2 E_B} + \frac{a}{(1-a^2)E_A + (2-a)a\,E_B}\right]^{-1}. \tag{2.8}$$

The expressions for the bulk and shear moduli follow from the relationships between the elastic constants. The expressions for the effective Poisson's ratio in [22] seem to contain errors. The values for upper and lower bounds are calculated

from the Poisson ratios called "parallel" and "perpendicular" that correspond to different unit cell sectioning directions. The "parallel" value is calculated according to the rule of mixtures as

$$\nu_{parallel} = f_A \nu_A + f_B \nu_B. \tag{2.9}$$

The "perpendicular" value is calculated according to the following formula

$$\nu_{perpendicular} = \frac{\left(f_A \nu_A + f_B \nu_B\right) E_A E_B}{\left(f_A E_A + f_B E_B\right)\left(f_A E_B + f_B E_A\right)} = \frac{\nu_{parallel} E^{Reuss}}{E^{Voigt}}. \tag{2.10}$$

From the expression (2.10) one can see that it is a proportionality relation between the Poisson ratios and the Young moduli. Such an assumption is not approvable for an isotropic material. Moreover, one bound for the Poisson ratio is derived from both bounds for the Young modulus. This approach leads to erroneous formulae for the bounds for the Poisson ratio. Consequently, also the bounds for $\overline{G}$ and $\overline{K}$, derived with the use of bounds for the Poisson ratio, are incorrect.

There are also some doubts with regard to Tuchinskii's formulation of the bounds for Poisson's ratio calculated from (2.9) and (2.10) as remarked by [7]. The expression for the upper bound in [22]

$$\overline{\nu} = \frac{\left[1 - a^2\left(1 - a^2\,\nu_B/\nu_A\right)\right]\left[1 - a\left(1 - m\right)\right]}{\left[1 - a\left(1 - n\right)\right]\left[1 - a\left(1 - 1/n\right)\right]}, \tag{2.11}_1$$

with

$$m = \frac{(1-a)^2 + a(2-a)(\nu_B/\nu_A)}{1 - a^2 + a^2(\nu_B/\nu_A)},$$
$$n = \frac{(1-a)^2 + (E_B/E_A)(2-a)a}{1 - a^2(E_B/E_A)a^2}, \tag{2.11}_{2,3}$$

is not in accordance with the model due to misprints. It is believed that the correct upper bound for $\overline{\nu}$ in model of [22] should read

$$\overline{\nu} = \frac{1 - a^2\left(3 - 2a\right)\left(1 - \nu_B/\nu_A\right)}{\left[1 - a\left(1 - n\right)\right]\left[1 - a\left(1 - 1/n\right)\right]}, \tag{2.12}_1$$

with a misprint removed in the denominator of the expression for n, i.e.

$$n = \frac{(1-a)^2 + (E_B/E_A)(2-a)a}{1-a^2 + (E_B/E_A)a^2}. \qquad (2.12)_2$$

The lower bound for $\bar{\nu}$ given in the original paper by [22]

$$\bar{\nu} = (1-a)^2 \nu_A + a^2 \nu_B + \frac{2a(1-a)((1-a)\nu_A + a\nu_B)\dfrac{E_B}{E_A}}{\left(1-a+a\dfrac{E_B}{E_A}\right)\left(a+(1-a)\dfrac{E_B}{E_A}\right)}, \qquad (2.13)$$

is correct. However, it can be shown that this bound falls outside the Voigt and Reuss bounds, which give the widest range of admissible effective moduli. It may, thus, be concluded that Tuchinskii's assumptions taken to evaluate the effective Poisson ratio are not fully justified. There are also formulae in [22] for the shear and bulk moduli. However, due to the errors in the formula for Poisson's ratio as discussed above, the estimates for $\bar{G}$ and $\bar{K}$ should also be taken with caution.

The model of Feng

Feng *et al*. [17,18] developed models for calculating the effective elastic constants of anisotropic multiphase composites, containing both interpenetrating phases and disconnected inclusions. His idea of a unit cell enabled investigation of various microstructures, more complex than in the Tuchinskii unit cell. As shown in Fig. 2.2, the Feng unit cell enables consideration of multiple 3-D cross phases that have different dimensions in each direction.

The microstructure of composite material in the Feng model is represented by the unit cell model. The representation of the phases depends on their connectivity which describes spatial arrangement of each phase and gives the number of dimensions in which each component is self-connected. The general assumptions of the Feng model are such that macroscopically the composite material is homogeneous and may consist of n phases. Elastic properties and spatial arrangements of individual phases may be anisotropic. The generic model allows n_1 phases that are continuously self-connected in three dimensions, and n_2 ($n_1 + n_2 = n$) phases that are well-defined, disconnected inclusions. Phases that are continuously self-connected, in the unit cell have the form of three orthogonal branches with

rectangular cross sections. The material existing both in the form of a continuous network and dispersed inclusions should be considered as two different phases: the matrix (denoted with *m*) comprising all the continuous phases which, in turn, contain all the inclusions.

In the Feng model the effective elastic constants for the composite containing inclusions are obtained by means of the Mori–Tanaka method (cf. [31]). The interpenetrating phase composite (with no inclusions) can be described using two or more continuous materials, i.e. when the composite consists of $n_1 = n$ continuous phases only. An example of such model with two interpenetrating phases is depicted in Fig. 2.3(a).

In this case a cubic unit cell is assumed, so the linear dimension of each side of the cell is equal to unity

$$a_1 + \mathrm{K} + a_n = b_1 + \mathrm{K} + b_n = c_1 + \mathrm{K} + c_n = 1. \tag{2.14}$$

Hence, the dimensions of interpenetrating phases can be represented by non-dimensional size parameters a_α, b_α, c_α that are related to the size of the cell. The volume fraction f_α of the α-th phase becomes [17]

$$f_\alpha = a_\alpha b_\alpha + a_\alpha c_\alpha + b_\alpha c_\alpha - 2a_\alpha b_\alpha c_\alpha \qquad (no\ sum). \tag{2.15}$$

The computation of the effective elastic constants is based on a combination of the iso-stress and iso-strain assumptions. The unit cell (consisting of n_1 self-connected phases) is divided into $n_1 \times n_1$ sub-cells, each consisting of n_1 series blocks. The effective moduli of each sub-cell are determined by adopting the iso-stress assumption. Finally, the elastic moduli of the whole cell can be calculated from the $n_1 \times n_1$ parallel sub-cells by using the iso-strain assumption. The boundary conditions are assumed as periodic. The unit cell is first decomposed along the boundaries between the phases, parallel to the coordinates (Fig. 2.3(b)).

The effective Young's modulus is given as

$$\overline{E} = \sum_{\alpha=1}^{n_1} \sum_{\beta=1}^{n_1} \left\{ \left[\left(\sum_{\gamma=1}^{n_1} \frac{V_{\alpha\beta\gamma}}{E_{\alpha\beta\gamma}} \right)^{-1} \sum_{\gamma=1}^{n_1} V_{\alpha\beta\gamma} \right] \sum_{\gamma=1}^{n_1} V_{\alpha\beta\gamma} \right\}, \tag{2.16}$$

where α, β, γ are serial numbers of a sub-cell in the x_1, x_2, x_3 directions and $V_{\alpha\beta\gamma}$ is the volume of the (α, β, γ) sub-cell.

The effective shear modulus has the same form as Young's modulus, namely

$$\overline{G} = \sum_{\alpha=1}^{n_1} \sum_{\beta=1}^{n_1} \left\{ \left[\left(\sum_{\gamma=1}^{n_1} \frac{V_{\alpha\beta\gamma}}{G_{\alpha\beta\gamma}} \right)^{-1} \sum_{\gamma=1}^{n_1} V_{\alpha\beta\gamma} \right] \sum_{\gamma=1}^{n_1} V_{\alpha\beta\gamma} \right\}. \tag{2.17}$$

For the isotropic composite it is assumed that all the directions of decomposition are equal (although for different directions of decomposition of the unit cell different formulas are obtained) and after averaging over the whole composite volume the differences between the results of decomposition in different directions will vanish. However, for the anisotropic composite it was not specified in original papers [17,18] how the decomposition directions should correspond to the anisotropy.

From the assumed uniform spatial distribution of both phases it follows that

$$a_1 = b_1 = c_1 = a, \quad a_2 = b_2 = c_2 = 1 - a\,. \tag{2.18}$$

The "reinforcing phase" and the "matrix" are further denoted as phase *1* and *2*, respectively. The volume fraction of the phase *1* is

$$f_1 = a^3(3 - 2a). \tag{2.19}$$

Using Eqs. (2.16), (2.18) and (2.19) the effective elastic moduli based on the Voigt and Reuss models were derived in [17,18] as

$$\overline{E} = a^2 E_1 + (1-a)^2 E_2 + 2a(1-a)\left(\frac{a}{E_1} + \frac{1-a}{E_2} \right)^{-1}, \tag{2.20}$$

$$\overline{G} = a^2 G_1 + (1-a)^2 G_2 + 2a(1-a)\left(\frac{a}{G_1} + \frac{1-a}{G_2} \right)^{-1}. \tag{2.21}$$

Even though the Feng model was designed for a two-phase interpenetrating composite, a generic model can easily be adopted for a variety of multi-phase composite geometries. It may be potentially very useful for different types of multi-phase composites as well as for two-phase interpenetrating composites with voids (damage) as a third phase.

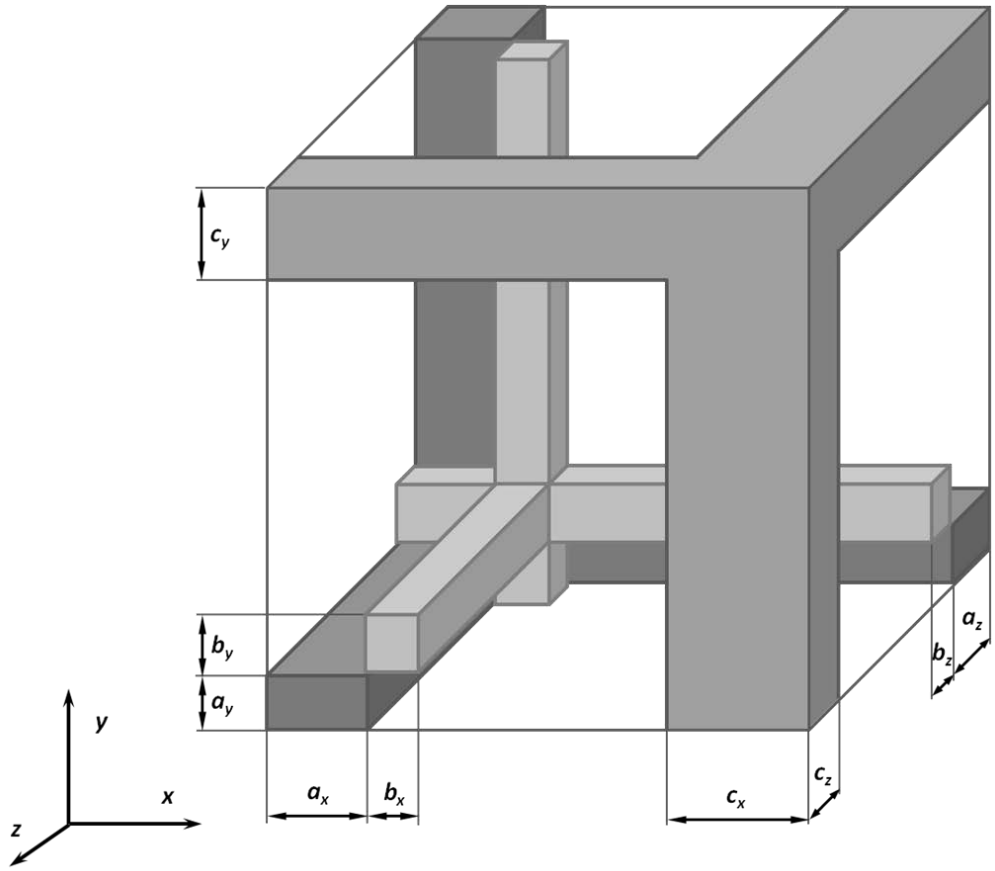

Figure 2.2 The Feng *et al*. [17,18] unit cell of an interpenetrating four-phase composite with phases that have different dimensions in each direction *x*, *y*, *z*; blue *a*, yellow *b* and green *c* phases visible, fourth phase invisible (based on [17,18], with the permission of publishers).

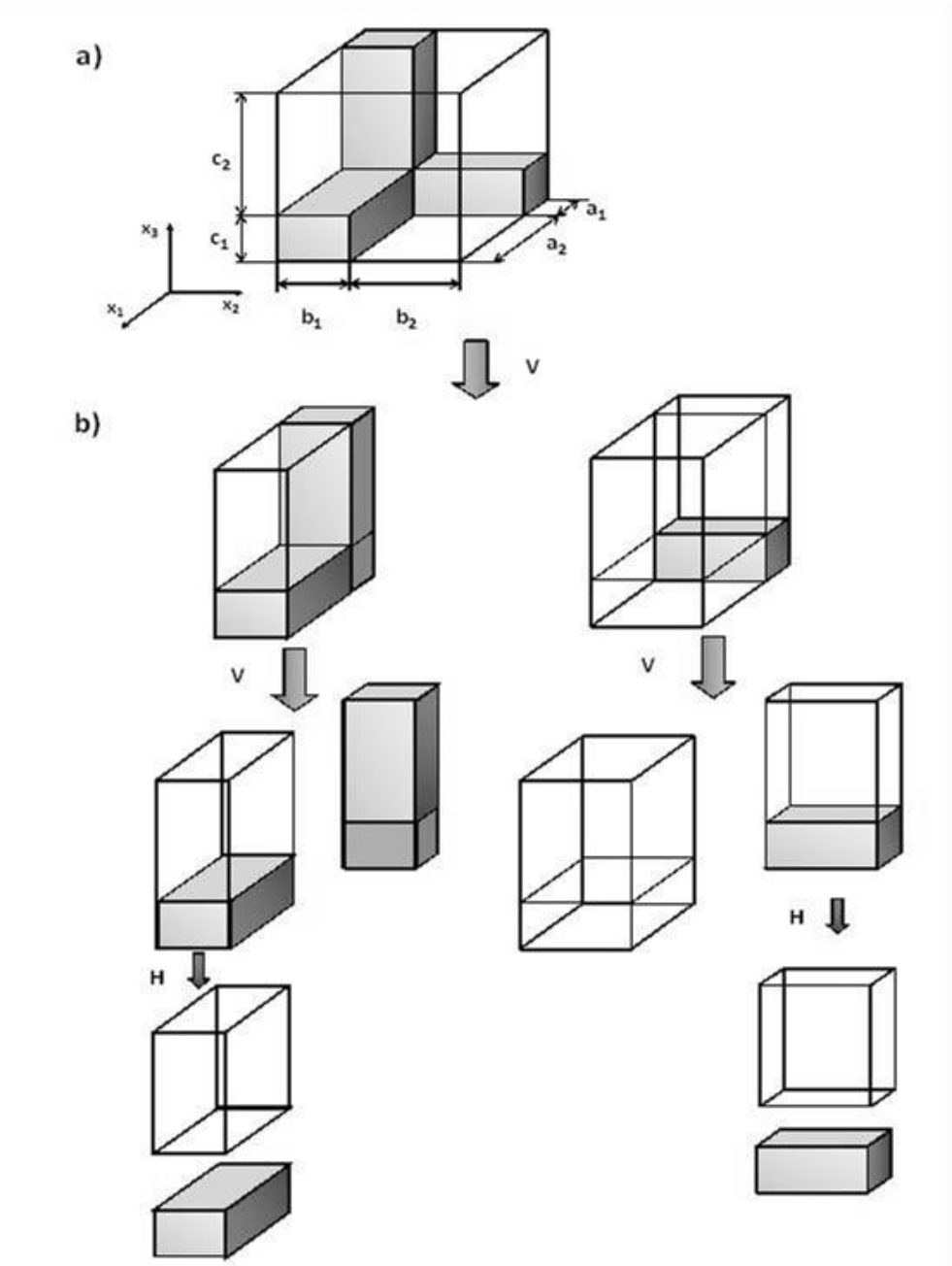

Figure 2.3 (a) Feng *et al*. [17,18] unit cell of an interpenetrating two-phase composite model and (b) its vertical (V) and horizontal (H) decomposition (based on [17,18], with the permission of publishers).

2.2. Numerical modelling of effective elastic properties of IPCs

In order to account for complicated, real microstructure of multi-phase materials, models using randomly generated microstructures were developed. However, to generate a microstructure that forms interpenetrating networks, it is necessary to apply some restrictions on the data [7]. It may be seen in Fig. A.6 (Appendix) that real interpenetrating microstructures may have different, specific topologies depending on manufacturing. Such differences cannot be properly addressed with a random generation of the composite phases. Therefore, the attention will be focused on arranged microstructures that ensure interpenetration of the phases either by generation of a simple interpenetrating microstructure, or by considering real IPC microstructures obtained from micro-CT experiments. It should also be noted, that in case of microstructures obtained from spherical or ellipsoidal particles, fulfillment of the conditions for percolating microstructure (that is, with volume fractions of phases within percolation limits), will not assure bearing tensile loads and thus, the non-zero stiffness of the percolating phase network. Arbitrarily created random microstructures can have quite high volume ratio of separate particles and do not need to be interpenetrating at all. Therefore, some additional conditions need to be applied to assure connectivity between neighbouring particles, and, in effect, interpenetrating microstructure.

A case described by [7] may serve as an example of such an approach. To sum up, random modelling in application to interpenetrating microstructures is limited and should not be taken without special caution. Deterministic approximations of interpenetrating microstructures have also been developed for numerical modelling of the effective material properties [9,34,37,45,46].

Random numerical models of IPC microstructure

Mishnaevsky [41] developed a numerical programme for generation of multiparticle or percolating bimaterial unit cells. The generated voxel-based FE models of composite microstructures were used to calculate the effective properties. The RVE was represented as an array of voxels carrying information about the local properties and, thus, representing the spatial distribution of phases. Three-dimensional random chessboard or graded microstructures were generated with the proposed programme, using a random number generator. The random distributions

of phases were generated in three directions in space to create 3D random chessboard microstructure. To create graded microstructure, along one of the directions graded distribution was applied, according to the formula allowing varying gradient interface smoothness. The percolation analysis of the obtained microstructures was performed. Percolating random microstructures were obtained for volume fractions of the phases between 32% and 68%.

A model of creating random composite microstructures is described in [7]. Two-phase, macroscopically homogeneous and isotropic materials were considered. A cubic piece of composite was created with a given voxel number and volume fraction of phases by assigning material properties of one of the phases to randomly chosen elements, and the properties of another phase to the remaining ones. Interpenetrating microstructure was ensured with the procedure checking the interconnections between voxels belonging to the same material. Voxels of the same material with common faces were considered as connected. Percolating microstructures were obtained for volume fractions of phases between 31.16% and 68.84%.

A random interpenetrating unit cell was proposed by Agarwal *et al*. [24] to evaluate the elastic properties of an IPC and to obtain the stress-strain curves for an elastic-plastic IPC with element free Galerkin method [25]. However, it was not explained in these works how the microstructure was created in 3D.

Randomly created composite microstructures were used also by [27] to model the effective mechanical properties of IPCs. These authors used the phase field method and the Cahn-Hilliard equation to create a random IPC microstructure.

Different methods of reconstruction of complex microstructures of engineering materials are given by [47]. Quantitative image analysis techniques aimed at the determination of global parameters characterizing geometrical features of the microstructure (*e.g*. mean intercept length or mean grain volume) such as methods describing the geometry of the grain boundaries, di-sector, point sampled intercepts or Saltykov reconstruction, were described. The methods of reconstruction of the microstructure of the ceramic foams from the micro-CT images based on statistical characteristics of the geometry of the pores, were proposed by [48] and [49]. The method of designing cellular microstructures with prescribed distribution of size and orientation of grains or cells was proposed by [50]. The Laguerre-Voronoi tesselations (LVT) were applied to obtain the microstructure of the self-supporting foam composed of interconnected cyllindrical struts by [51]. Also the limitations of the methods of randomized tesselations were pointed out therein.

Deterministic and micro-CT based numerical models of IPC microstructure

Besides random numerical models different deterministic numerical models with simplified IPC geometry were developed (cf. [9,34,37,46]). In these models the IPC microstructure is often approximated as periodic, with unit cells consisting of different composite components of simple geometry. For example in the models of [34,37,46], the unit cell model is based on *Kelvin cell*, approximating the microstructure of syntactic foam based, lightweight polymer IPCs.

The most accurate representation of real IPC microstructures may be achieved with techniques of 3D microstructure mapping, such as slicing a composite piece to obtain series of 2D images (*cf*. [52]). Nondestructive methods of reconstruction of composite microstructure include DVI (Digital Volume Imaging) technique delivering a series of 2D files, or computed microtomography (micro-CT), providing 3D images. Both DVI and micro-CT techniques were used by [53,54] to represent the microstructures with non-woven fibres with finite element meshes. For the creation of the FEM mesh from 3D microstructure image, the Simpleware ScanIP/FE software was used. Also particle reinforced metal-matrix composites were modelled using micro-CT spatial images by [55,56]. The model of mapping the small geometry features such as small pores and fissures below the micro-CT resolution, was proposed by [57]. Roux *et al*. [58] used X-ray computed tomography to estimate the three-dimensional deformation fields in polypropylene solid foam undergoing compression test. SiC/Al IPC was modelled by [59] using real microstructure micro-CT images, transferred into ANSYS/LS DYNA FE meshes with Simpleware ScanIP/FE software. The issue of representative volume element (RVE) size for microstructure images of IPCs obtained from micro-CT was analyzed by [60], *cf*. also [48].

3

Modelling of deformation and fracture of IPC

The mechanical and thermal properties of the phase materials in metal-ceramic composites usually manifest significant differences, which affect the fracture mechanisms of the composite. Additionally, in the case of IPCs the complex microstructure of mutually interpenetrating phases makes modelling of the crack onset and growth quite difficult. Experimental measurements of fracture properties of IPCs are cumbersome and expensive due to the high cost of pressure-assisted infiltration of ceramic preforms and tough machining of notched specimens for the fracture tests (*e.g.* SEVNB or Compact Tension). Therefore, reliable predictions of the stress intensity factors or *J*-integral for IPCs along with their critical values (fracture toughness) by modelling are of considerable scientific and practical importance.

According to Seweryn [61] three main stages of the fracture process computations may be distinguished: (1) establishing the shape, initial and boundary conditions, load history for the structural element, and computation of stress and displacement fields, (2) indication of element "hot spots" most prone to failure and estimation of the failure load, (3) computation of the fracture process until the element failure with the use of fracture mechanics criteria and methods. Numerical approach is required for the analysis of stress fields with singularities in elements of complicated shapes. This observation is quite relevant for irregular microstructures of the interpenetrating phase composites investigated in this thesis.

For quasi-brittle materials two ways of modelling of fracture may be followed [62]. The *continuum mechanics* approach, when damage and fracture are modelled within the constitutive models at the continuum level, was developed *e.g.* in the works of [62,63]. Another approach to modelling of fracture in quasi-brittle materials is the *discontinuum* approach, where the crack in the numerical model is treated as a geometric discontinuity (*cf.* [62]). The methodology of modelling the crack problem

in metal-ceramic IPCs undertaken within the present thesis, will represent the discontinuum approach.

Different toughening mechanisms may impede the crack growth in metal-ceramic composites. The most frequently observed ones are (Fig. 3.1): crack bridging [64–70], crack deflection [71,72], crack shielding [73,74], crack branching [75,76] and fibre pullout [77–82].

While numerous experimental reports on fracture of IPCs were recently published [83–88], there are still not too many works on analytical and numerical modelling of the crack growth in this specific type of composites. In the general context of metal-ceramic composites (including MMCs, cermets and IPCs) the literature relevant to this issue is substantial. A state of the art in modelling of fracture of metal-ceramic composites with ductile reinforcements, including the subclass of IPCs, was presented *e.g.* by [3] and updated in [89].

Budiansky *et al.* [90] described *bridging-spring* model. The authors studied the *small-scale bridging* case and the fracture toughness of ceramics reinforced with particles. Sigl *et al.* [91] considered ductile particles bridging the crack in ceramics and proposed a necking particle model. Beldica and Botsis [92] presented BEM numerical model of Compact Tension specimen of a composite with long aligned fibres. In their model fibres were parallel to the loading direction. No bridging model was given. The bridging mechanism was extensively modelled by [93] with the main objective to determine the nominal stresses in the reinforcing ductile ligament. Once the nominal stresses are determined the elastic energy release rate increase ΔG due to crack bridging can be computed. Emmel [64] studied the problem of a plastically deformable bridging fibre embedded in an elastic matrix with numerical models based on the model of [93] and experiments of [94]. The σ–u relationships resulting from the model of axisymmetric fibre perpendicular to the crack plane were then used in a model of the Compact Tension test for a metal fibre reinforced composite. The J-integral and K–factors were calculated numerically using ABAQUS.

Grassi and Zhang [66] developed a FEM model of interlaminar fracture of a carbon-epoxy composite with z-fibre reinforcements with nonlinear interface elements and showed that the bridging reinforcements increase the crack growth resistance and delay the delamination growth. Lapczyk and Hurtado [95] developed an anisotropic model of damage to describe failure and post-failure behaviour of linear elastic materials with fibres in plane strain, using various criteria for damage initiation and modes of failure. Bobiński and Tejchman [96] compared continuous

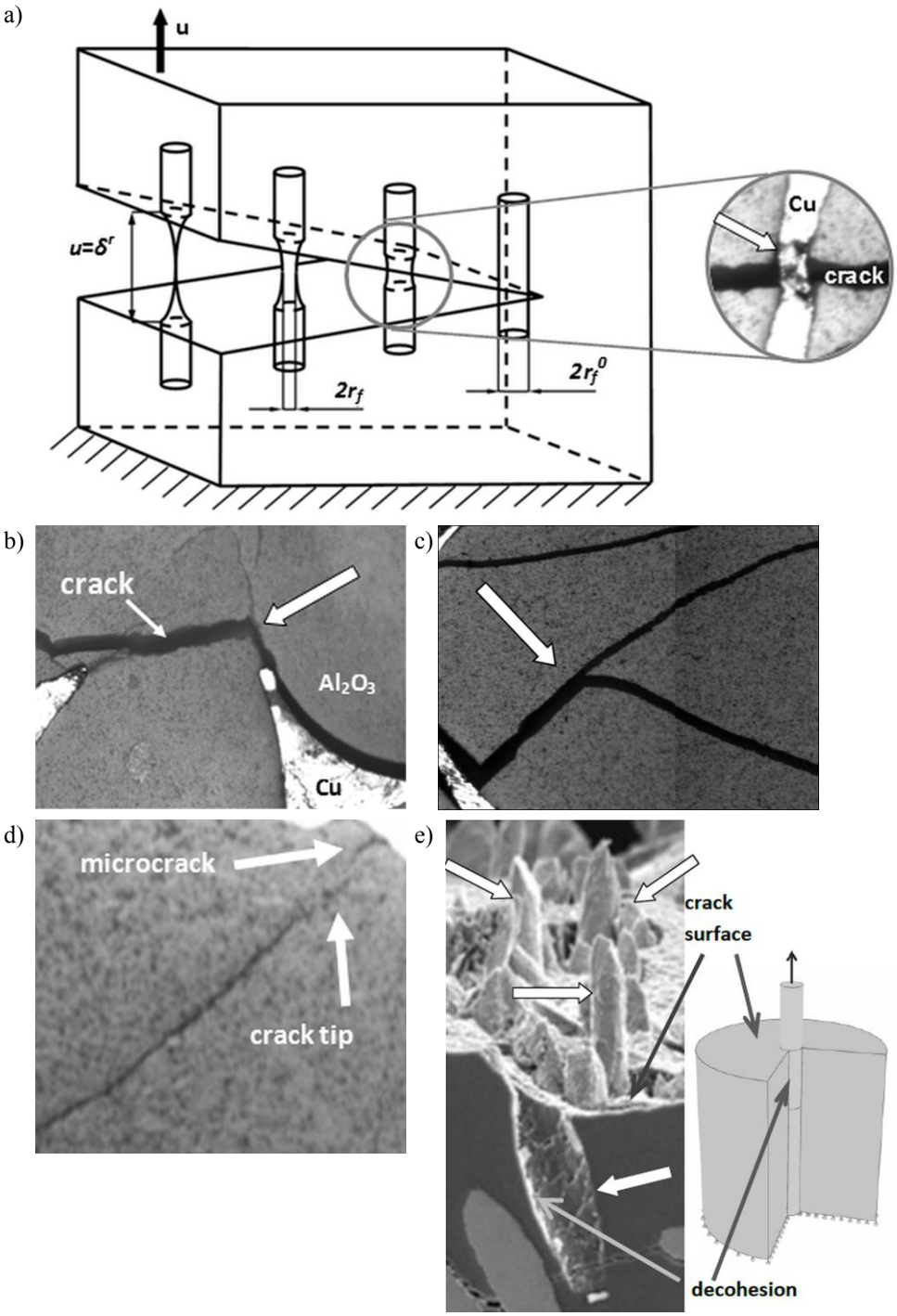

Figure 3.1. Schemes of crack toughening mechanisms in metal-ceramic composites (yellow arrows mark respective physical mechanisms); (a) crack bridging (reproduced from [89] with

permission of *Int. J. Damage Mechanics*, (b) crack deflection, (c) crack branching, (d) crack shielding, (e) fibre pullout with matrix decohesion (SEM image from [97]).

and discrete constitutive models of fracture in concrete. A micromechanical elastoplastic damage model to estimate the overall mechanical behaviour and interfacial microcrack growth in fibre-reinforced composites was proposed by [98].

The behaviour of composites with ductile reinforcements and crack bridging is related to the effect of debonding at the fibre/matrix interface [89]. The fracture toughness and the failure mode of the composite are affected by the mechanical properties of the fibre/matrix interface. The gradual decohesion and failure of the cohesive interface was modelled in ABAQUS for the heat curing epoxy adhesive layer by [99], hybrid, single lap, and double lap joints by [100], or the interface in WC/Co composite by [101]. An important factor influencing not only the interface behaviour but also the overall behaviour of the composite, is porosity (*cf*. 102–104]). The interfacial strength is often evaluated experimentally using the fibre pullout test. The fibre pullout test was used by [78] to obtain material properties of a composite reinforced with fibres assuming different models for frictional stresses on the debonded interface. This test was also modelled analytically and numerically *e.g*. by [82,105–107].

The cohesive zone model (CZM) relates the interfacial force with the crack opening displacement. The zone of fracture process is reduced to a zero-thickness zone made up of two coinciding cohesive surfaces that separate under loading according to a certain traction–separation law. Analytical and numerical modelling of the pullout problem and comparison with experiments was given by [79]. Cohesive elements were used by [96] to model crack nucleation and propagation at the interfaces between matrix and grains in concrete. The pullout test of a single fibre was analysed numerically with the use of CZM by [80]. The pullout problem of a brittle composite with embedded fibre, where the process of fibre debonding was modelled as a mode II crack with frictional sliding, was discussed by [77]. Cohesive damage modelling was used by [82] to develop a FEM model for a single fibre pullout with debonding, aiming at determination of the load-displacement relationship for the fibre. An extension of the model of [82] is a part of this thesis and will be described in Sec. 6.

Real material microstructure images obtained with micro-CT technique were used for modleling of fracture in concrete bending beams by [108]. The concrete was modelled as a four-phase material, with regard to interfacial transition zones (ITZ) and macrovoids. The microstructure of concrete and the developing crack

were observed with micro-CT technique before and after four-point bending test. Microstructure image obtained from micro-CT was applied in 2D numerical model of four-point bending test. Kozicki and Tejchman [109] modelled fracture using discrete lattice model for concrete reinforced with randomly distributed short steel fibres during three-point bending test.

Emmel [110] proposed a numerical model of a Compact-Tension specimen made of layered $Al_2O_3/Cu/Al_2O_3$ composite, with elastic ceramic outer parts and an inner thin stripe of elastic-plastic copper, in which a crack propagated along the metal-ceramic interface due to the fact that the pre-crack was co-linear with the interface between alumina and copper. The presence of spherical cavities and spherical inclusions of copper oxide in the copper layer was included in the model. The spherical inclusions of copper oxide were modelled at the copper-alumina interface. Cavity growth was analysed in the plastically deformable copper phase. The other materials, *i.e.* alumina and copper oxide, were taken as linear elastic. The problem of the macrocrack growth in a compact-tension specimen made of such a composite was investigated and modelled numerically.

3.1. Crack toughening by bridging – basic concepts and overview of the main models

One of the primary objectives in fracture modelling of IPC materials is the determination of fracture energy and fracture toughness increase due to plastically deforming ligaments connecting the crack surfaces. A key ingredient of all such models is the force-displacement relationship in the reinforcing ligament. It is a challenging issue in analytical and numerical models due to a complex state of deformation comprising *i.a.* large plastic strains and necking of the ligament, ligament/matrix decohesion and crack opening and growth. Among the crack toughening mechanisms encountered in metal-ceramic composites (*cf.* Fig. 3.1) crack bridging is typically reported as the dominating mechanism in IPCs as shown in Fig. 3.2.

In order to make a review of the existing crack bridging models more comprehensive and, at the same time, prepare the ground for the introduction of own numerical models for fracture parameters of a bridged crack (cf. Sec. 6), the basic concept of *J*-integral and its relation to the elastic energy release rate G and the stress intensity factor K_I in mode I will now be recalled (see also [44,61] for further discussion).

The *J*-integral introduced independently by [111] and [112] is defined as the integral of the strain energy density U and tractions $\mathbf{T} = \boldsymbol{\sigma} \cdot \mathbf{n}$, $T_i = \sigma_{ij} n_j$, acting inside and along contour Γ in a homogeneous elastic material under a two-dimensional small deformation field, with the assumptions of zero volume forces acting on the material.

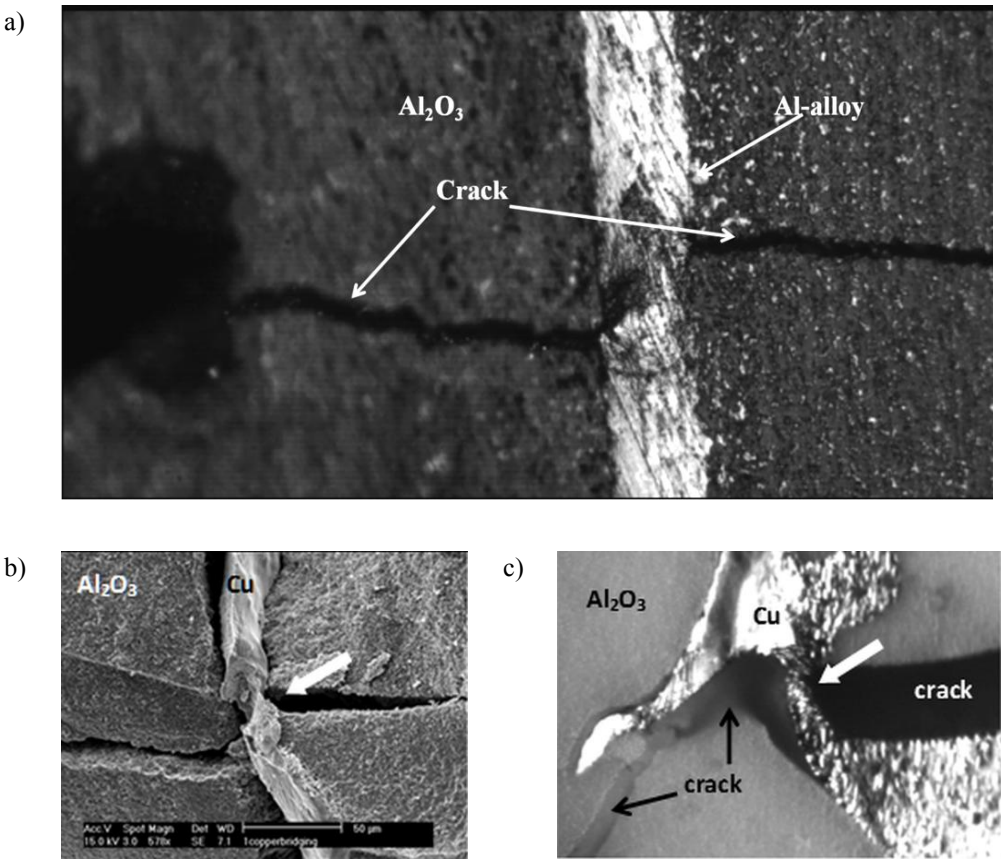

Figure 3.2. Crack bridging by metal ligament undergoing plastic deformation and decohesion from the surrounding ceramic matrix; (a) Al_2O_3/Al infiltrated composite (courtesy of PZMK IPPT PAN); (b) Al_2O_3/Cu infiltrated composite (reproduced from [89] with permission of *Int. J. Damage Mechanics*); (c) Al_2O_3/Cu infiltrated composite.

For a straight traction-free crack and a contour Γ connecting the opposite sides of a crack and surrounding its tip, the *J*-integral takes the following form (*e.g.* [113])

$$J = \int_{\Gamma} \left(Udy - \mathbf{T} \cdot \frac{\partial \mathbf{u}}{\partial x} ds \right), \tag{3.1}$$

where **u** – displacement vector, *ds* – arc element of *Γ*, ***n*** – unit outward vector normal to *Γ*.

The *J*-integral may also be formulated using the *configurational forces* approach, originating from [114] solution. The concept and applications of the configurational forces may be found in [115–121]. Using the configurational forces approach, the *J*-integral may be expressed in vector form (*cf.* [44]). If the crack develops within a homogeneous elastic material with arbitrary nonlinearities and anisotropy, zero volume forces and small deformations assumed, the *J*-integral vector is

$$J_k = \int_{\partial V} b_{kj} n_j dA = \int_{\partial V} \left(U\delta_{jk} - \sigma_{ij} u_{i,k} \right) n_j dA, \qquad k, j = 1, 2, 3, \tag{3.2}$$

where: $U(\varepsilon_{ij})$ - strain energy density, n_j - unit vector, normal and directed outward to closed surface ∂V, $b_{kj} = U\delta_{jk} - \sigma_{ij} u_{i,k}$ - the Eshelby stress tensor. The components J_k of the *J*-integral vector depend on loading modes. For pure mode I and pure mode II the component J_2 vanishes, while for mixed mode loading J_2 is nonzero and depends on the path.

For a crack-free material $J_k = 0$. In the plane case the *J*-integral (3.2) becomes a contour integral of the form

$$J = J_1 = \int_{C} \left(U\delta_{1\beta} - \sigma_{i\beta} u_{i,1} \right) n_\beta dc = \int_{C} \left(Udy - t_i u_{i,x} dc \right), \tag{3.3}$$

where: *C* denotes an open contour from one crack face to another surrounding the crack tip; $\beta = 1, 2$ are directions parallel and perpendicular to the crack propagation direction, respectively.

It has been shown in fracture mechanics that for elastic material, the *J*-integral is equal to the energy release rate *G* during the crack development

$$J = G. \tag{3.4}$$

As shown by [122] the energy release rate *G* may be related to the stress intensity factors. In mode I these relations take the following simple forms

$$\frac{K_I^2}{E} = G_I, \qquad \frac{(1-\nu^2)K_I^2}{E} = G_I, \tag{3.5}$$

in plane stress or plane strain conditions, respectively.

Calculation of the *J*-integral for a composite material with ductile reinforcements, thus inhomogeneous with discontinuities in material properties on the interfaces, has been undertaken only recently in the literature. There were analytical and numerical analyses performed for the materials with continuous spatial variation of mechanical or thermal properties, *e.g.* by [123–126]. Simha *et al*. [127] investigated the crack-driving force in elastic and elastic-plastic bimaterials. Provided that the microstructural features are small compared to overall dimensions, [128], followed by [129,130], applied *J*-integral method in fracture calculations of fibre reinforced composites with regard to the residual stresses occuring from nonelastic strains due to *e.g*. thermal expansion mismatch, phase transformation or plasticity.

The problem of the crack with ductile reinforcements and modelling of the increase of the energy release rate due to bridging, can be analyzed with the use of the *cohesive zone model*, as described by [131]. The cohesive zone models assume the presence of the cohesive zone within the narrow band along the crack faces. In the cohesive zone, opposite crack faces interact with each other by the cohesive stresses. The *J*-integral is calculated along the contour *C* close to crack faces. The cohesive models can be applied to elastic materials reinforced with particles or fibres as in Fig. 3.1(a), materials with microcracks, or to ductile materials with cavities. The continuous cohesive stress distribution $t(\delta)$ can be replaced with a discrete distribution of stresses $\sigma(u)$ in the reinforcing bridging ligaments depending on the displacements u in these bridges.

The cohesive zone model can be adapted for determination of the energy release rate increase ΔG in IPCs due to presence of the crack reinforcing bridges. The energy release rate increase may be calculated taking discrete stress distribution $\sigma(u)$ in the bridging fibres instead of the continuous distribution of cohesive stresses $t(\delta)$. Gross and Seelig [131] expressed the *J*-integral for the cohesive zone model using the relationship between stresses t and displacements δ in the bridging fibre

$$J = -\int_a^{a+d} t(x)\frac{d}{dx}[v^+ - v^-]dx = -\int_a^{a+d} t(x)\frac{d\delta}{dx}dx = \int_0^{\delta_c} t(\delta)d\delta, \tag{3.6}$$

where: a is the crack length, d - cohesive zone length, $d \ll a$, δ - relative displacement of the crack faces (separation), $\delta = v^+ - v^-$, $\delta_c = \delta^r$ (*cf*. Fig. 3.1) - crack opening displacement at the physical crack tip, *i.e*. at the point of rupture of the reinforcing ligament, t – intermolecular cohesive stress.

Thus, the value of J-integral depends on the cohesive stress distribution $t(\delta)$ related to separation δ. Assuming that equality (3.4) holds for the bridged crack in elastic matrix, the elastic energy release rate becomes [131]

$$G = \int_0^{\delta_c} t(\delta) d\delta. \tag{3.7}$$

Existing theoretical models assume some form of the stress-displacement relationship for the ligament. Mataga [94] assumed that the necking ligament has the geometrical shape of a paraboloid of rotation. Gross and Seelig [131] assumed this relation in an exponential form $t = e\sigma_C \frac{\delta}{\delta_0} e^{-\delta/\delta_0}$, $e \approx 2.72$, which results in a characteristic shape of the σ-δ relationship with softening.

To avoid prior assumptions as to the stress-displacement relationship for the ligament, it was decided in the present study to solve this problem numerically (*cf*. Sec. 6). In preparation for that some reference models from the literature will be reviewed in the following sections.

3.2. The model of Mataga

Mataga *et al*. [93] proposed an analytical approach to the problem of a plastic ligament surrounded by an elastic matrix to compute the increase of fracture toughness based on the crack bridging model (Fig. 3.1(a)). His work was motivated by the experimental investigations of [91], which showed that an addition of a ductile phase to brittle material could cause a rise in the fracture toughness.

The main objective of the Mataga model was to determine the nominal stresses in the reinforcing ligament. If the bridging stresses are determined the elastic energy release rate increase ΔG due to bridging is also obtained according to the following formula [93]

$$\Delta G = G - G_m = f \int_0^{\delta^r} \sigma du - f G_m, \tag{3.8}$$

where G is the elastic energy release rate of the composite, G_m – elastic energy release rate of the matrix, σ – nominal stress carried by the reinforcing ligament at displacement u ($\sigma \to 0$ at $u=\delta^r$, δ^r – crack opening displacement COD at failure), f – volume fraction of the ductile phase (assumed to be equal to the area fraction intercepted by the crack).

In Eq. 3.8, the term $-fG_m$ reflects the fact that the area of matrix fracture is reduced by the area of reinforcement sections. A scaled form of relationship 3.8 is [93]

$$G = f\sigma_0 r_f^0 w + (1-f)G_m, \tag{3.9}$$

where r_f^0 is the initial radius of the ligament, σ_0 denotes the initial yield stress of the ductile phase; w is a scalar carrying the information on the geometric constraints experienced during the deformation of the ligament, strain-hardening and the ligament rupture, and can further be expressed as

$$w = \int_0^{\delta^r/r_f^0} \frac{\sigma}{\sigma_0} d\left(\frac{u}{r_f^0}\right). \tag{3.10}$$

Hence, to determine G it is necessary to derive the relationship between dimensionless stresses (σ/σ_0) and displacements (u/r_f^0) in the reinforcing ligament.

After relating the critical energy release rate to the fracture toughness (plane strain case) the formula for w takes the form

$$w = \frac{1}{f\sigma_0 r_f^0}\left[\frac{(1-\nu^2)K^2}{E} - \frac{(1-f)(1-\nu_m^2)K_m^2}{E_m}\right], \tag{3.11}$$

where (K_m, E_m, ν_m) and (K, E, ν) denote the bulk modulus, the Young modulus and the Poisson ratio of the matrix material and the composite, respectively.

Assuming the shape of the reinforcing ligament at necking as a paraboloid of rotation of constant volume, applying the result of [132] and the power law form of the true stress-strain relationship of [133], one can obtain the relationship for the nominal stress in the reinforcing ligament. Such a relationship was obtained by [93] and reformulated by [89], with corrected misprint, as follows

$$\frac{\sigma}{\sigma_0} = (1-\rho)^2 \left[1 + \frac{4h_0(h_0+u)+u^2}{4\rho(1-\rho)\left(r_f^0\right)^2}\right] ln\left[1 + \frac{4\rho(1-\rho)\left(r_f^0\right)^2}{4h_0(h_0+u)+u^2}\right] \left(ln\left[\frac{1}{(1-\rho)^2}\right]\frac{1}{\varepsilon_0}\right)^{\frac{1}{n}},$$
$$\rho = 1 - \frac{r_f}{r_f^0}, \quad \frac{u}{r_f^0} = \frac{2h_0}{r_f^0}\frac{\frac{4}{3}\rho - \frac{8}{15}\rho^2}{1 - \frac{4}{3}\rho + \frac{8}{15}\rho^2}, \tag{3.12}$$

where: $2h_0$ – initial length of the bridging part of the fibre, $2h = 2h_0 + u$ – current length of the reinforcing fibre part (see Fig. 3.3).

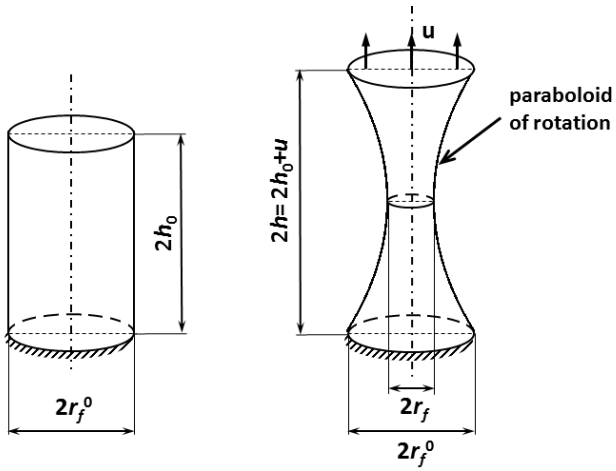

Figure 3.3. Geometry of the necking ligament in the model of Mataga [93].

In the solution obtained by [93] a softening part of the $\sigma(u)$ relationship is included which is due to necking of the ligament. This softening behaviour indicates that the bridging ligaments undergo large stretches across the growing crack faces and reduce the crack opening. The normalized stresses in Mataga's model evaluated with Eq. 3.12 were used as a reference analytical solution for comparison of the numerical results obtained by FEM in [89]. This numerical approach will further be used in this thesis.

3.3. The model of Emmel

Emmel [64] studied numerically the problem of a plastically deformable bridging fibre embedded in an elastic matrix in order to apply the results in a 2D numerical model of Compact-Tension test for a metal fibre reinforced composite. His model of the bridging fibre was based on the model of [93] and was intended as a numerical reproduction of the experiments by [94].

Firstly, the case of a single reinforcing ceramic fibre (Al_2O_3) in an elastic-plastic matrix (Al-alloy) was investigated. The axisymmetric metal fibre was embedded in two separate blocks of ceramics at both ends (mimicking an open crack) and subject to a tensile loading. The calculations were made for a chosen set of nondimensional fibre/matrix debonding parameters, which were assumed constant during the deformation process. In addition the Gurson damage model [134] was assumed for the fibre reinforcing the crack faces. The calculations were made in ABAQUS. The obtained $\sigma(u)$ relationships were compared with the results of theoretical model of [93]. They were further applied in a simple 2D ABAQUS model of a Compact-Tension test as the stress-displacement response of reinforcing fibres considered as truss elements (only axial force, no bending moment). The material with multiple reinforcing elastic-plastic metal fibres in a linear elastic ceramic matrix was modelled taking the computed $\sigma(u)$ relationship and applying the obtained data via UMAT procedure in ABAQUS. The truss element T2D2 was taken as the fibre model. The crack opening simulation was made with the MPC procedure. The *J*-integral and *K*–factors were calculated with the use of author's procedure written in FORTRAN.

In the present thesis the model of [64] was used when developing two- and three-dimensional numerical models of reinforcing fibres and the Compact-Tension test described in Sec. 6.

3.4. Other approaches in modelling of fracture of IPC

The issue of fracture toughness in advanced materials was discussed by [135] for different types of materials, including composites. The fracture in composite materials was discussed *e.g.* in the book [136], for the domain restricted to fibre reinforced shells having one of the dimensions significantly smaller than the remaining two, and thus regarding mainly planar properties of sheets. Schmauder

and Mishnaevsky [137] discussed micromechanical analyses and numerical simulations of damage and fracture in different types of composites of complex microstructures, including IPCs. Element removal method, embedded unit cells, or microvoid growth methods were described. The matricity model was developed and applied for graded IPCs. Voxel based method of 3D FE mesh generation was also described.

Węglewski and Basista [138], Węglewski *et al*. [103] and Basista *et al.* [139] developed a generic modelling methodology for thermal residual stresses, damage and fracture in arbitrary composites, making use of the computed microtomography images of the real composite microstructure to generate FE mesh. The FE mesh generation was performed with the use of Simpleware ScanIP+ScanFE commercial software. Damage in IPC's was also modelled by [42,140], together with deformation analysis, using numerical approach. 3D finite element mesh generation models were compared for isotropic and gradiented IPCs.

3.5. Numerical modelling of crack propagation by XFEM

The crack propagation in real IPCs can be modelled numerically using *Extended Finite Element Method* (XFEM) that is implemented in ABAQUS software. The idea of XFEM method was introduced by [141] and was described in detail *e.g*. by [142]. Bobiński and Tejchman [96] applied XFEM approach to modelling of fracture in concrete. Zangmeister [143] analysed numerical aspects of application of XFEM to modelling of heterogeneous materials undergoing elastic-plastic deformation. The XFEM is suitable to model discontinuities in the material as an enriched feature, where cracks are represented in the finite elements as the embedded discontinuities. As a consequence the re-meshing with the evolution of the crack can be avoided. XFEM enables the crack propagation of arbitrary, solution dependent direction and path. The crack path is not restricted to edges of the elements but may continuously propagate through them due to arbitrary enhancement functions that are incorporated in the finite element approximation.

In ABAQUS [144] used for calculations in Sec. 6 of this thesis, the solution of the displacement field $\boldsymbol{u}$ obtained with XFEM is formulated as the following sum:

$$\boldsymbol{u} = \sum_{i=1}^{n} N_i(x) \left[\boldsymbol{u}_i + H(x)\boldsymbol{a}_i + \sum_{\alpha=1}^{4} F_\alpha(x)\boldsymbol{b}_i^\alpha \right], \tag{3.13}$$

where: $N_i(x)$ - nodal shape functions, $\boldsymbol{u}_i$ – continuous part of the displacement field vector, $H(x)$ – discontinuous jump function across the crack surfaces, $\boldsymbol{a}_i$, $\boldsymbol{b}_i^{\alpha}$– vectors of the nodal enriched degrees of freedom, $F_{\alpha}(x)$ - elastic asymptotic crack tip functions.

The displacement field $\boldsymbol{u}$ is, thus, composed of three terms, of which the first one applies to all the nodes in the model, while the other two apply only to the nodes linked with the crack: the second term applies to nodes with shape function support cut by the crack interior, and the third one applies for nodes with shape function support cut by the crack tip.

The results of literature search on modelling of fracture in IPCs presented in this Section show that this problem is still not well covered. More often the published research was devoted to experimental characterization of fracture properties of IPCs than to modelling of their mechanical properties. A substantial effect of interpenetrating microstructure on the improvement of measured fracture properties has been reported. Following [135], the strength and fracture toughness are almost mutually exclusive for most of the materials, while limitations on engineering materials are in most cases connected with fracture toughness. It is, thus, important to develop toughening mechanisms in the regarded materials.

At the same time, there is a lack of numerical attempts to the problem of fracture in IPCs. The existing numerical works treat the problem using simple geometry and plane case situations (*e.g.* [64,88]).

In line with the specific objectives stated in Sec. 4, the main goal of this thesis is to provide numerical analysis of the deformation and crack development in interpenetrating metal-ceramic composites taking into account the real material microstructure and the main crack toughening mechanism occurring in the IPCs.

Motivation, aim and theses of the dissertation

In the previous Section, a background for modelling of elastic properties and fracture in metal-ceramic interpenetrating phase composites was outlined. The experimental investigations of IPC materials show that detailed investigation of the deformation and fracture processes is necessary for a proper identification and description of the IPC behaviour under in-service conditions. Due to the high costs of the IPCs processing and difficulties that occur during their characterization, numerical modelling can be very helpful to reach this goal.

Motivation of this thesis comes from the necessity to investigate mechanical and physical properties of newly designed IPC materials. While numerous IPC materials were already manufactured and tested, there is still lack of reliable analytical models, appropriate for special IPC microstructures. There is also a need for reliable numerical models that would be both detailed enough to catch the most important features of the IPC microstructure, and, at the same time, not too complicated to apply. The present work is intended to fulfill these needs by proposing a number of analytical and numerical models to predict effective elastic properties and fracture parameters of IPCs.

Succinctly stated, the main objectives of this work are as follows:

1. to develop analytical and numerical models predicting the effective elastic properties of metal-ceramic composites with interpenetrating microstructure, and to verify the obtained models by comparison with other methods and experimental data;
2. to develop analytical and numerical models of deformation of IPCs with account of large plastic deformations of metal ligaments, matrix-reinforcement delamination and toughening mechanism by crack bridging;
3. to develop numerical models for the macroscopic fracture in IPC materials with account of real material microstructure from micro-CT images.

Since the present study is concerned with the effective elastic properties and deformation and fracture parameters of IPCs, it is divided into two main parts: the first one concerning modelling of the effective material properties of IPCs, and the second one focused on modelling of deformation and fracture in IPCs. As novel materials are being modelled here some relevant experimental background of material manufacturing and characterization are included in Appendix.

The main theses of this dissertation may be formulated as follows:

1. The microstructure of IPC materials has a significant effect on their macroscopic properties.
2. Numerical procedures for calculating the effective elastic and thermal properties, when combined with computed micro-tomography images make it possible to analyze different actual microstructures and their impact on the IPC properties on macroscale.
3. Comparison of analytical predictions and experimental measurements of elastic properties at room temperature enables fast identification of a composite microstructure with optimum properties.
4. Numerical models are capable to account for phenomena that may occur in real IPC materials, such as interconnected fibres, delamination, skew fibres, contact between delaminated fibre and matrix, interaction between bridging fibres.
5. Crack growth in metal-ceramic interpenetrating composites is best captured by numerical models due to complexity of IPC microstructure.

In the following sections an attempt will be made to give evidence in support of these theses using analytical and numerical methods of contemporary mechanics as applied to composite materials with interpenetrating metal-ceramic networks.

5

Effective elastic and thermal properties of IPCs - analytical and numerical modelling

In this Section analytical and numerical models for the effective elastic and thermal properties of interpenetrating phase composites will be proposed. The main objective, besides prediction of effective material properties, is to investigate the influence of different composite microstructures and volume fractions of phases on macroscopic mechanical and thermal characteristics of IPCs.

A part of research reported in this Section was conducted by the author in the framework of the KMM-NoE Project of the 6th EU Framework Programme (http://aisbl.kmm-vin.eu/node/180), including research stays at the Institute of Mechanics of Darmstadt University of Technology (TUD) in Germany.

The models of effective properties to be presented were developed for material microstructures that were either idealized and simplified, or obtained from the real composites via computed microtomography (micro-CT). The obtained models were numerically implemented for specific composite materials Al_2O_3/Al and Al_2O_3/Cu. Manufacturing and characterization of the Al_2O_3/Cu IPC was performed in part within this thesis, and will be described in the Appendix.

For the purposes of this thesis, it is assumed that metal (copper or aluminum) and ceramic Al_2O_3 phases of the composite are isotropic (for details on the crystallographic microstructure see *cf*. [145], for detailed analysis of symmetry properties and anisotropy analysis of single crystals check [146]. A simplified unit cell (cross) with idealized internal structure representing interpenetration of phases shown in Fig. 5.1(a) will be used in analytical and numerical estimations of the effective elastic constants. The IPC microstructure, depicted in Fig. 5.1(a), has cubic symmetry and is generally anisotropic. However, real IPCs have irregular microstructure (*cf*. Fig. A6 in Appendix), in which such a unit cell can be regarded

for different material points, as positioned at different angles to the macroscopic loading direction. The effects occuring due to different positions mutually annihilate, and, thus, the macroscopic composite body may be considered as isotropic. Moreover, Young's moduli of IPCs measured within this thesis in two orthogonal directions generally did not differ more than 1% (*cf*. Table A2 in Appendix). Hence, it was assumed that the investigated composites are macroscopically isotropic [17,18,7].

The following effective elastic constants, selected for their practical importance, will be modelled analytically: Young's modulus, shear modulus, bulk modulus and Poisson's ratio in Subsec. 5.1.1, and the effective coefficient of thermal expansion in Subsec. 5.1.2. Besides analytical estimates, numerical models of the effective Young's modulus, shear modulus and Poisson's ratio will be presented in Subsec. 5.2.

The state of the art in modelling of the overall mechanical constants of IPC's has been presented in Sec. 2. The results presented below were partially published in [7] and [147].

5.1. Analytical approximations

The main issue in deriving analytical extensions of the existing models and bounds on the overall material constants, was determination of the effective elastic constants for IPCs directly from the stiffness tensor. In what follows analytical extensions of the [22] and [17,18] models and bounds on the effective Young's modulus, shear modulus and Poisson's ratio will be obtained directly from the stiffness tensor. The effective coefficient of thermal expansion as derived from the [36] relationship will also be provided.

5.1.1. Modified Feng-Tuchinskii model for effective elastic properties

The models of [17,18,22] of the effective elastic moduli of composites with interpenetrating microstructure described in Subsec. 2.1.2, were derived from *i.e*. Young's moduli and Poisson's ratio. Below, the modification to the approximations of [17,18,22] will be shown. The results presented in this Subsection, *i.e*. analytical formulae and their graphical representations, were first published in the paper of [7]. However, neither detailed derivation nor the final full-length formulae for the

effective Young's moduli and Poisson's ratios, were not included therein due to their enormous size and will be shown in this Subsection.

The idea of [22] and [17,18] for derivation of the effective elastic moduli of IPCs was based on a series of divisions of the unit cell till it was decomposed into pieces made up of only one material phase, and thus having the effective material properties equal to the properties of this phase. According to the iso-strain and iso-stress assumptions, the effective properties of groups of neighbouring pieces can be calculated. Then, these groups can be put together to form layers and their effective properties can also be derived. Finally, the effective properties of the whole unit cell, composed of these layers, can be obtained. Tuchinskii [22] divided the unit cell according to the iso-strain and iso-stress assumptions relative to the applied uniaxial stress direction. However, the unit cell can be divided into layers in two different ways. Then, for one of these ways, layers can be divided into sublayers also in two different ways. In total, there are three ways of unit cell division possible (*cf*. Table 5.1) and all of them lead to different results, what will be shown below. The iso-stress and iso-strain assumptions lead to bounds on effective constants. Such bounds were considered by [22]. The third division direction procedure (Fig. 5.1(b)) could be considered as a model for a particular effective response of the material.

Table 5.1. Different ways of division of the unit cell depicted in Fig. 5.1(a).

Naming convention	Procedure stages		
	i	ii	iii
	layers	sublayers	elementary cells
V-R-V	vertical – iso-strain – Voigt model	horizontal – iso-stress – Reuss model	vertical – iso-strain – Voigt model
V-V-R	vertical – iso-strain – Voigt model	vertical – iso-strain – Voigt model	horizontal – iso-stress – Reuss model
R-V-V	horizontal – iso-stress – Reuss model	vertical – iso-strain – Voigt model	vertical – iso-strain – Voigt model

Both [22] and [17,18] derived the effective Young's modulus as if it would be one of eigenmoduli of the isotropic stiffness tensor, which is not the case. If formulae for Young's modulus and effective Poisson's ratio were derived from the

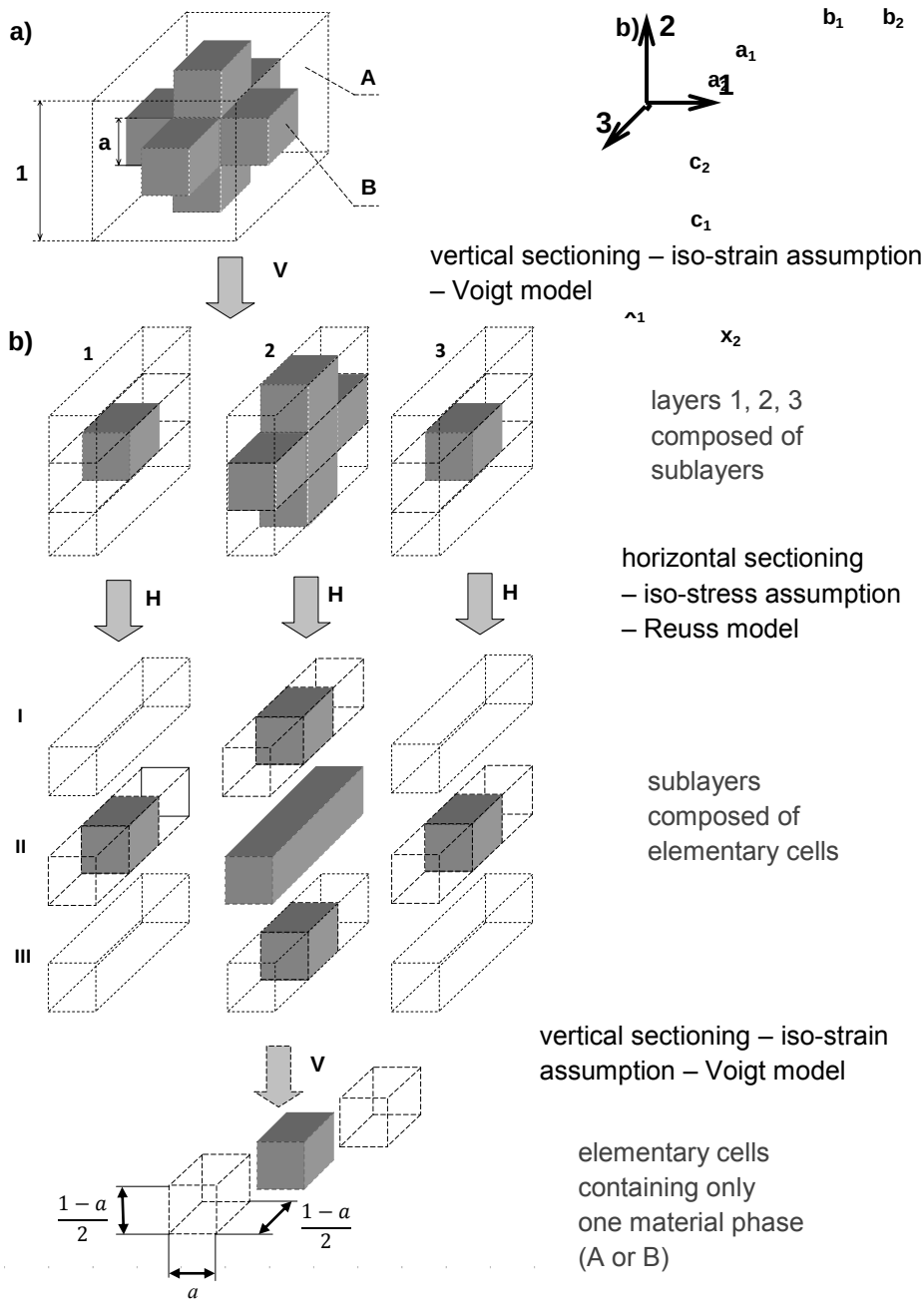

Figure 5.1. (a) Unit cell of a simplified interpenetrating microstructure ("cross microstructure") based on the models of [21,22] and [17,18], used in modelling of effective mechanical properties of IPCs, (b) decomposition sequence of the unit cell according to the

"extended" *V-R-V* model in vertical (V) and horizontal (H) directions (reprinted with permission of *Computational Materials Science*).

effective bulk and shear moduli, they would have different forms as will be shown below. In this thesis, extended models will be proposed for the effective bulk and shear moduli, which are the eigenmoduli of the isotropic stiffness tensor.

According to the definition of effective elastic moduli (*cf.* [29,30] or [44]), the average stress $\boldsymbol{\sigma}$ tensor in a representative volume element (RVE) of a composite subjected to homogeneous displacement boundary conditions is related to the average strain $\boldsymbol{\varepsilon}$ tensor by the effective elastic stiffness tensor $\mathbf{C}^*$

$$\overline{\boldsymbol{\sigma}} = \mathbf{C}^*\overline{\boldsymbol{\varepsilon}}, \quad \text{or:} \quad \bar{\sigma}_{ij} = C^*_{ijkl}\bar{\varepsilon}_{kl}. \tag{5.1}$$

Alternatively, when homogeneous traction boundary conditions are imposed on the RVE the average strain tensor is related to the average stress tensor by the effective compliance tensor $\mathbf{S}^*$

$$\overline{\boldsymbol{\varepsilon}} = \mathbf{S}^*\overline{\boldsymbol{\sigma}}, \quad \text{or:} \quad \bar{\varepsilon}_{ij} = C^*_{ijkl}\bar{\sigma}_{kl}. \tag{5.2}$$

The components of the stiffness tensor C_{ijkl} for an isotropic material can be expressed as (*cf.* [146,148])

$$\begin{aligned} \mathbf{C} &= 3K\frac{1}{3}\mathbf{I}_\mathrm{P} + 2\mu\mathbf{I}_\mathrm{D} = 3K\frac{1}{3}\mathbf{1}\otimes\mathbf{1} + 2\mu\left(\mathbf{I}^S - \frac{1}{3}\mathbf{1}\otimes\mathbf{1}\right), \\ C_{ijkl} &= \lambda\delta_{ij}\delta_{kl} + \mu\left(\delta_{ik}\delta_{jl} + \delta_{il}\delta_{jk}\right), \end{aligned} \tag{5.3}$$

where $\mathbf{1}$ is a 2nd rank unity tensor, $1 = \delta_{ij}$, $\mathbf{I}^s$ is the symmetric part of a 4th rank unity tensor $\mathbf{I}$, $I_{ijkl} = \delta_{ik}\,\delta_{jl}$, $I^S_{ijkl} = \frac{1}{2}\left(\delta_{ik}\delta_{jl} + \delta_{il}\delta_{jk}\right)$, with $\mathbf{I}_\mathrm{D} = \mathbf{I}^S - \frac{1}{3}\mathbf{1}\otimes\mathbf{1}$ – deviatoric part and $\mathbf{I}_\mathrm{P} = \mathbf{I}^S - \mathbf{I}_\mathrm{D} = \frac{1}{3}\mathbf{1}\otimes\mathbf{1}$ – spherical part, λ and μ are Lamé constants, δ_{ij} is the Kronecker delta.

Thus, according to the relationships between Lamé constants and the elastic constants (Young's modulus E, Poisson's ratio ν, bulk modulus K, and shear modulus μ), only the bulk modulus K and shear modulus μ are the eigenvalues of the stiffness tensor:

$$\begin{aligned} C_{1111} &= C_{2222} = C_{3333} = 2\mu + \lambda = K + \tfrac{4}{3}\mu, \\ C_{1122} &= C_{1133} = C_{2233} = \lambda = K - \tfrac{2}{3}\mu, \end{aligned} \tag{5.4}$$

while the other elastic constants are interrelated, for instance Young's modulus E and Poisson's ratio v, namely

$$2\mu + \lambda = \frac{E(1-v)}{(1+v)(1-2v)}, \qquad \lambda = \frac{Ev}{(1+v)(1-2v)}. \tag{5.5}$$

Consequently, the formulae for the effective elastic constants in [17,18,22] should have been derived from direct components of the stiffness tensor, *e.g.* bulk modulus K and shear modulus μ, but neither Young's modulus E nor Poisson's ratio v. Moreover, the Tuchinskii model [22] contains some errors and misprints as shown in [7].

According to the idea of unit cell sectioning (*cf.* Fig. 5.1(b) and Table 5.1), the effective elastic properties for IPC modelled by the cross microstructure (Fig. 5.1(a)), can be derived as described below (note that for isotropic materials, the engineering constant G known as shear modulus, is equal to the Lamé constant μ, thus for convenience μ will be replaced by G in the sequel).

A 3D-cross cubic unit cell shown in Fig. 5.1(a) is composed of two mutually interpenetrating phases A and B, where phase B has ligaments with geometry of a square section characterized by the dimension a ($0 \leq a \leq 1$). The total volume fraction f of the phase B in the cubic unit cell from Fig. 5.1(a) may be expressed as the sum of the volumes of one cube with the phase B in the middle and six "branching" cuboids with the phase B of identical dimensions, as related to the total volume of the unit cube

$$f = \frac{a^3 + 6a^2\,(1-a)/2}{1 \cdot 1 \cdot 1} = a^3 + 3a^2(1-a) = a^3 + 3a^2 - 3a^3$$
$$= 3a^2 - 2a^3 = a^2(3-2a) \qquad (dimensionless). \tag{5.6}$$

When tensile loading acts along the axis "2", the unit cell can be divided by planar surfaces perpendicular to the axes of the coordinate system into layers and then sublayers until elementary cells, where each cell is composed of only one phase material. Let us first consider the division direction presented in Fig. 5.1(b) according to the following "extended" *V-R-V* model.

The "extended" V-R-V model

First, the unit cell is divided into layers perpendicularly to the axis "1", according to the Voigt iso-strain assumption. The effective shear and bulk modulus of the unit cell may be formulated in terms of the respective properties of each layer

$$G^* = \sum_{\mathrm{i}=1}^{3} c_i G_i = c_1 G_1 + c_2 G_2 + c_3 G_3 = 2c_1 G_1 + c_2 G_2,$$
$$K^* = \sum_{\mathrm{i}=1}^{3} c_i K_i = c_1 K_1 + c_2 K_2 + c_3 K_3 = 2c_1 K_1 + c_2 K_2, \tag{5.7}$$

where: i - identifier of the layer, c_i - volume fraction of the i-th layer, $c_1 = c_3$, $c_2 = 1 - 2c_1$, G_i - shear modulus of the i-th layer, K_i - bulk modulus of the i-th layer, $G_1 = G_3$, $K_1 = K_3$, G^* effective shear modulus of the whole unit cell, K^* - effective bulk modulus of the whole unit cell.

The volume fraction of the i-th layer is related to the characteristic dimension a of the phase B as

$$c_1 = c_3 = \frac{V_{1-3}}{1 \cdot 1 \cdot 1} = 1 \cdot 1 \cdot \frac{1-a}{2} = \frac{1-a}{2} \quad (dimensionless),$$
$$c_2 = 1 - 2c_1 = \frac{V_2}{1 \cdot 1 \cdot 1} = 1 \cdot 1 \cdot a = a \quad (dimensionless). \tag{5.8}$$

Then, each layer is divided into sublayers according to the Reuss iso-stress assumption perpendicularly to the axis "2"

$$\begin{aligned} G^*_{layer} &= \left(\sum_{j=1}^{III} \frac{c_j}{G_{sublayer,j}} \right)^{-1} = \\ &= \left(\frac{c_I}{G_{sublayer,I}} + \frac{c_{II}}{G_{sublayer,II}} + \frac{c_{III}}{G_{sublayer,III}} \right)^{-1} = \\ &= \left(\frac{2c_I}{G_{sublayer,I}} + \frac{c_{II}}{G_{sublayer,II}} \right)^{-1} = \\ &= \left(\frac{2c_I}{G_{sublayer,I}} + \frac{1-2c_I}{G_{sublayer,II}} \right)^{-1} = \\ &= \left(\frac{2c_I G_{sublayer,II} + (1-2c_I) G_{sublayer,I}}{G_{sublayer,I} G_{sublayer,II}} \right)^{-1}, \end{aligned} \tag{5.9}$$

$$
\begin{aligned}
K^*_{layer} &= \left(\sum_{j=1}^{III} \frac{c_j}{K_{sublayer,j}} \right)^{-1} = \\
&= \left(\frac{c_I}{K_{sublayer,I}} + \frac{c_{II}}{K_{sublayer,II}} + \frac{c_{III}}{K_{sublayer,III}} \right)^{-1} = \\
&= \left(\frac{2c_I}{K_{sublayer,I}} + \frac{c_{II}}{K_{sublayer,II}} \right)^{-1} = \\
&= \left(\frac{2c_I}{K_{sublayer,I}} + \frac{1-2c_I}{K_{sublayer,II}} \right)^{-1} = \\
&= \left(\frac{2c_I K_{sublayer,II} + (1-2c_I) K_{sublayer,I}}{K_{sublayer,I} K_{sublayer,II}} \right)^{-1},
\end{aligned}
\tag{5.9 [cont.]}
$$

where: j –identifier of the sublayer, c_j - volume fraction of the j-th sublayer, $c_{\mathrm{I}} = c_{\mathrm{III}}$, $c_{\mathrm{II}} = 1 - 2c_{\mathrm{I}}$, $G_{sublayer,j}$ - shear modulus of the j-th sublayer, $K_{sublayer,j}$ - bulk modulus of the j-th sublayer, $G_{\mathrm{I}} = G_{\mathrm{III}}$, $K_{\mathrm{I}} = K_{\mathrm{III}}$, G^*_{layer} - effective shear modulus of the layer composed of sublayers, K^*_{layer} - effective bulk modulus of the layer composed of sublayers.

Depending on the layer, the volume fractions of sublayers related to the volumes of layers (for we calculate now the effective properties of layers), may be expressed as

for layers 1 and 3

$$
\begin{aligned}
c_I = c_{III} &= \frac{V_{I-III}}{V_{1-3}} = \frac{1 \cdot \frac{1-a}{2} \cdot \frac{1-a}{2}}{\frac{1-a}{2}} = \frac{1-a}{2}, \\
c_{II} = 1 - 2c_I &= \frac{V_{II}}{V_{1-3}} = \frac{1 \cdot a \cdot \frac{1-a}{2}}{\frac{1-a}{2}} = a,
\end{aligned}
\tag{5.10}
$$

for layer 2

$$
\begin{aligned}
c_I = c_{III} &= \frac{V_{I-III}}{V_2} = \frac{1 \cdot a \cdot \frac{1-a}{2}}{1 \cdot 1 \cdot a} = \frac{1-a}{2}, \\
c_{II} = 1 - 2c_I &= \frac{V_{II}}{V_2} = \frac{1 \cdot a \cdot a}{1 \cdot 1 \cdot a} = a\,.
\end{aligned}
\tag{5.11}
$$

Each sublayer can be divided into elementary cells composed of only one phase *A* or *B*, perpendicularly to the axis "3", according to the Voigt iso-strain assumption in each of the sublayer's elementary cell. However, sublayers should be characterized in three groups.

For sublayers (1, II), (2, I), (2, III), (3, I)

$$\begin{aligned} G^*_{sublayer} &= \sum_{k=A,B} c_k G_k = 2c_A G_A + c_B G_B = \\ &= c_B G_B + (1 - c_B) G_A = a G_B + (1 - a) G_A, \\ K^*_{sublayer} &= \sum_{k=A,B} c_k K_k = 2c_A K_A + c_B K_B = \\ &= c_B K_B + (1 - c_B) K_A = a K_B + (1 - a) K_A, \end{aligned} \tag{5.12}$$

where k –identifier of the phase A or B, G_k - shear modulus of the k-th phase, K_k - bulk modulus of the k-th phase, c_k - volume fraction of the k-th phase in each sublayer, $c_B = 1 - c_A = a$, c_B - volume fraction of the phase B in each sublayer, $G^*_{sublayer}$ - effective shear modulus of the sublayer composed of elementary cells, $K^*_{sublayer}$ - effective bulk modulus of the sublayer composed of elementary cells.

For sublayers (1, I), (1, III), (3, I), (3, III)

$$G^*_{sublayer} = G_A, \qquad K^*_{sublayer} = K_A, \tag{5.13}$$

while for sublayer (2, II):

$$G^*_{sublayer} = G_B, \qquad K^*_{sublayer} = K_B, \tag{5.14}$$

Now, the effective properties of layers may be calculated. For layers *1* and *3*, according to Eq. (5.9) combined with (5.10) and (5.13) gives

$$\begin{aligned} G^*_{layer1,3} &= \left(\frac{2c_I}{G_{sublayer,I}} + \frac{c_{II}}{G_{sublayer,II}} \right)^{-1} = \\ &= \left(\frac{2\left(\frac{1-a}{2}\right)}{G_{sublayer,I}} + \frac{a}{G_{sublayer,II}} \right)^{-1} = \\ &= \left(\frac{1-a}{G_A} + \frac{a}{aG_B + (1-a)G_A} \right)^{-1} = \end{aligned} \tag{5.15}$$

$$
\begin{aligned}
&= \left(\frac{(1-a)(aG_B + (1-a)G_A) + aG_A}{G_A(aG_B + (1-a)G_A)} \right)^{-1}, \\
K^*_{layer1,3} &= \left(\frac{2c_I}{K_{sublayer,I}} + \frac{c_{II}}{K_{sublayer,II}} \right)^{-1} = \\
&= \left(\frac{2\left(\frac{1-a}{2}\right)}{K_{sublayer,I}} + \frac{a}{K_{sublayer,II}} \right)^{-1} = \\
&= \left(\frac{1-a}{K_A} + \frac{a}{aK_B + (1-a)K_A} \right)^{-1} = \qquad \text{[cont.]} \\
&= \left(\frac{(1-a)(aK_B + (1-a)K_A) + aK_A}{K_A(aK_B + (1-a)K_A)} \right)^{-1}.
\end{aligned}
\tag{5.15}
$$

The effective elastic properties of layer *2*, according to Eq. (5.9) with the use of Eqs (5.11) and (5.14) can be expressed as

$$
\begin{aligned}
G^*_{layer,2} &= \left(\frac{2c_I}{G_{sublayer,I}} + \frac{c_{II}}{G_{sublayer,II}} \right)^{-1} = \\
&= \left(\frac{2\left(\frac{1-a}{2}\right)}{aG_B + (1-a)G_A} + \frac{a}{G_B} \right)^{-1} = \\
&= \left(\frac{1-a}{aG_B + (1-a)G_A} + \frac{a}{G_B} \right)^{-1} = \\
&= \left(\frac{(1-a)G_B + a(aG_B + (1-a)G_A)}{G_B(aG_B + (1-a)G_A)} \right)^{-1}, \\
K^*_{layer,2} &= \left(\frac{2c_I}{K_{sublayer,I}} + \frac{c_{II}}{K_{sublayer,II}} \right)^{-1} = \\
&= \left(\frac{2\left(\frac{1-a}{2}\right)}{aK_B + (1-a)K_A} + \frac{a}{K_B} \right)^{-1} = \\
&= \left(\frac{1-a}{aK_B + (1-a)K_A} + \frac{a}{K_B} \right)^{-1} = \\
&= \left(\frac{(1-a)K_B + a(aK_B + (1-a)K_A)}{K_B(aK_B + (1-a)K_A)} \right)^{-1}.
\end{aligned}
\tag{5.16}
$$

Upon substitution of Eqs (5.8), (5.15) and (5.16), to (5.7) the effective elastic shear and bulk moduli of the unit cell may be written as

$$\begin{aligned} G^*_{VRV} &= 2c_1 G_{layer1,3} + c_2 G_{layer,2} = \\ &= 2\left(\frac{1-a}{2}\right)\left(\frac{(1-a)(aG_B+(1-a)G_A)+aG_A}{G_A(aG_B+(1-a)G_A)}\right)^{-1} + \\ &\quad +a\left(\frac{(1-a)G_B+a(aG_B+(1-a)G_A)}{G_B(aG_B+(1-a)G_A)}\right)^{-1} = \\ &= (1-a)\left(\frac{(1-a)(aG_B+(1-a)G_A)+aG_A}{G_A(aG_B+(1-a)G_A)}\right)^{-1} + \\ &\quad +a\left(\frac{(1-a)G_B+a(aG_B+(1-a)G_A)}{G_B(aG_B+(1-a)G_A)}\right)^{-1}, \end{aligned}$$

$$\begin{aligned} K^*_{VRV} &= 2c_1 K_{layer1,3} + c_2 K_{layer,2} = \\ &= 2\left(\frac{1-a}{2}\right)\left(\frac{(1-a)(aK_B+(1-a)K_A)+aK_A}{K_A(aK_B+(1-a)K_A)}\right)^{-1} + \\ &\quad +a\left(\frac{(1-a)K_B+a(aK_B+(1-a)K_A)}{K_B(aK_B+(1-a)K_A)}\right)^{-1} = \\ &= (1-a)\left(\frac{(1-a)(aK_B+(1-a)K_A)+aK_A}{K_A(aK_B+(1-a)K_A)}\right)^{-1} + \\ &\quad +a\left(\frac{(1-a)K_B+a(aK_B+(1-a)K_A)}{K_B(aK_B+(1-a)K_A)}\right)^{-1}. \end{aligned} \tag{5.17}$$

The formula $(5.17)_1$ was first published in [7]. It was noted that the formula for the effective bulk modulus (5.17(b)) would have the same form with substitution of G by K.

The formulae for the "extended" *V-R-V* model of the effective Young's modulus and Poisson's ratio may be obtained from the well-known relationships between elastic constants, such as (5.4) and (5.5) as follows

$$\begin{aligned} E^*_{VRV} &= \frac{9G^*_{VRV}K^*_{VRV}}{3K^*_{VRV}+G^*_{VRV}}, \\ \nu^*_{VRV} &= \frac{3K^*_{VRV}-2G^*_{VRV}}{2G^*_{VRV}+6K^*_{VRV}}. \end{aligned} \tag{5.18}$$

The full-length Eq. (5.18) for the effective elastic Young's modulus and Poisson's ratio according to the "extended" *V-R-V* model, due to their enormous size, will be additionally presented on separate pages in the final part of this Subsection.

The relationships (5.17) and (5.18), related to the volume fraction of metal phase with the formula (5.6) are graphically represented as the "extended *V-R-V* model" in Figs 5.2 – 5.5 at the end of this Section.

The "extended" V-V-R model

To derive the formulae for the "extended" *V-V-R* models to the effective elastic constants, the unit cell is divided into layers as in the previous case, perpendicularly to the axis "1" (*cf.* Fig. 5.1 and Table 5.1), according to the Voigt iso-strain assumption.

The effective shear and bulk moduli of the unit cell will, thus, have identical form as the formulae (5.7)

$$G^* = \sum_{i=1}^{3} c_i G_i = c_1 G_1 + c_2 G_2 + c_3 G_3 = 2c_1 G_1 + c_2 G_2,$$
$$K^* = \sum_{i=1}^{3} c_i K_i = c_1 K_1 + c_2 K_2 + c_3 K_3 = 2c_1 K_1 + c_2 K_2, \tag{5.19}$$

where: i - identifier of the layer, c_i - volume fraction of the i-th layer, $c_1 = c_3$, $c_2 = 1 - 2c_1$, G_i - shear modulus of the i-th layer, K_i - bulk modulus of the i-th layer, $G_1 = G_3$, $K_1 = K_3$, G^*- effective shear modulus of the whole unit cell, K^* - effective bulk modulus of the whole unit cell.

Volume fractions of the layers related to the characteristic dimension a of the phase B, regardless of the unit cell division direction, remain the same according to formulae (5.8), (5.10) and (5.11).

The second division direction of layers into sublayers follows the Voigt iso-strain assumption again and is made perpendicularly to the axis "3"

$$
\begin{aligned}
G^*_{layer} &= \sum_{j=I}^{III} c_j G_{sublayer,j} = \\
&= c_I G_{sublayer,I} + c_{II} G_{sublayer,II} + c_{III} G_{sublayer,III} = \\
&= 2c_I G_{sublayer,I} + c_{II} G_{sublayer,II}, \\
K^*_{layer} &= \sum_{j=I}^{III} c_j K_{sublayer,j} = \\
&= c_I K_{sublayer,I} + c_{II} K_{sublayer,II} + c_{III} K_{sublayer,III} = \\
&= 2c_I K_{sublayer,I} + c_{II} K_{sublayer,II},
\end{aligned}
\tag{5.20}
$$

where: j –identifier of the sublayer, c_j - volume fraction of the j-th sublayer, $c_{\mathrm{I}} = c_{\mathrm{III}}$, $c_{\mathrm{II}} = 1 - 2c_{\mathrm{I}}$, $G_{sublayer,j}$ - shear modulus of the j-th sublayer, $K_{sublayer,j}$ - bulk modulus of the j-th sublayer, $G_{\mathrm{I}} = G_{\mathrm{III}}$, $K_{\mathrm{I}} = K_{\mathrm{III}}$, G^*_{layer} - effective shear modulus of the layer composed of sublayers, K^*_{layer} - effective bulk modulus of the layer composed of sublayers.

Finally, each sublayer is divided into elementary cells, composed of only one phase A or B, perpendicularly to the axis "2", according to the Reuss iso-stress assumption of equal stress in each of the sublayer's elementary cell. As for the previous case, sublayers are characterized in three groups. For the sublayers respective to (1, II), (2, I), (2, III), (3, I) from Fig. 5.1(b)

$$
\begin{aligned}
G^*_{sublayer} &= \left(\sum_{k=A,B} \frac{c_k}{G_{sublayer,k}} \right)^{-1} = \\
&= \left(\frac{2c_A}{G_A} + \frac{c_B}{G_B} \right)^{-1} = \left(\frac{1 - c_B}{G_A} + \frac{c_B}{G_B} \right)^{-1} = \\
&= \left(\frac{1 - a}{G_A} + \frac{a}{G_B} \right)^{-1}, \\
K^*_{sublayer} &= \left(\sum_{k=A,B} \frac{c_k}{K_{sublayer,k}} \right)^{-1} = \\
&= \left(\frac{2c_A}{K_A} + \frac{c_B}{K_B} \right)^{-1} = \left(\frac{1 - c_B}{K_A} + \frac{c_B}{K_B} \right)^{-1} = \\
&= \left(\frac{1 - a}{K_A} + \frac{a}{K_B} \right)^{-1},
\end{aligned}
\tag{5.21}
$$

where k –identifier of the phase A or B, G_k - shear modulus of the k-th phase, K_k - bulk modulus of the k-th phase, c_k - volume fraction of the k-th phase in each sublayer, $c_B = 1 - c_A = a$, c_B - volume fraction of the phase B in each sublayer, $G^*_{sublayer}$ - effective shear modulus of the sublayer composed of elementary cells, $K^*_{sublayer}$ - effective bulk modulus of the sublayer composed of elementary cells.

For sublayers respective to (1, I), (1, III), (3, I), (3, III) and (2, II) from Fig. 5.1(b), the relations 5.13 and 5.14 remain as

$$G^*_{sublayer} = G_A, \qquad K^*_{sublayer} = K_A, \tag{5.22}$$

while for a sublayer with regard to (2, II) from Fig. 5.1(b) we get

$$G^*_{sublayer} = G_B, \qquad K^*_{sublayer} = K_B, \tag{5.23}$$

The effective properties of layers may now be calculated. For layers *1* and *3*, according to Eq. (5.20) with the use of (5.10), (5.21) and (5.22) it follows that

$$\begin{aligned} G^*_{layer1,3} &= 2c_I G_{sublayer,I} + c_{II} G_{sublayer,II} = \\ &= 2\frac{1-a}{2} G_A + a\left(\frac{1-a}{G_A} + \frac{a}{G_B}\right)^{-1} = \\ &= (1-a)G_A + a\left(\frac{1-a}{G_A} + \frac{a}{G_B}\right)^{-1}, \\ K^*_{layer1,3} &= 2c_I K_{sublayer,I} + c_{II} K_{sublayer,II} = \\ &= 2\frac{1-a}{2} K_A + a\left(\frac{1-a}{K_A} + \frac{a}{K_B}\right)^{-1} = \\ &= (1-a)K_A + a\left(\frac{1-a}{K_A} + \frac{a}{K_B}\right)^{-1}, \end{aligned} \tag{5.24}$$

The effective elastic properties of layer *2*, according to formulae (5.20) combined with (5.11), (5.21) and (5.23) can be expressed as

$$\begin{aligned} G^*_{layer,2} &= 2c_I G_{sublayer,I} + c_{II} G_{sublayer,II} = \\ &= 2\frac{1-a}{2}\left(\frac{1-a}{G_A} + \frac{a}{G_B}\right)^{-1} + aG_B = \\ &= (1-a)\left(\frac{1-a}{G_A} + \frac{a}{G_B}\right)^{-1} + aG_B, \end{aligned} \tag{5.25}$$

$$
\begin{aligned}
K^*_{layer,2} &= 2c_I K_{sublayer,I} + c_{II} K_{sublayer,II} = \\
&= 2\frac{1-a}{2}\left(\frac{1-a}{K_A}+\frac{a}{K_B}\right)^{-1} + aK_B = \\
&= (1-a)\left(\frac{1-a}{K_A}+\frac{a}{K_B}\right)^{-1} + aK_B.
\end{aligned}
\tag{5.25}
$$

[cont.]

Using the formulae (5.8), (5.24) and (5.25) the expressions (5.19) for the *V-V-R* models of the effective shear and bulk moduli of the unit cell may be written as

$$
\begin{aligned}
G^*_{VVR} &= 2c_1 G_{layer1,3} + c_2 G_{layer,2} = \\
&= 2\frac{1-a}{2}\left((1-a)G_A + a\left(\frac{1-a}{G_A}+\frac{a}{G_B}\right)^{-1}\right) + \\
&\quad + a\left((1-a)\left(\frac{1-a}{G_A}+\frac{a}{G_B}\right)^{-1} + aG_B\right) = \\
&= a^2 G_B + (1-a)^2 G_A + 2a(1-a)\left(\frac{a}{G_B}+\frac{1-a}{G_A}\right)^{-1},
\end{aligned}
$$

$$
\begin{aligned}
K^*_{VVR} &= 2c_1 K_{layer1,3} + c_2 K_{layer,2} = \\
&= 2\frac{1-a}{2}\left((1-a)K_A + a\left(\frac{1-a}{K_A}+\frac{a}{K_B}\right)^{-1}\right) + \\
&\quad + a\left((1-a)\left(\frac{1-a}{K_A}+\frac{a}{K_B}\right)^{-1} + aK_B\right) = \\
&= a^2 K_B + (1-a)^2 K_A + 2a(1-a)\left(\frac{a}{K_B}+\frac{1-a}{K_A}\right)^{-1},
\end{aligned}
\tag{5.26}
$$

with the same relations (upon substitution of *K* by *G*) for *V-V-R* model for shear modulus *G**.

The formula for the *V-V-R* model for shear modulus $(5.26)_1$ is identical with formula (2.21) of the Feng model. The formula $(5.26)_2$ was first published in [7], with a misprint (invalid bracket placement) in the equation (6) therein. It was noted, that the formula for the effective shear modulus $(5.26)_1$ would have the same form with *K* substituted by *G*.

Using the well-known relationships between elastic constants (5.4) and (5.5), the *V-V-R* models for the effective Young's modulus and Poisson's ratio may be obtained

$$E^*_{VVR} = \frac{9G^*_{VVR}K^*_{VVR}}{3K^*_{VVR} + G^*_{VVR}},$$
$$\nu^*_{VVR} = \frac{3K^*_{VVR} - 2G^*_{VVR}}{2G^*_{VVR} + 6K^*_{VVR}}. \tag{5.27}$$

The relationships (5.26) and (5.27), related to the volume fraction of metal phase with the formula (5.6), are depicted in Figs 5.2 – 5.5 as the "extended" *V-V-R* models.

The "extended" R-V-V model

For derivation of the "extended" *R-V-V* model the unit cell is first divided into layers perpendicularly to the axis "2", according to the Reuss iso-stress assumption (*cf*. Fig. 5.1 and Table 5.1). The effective shear and bulk moduli of the unit cell formulated in terms of the respective properties of each layer read

$$G^* = \left(\sum_{i=1}^{3}\frac{c_i}{G_i}\right)^{-1} = \left(\frac{c_1}{G_1} + \frac{c_2}{G_2} + \frac{c_3}{G_3}\right)^{-1} = \left(\frac{2c_1}{G_1} + \frac{c_2}{G_2}\right)^{-1} = \left(\frac{2c_1}{G_1} + \frac{1-2c_1}{G_2}\right)^{-1},$$
$$K^* = \left(\sum_{i=1}^{3}\frac{c_i}{K_i}\right)^{-1} = \left(\frac{c_1}{K_1} + \frac{c_2}{K_2} + \frac{c_3}{K_3}\right)^{-1} = \left(\frac{2c_1}{K_1} + \frac{c_2}{K_2}\right)^{-1} = \left(\frac{2c_1}{K_1} + \frac{1-2c_1}{K_2}\right)^{-1}, \tag{5.28}$$

where: i - identifier of the layer, c_i - volume fraction of the i-th layer, $c_1 = c_3$, $c_2 = 1 - 2c_1$, G_i - shear modulus of the i-th layer, K_i - bulk modulus of the i-th layer, $G_1 = G_3$, $K_1 = K_3$, μ^* - effective shear modulus of the whole unit cell, K^* - effective bulk modulus of the whole unit cell.

Volume fractions of the layers related to the characteristic dimension a of the phase B, regardless of the unit cell division direction, remain the same and are given by formulae (5.8), (5.10) and (5.11).

The second division direction of layers into sublayers follows the Voigt iso-strain assumption again and is made perpendicularly to the axis "3":

$$
\begin{aligned}
G^*_{layer} &= \sum_{j=I}^{III} c_j G_{sublayer,j} = \\
&= c_I G_{sublayer,I} + c_{II} G_{sublayer,II} + c_{III} G_{sublayer,III} = \\
&= 2c_I G_{sublayer,I} + c_{II} G_{sublayer,II}, \\
K^*_{layer} &= \sum_{j=I}^{III} c_j K_{sublayer,j} = \\
&= c_I K_{sublayer,I} + c_{II} K_{sublayer,II} + c_{III} K_{sublayer,III} = \\
&= 2c_I K_{sublayer,I} + c_{II} K_{sublayer,II},
\end{aligned}
\tag{5.29}
$$

where: j –identifier of the sublayer, c_j - volume fraction of the j-th sublayer, $c_{\mathrm{I}} = c_{\mathrm{III}}$, $c_{\mathrm{II}} = 1 - 2c_{\mathrm{I}}$, $G_{sublayer,j}$ - shear modulus of the j-th sublayer, $K_{sublayer,j}$ - bulk modulus of the j-th sublayer, $G_{\mathrm{I}} = G_{\mathrm{III}}$, $K_{\mathrm{I}} = K_{\mathrm{III}}$, G^*_{layer} - effective shear modulus of the layer composed of sublayers, K^*_{layer} - effective bulk modulus of the layer composed of sublayers.

The division of the sublayers into elementary cells, composed of only one phase A or B, is made perpendicularly to the axis "1", according to the Voigt iso-strain assumption of equal strain in each of the sublayer's elementary cell. Sublayers are characterized in three groups, as in previous cases. For the sublayers respective to (1, II), (2, I), (2, III), (3, I) from Fig. 5.1(b) we obtain

$$
\begin{aligned}
G^*_{sublayer} &= \sum_{k=A,B} c_k G_k = 2c_A G_A + c_B G_B = \\
&= c_B G_B + (1 - c_B) G_A = a G_B + (1 - a) G_A, \\
K^*_{sublayer} &= \sum_{k=A,B} c_k K_k = 2c_A K_A + c_B K_B = \\
&= c_B K_B + (1 - c_B) K_A = a K_B + (1 - a) K_A,
\end{aligned}
\tag{5.30}
$$

where: k –identifier of the phase A or B, G_k - shear modulus of the k-th phase, K_k - bulk modulus of the k-th phase, c_k - volume fraction of the k-th phase in each sublayer, $c_B = 1 - c_A = a$, c_B - volume fraction of the phase B in each sublayer, $G^*_{sublayer}$ - effective shear modulus of the sublayer composed of elementary cells, $K^*_{sublayer}$ - effective bulk modulus of the sublayer composed of elementary cells.

For the sublayers respective to (1, I), (1, III), (3, I), (3, III) and (2, II) from Fig. 5.1(b), the relations (5.13)/(5.22) and (5.14)/(5.23) hold as before:

$$G^*_{sublayer} = G_A, \qquad K^*_{sublayer} = K_A, \tag{5.31}$$

and for the sublayer respective to (2, II) from Fig. 5.1(b)

$$G^*_{sublayer} = G_B, \qquad K^*_{sublayer} = K_B, \tag{5.32}$$

The effective properties of layers *1* and *3*, according to formulae (5.29) with regard to (5.10), (5.30) and (5.31), take the form

$$\begin{aligned} G^*_{layer1,3} &= 2c_I G_{sublayer,I} + c_{II} G_{sublayer,II} = \\ &= 2\frac{1-a}{2} G_A + a(aG_B + (1-a)G_A) = \\ &= (1-a)G_A + a^2 G_B + a(1-a)G_A = \\ &= (1+a)(1-a)G_A + a^2 G_B = \\ &= (1-a^2)G_A + a^2 G_B, \end{aligned} \tag{5.33}$$

$$\begin{aligned} K^*_{layer1,3} &= 2c_I K_{sublayer,I} + c_{II} K_{sublayer,II} = \\ &= 2\frac{1-a}{2} K_A + a(aK_B + (1-a)K_A) = \\ &= (1-a)K_A + a^2 K_B + a(1-a)K_A = \\ &= (1+a)(1-a)K_A + a^2 K_B = \\ &= (1-a^2)K_A + a^2 K_B. \end{aligned}$$

The effective elastic properties of layer *2*, according to formulae (5.20) combined with (5.11), (5.21) and (5.23) become

$$\begin{aligned} G^*_{layer,2} &= 2c_I G_{sublayer,I} + c_{II} G_{sublayer,II} = \\ &= 2\frac{1-a}{2}(aG_B + (1-a)G_A) + aG_B = \\ &= a(1-a)G_B + (1-a)^2 G_A + aG_B = \\ &= (1-a)^2 G_A + a(2-a)G_B, \end{aligned} \tag{5.34}$$

$$\begin{aligned} K^*_{layer,2} &= 2c_I K_{sublayer,I} + c_{II} K_{sublayer,II} = \\ &= 2\frac{1-a}{2}(aK_B + (1-a)K_A) + aK_B = \\ &= a(1-a)K_B + (1-a)^2 K_A + aK_B = \\ &= (1-a)^2 K_A + a(2-a)K_B. \end{aligned}$$

Substituting (5.8), (5.33) and (5.34) to Eqs (5.28) for the *R-V-V* model of the effective shear and bulk moduli of the unit cell, may be written as

$$
\begin{aligned}
G^*_{RVV} &= \left(\frac{2c_1}{G_{layer1,3}} + \frac{c_2}{G_{layer,2}}\right)^{-1} = \\
&= \left(\frac{2\dfrac{1-a}{2}}{(1-a^2)G_A + a^2 G_B} + \frac{a}{(1-a)^2 G_A + a(2-a)G_B}\right)^{-1} = \\
&= \left(\frac{1-a}{(1-a^2)G_A + a^2 G_B} + \frac{a}{(1-a)^2 G_A + a(2-a)G_B}\right)^{-1}, \\
K^*_{RVV} &= \left(\frac{2c_1}{K_{layer1,3}} + \frac{c_2}{K_{layer,2}}\right)^{-1} = \\
&= \left(\frac{2\dfrac{1-a}{2}}{(1-a^2)K_A + a^2 K_B} + \frac{a}{(1-a)^2 K_A + a(2-a)K_B}\right)^{-1} = \\
&= \left(\frac{1-a}{(1-a^2)K_A + a^2 K_B} + \frac{a}{(1-a)^2 K_A + a(2-a)K_B}\right)^{-1},
\end{aligned}
\tag{5.35}
$$

with the same relations (with substitution of K by G) for *R-V-V* model for shear modulus G^*. The formula $(5.35)_2$ was first published in [7], with a misprint (missing power) in the equation (7) therein. It was noted, that the formula for the effective shear modulus $(5.35)_1$ would have the same form with substitution of K by G.

Using the relationships (5.4) and (5.5) between elastic constants the formulae for the effective Young's modulus and Poisson's ratio, respectively, according to the "extended" *R-V-V* model can be expressed in usual way

$$
\begin{aligned}
E^*_{RVV} &= \frac{9G^*_{RVV}K^*_{RVV}}{3K^*_{RVV} + G^*_{RVV}} \\
\nu^*_{RVV} &= \frac{3K^*_{RVV} - 2G^*_{RVV}}{2G^*_{RVV} + 6K^*_{RVV}}
\end{aligned}
\tag{5.36}
$$

with G^*_{RVV} and K^*_{RVV} given by Eqs $(5.35)_{1,2}$.

The relationships (5.35) and (5.36) with the volume fraction of metal phase defined by the formula (5.6), are depicted in Figs 5.2 – 5.5 as the "extended" *R-V-V* models.

Comparison of analytical models for the effective elastic constants

The relationships of the "extended" models of the effective elastic moduli of IPCs, expressed with formulae (5.17), (5.18), (5.26), (5.27), (5.35) and (5.36), with the volume fraction of metal phase given by the formula (5.6), are depicted in Figs 5.2, 5.3, 5.4 and 5.5. These relationships are collected and compared with existing bounds and models for the effective elastic constants described in Sec. 2.

The material constants of the investigated IPCs' components: alumina Al_2O_3, aluminum Al and copper Cu, that were used for calculations, are collected in Table 5.2.

The full-length formulae (5.18) for the effective elastic Young's modulus and Poisson's ratio according to the "extended" *V-R-V* model, are presented separately on the next page due to their enormous size. Similarly obtained full-length formulae (5.27) and (5.36), will not be presented.

Table 5.2. Material constants used in calculations. The data were obtained from: [33] for alumina and aluminum, material data tables of [149,150] for Cu; the values of bulk and shear moduli were calculated from Young's moduli and Poisson's ratios for the respective materials using relations (5.4) and (5.5) between the elastic constants.

	Al_2O_3	Cu	Al
E_A, E_B[GPa]	390.0	110.0	69.0
G_A, G_B [GPa]	162.5	40.7	25.9
K_A, K_B [GPa]	216.7	122.2	76.0
ν_A, ν_B	0.2	0.35	0.33

$$E^*_{VRV} = \frac{9G^*_{VRV}K^*_{VRV}}{3K^*_{VRV} + G^*_{VRV}} = \frac{9 \cdot \mathrm{A1} \cdot \mathrm{A2}}{3 \cdot \mathrm{A2} + \mathrm{A1}} = \frac{9 \cdot \mathrm{A3} \cdot \mathrm{A4}}{3 \cdot \mathrm{A4} + \mathrm{A3}},$$

$$\nu^*_{VRV} = \frac{3K^*_{VRV} - 2G^*_{VRV}}{2G^*_{VRV} + 6K^*_{VRV}} = \frac{3 \cdot \mathrm{A2} - 2 \cdot \mathrm{A1}}{2 \cdot \mathrm{A1} + 6 \cdot \mathrm{A2}} = \frac{3 \cdot \mathrm{A4} - 2 \cdot \mathrm{A3}}{2 \cdot \mathrm{A3} + 6 \cdot \mathrm{A4}}, \tag{5.18}_{1,2}$$

where:

$$A1 = (1-a)\left(\frac{(1-a)(aG_B + (1-a)G_A) + aG_A}{G_A(aG_B + (1-a)G_A)}\right)^{-1} + a\left(\frac{(1-a)G_B + a(aG_B + (1-a)G_A)}{G_B(aG_B + (1-a)G_A)}\right)^{-1},$$

$$A2 = (1-a)\left(\frac{(1-a)(aK_B + (1-a)K_A) + aK_A}{K_A(aK_B + (1-a)K_A)}\right)^{-1} + a\left(\frac{(1-a)K_B + a(aK_B + (1-a)K_A)}{K_B(aK_B + (1-a)K_A)}\right)^{-1},$$

$$A3 = \frac{(1-a)G_A(aG_B + (1-a)G_A)}{(1-a)(aG_B + (1-a)G_A) + aG_A} + \frac{aG_B(aG_B + (1-a)G_A)}{(1-a)G_B + a(aG_B + (1-a)G_A)}, \tag{5.18}_{3,4,5,6}$$

$$A4 = \frac{(1-a)K_A(aK_B + (1-a)K_A)}{(1-a)(aK_B + (1-a)K_A) + aK_A} + \frac{aK_B(aK_B + (1-a)K_A)}{(1-a)K_B + a(aK_B + (1-a)K_A)}.$$

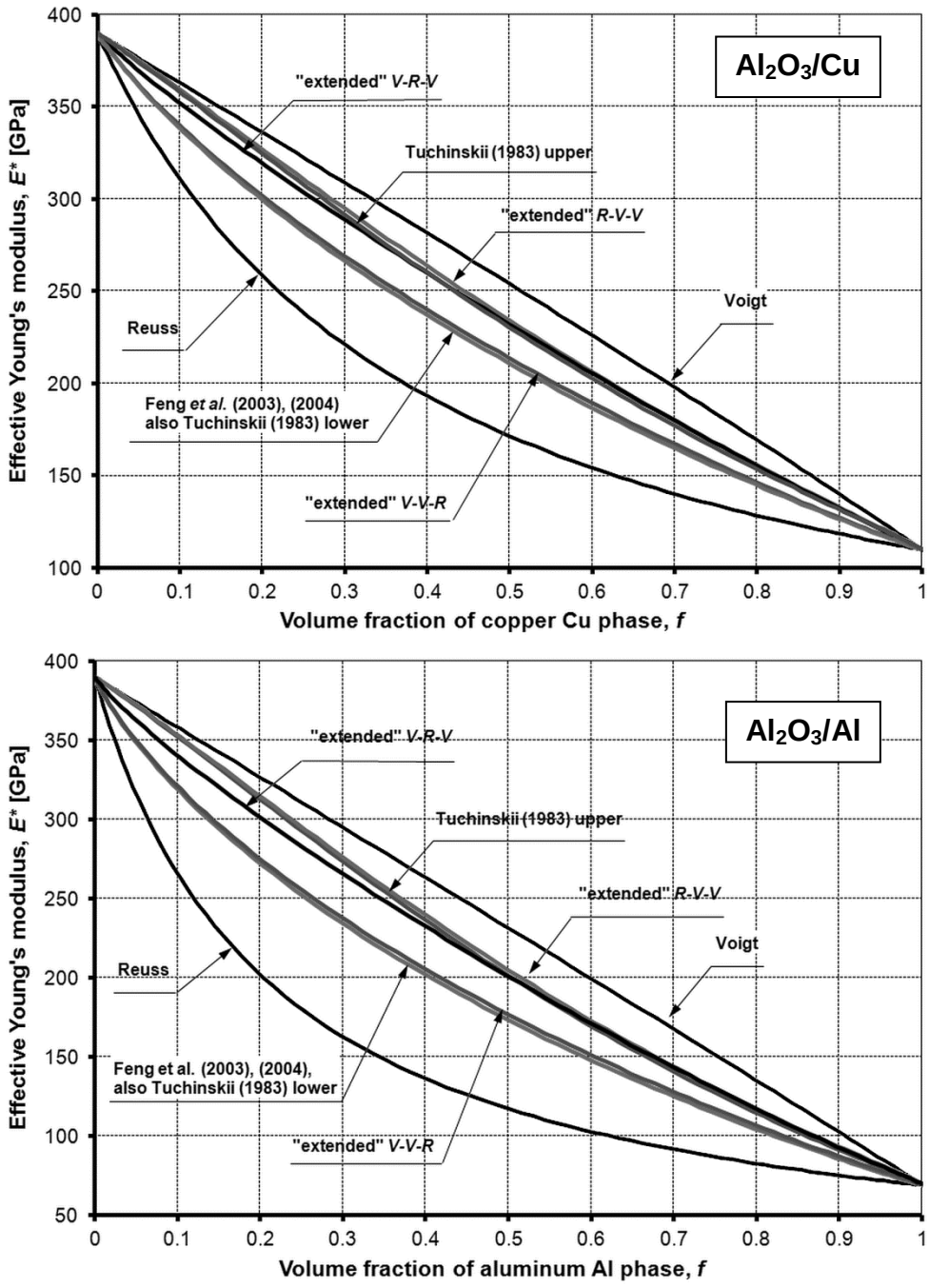

Figure 5.2. Effective Young's moduli vs. volume fractions of metal phase (graph for Al_2O_3/Cu based on [7,139] and [147], reprinted with permission of the publishers).

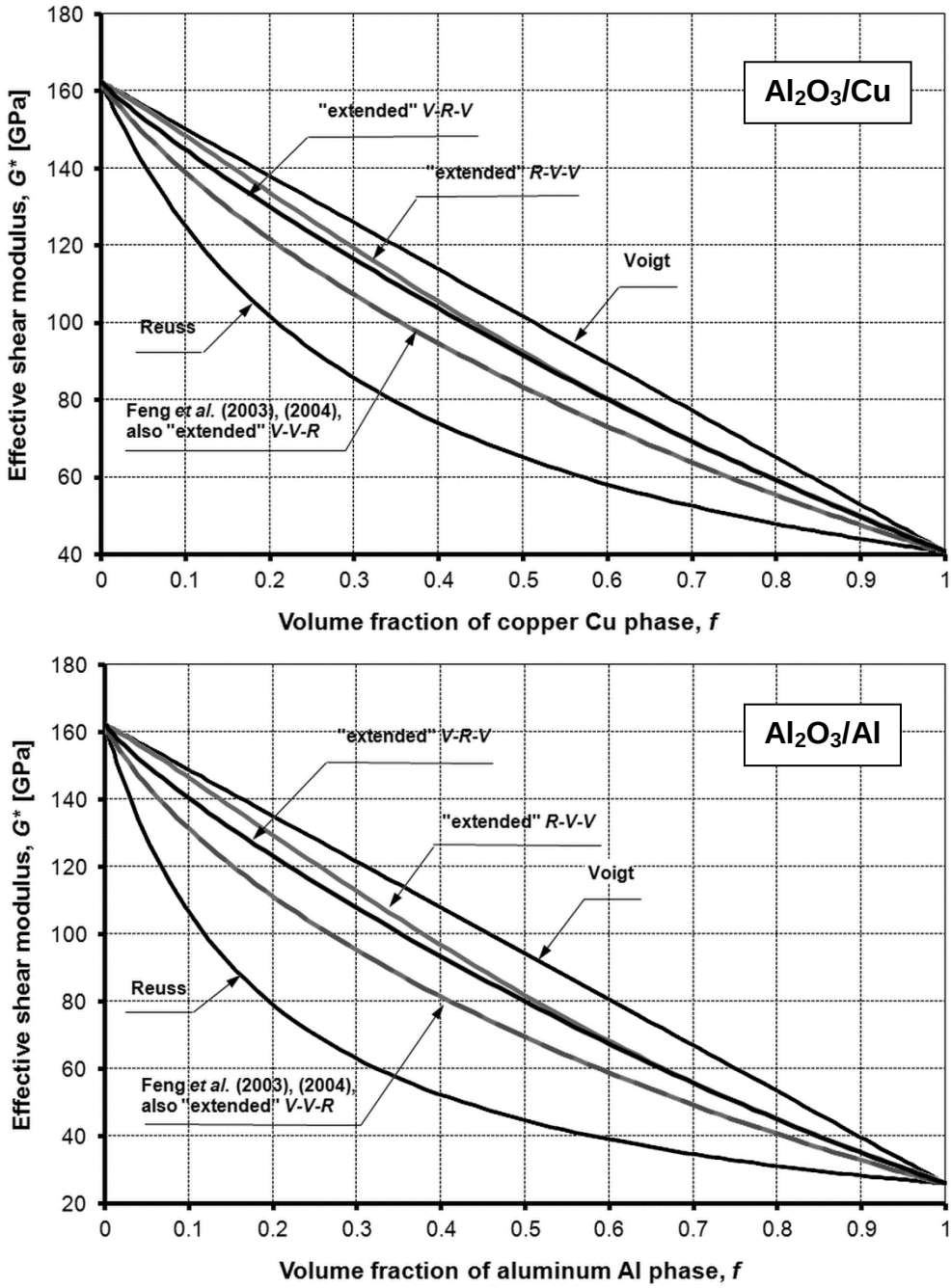

Figure 5.3. Effective shear moduli vs. volume fractions of metal phase (graph for Al_2O_3/Cu based on [7], reprinted with permission of the publisher).

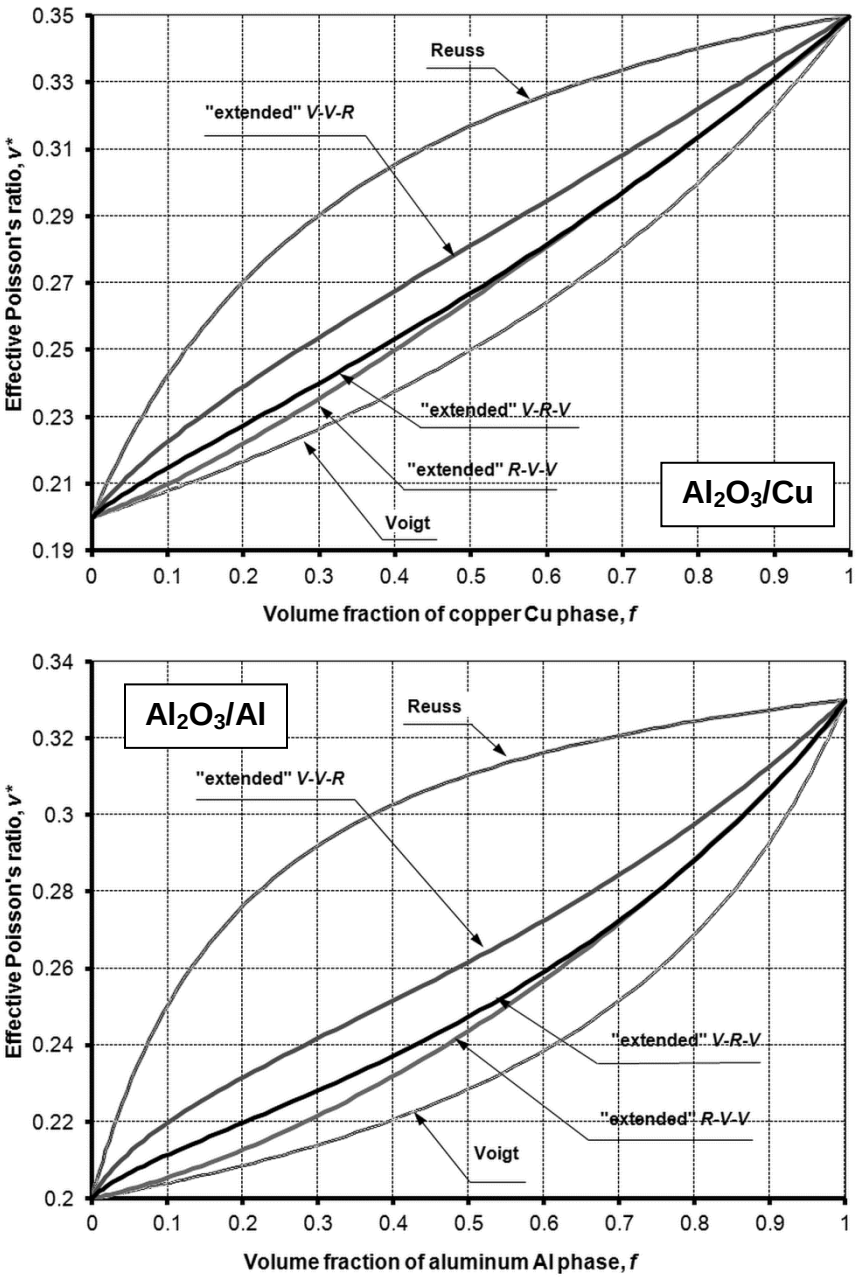

Figure 5.4. Effective Poisson's ratio vs. volume fractions of metal phase (graph for Al_2O_3/Cu based on [7], reprinted with permission of the publisher).

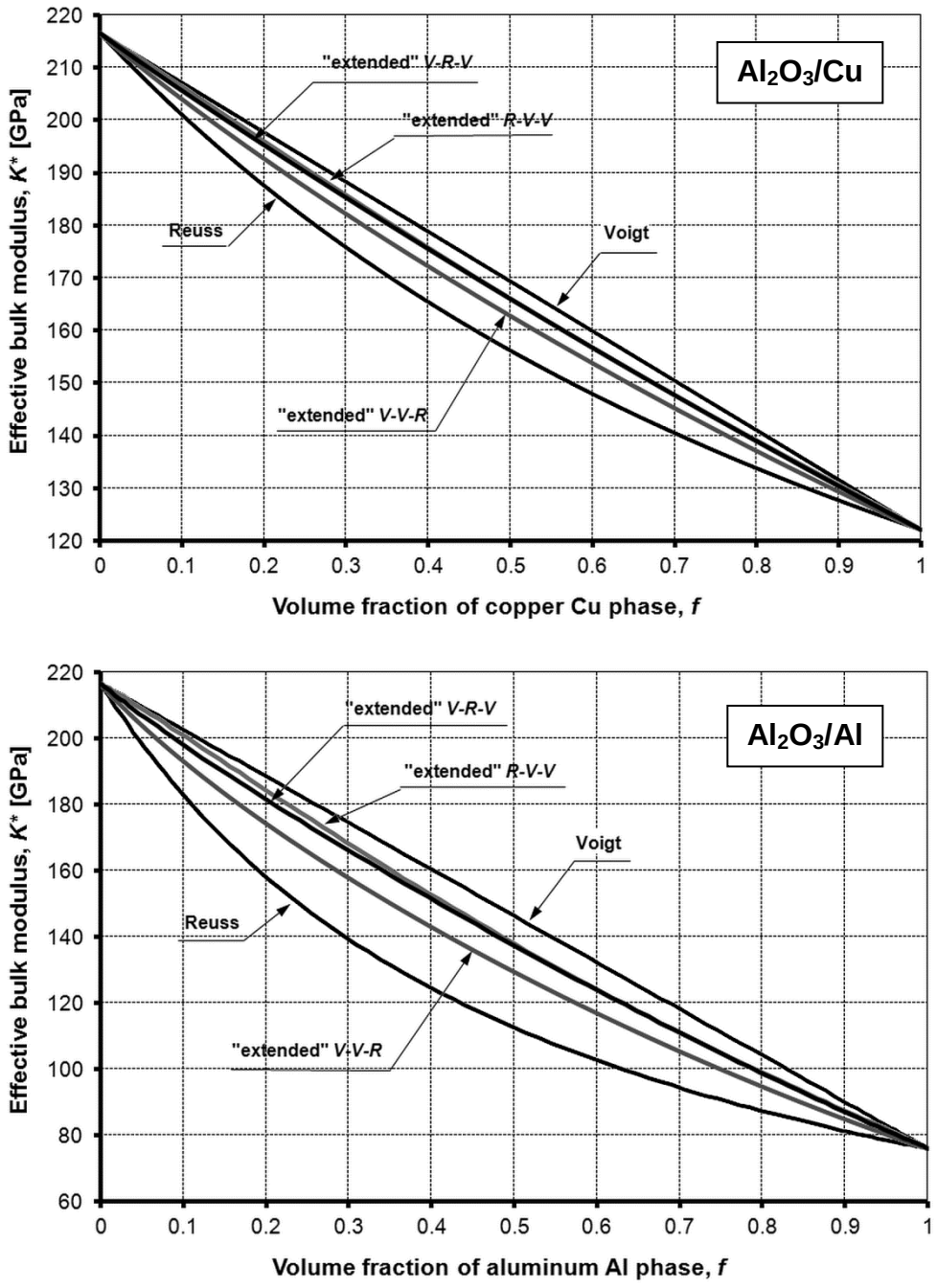

Figure 5.5. Effective bulk moduli vs. volume fractions of metal phase.

In Figs 5.2 – 5.5, the effective elastic constants developed according to the "extended" models, are compared with the Voigt and Reuss bounds and the models of [17,18] and [22].

The widest bounds for the effective material properties, according to the principles of minimum potential and complementary energy, are given by the Voigt and Reuss approximations (*cf*. [44]). The estimated values for composite effective properties should fit between these bounds. As it can be seen from Figs 5.2 – 5.5, all the presented models for Young's modulus, shear modulus and Poisson's ratio, fulfill this requirement and fit between the Voigt and Reuss bounds.

The "extended" *V-V-R* model estimates of the effective Young's modulus and shear modulus (Eqs $(5.26)_1$ and $(5.27)_1$), are in accordance with estimates of [17,18,22]. The "extended" *V-V-R* estimate of the effective Young's modulus (Eqs $(5.27)_1$) is close to Tuchinskii [22] and Feng *et al*. [17,18] models. The "extended" *V-V-R* estimate of the effective shear modulus (Eq. $(5.26)_1$) is identical with Feng *et al*. [17,18] model.

As it can be seen in Fig. 5.4, the "bounds" for the Poisson's ratio are reversed: the Reuss model serves as the upper bound on the effective Poisson's ratios, while the Voigt model serves as the lower bound. Also the "extended" *V-V-R* and *R-V-V* models behave this way[1] and that is the reason for the lower bound at higher Poisson's ratio values than for the upper bound.

The results yielded by the "extended" *V-R-V* model (*cf*. Figs 5.2 – 5.5) for both material compositions and for all the presented effective elastic constants *i.e*. Young's modulus, shear modulus, bulk modulus and Poisson's ratio, are close to the "extended" *R-V-V* model, and for the metal volume fractions higher than 0.6, both models almost coincide. The reason for that can be the same initial sectioning of the whole unit cell according to the Voigt model for both the *R-V-V* and *V-R-V* "extended" models.

For the Al_2O_3/Al material composition the differences between respective models are greater than for Al_2O_3/Cu composites due to greater differences between the elastic constants of the alumina ceramic and the respective metal components: Al and Cu.

[1] In Fig. 9 in [7] both "extended" bounds were named according to their actual roles – the "lower" was changed to "upper" and "upper" to "lower".

5.1.2. Estimates for the effective coefficient of thermal expansion

The effective *coefficient of thermal expansion* for a composite with interpenetrating microstructure was modelled in this thesis according to the estimate of [38]. The Voigt and Reuss approximations, as well as the modified Feng-Tuchinskii models described in the preceding Subsection, were included in the model. The effective coefficients of thermal expansion were estimated relative to the volume fraction of the metal phase. Calculations were made for Al_2O_3/Al and Al_2O_3/Cu IPCs. It was assumed that both metal and ceramic phases were elastically and thermally isotropic, so was the whole composite on the macroscale.

The Duhamel-Neumann law in the representative volume element (RVE) of a composite subjected to homogeneous displacement boundary conditions and uniform temperature increase from T_1 to T_2 relates the average stress tensor $\overline{\boldsymbol{\sigma}}$ with the average strain tensor $\overline{\boldsymbol{\varepsilon}}$ as

$$\overline{\boldsymbol{\sigma}} = \mathbf{C}^*(\overline{\boldsymbol{\varepsilon}} - \boldsymbol{\varepsilon}^T), \qquad where \quad \boldsymbol{\varepsilon}^T = \alpha^*(T_2 - T_1)\mathbf{1}, \tag{5.37}$$

where $\mathbf{C}^*$ denotes the effective stiffness tensor and α^* denotes the effective coefficient of thermal expansion, $\mathbf{1}$ is the unit 2nd rank tensor; the average strain tensor $\overline{\boldsymbol{\varepsilon}}$ may be decomposed into the elastic part $\boldsymbol{\varepsilon}^E$ and thermal part $\boldsymbol{\varepsilon}^T$ (*cf.* [44,148]).

The estimates of the effective coefficients of thermal expansion α^* were derived from the Eq. (2.6) of [38]:

$$\alpha^* = \alpha^{Voigt} + (\alpha_A - \alpha_B)\left(\frac{1}{K_A} - \frac{1}{K_B}\right)^{-1}\left[\frac{1}{K^*} - \left\{\frac{1}{K}\right\}^{Voigt}\right], \tag{5.38}$$

where the indices denote: $_A$, $_B$ – composite phases, * – effective quantity, ^{Voigt} - volume average according to Voigt model, $\alpha^{Voigt} = f_A\alpha_A + f_B\alpha_B$ – Voigt estimate of averaged coefficient of thermal expansion, $\left\{\frac{1}{K}\right\}^{Voigt} = \frac{f_A}{K_A} + \frac{f_B}{K_B}$ – is the Voigt estimate of averaged inverse of bulk modulus, f_A, f_B are volume fractions of the respective phases.

Depending on the approximation method to obtain the effective bulk modulus K^*, different formulae for the effective coefficient of thermal expansion α^* can be obtained. In what follows the Rosen and Hashin [38] estimates of the effective coefficients of thermal expansion will be formulated with substitution in the formula (5.38) of the upper and lower bounds on the effective bulk modulus according to Voigt and Reuss, by the expressions $(2.1)_2$ and $(2.4)_2$. The relationship for the Rosen

and Hashin [38] estimates of the effective coefficients of thermal expansion putting the Voigt upper bound on the bulk modulus K^*_{Voigt} $(2.1)_2$ in place of K^* takes the form

$$\alpha^*_{RH-Voigt} = \alpha^{Voigt} + (\alpha_A - \alpha_B)\left(\frac{1}{K_A} - \frac{1}{K_B}\right)^{-1}\left[\frac{1}{K^*_{Voigt}} - \left\{\frac{1}{K}\right\}^{Voigt}\right] =$$
$$= \alpha^{Voigt} + (\alpha_A - \alpha_B)\left(\frac{1}{K_A} - \frac{1}{K_B}\right)^{-1}\left[\frac{1}{(1-a)K_A + aK_B} - \left\{\frac{1}{K}\right\}^{Voigt}\right]. \tag{5.39}$$

When the Reuss lower bound on the bulk modulus K^*_{Reuss} $(2.4)_2$ is substituted for K^* in Eq. (5.38), the Rosen and Hashin [38] relationship (5.38) for the effective coefficients of thermal expansion becomes

$$\alpha^*_{RH-Reuss} = \alpha^{Voigt} + (\alpha_A - \alpha_B)\left(\frac{1}{K_A} - \frac{1}{K_B}\right)^{-1}\left[\frac{1}{K^*_{Reuss}} - \left\{\frac{1}{K}\right\}^{Voigt}\right] =$$
$$= \alpha^{Voigt} + (\alpha_A - \alpha_B)\left(\frac{1}{K_A} - \frac{1}{K_B}\right)^{-1}\left[\frac{1}{\left((1-a)/K_A + a/K_B\right)^{-1}} - \left\{\frac{1}{K}\right\}^{Voigt}\right]$$
$$= \alpha^{Voigt} + (\alpha_A - \alpha_B)\left(\frac{1}{K_A} - \frac{1}{K_B}\right)^{-1}\left[\frac{1-a}{K_A} + \frac{a}{K_B} - \left\{\frac{1}{K}\right\}^{Voigt}\right]. \tag{5.40}$$

In the equations (5.39) and (5.40) i – denotes identifier of the phase A or B, a – denotes volume fraction of the phase B, α_i – denotes coefficient of thermal expansion of the i-th phase, * – denotes the effective quantity.

Substituting the relations $(5.17)_2$, $(5.26)_2$ and $(5.35)_2$ for the "extended" effective bulk moduli from the preceding Subsection into the expression (5.38), the Rosen and Hashin [38] estimates of the effective coefficients of thermal expansion with the "extended" *V-R-V*, *V-V-R* and *R-V-V* models for bulk modulus, were obtained as shown below.

Using the "extended" *V-R-V* model for the effective bulk modulus $(5.17)_2$, the Rosen and Hashin [38] estimate of the effective coefficient of thermal expansion (5.38) takes the form

$$\alpha^*_{RH\,-VRV} = \alpha^{Voigt} + (\alpha_A - \alpha_B)\left(\frac{1}{K_A} - \frac{1}{K_B}\right)^{-1}\left[\frac{1}{K^*} - \left\{\frac{1}{K}\right\}^{Voigt}\right] =$$
$$= \alpha^{Voigt} + (\alpha_A - \alpha_B)\left(\frac{1}{K_A} - \frac{1}{K_B}\right)^{-1}\left[\frac{1}{K^*_{VRV}} - \left\{\frac{1}{K}\right\}^{Voigt}\right] = \tag{5.41}$$

$$= \alpha^{Voigt} + (\alpha_A - \alpha_B)\left(\frac{1}{K_A} - \frac{1}{K_B}\right)^{-1}$$
$$\cdot \left[\left((1-a)\left(\frac{(1-a)(aK_B + (1-a)K_A) + aK_A}{K_A(aK_B + (1-a)K_A)}\right)^{-1}\right.\right.$$
$$\left.\left. + a\left(\frac{(1-a)K_B + a(aK_B + (1-a)K_A)}{K_B(aK_B + (1-a)K_A)}\right)^{-1}\right)^{-1} - \left\{\frac{1}{K}\right\}^{Voigt}\right]. \quad (5.41)\ [\text{cont.}]$$

The Rosen and Hashin [38] bound on the effective coefficient of thermal expansion (5.38) with applied "extended" *V-V-R* model on the effective bulk modulus $(5.26)_2$ can be expressed as follows

$$\alpha^*_{RH-VVR} = \alpha^{Voigt} + (\alpha_A - \alpha_B)\left(\frac{1}{K_A} - \frac{1}{K_B}\right)^{-1}\left[\frac{1}{K^*_{VVR}} - \left\{\frac{1}{K}\right\}^{Voigt}\right] =$$
$$= \alpha^{Voigt} + (\alpha_A - \alpha_B)\left(\frac{1}{K_A} - \frac{1}{K_B}\right)^{-1}$$
$$\cdot \left[\left(a^2K_B + (1-a)^2K_A + 2a(1-a)\left(\frac{a}{K_B} + \frac{1-a}{K_A}\right)^{-1}\right)^{-1}\right.$$
$$\left. - \left\{\frac{1}{K}\right\}^{Voigt}\right] \quad (5.42)$$

The Rosen and Hashin [38] bound on the effective coefficient of thermal expansion (5.38) with applied "extended" *R-V-V* model of the effective bulk modulus $(5.35)_2$, reads

$$\alpha^*_{RH-RVV} = \alpha^{Voigt} + (\alpha_A - \alpha_B)\left(\frac{1}{K_A} - \frac{1}{K_B}\right)^{-1}\left[\frac{1}{K^*_{RVV}} - \left\{\frac{1}{K}\right\}^{Voigt}\right]$$
$$= \alpha^{Voigt} + (\alpha_A - \alpha_B)\left(\frac{1}{K_A} - \frac{1}{K_B}\right)^{-1}$$
$$\cdot \left[\left(\left(\frac{1-a}{(1-a^2)K_A + a^2K_B} + \frac{a}{(1-a)^2K_A + a(2-a)K_B}\right)^{-1}\right)^{-1}\right.$$
$$\left. - \left\{\frac{1}{K}\right\}^{Voigt}\right] \quad (5.43)$$

$$= \alpha^{Voigt} + (\alpha_A - \alpha_B)\left(\frac{1}{K_A} - \frac{1}{K_B}\right)^{-1} \cdot \left[\frac{1-a}{(1-a^2)K_A + a^2 K_B} + \frac{a}{(1-a)^2 K_A + a(2-a)K_B} - \left\{\frac{1}{K}\right\}^{Voigt}\right] \quad (5.43)\ \text{[cont.]}$$

The Rosen and Hashin [38] estimates (5.41), (5.42) and (5.43), with the Voigt and Reuss bounds, (5.39) and (5.40), and with the *V-R-V*, *V-V-R* and *R-V-V* models are depicted in Figs 5.6 and 5.7 for two material compositions: Al_2O_3/Cu and Al_2O_3/Al. Material parameters of alumina Al_2O_3, aluminum and copper, that were used for calculations, are shown in Table 5.3.

Table 5.3. Material properties used in calculations. The data were obtained from: [33,151] for alumina and aluminum, material data tables of [149,150] for Cu; the values of bulk and shear moduli were calculated from Young's moduli and Poisson's ratios for the respective materials using relations (5.4) and (5.5) between the elastic constants.

	Al_2O_3	Cu	Al
E_A, E_B[GPa]	390.0	110.0	69.0
G_A, G_B [GPa]	162.5	40.7	25.9
K_A, K_B [GPa]	216.7	122.2	76.0
ν_A, ν_B	0.2	0.35	0.33
α_A, α_B [ppmK^{-1}]	6.55	16.8	25.0

As it can be seen in Figs 5.6 and 5.7, for both IPC material compositions, Al_2O_3/Cu and Al_2O_3/Al, the outermost estimates on the effective coefficients of thermal expansion are provided by the Rosen and Hashin [38] estimates with the Voigt and Reuss approximations used. According to [152], these estimates with applied bounds on the effective elastic moduli, may be regarded as bounds on the effective coefficients of thermal expansion. All three remaining Rosen and Hashin estimates incorporating the "extended" *V-R-V*, *V-V-R* and *R-V-V* models, fit between these bounds.

It can be noted from Figs 5.6 and 5.7 that the Rosen and Hashin [38] approximations with the Voigt and Reuss bounds and with the *V-V-R* and *R-V-V* models manifest reversed behaviour as compared to the Voigt and Reuss bounds and the *V-V-R* and *R-V-V* models themselves for the effective elastic moduli: Young's

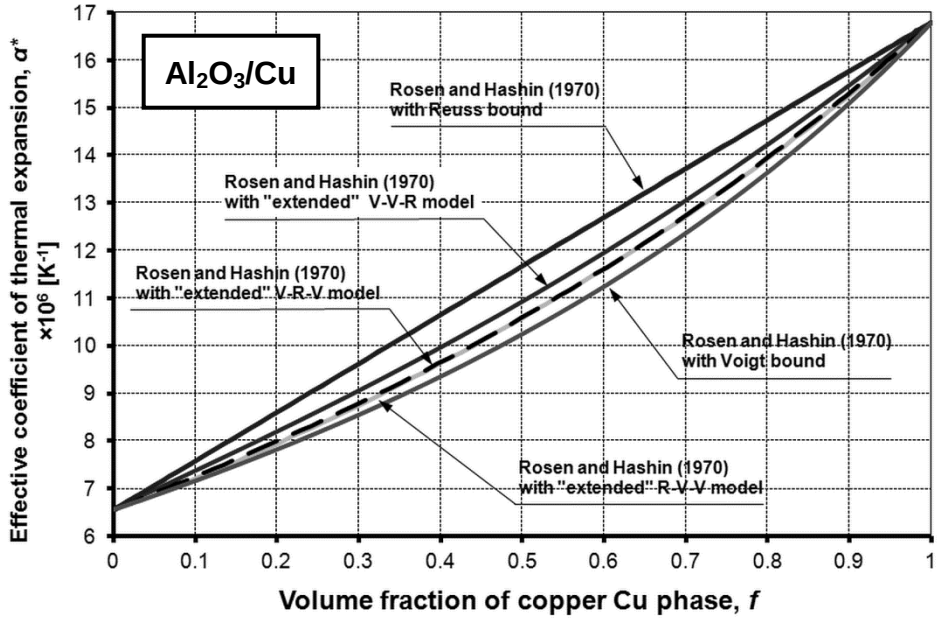

Figure 5.6. Effective coefficient of thermal expansion vs. volume fraction of metallic phase for Al_2O_3/Cu composite.

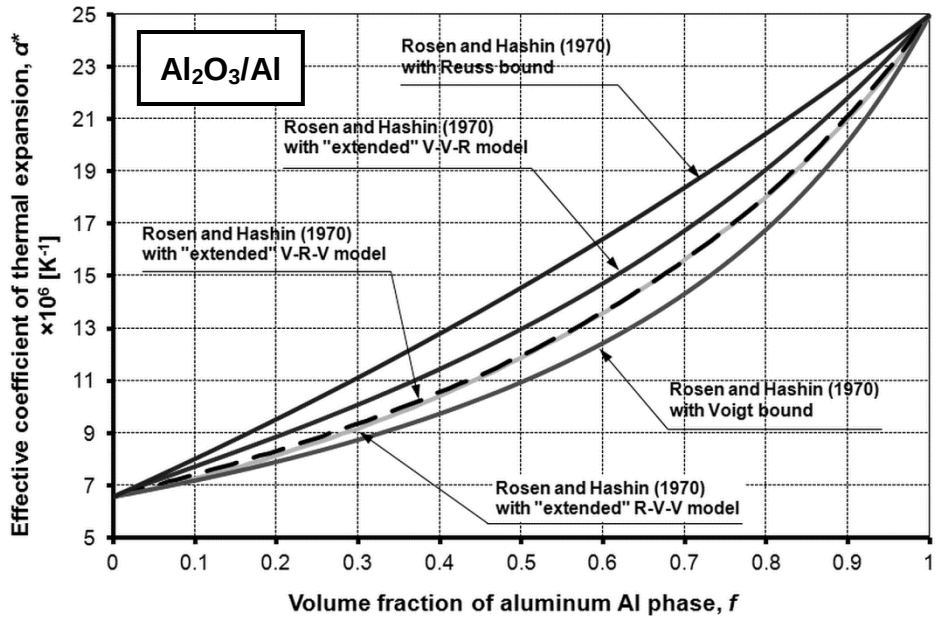

Figure 5.7. Effective coefficient of thermal expansion vs. volume fraction of metallic phase for Al_2O_3/Al composite.

modulus, shear modulus and bulk modulus. The Rosen and Hashin estimate with the Reuss approximation takes high values and may be regarded as the upper bound on the effective coefficients of thermal expansion. The Rosen and Hashin estimate with the Voigt model, takes low values and may serve as the lower bound. Similarly, the Rosen and Hashin estimate with the *V-V-R* model takes high values, in opposite to low values for the *V-V-R* model for the elastic moduli. The Rosen and Hashin estimate with the *R-V-V* model takes low values in opposite to high values for the *R-V-V* model for the elastic moduli.

For both material compositions and for metal volume fractions less than appox. 0.5, the Rosen and Hashin estimations with the *V-R-V* and *R-V-V* models, almost coincide.

For the Al_2O_3/Al composite the differences between respective models are greater than for the Al_2O_3/Cu, which may be due to the larger contrast in phase properties between the elastic constants: shear modulus and bulk modulus, for alumina (Al_2O_3) and aluminum than for alumina and copper.

5.2. Numerical models

In this Section numerical models for estimation of the effective elastic constants of IPCs will be proposed. The influence of the microstructure on the effective composite properties will be shown on a simple example using Mishnaevsky [41,140,153] codes. Then, Finite Element Method (FEM) models for two kinds of IPC microstructures: simplified 3D "cross" microstructure and real IPC microstructure obtained with computed microtomography (micro-CT), will be presented. For the real IPC microstructure, the mesh of the voxel type and the mesh with smoothed boundaries between composite's phases containing tetragonal and hexagonal elements, will be used. The results of the effective elastic constants obtained with different numerical models will be presented and compared with the analytical models developed in Subsec. 5.1.1 and with the experimental results described in Appendix.

The models and results presented in this Subsection were published in part in [7,139,147].

5.2.1. Mishnaevsky model

It is commonly known that the microstructure of a composite influences its overall properties (see for example [154,155]). Analytical models for the effective elastic properties work fairly well for idealized and simplified microstructures but usually fail for more complex material microstructures. In such cases numerical approaches are usually applied as they enable estimation of the effective material moduli for irregular and complicated microstructures like those manifested by the interpenetrating phase composites. The models of Mishnaevsky [41,140,153], may serve as an example of using numerical approach to calculate the effective elastic constants of two-phase composites with various types of microstructures.

The programme of Mishanevsky [140,153] was used in a simple example that will be shown below to examine the influence of the composite's microstructure on the effective elastic properties [7]. The two- or three-dimensional composite microstructure was represented with square or cubic cells, respectively. The programme can generate a random microstructure, or an input from prescribed microstructure data can be used.

In the 2D case a cell may be composed of one or both materials. The microstructure of the material is mapped and the effective mechanical properties for all particular cells, rows of cells, and finally of the whole composite, are derived. A procedure with the Voigt iso-strain assumption is used for the rows of cells [140], namely

$$E^{layer} = \left(1 - c^{layer}\right)E_B + c^{layer}E_A, \tag{5.44}$$

where c^{layer} is the area fraction of the phase A, E_A, E_B are Young's moduli of the A nad B phase, respectively.

The effective Young moduli of the composite E^* are obtained using the Reuss iso-stress assumption:

$$E^* = \left(\sum_{i=1}^{n} \frac{1}{nE_i^{layer}}\right)^{-1}. \tag{5.45}$$

In Fig. 5.8 the effective Young's moduli estimated with the Mishnaevsky code [153] are compared for two different microstructures of Al_2O_3/Cu composite. The material data of alumina and copper used in the numerical calculations of this Subsection are shown in Table 5.4. It is seen in Fig. 5.8 that for the same volume fractions of the "black" Cu phase (white colour denotes Al_2O_3) the effective moduli

are substantially different for different microstructures. Hence, it can be deduced that the composite microstructure affects its overall elastic properties.

Table 5.4. Material properties used in numerical models of this Subsection; for alumina ceramic the data were adopted from [33,151], whereas for copper the material data tables of [149,150] were used; the values of bulk and shear moduli were taken from [7] as calculated from Young's moduli and Poisson's ratios for the respective materials using the relations (5.4) and (5.5) between the elastic constants.

	Al_2O_3	Cu
E_A, E_B [GPa]	390.0	110.0
G_A, G_B [GPa]	162.5	40.7
K_A, K_B [GPa]	216.7	122.2
ν_A, ν_B	0.2	0.35

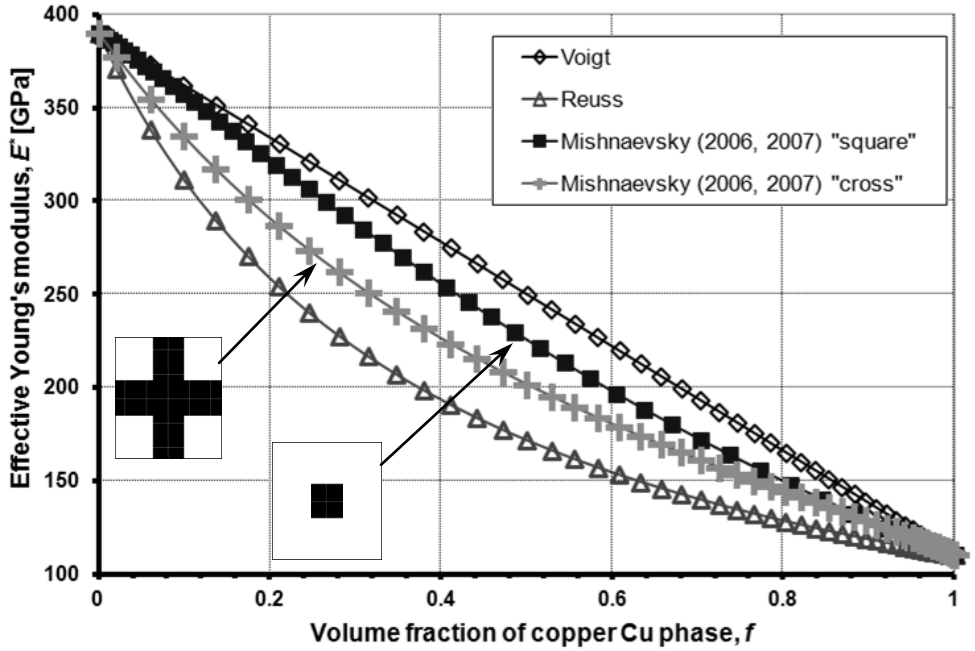

Figure 5.8. Influence of the model microstructure on the effective Young's modulus of Al_2O_3/Cu composite: the results of Mishnaevsky [140,153] procedure implemented for two

different microstructures – "cross" microstructure and matrix – inclusion "square" microstructure (reproduced from [7] with permission of the publisher)

5.2.2. Three-dimensional cross model

A numerical model for a two-phase IPC microstructure from Fig. 5.1(a) was created using a three-dimensional cross unit cell with a varying branch section, as presented in Fig. 5.9 (*cf.* [7]). The numerical models for the effective Young's modulus, Poisson's ratio and shear modulus were developed and implemented using FEAP [156] programme. At this stage of model development the effect of anisotropy of the cross microstructure (Fig. 5.9) was neglected.

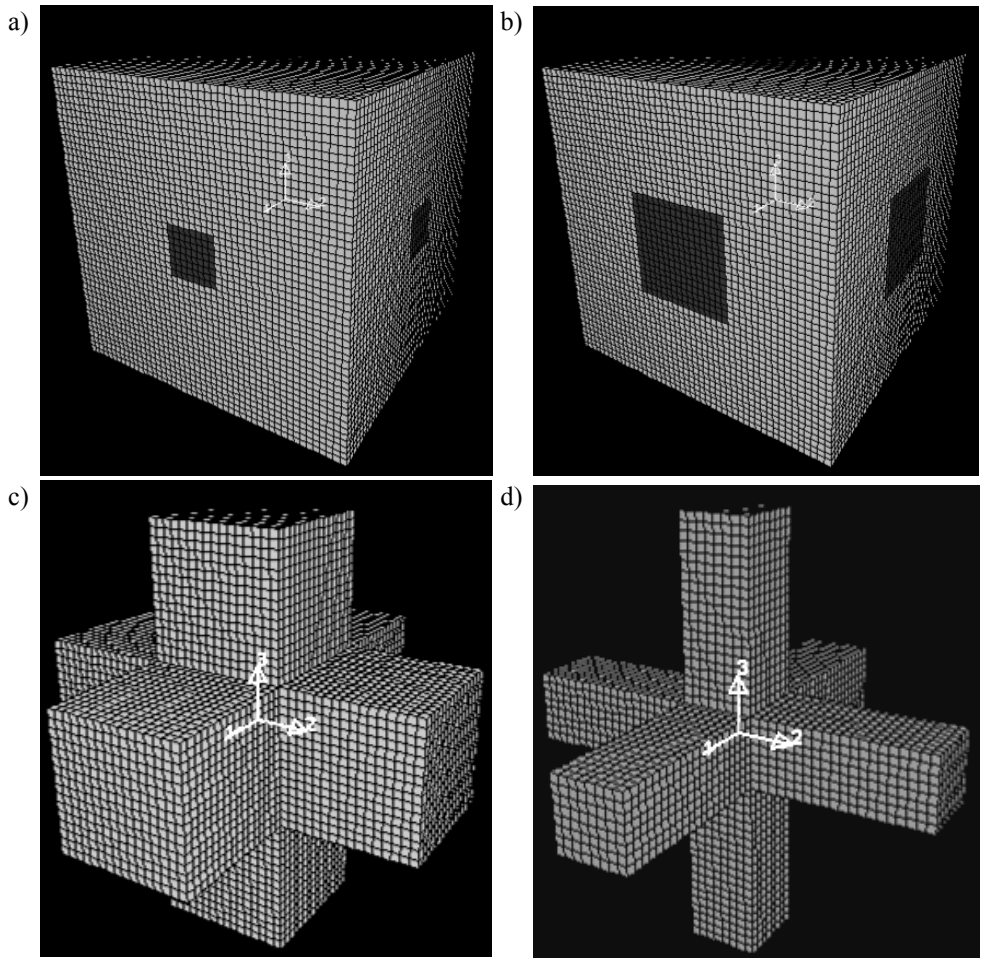

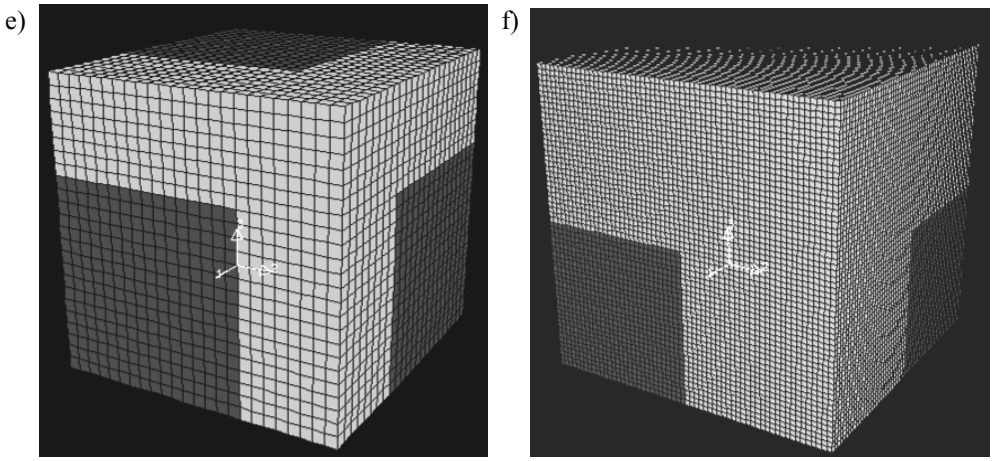

Figure 5.9. FEM model of the cubic unit cell created with FEAP 7.5 for different metal volume fractions; dark phase – alumina, light phase – copper. (a, b) Unit cell model used for the calculations of the effective Young's modulus and Poisson's ratio, (c, d) – one of the phases with another phase invisible, (e, f) –1/8th of the unit cell used for the effective shear modulus calculations. Volume fractions of metal: a), d) 0.93, b), c) 0.74, e) 0.26, f) 0.50, finer mesh.

The unit cubic cell with three-dimensional cross microstructure composed of two mutually interpenetrating phases is shown in Fig. 5.9(a,b). The varying cross section made it possible to analyze the influence of metal volume fractions on the effective moduli. For the effective Young's modulus and Poisson's ratio the unit cell shown in Fig. 5.9(a,b) was used. Due to the problem symmetry, only 1/8th of the unit cell (Fig. 5.9(a,b)) was considered. The unit cell was cut along three symmetry planes perpendicular to the coordinate system axes and relevant symmetry conditions were applied

$$\begin{cases} u_1 = 0.0 & on\ symmetry\ plane\ perpendicular\ to\ x_1 \colon x_1 = 0.0, \\ u_2 = 0.0 & on\ symmetry\ plane\ perpendicular\ to\ x_2 \colon x_2 = 0.0, \\ u_3 = 0.0 & on\ symmetry\ plane\ perpendicular\ to\ x_3 \colon x_3 = 0.0, \end{cases} \tag{5.46}$$

where u_i – component of the displacement in i^{th} direction, x_i – i^{th} axis of the Cartesian coordinate system, $i = 1..3$.

The applied boundary conditions were of mixed type (*cf.* [157]), as described in [7]. The Young's modulus and Poisson's ratio were determined simulating the material behaviour during tensile test (*cf.* [158,159] standards, respectively; see also: [160], who measured Young's modulus and Poisson's ratio for thin Cu, Ag and Ni films in tensile tests, or [161], where tensile tests were used to measure Young's

modulus of polycrystalline pure iron), with the following gradient of deformation **E** applied (*cf.* [162,163]):

$$\mathbf{E} = \begin{bmatrix} \lambda & 0 & 0 \\ 0 & \lambda^{-1/2} & 0 \\ 0 & 0 & \lambda^{-1/2} \end{bmatrix} = \begin{bmatrix} 1.0004 & 0 & 0 \\ 0 & 0.9998 & 0 \\ 0 & 0 & 0.9998 \end{bmatrix}, \tag{5.47}$$

where $\lambda = \frac{l}{l_0}$ is the principal stretch along the axis *1*.

For the effective shear modulus, the unit cell as in Fig. 5.9(e,f), being 1/8th of the unit cell for the effective Young's modulus and Poisson's ratio, was applied. Displacement loading was applied to simulate simple shear. Simple shear state was addressed *e.g.* by [162,163] and used to determine shear modulus by [164], who modelled simple shear with a FE model supporting experimental measurements of shear modulus of wood. Hussnätter and Merklein [165] used simple shear for experimental determination of the shear modulus of lightweight alloys of aluminum AA6016 (wrought alloy) and magnesium AZ31. Nunes [166] and Nunes and Moreira [167] analysed simple shear under large deformations of polydimethylsiloxane (PDMS), modelled as a nonlinear elastic solid. It has been noted in the literature [168-170] that for small deformations the effects of simple shear and pure shear are the same. Therefore, in this thesis simple shear was applied, with the deformation gradient **E** in the form (*cf.* [162,163]):

$$\mathbf{E} = \begin{bmatrix} 1 & \gamma & 0 \\ 0 & 1 & 0 \\ 0 & 0 & 1 \end{bmatrix} = \begin{bmatrix} 1 & 0.0048 & 0 \\ 0 & 1 & 0 \\ 0 & 0 & 1 \end{bmatrix}, \tag{5.48}$$

where γ denotes the amount of shear.

The model was meshed with eight-node brick elements amounting to 17551 nodes and 13824 elements (Fig. 5.9e). Finer mesh with 237367 nodes and 216000 elements shown in Fig. 5.9f was used, too. The materials of the phases: alumina Al_2O_3 and copper Cu, were assumed to be linear elastic. The material data of Al_2O_3 and Cu from Table 5.4 were used for calculations. The iterative solution method was employed. The chosen displacement and stress distributions are depicted in Fig. 5.10. The effective elastic properties resulting from calculations are collected and compared with other results in Figs 5.14 – 5.16 at the end of this Subsection.

a)

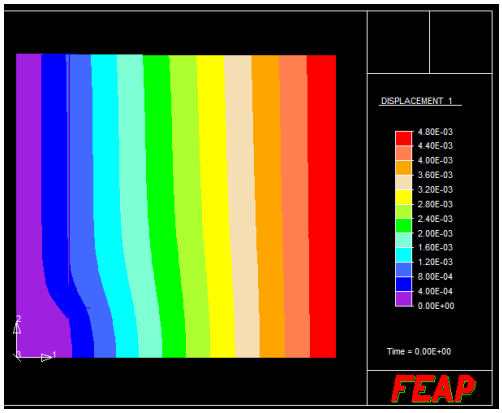

b)

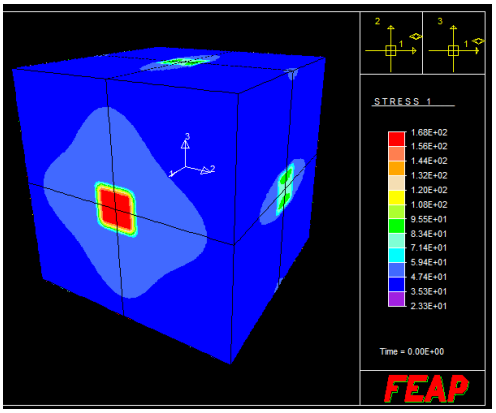

c)

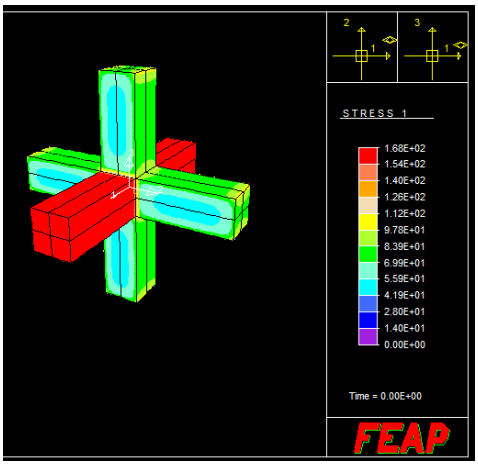

d)

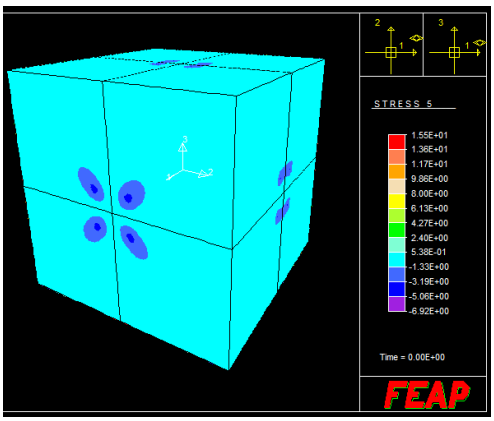

e)

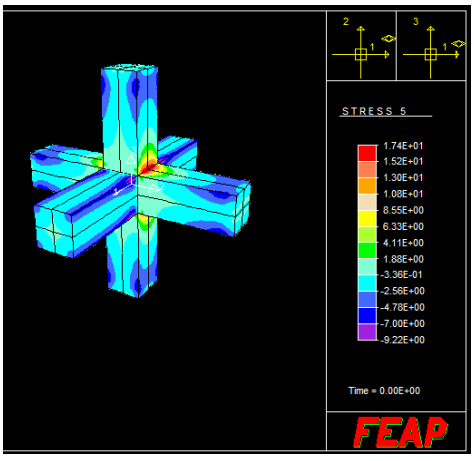

f)

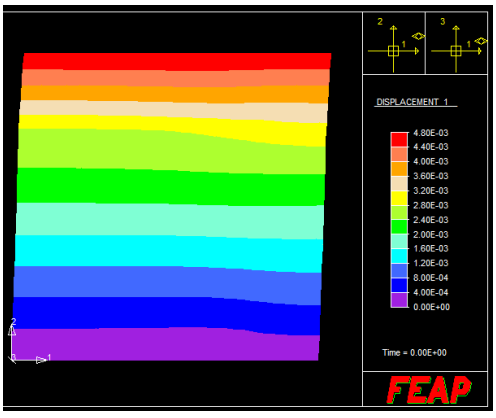

g) h)

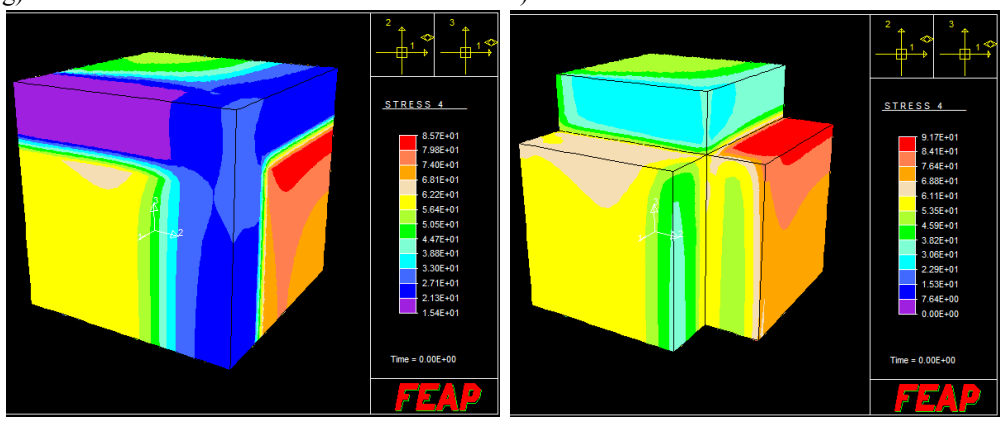

Figure 5.10. Sample results of the calculations for the 3D cross FEM model in FEAP [156], (a–e) uniaxial tension, 0.93 of metal volume fraction, (f–h) simple shear, 0.16 of metal volume fraction: a) distribution of displacements in loading direction u_1, showed in deformed state enlarged 100 ×, (b, c) distributions of normal stresses in loading direction σ_{11}, (d, e) distributions of shear stresses in loading direction τ_{23}, f) distribution of displacements in loading direction u_1, showed in deformed state enlarged 100 ×, (g, h) distributions of shear stresses in direction perpendicular to loading τ_{12}. Stresses in (b, c, d, e, g, i, h) in MPa.

5.2.3. Real microstructure model

In this Subsection the FE models representing the real material microstructure of an IPC obtained with computed microtomography (micro-CT) technique will be described. The original research results presented herein were published in part in [7,139,147].

As already stated in this thesis the basic motivation for using micro-CT images in mechanical models was to represent the details of the real IPC material microstructure with no necessity to make any assumptions as to the geometry of the composite's phases. The microstructure of the real composites is usually complicated and irregular, thus difficult to model. Any geometrical simplification may suppress important details of the microstructure and affect the modelling output. This is especially true in fracture problems as these are sensitive to local effects. In the case of effective elastic properties the exact representation of internal composite structure is deemed to be less important as these properties are governed by the volume fractions of phases and not by the exact morphology of the ceramic

matrix and the interpenetrating metal reinforcement. The micro-CT based modelling of the effective elastic properties will shed some light on this statement.

The Al_2O_3/Cu IPCs manufactured at the Institute of Materials Science of Darmstadt University of Technology in Germany by pressure-assisted infiltration of molten copper into porous alumina preforms were used for the modelling purposes of this Subsection. The manufacturing procedure was described in a concise form in [139], whereas the investigated IPC materials and their characterization in the Appendix to this thesis. The microstructures of the IPCs were pre-determined by the structure of compressed polymer foam and natural wool felt as the sacrificial pore forming agents (PFA) into which alumina slurry made of 0.1 μm grain diameter alumina powder (TAIMICRON TM DAR) was cast to form porous preforms after sintering (Nabertherm HT 16/17 furnace). The infiltration of high purity copper (99.95%, Bikar Metalle) into porous alumina preforms was performed in the Fine Ceramics Technology FPW furnace at 1200°C and 100 bar.

The micro-CT input data used in the present numerical models were provided by G. Geier from the Osterreichisches Gießerei-Institut (Austrian Casting Institute) in Leoben. The Al_2O_3/Cu IPC specimens were cylinders of approx. 5 mm in diameter and 5 mm in height. The procedure of obtaining the microstructure data and transferring it into a FE mesh was described in detail by [139]. In micro-CT technique the density of the material is detected and represented as a greyscale value. The whole volume of the examined specimen is divided into a regular grid of cubic or cuboid *voxels* – "volumetric picture elements", being the smallest distinguishable parts of the volume. The size of voxels is generally determined by the resolution of the micro-CT device. Each voxel carries the number representing its density. The volumetric density array is then composed of densities measured at the middle of each voxel. Such volume of voxels is written as a binary file, either single volumetric data file, or a set of planar images.

The volumetric data obtained for the investigated IPCs in the form of single 3D microstructure data files, were transferred into eight-node cubic finite elements in two ways. The first way, named "voxel 1", operated on the integer microstructure data, that was earlier obtained from the binary volumetric microstructure data file and provided by the Institute of Mechanics of Darmstadt University of Technology (TUD) in Germany. The transfer of the integer microstructure data into FEAP and ABAQUS FE meshes was made with a set of self-written codes in FORTRAN. The material data can be assigned to finite elements according to the data set of the scan, setting the threshold value between material phases based on density gradients. The volumetric density array was, for a two phase composite, binarized, by extracting

from it voxels containing one of the phases and assigning a common digit to them (*i.e.* 1) instead of the density value, and then assigning other digit (*i.e.* 2) to voxels belonging to the other phase. It was remembered which digit had been assigned to which density range, corresponding to one of the materials. The coordinates of nodes and then the eight-node brick elements were created by replicating the grid of voxels. Both materials were assigned to respective elements. The FE meshes created this way were adapted for FEAP [156] and ABAQUS [144] programmes and named as a "voxel 1" type.

The second way of transferring a single 3D microstructure data file into eight-node cubic finite elements in this thesis made use of the commercial software Simpleware ScanIP/ScanFE [8]. The ScanIP programme enables an import of the graphic files. The graphical editing with relevant tools and filters is followed by separating of the image masks representing two or more phases of the material. The programme divides the surfaces that are bounding the phases into finite elements, and initially prepares finite element meshes for the chosen masks. The files with the FE meshes containing hexagonal, tetragonal or mixed elements that are input files for commercial FEM software (*e.g.* ABAQUS) are created with the ScanFE programme. The microstructure can be divided into voxels ("voxel 2" mesh type); smoothing of the boundaries between different materials and mesh optimization are also possible.

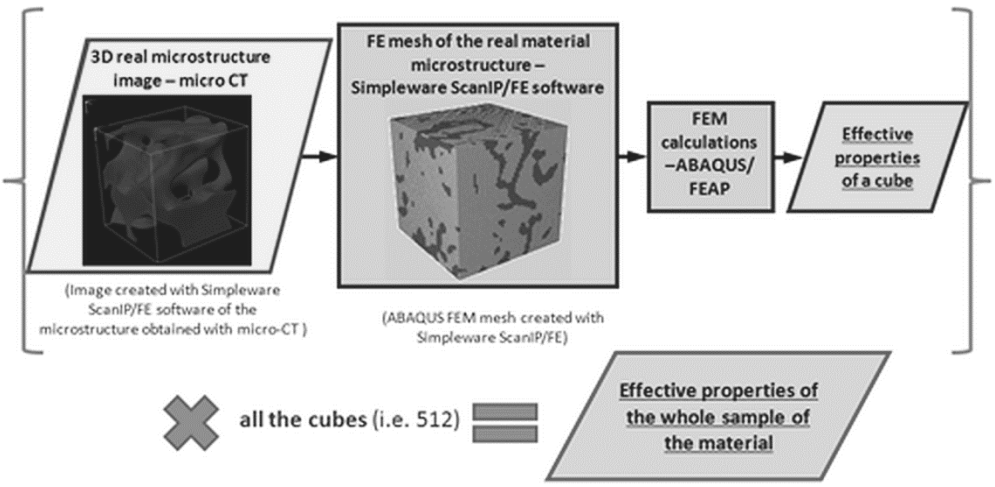

Figure 5.11. Scheme of the numerical approach used for the real composite microstructures.

The scheme of the generic numerical method for real microstructures can be described as follows: 1) acquiring the 3D data of the composite microstructure via micro-CT scans or similar technique, 2) creating FEM mesh of the material microstructure using commercial software [8], 3) performing FEM calculations using the obtained FEM mesh for the material microstructure (*cf*. Fig. 5.11).

For the segmented pieces of the real Al_2O_3/Cu IPC microstructures the effective elastic constants, Young's modulus, Poisson's ratio and shear modulus, were numerically estimated using [144] or [156] programmes, as voxel 1 (based on self-written FORTRAN codes) and voxel 2 (based on [8] software) modelling approaches were used alternatively (in fact, meshes resulting from the same input data, voxel size and threshold value, should be the same in both approaches). For the calculations, inner cubes of a polymer foam PFA-based sample ("microstructure 1") of 400 × 400 × 400 voxels and of a wool PFA-based sample ("microstructure 2") of 105 × 105 × 105 voxels were cut out. Since these models were too big for the available hardware and software, the cubes were divided into 512 (microstructure 1) and 27 (microstructure 2) smaller cubic subvolumes, each of 50 × 50 × 50 voxels and 35 × 35 × 35 voxels, respectively. For microstructure 2 also other mesh sizes were tested. The calculations for each subvolume were conducted separately. Two types of FE meshes were used: voxel and smoothed, the latter had smoothed interfaces between phases with tetragonal elements.

In numerical models based on real material microstructures the size of the representative volume element (RVE) is an outstanding issue. In practical terms the RVE size can be estimated by checking if for a few volume sizes the computed results for the property at hand (e.g. Young's modulus) converge to a certain value with growing volume size. The smallest volume for which the results are close enough to that value can be regarded as representative. Another way of determining the RVE size for multiphase materials is to use a statistical approach. In the statistical procedure proposed by [171] the *Chi-square* (χ^2) *criterion* is used to measure the standard deviation of the response of the single tested specimen from the mean of its class of realizations. This procedure can be summarized as follows:

- for the initial volume size depending on the maximal characteristic dimension of the phases and for each volume fraction of the phases, at least five realizations of the investigated volume should be generated,
- FEM calculations should be performed and loading-displacement characteristics should be prepared,

- the *Chi-square* χ^2 criterion should be evaluated and the accuracy of the obtained statistical results should be compared with the desired accuracy,
- if the accuracy is satisfactory, the investigated volume can be assumed as RVE, if not, the calculations should be repeated for the enlarged volume.

The images of the microstructures and the FEM meshes used for calculations, created with Simpleware ScanIP/FE software, are presented in Fig. 5.12. The comparison between voxel and smoothed meshes is depicted in Fig. 5.13.

a) b)

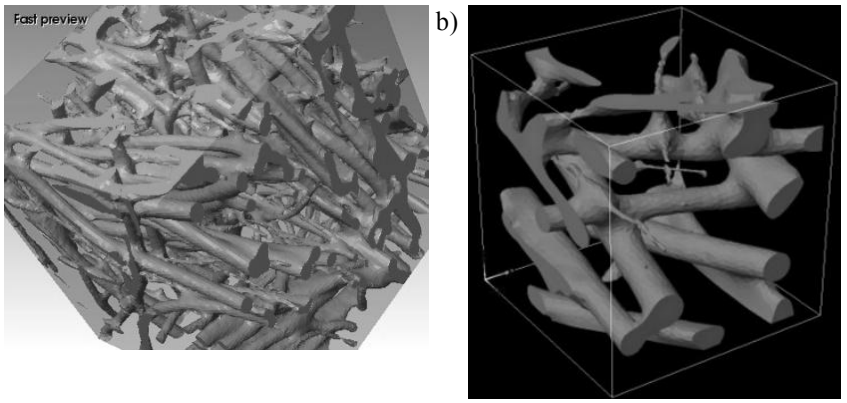

c) d)

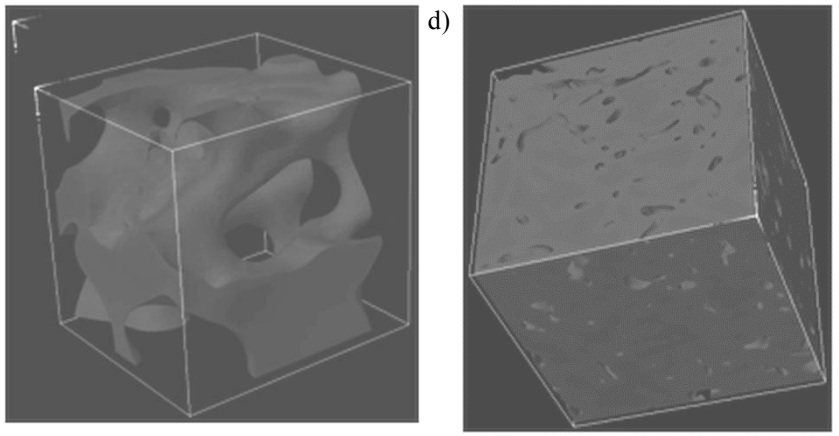

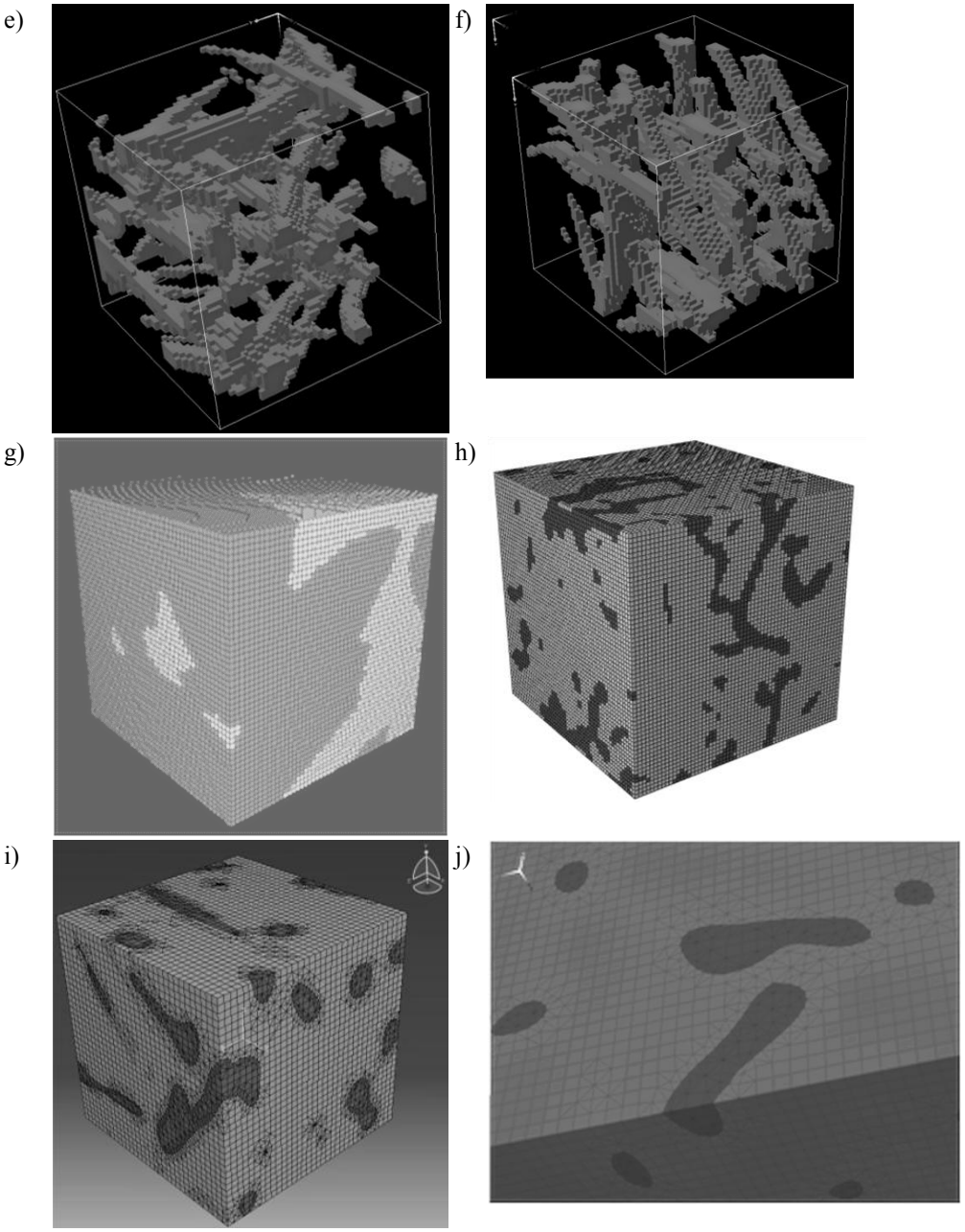

Figure 5.12 Microstructure images obtained with Simpleware ScanIP programme: (a-f), FE meshes used for calculations (g-j), (e-h) - voxel meshes, (i, j) - smoothed meshes: g) microstructure "1", image created with FEAP [156], (h, i) microstructure "2" image created

with ABAQUS [144], j) mesh created with [8]. Figures a), b) and i) reprinted with permission of Advanced Engineering Materials.

The procedure of calculations was similar to the procedure presented in the previous Subchapter for the 3D-cross-microstructures, with the exception of boundary conditions suited for irregular, non-symmetric microstructure of a real IPC. Unit tensile loading was used to simulate uniaxial tension and to calculate the effective Young's modulus and Poisson's ratio, unit shear loading was used to simulate simple shear and to calculate the effective shear modulus. The results of numerical calculations are presented in Figs 5.14 – 5.16, together with analytical estimations.

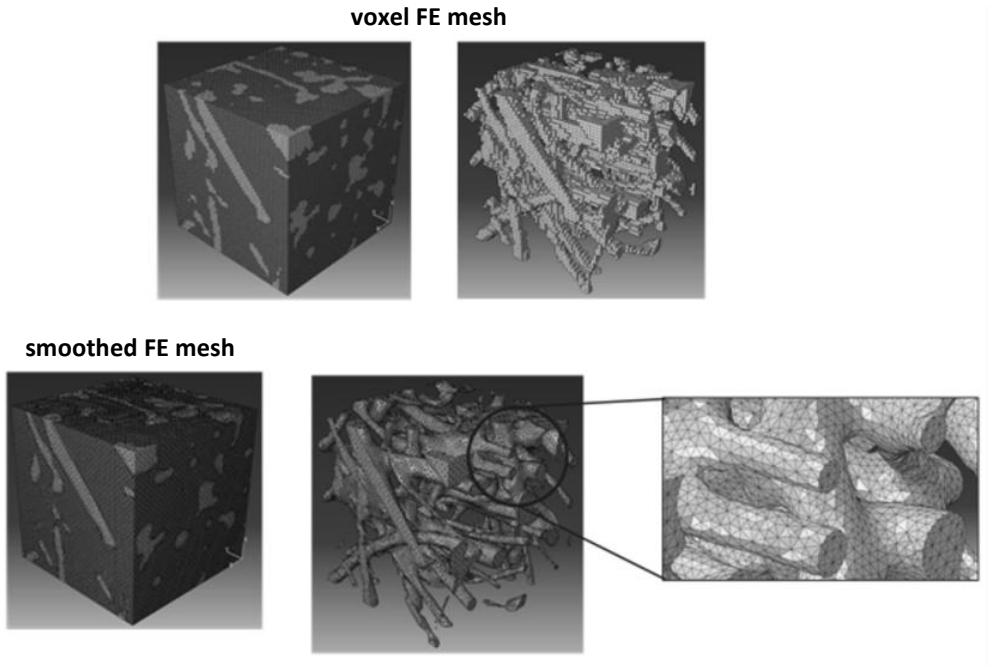

Figure 5.13 Effect of mesh smoothing, microstructure images obtained with [8,144].

In Figs 5.14 – 5.16 the proposed analytical and numerical models for estimation of the effective elastic properties of IPCs are compared. It can be seen that all the analytical and numerical results fit between the Voigt and Reuss bounds. It is also noted that the numerical results fit between the curves obtained with the extended *V-V-R* and *R-V-V* models. The numerical results for Young's modulus and shear modulus are closer to the extended *R-V-V* models, while for Poisson's ratio results for numerical models are closer to the extended *V-V-R* model.

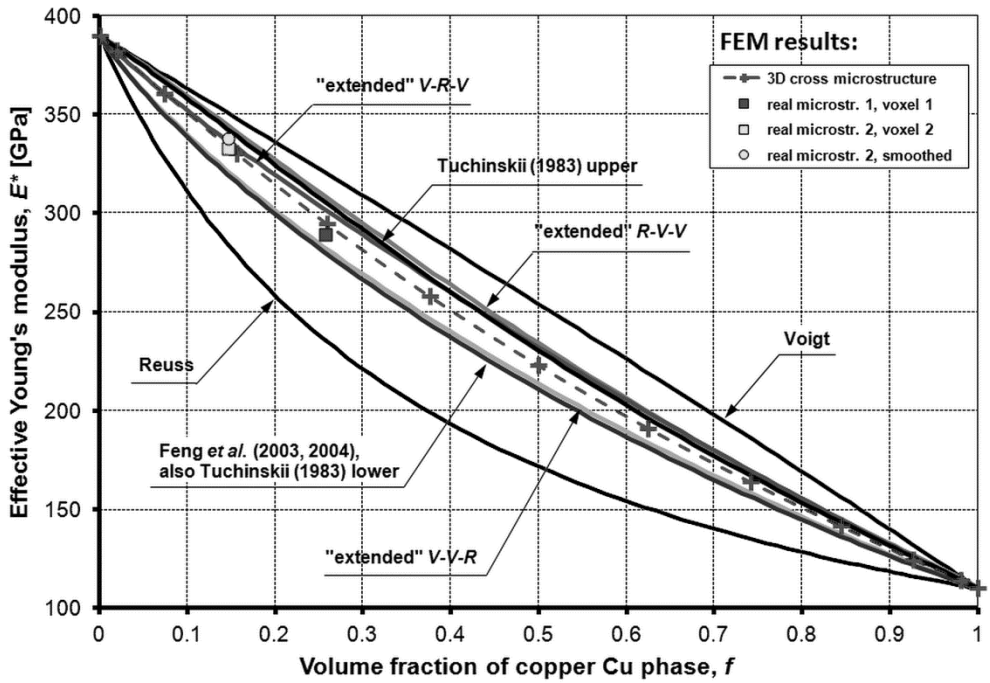

Figure 5.14. Effective Young's modulus of Al_2O_3/Cu IPC in function of copper volume fraction; numerical results for three different microstructures – 3D cross and two real microstructures distinguished with different colours; for one of the real microstructures (yellow marks) two different FEM mesh variants (voxel and smoothed) were used.

When two modelling approaches – voxel and smoothed are compared, it can be seen in Fig. 5.14 that they give similar results for the effective Young's modulus, however the results for the voxel model are lower than for the model with smoothed interfaces. The opposite occurs for the effective shear modulus (Fig. 5.15), where the results for the voxel model are higher than the results for model with smoothed interfaces. These results also differ more significantly between each other. A reason for that may be the local microstructure irregularities of the relatively small, thus insufficient, sample dimensions that also caused quite a low volume ratio of the copper phase (approx. 0.15) compared to the desired nominal value measured (*cf.* Appendix) for the macroscopic specimens (approx. 0.25).

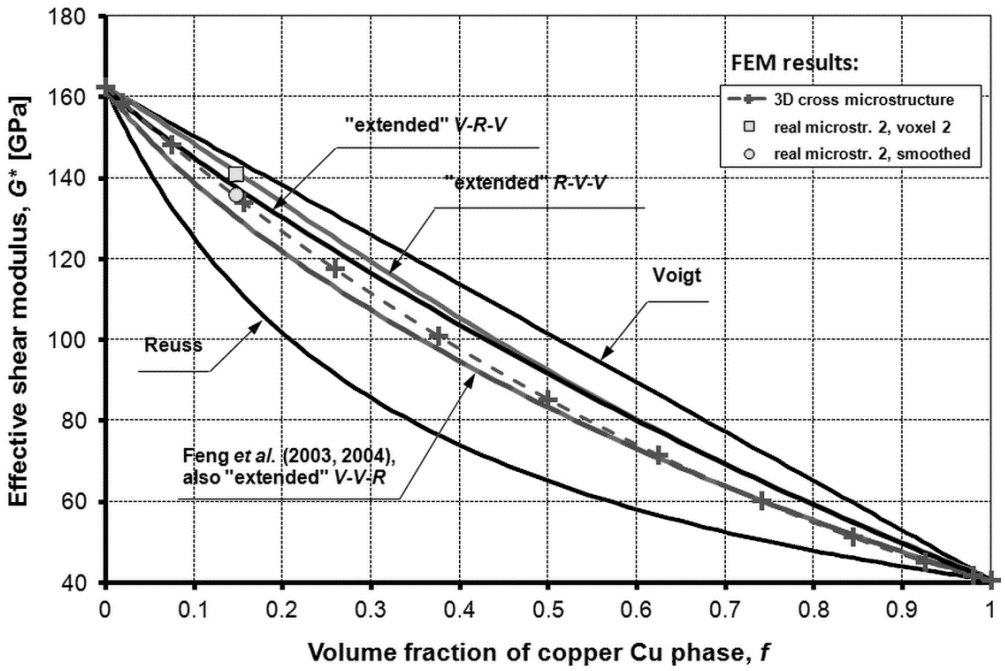

Figure 5.15. Effective shear modulus vs. copper volume fraction; numerical results for two microstructures – 3D cross and real microstructure 2, modelled with both voxel and smoothed meshes.

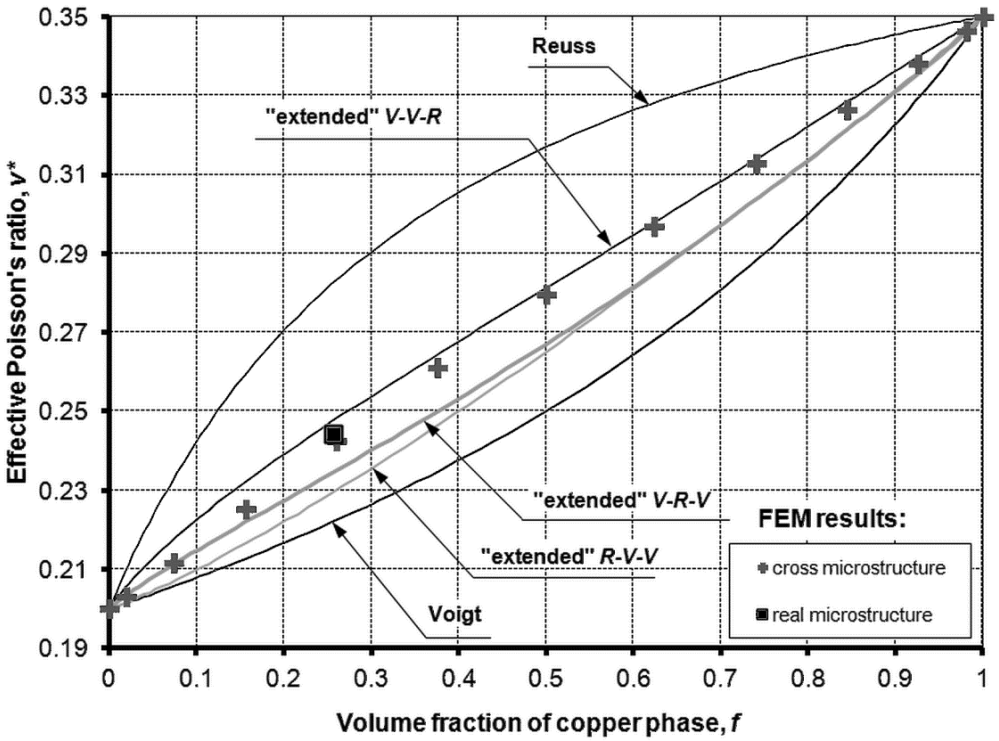

Figure 5.16. Effective Poisson's ratio vs. copper volume fraction; numerical results for two different microstructures – 3D cross and real microstructure "2" of voxel 2 type mesh.

6

Deformation and fracture of metal-ceramic interpenetrating phase composites

In this Section a numerical modelling approach will be proposed to determine fracture parameters of IPCs in order to support complex and costly experimental measurements like those in Compact Tension (C-T) tests. Experience from C-T tests shows that measuring of fracture toughness of IPCs can be technically cumbersome and expensive (*cf*. Subsec. 6.1). One of the main problems is the small size of composite specimens due to manufacturing techniques, which is often insufficient for a standard C-T test. Another issue is the machining of test specimens made of ceramic-metal composites.

The objective pursued in this part of the thesis is to determine the *J*-integral for a crack with ductile bridging ligaments that grows in a composite with interpenetrating microstructure. As it was shown by Eq. 3.6 in Sec. 3, the *J*-integral for the cohesive zone model depends on the relationship between stresses t and displacements δ (or u) in the bridging fibre. This relationship will be sought numerically assuming that the bridged macroscopic crack grows in an elastic material with effective elastic constants calculated according to a model relevant for the IPC microstructure.

In real interpenetrating phase composites (*cf*. Fig. 6.1) the fibres reinforcing the crack surfaces are positioned at different angles. Nevertheless, for the purpose of modelling and by observing the symmetry effects in fibre positions a simplifying assumption can be made that they are perpendicular to the crack plane. In the following numerical models the initially skewed fibre will be then replaced with the fibre perpendicular to the crack plane.

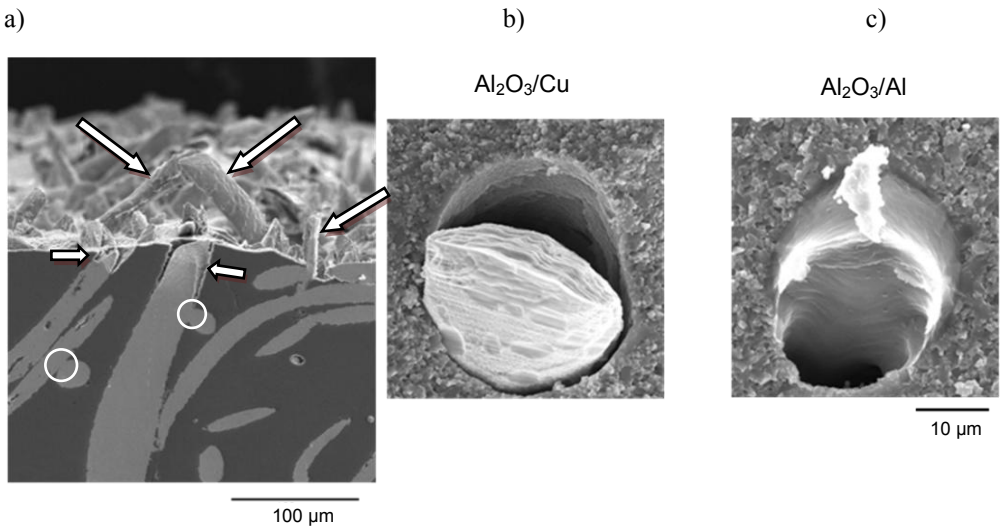

Figure 6.1. Fracture of IPC composites: a) interconnected fibres forming interpenetrating microstructure (connections between fibres marked with circles), different angles between fibres and crack surface (marked with long arrows), and debonding between fibre and matrix (marked with short arrows), b) and c) – different shapes and sizes of debonding on examples of alumina-copper and alumina-aluminum composites (SEM images from: a) and c) reports of KMM-NoE FP6 EU project by L. Weiler, TU Darmstadt and J. Dusza, IMR SAS, b) J. Winzer [97]).

The specific effects occurring during fracture of real IPCs should be taken into account during modelling. The main effects are: interconnection of both phases, deformation-induced debonding between the IPC phases, and different slope angles between the reinforcing fibres and the crack surface. These effects are visible in Fig. 6.1.

In what follows two sets of numerical models for determining the fracture toughness increase due to crack bridging will be presented: (i) models of elastic-plastic fibre reinforcing the crack in an elastic matrix (the reverse case with an elastic fibre reinforcing elastic-plastic matrix is also conceivable) and (ii) models of Compact-Tension test to calculate the fracture toughness increase of IPCs via the *J*-integral.

The first set of models presented in Subsec. 6.2.1. is aimed at numerical determination of the fundamental relationship $\sigma(u)$ in the elastic-plastic bridging fibre undergoing large plastic deformations, necking and debonding from the surrounding ceramic preform. The evolution of debonding will be modelled to

identify the fibre-matrix interface properties that are prerequisite for the model of the Compact-Tension presented in Subsec. 6.2.2.

The second set of models presented in Subsec. 6.2.2 is aimed at modelling crack propagation in real IPC during Compact-Tension test and estimation of the elastic energy release rate increase due to the bridging effect. Two- and three-dimensional models of the C-T test are proposed. Real microstructure of an IPC obtained by means of computed microtomography (micro-CT) method are included in the model. The elastic-plastic metal fibre behaviour and large deformations are taken into account in FEM calculations made with the ABAQUS [144] programme.

6.1. Experimental observations and measurements

In this Section experimental characterization of fracture properties of IPCs will be presented on an example of Al_2O_3/Cu composite to collect information for modelling purposes and for comparison with results of analytical and numerical modelling. The experiments were performed at the Institute of Materials Science of Darmstadt University of Technology (TUD) in Germany during the research stay of the author within the fellowship made possible by the KMM-NoE project of the 6th Framework Programme (http://aisbl.kmm-vin.eu/node/180).

6.1.1. Crack propagation

Microscopic observations of crack propagation were made on an Al_2O_3/Cu infiltrated composite with microstructure based on a polymer foam as the pore forming agent (PFA). Specimens placed in a testing machine during the four-point bending tests were at the same time observed with the optical microscope Leica 301-371.011, Wetzlar. The four-point bending tests were performed under the load control. The test description is given in Sec. 6.1.2.

The aim of the observations of specimens' surfaces was to detect the developing crack, to localize the crack tip, and to identify the phenomena that occur during crack propagation in the IPC composite.

It was difficult to catch the position of the crack tip with the microscope. For the most part of the experiment the crack was invisible and only multiple microcracks and interfaces near the notch tip were getting broader. That could be due to local strengthening of the observed surface caused by polishing one (observed) side of the specimen. The crack in an inhomogeneous material probably developed first in the

more prone to cracking part under the observed surface, staying invisible for most part of the experiment. Thus the evident crack shape appeared only nearly the end of the test. This is the reason of very few points caught during experiments. It could be thus postulated to polish both opposite specimen's surfaces before microscope observations and *R*-curve measurements in IPCs.

The cracks developed mostly along the interfaces between copper and ceramics, that showed weak bonding between these phases. In some places the cracks developed from the already existing microcracks in the ceramics. It was not possible to break completely any of the specimens during the tests. After the crack fully developed there was still a strong copper bridging that kept the specimen together.

The microscopic pictures shown in Fig. 6.2(a-d) confirm the existence of large plastic strains, debonding and microcracks that accompany the growing crack. The effect of IPC microstructure on the crack growth trajectory is shown in Fig. 6.3.

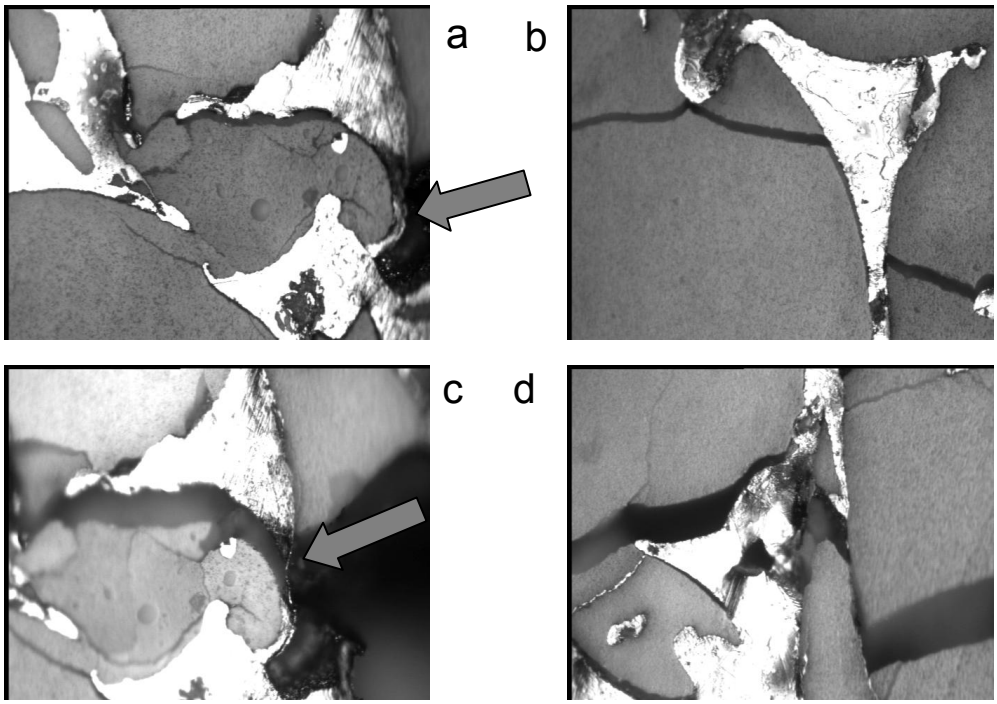

Figure 6.2. Crack development in Al_2O_3/Cu IPC specimen: a) initial load (~40 N), notch end area with widening debonding (arrow indicates a copper bridge that hinders crack growth, b) crack developing along interfaces in the middle of the specimen (load ~100 N), c) notch end

area with copper ligament that just has broken (indicated by arrow) with visible large plastic deformation, d) middle of the specimen with strong crack bridging.

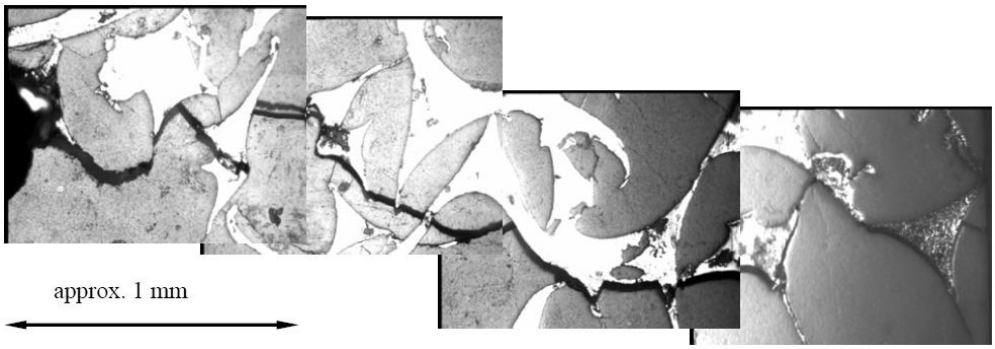

Figure 6.3. Panoramic view of the crack path in Al_2O_3/Cu IPC specimen.

6.1.2. Measurement of fracture toughness

The fracture toughness of the Al_2O_3/Cu IPC was measured in the four-point bending test (Fig. 6.4), with simultaneous observation of the crack growth using Leica 301-371.011 Wetzlar microscope equipped with Leica QWin and Leica Remote software. The advantage, and justification of four-point bending test here, is constant bending moment between loading supports. Assuring constant bending moment between loading supports is important when inhomogeneous materials (such as IPCs) are tested, since the crack may propagate outside of the specimen symmetry plane (*cf*. Fig. 6.3).

The microstructure of the measured Al_2O_3/Cu IPC was based on polymer foam PFA. Four specimens with dimensions $l \times n \times b$ as in Fig. 6.4 were chosen for this experiment (2, 7, 9 and 11). One side (along the length l and width n) of the specimens was polished. The specimens 2 and 7 were notched with a razor blade and had V-shaped notches, the specimens 9 and 11 were notched with a diamond wire saw and had U-shaped notches. All the notch tips were additionally sharpened with a razor blade according to ISO [172] standard. The dimensions of the notches (depths and tip radii) are presented in Table 6.1.

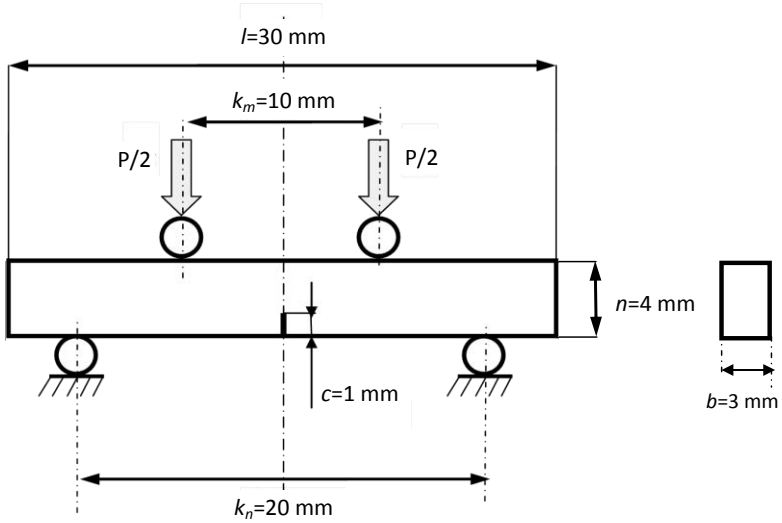

Figure 6.4. Scheme of the four-point bending test.

Table 6.1. Depths and tip radii of the notches.

Specimen No.	Notch depth [mm]	Notch tip radius [μm]
2	0.90	30
7	0.95	15
9	1.13	15
11	1.10	15

The fracture toughness K_{IC} was calculated according to ISO [172] standard:

$$K_{IC} = \frac{P}{bn^{0.5}} \cdot \frac{k_n - k_m}{n} \cdot \frac{3\left(\frac{c}{n}\right)^{0.5}}{2\left(\frac{n-c}{n}\right)^{1.5}} \cdot f\left(\frac{c}{n}\right), \tag{6.1}$$

where P is the maximum recorded load, b, n denote specimen thickness and width, respectively, k_m, k_n are distances between loading and supporting pins, respectively, c is the crack length (*cf.* Fig. 6.4), $f\left(\frac{c}{n}\right)$ - dimensionless function of crack length to specimen width ratio given by

$$f\left(\frac{c}{n}\right) = 1.9887 - 1.326\left(\frac{c}{n}\right) - \frac{\left(3.49 - 0.68\left(\frac{c}{n}\right) + 1.35\left(\frac{c}{n}\right)^2\right)\left(1 - \left(\frac{c}{n}\right)\right)\left(\frac{c}{n}\right)}{\left(1 + \left(\frac{c}{n}\right)\right)^2}. \quad (6.2)$$

The results of fracture toughness measurements are presented in Fig. 6.5.

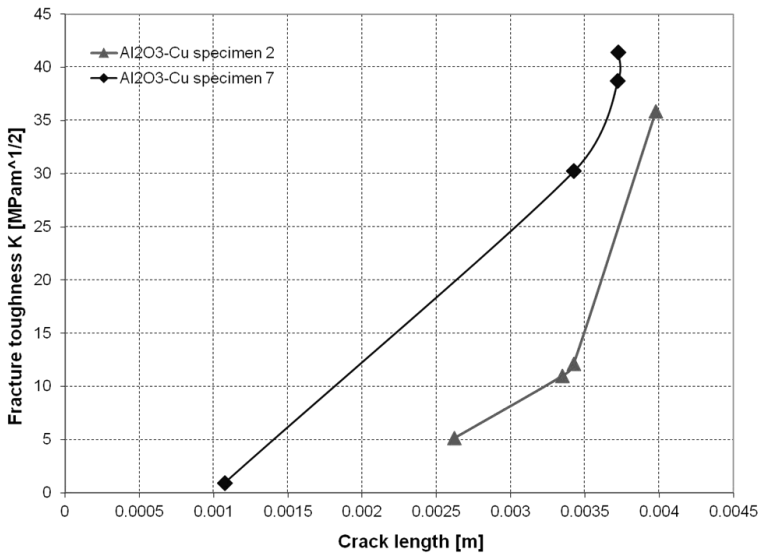

Figure 6.5. Experimental measurements of fracture toughness of Al_2O_3/Cu IPC in four-point bending as a function of crack length (*R-curves*).

As can be seen from the obtained *R*-curves (Fig. 6.5) the initial fracture toughness was above 5 MPa·m$^{1/2}$ but the resistance to crack growth increased significantly with the crack length. This growth in fracture toughness was apparently due to the increase of area fraction of copper reinforcing the crack faces as the growing crack encountered more and more of copper ligaments along its path. High values of the resistance to crack growth at the end of measurements correspond to fracture toughness values for pure copper and copper alloys reported *e.g.* by [173].

Moreover, Winzer [97] who investigated Al_2O_3/Cu IPCs with varying ligament diameters of up to 30 μm, observed an increase in *R*-curves values with coarsening of the microstructures, and at the same time tendency of *R*-curves to grow with the crack length rather than reaching a plateau. It was pointed out that the propagated crack length was not long enough to allow series of measurements at constant

number of ligaments bridging the propagating crack. Thus the results presented in Fig. 6.5 for microstructures with ligament diameter of approx. 100 μm, are in accordance with the results obtained by [97].

The cracks developed mostly along the interfaces between copper and ceramic because of the inferior bonding between these phases. The weak bonding between alumina and copper may be compared in Fig. 6.1(b) with the strong bonding between alumina and aluminum (Fig. 6.1(c)). In some places the cracks developed from the existing microcracks in the ceramic. It can be interpreted that the existing microcracks weakened the composite significantly.

6.1.3. Fracture surfaces

The SEM micrographs of fracture surfaces of specimens 2 and 7 are shown in Figs 6.6- 6.8. It can be seen that crack bridging in this alumina-copper composite is mostly due to plastic deformation of copper ligaments. Sliding of copper fibres is less important because of a weak bonding between copper and alumina.

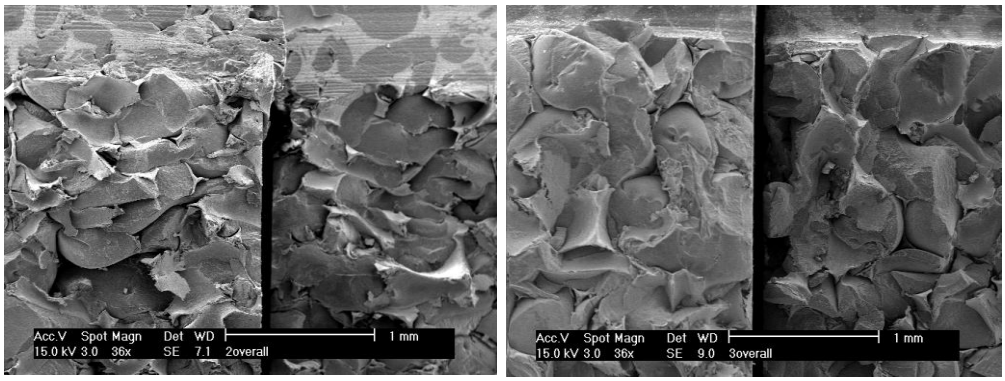

Figure 6.6. The fracture surfaces of specimens 2 (left pair) and 7 (right pair). Fracture surfaces are uneven with visible very weak bonding between copper and ceramic – copper was just pulled out of alumina.

The results of observations of crack propagation and the measurements of fracture toughness of IPCs presented in this Section will further be used in numerical calculations of *J*-integral in Section 6.2.

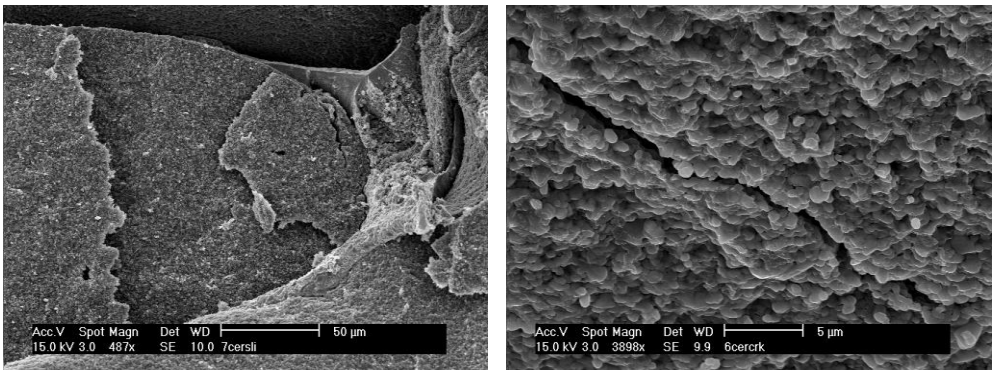

Figure 6.7. On the left - slices of the ceramics torn away from the grain with visible triangle form of torn copper; on the right - microcrack in the alumina.

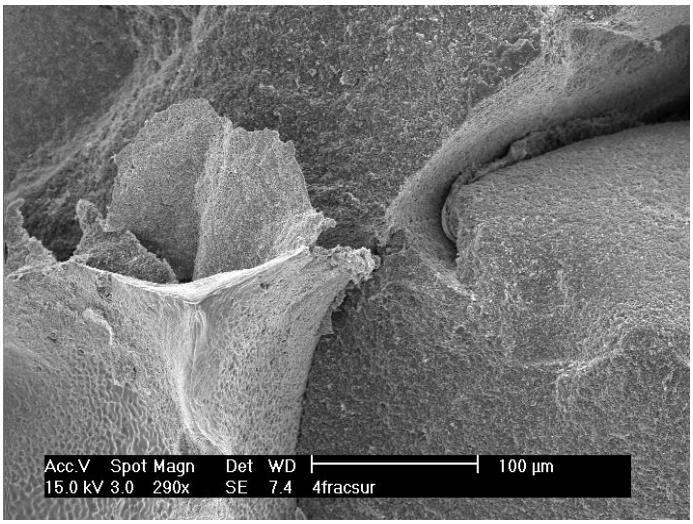

Figure 6.8. Fracture surface of copper with visible smoother zone of necking.

6.2. Numerical determination of *J*-integral in IPCs

In this Section numerical FEM models for determination of the *J*-integral in interpenetrating phase composites with account of the crack bridging effect will be presented. As a prerequisite for that some auxiliary models (called "prerequisite

models" in the sequel) will be developed to predict the bridging fibre behaviour and to identify material and failure parameters of the fibre/matrix interface.

The prerequisite numerical models of a single reinforcing fibre presented in this thesis in Subsec. 6.2.1 were inspired by the experiments of [133], analytical model of [93] and numerical model of [64], investigating the stress–displacement relationships in the metallic ligament reinforcing the crack faces. As a first step, a 2D model of a skew reinforcing fibre will be shown. Then, a model with axisymmetric reinforcing fibre with fixed debonding lengths based on the model described by [64] will follow. In the prerequisite models of the pullout problem with and without debonding evolution a cohesive interface between fibre and matrix is introduced. These two models were recently published in [89].

In Subsection 6.2.2 the FEM models of the Compact-Tension test for the determination of the energy release rate increase that is due to the presence of the ligaments reinforcing the crack faces, will be presented. First, 2D models with either single or multiple reinforcements will be described. Then, a 3D model with multiple cylindrical reinforcing fibres will be shown. Finally, a 3D model of the specimen with real IPC microstructure obtained with micro-computed tomography (micro-CT), will be presented. The initial results obtained for this model were described in [139].

The prerequisite model of the skew reinforcing fibre and the model of the C-T test with single reinforcing fibre, were partially developed during the research stays at the Institute of Applied Mechanics at University of Kaiserslautern, Germany.

6.2.1. Prerequisite numerical (FEM) models of single reinforcing fibre

In this Subsection the mechanism of crack bridging with a single reinforcing fibre will be investigated with series of models. The purpose of these models is to help identify the material properties of the interface between fibre and matrix. Four numerical models of an elastic-plastic reinforcing copper (Cu) fibre embedded in an elastic alumina (Al_2O_3) matrix will be presented. Aluminum (Al) fibre was also considered, and some results for the case of Al fibre will also be presented. The reinforcing fibre is subjected to large deformations and debonding from the matrix. The debonding is modelled in a twofold manner: (i) using finite values of the debonding length, and (ii) as progressing debonding using cohesive model for the matrix-fibre interface.

As was shown in the preceding subsections bridging metallic ligaments undergo debonding from the ceramic matrix (*cf*. Fig. 6.1.). Prior to modelling real IPC with multiple reinforcing fibres it is first necessary to know the behaviour of a single bridging fibre. According to the literature studies there are no credible experimental data on the mechanical properties of the Al_2O_3/Cu interfaces existing up to date. Thus, the following prerequisite models will be used to provide the missing input data on the alumina-copper interface behaviour necessary in modelling of fracture parameters of the IPC.

Two-dimensional model: skew reinforcing fibre

The first prerequisite model to be considered is a simple 2D model of a skew metallic fibre reinforcing ceramic matrix which inclined to the loading direction at an angle different than 90°. The influence of the varying slope angles between fibres and loading direction on the stress-displacement behaviour of an extending ductile fibre was described by [94]. From the observations of IPC fracture surface presented in the previous Section (*cf*. Fig. 6.1), it can be noticed that the fibres reinforcing the crack are inclined at different angles to the crack face. However, for the reasons explained at the beginning of Sec. 6 in the latter parts of this thesis the assumption will be taken of the bridging fibres' influence on the IPC fracture toughness coming only from ligaments either perpendicular to the crack faces, or from the respective projections of the other ligaments on the direction normal to the crack faces.

Consider an elastic-plastic fibre (*e.g*. copper) reinforcing the crack in an elastic matrix (*e.g*. alumina ceramic). The reverse case with an elastic fibre reinforcing elastic-plastic matrix was also analyzed and will be presented at the end of this Subsection. This is a plane strain model with the fibre and matrix materials assumed to be isotropic. The interface between fibre and matrix is assumed as fully bonded. As the deformation process proceeds the fibre may undergo necking and debonding from the matrix. The evolution of debonding is not yet modelled but its effect is analyzed for a few fixed values of the debonding length.

The nondimensional debonding parameter ψ is defined as the ratio of the debonding length l_d to the initial fibre radius r_f^0:

$$\psi = \frac{l_d}{r_f^0} \tag{6.3}$$

The results of the performed calculations will be presented for three values of the debonding parameter ψ = 0.5, 1.0 and 1.5.

In order to avoid contact in the debonding regions between the fibre undergoing debonding and the surrounding matrix, the parts of the matrix FE mesh that have penetrated the necking fibre, were removed.

To model the plastic response of the fibre material (Cu) the plasticity model implemented in [156], described by [174], also by [175, 176], was applied. The material of the fibre is described by the J_2 flow plasticity. A quasi-static tension simulation of the skew reinforcing fibre was performed in FEAP [156] using the elastic-plastic model with Huber-Mises-Hencky yield condition and isotropic hardening law. The geometrical and material properties: r_f^0 – radius of the fibre, α – inclination angle for which the results will be presented, E_m, E_f, v_m, v_f, - Young's moduli and Poisson's ratios of alumina (Al_2O_3) matrix and copper (Cu) fibre, respectively, Y_0 - yield stress of Cu, H_{iso} - isotropic hardening modulus of Cu, used in calculations are collectively displayed in Table 6.2. The displacement control and tensile loading were applied. The FEM mesh and applied boundary conditions are depicted in Fig. 6.9(a). The materials are marked in Fig. 6.9(b). FEM calculations were made with FEAP [156] programme. As a result, the stresses in the bridging fibre are obtained and depicted in Fig. 6.10(a-c). The comparison of the influence of the debonding size on stress distributions is depicted in Fig. 6.11(a-c) for normal stresses parallel to the loading direction. The influence of debonding on composite's load-displacement behaviour is presented in Fig. 6.11(d).

Table 6.2. Material and geometrical parameters used in the skew reinforcing fibre model.

	Al_2O_3	Cu
E [GPa]	390.0	110.0
v	0.2	0.35
Y_0 [MPa]	-	130.00
H_{iso}	-	8000
r_f^0 [mm]	-	0.9474
α[°]	-	62.5

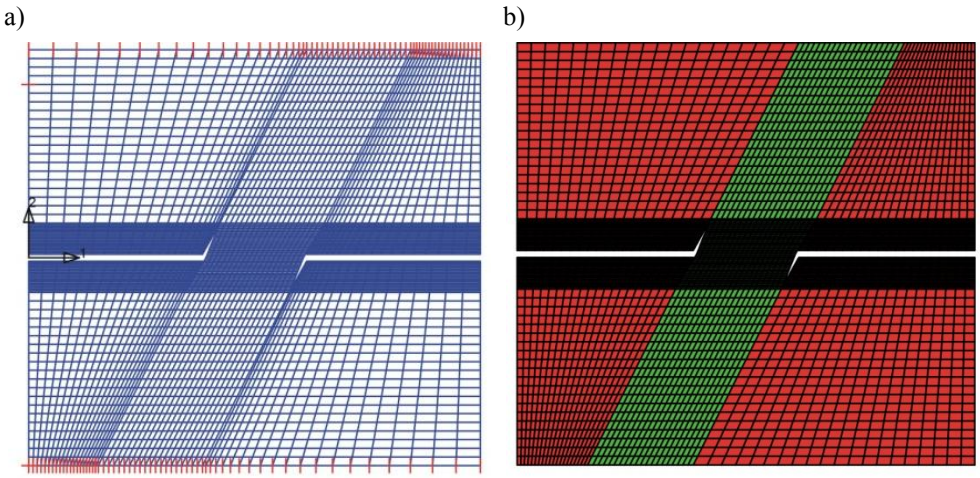

Figure 6.9. a) FEM mesh and boundary conditions, b) materials: red – Al_2O_3, green – Cu

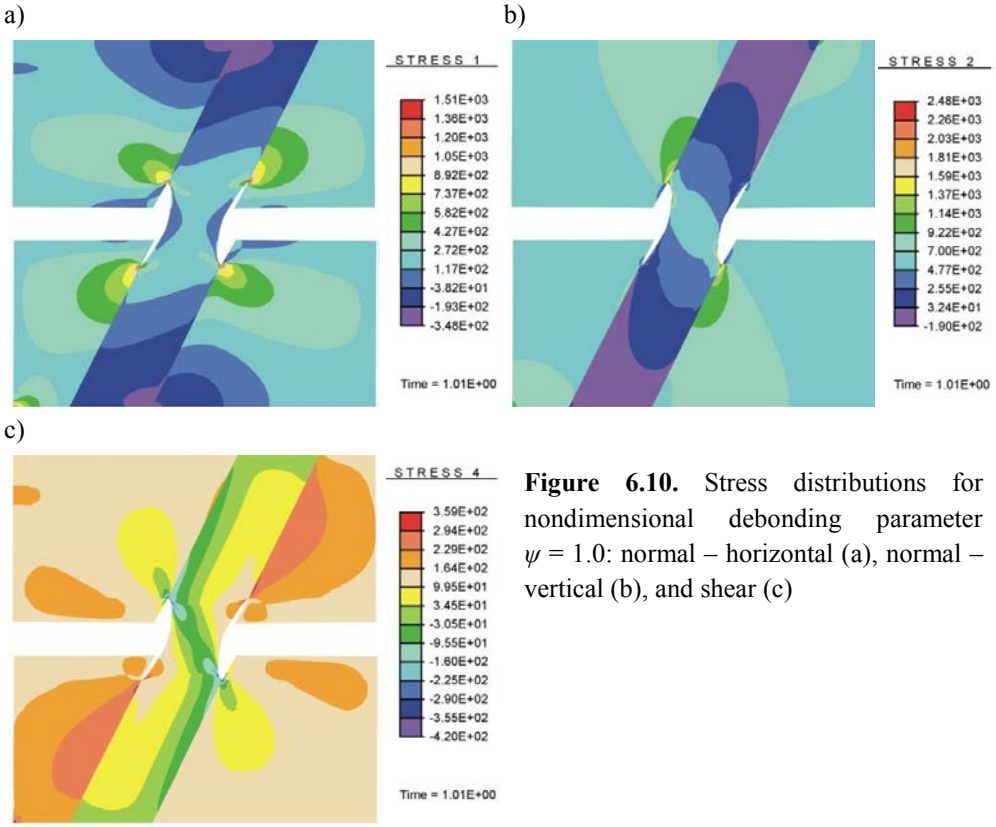

Figure 6.10. Stress distributions for nondimensional debonding parameter $\psi = 1.0$: normal – horizontal (a), normal – vertical (b), and shear (c)

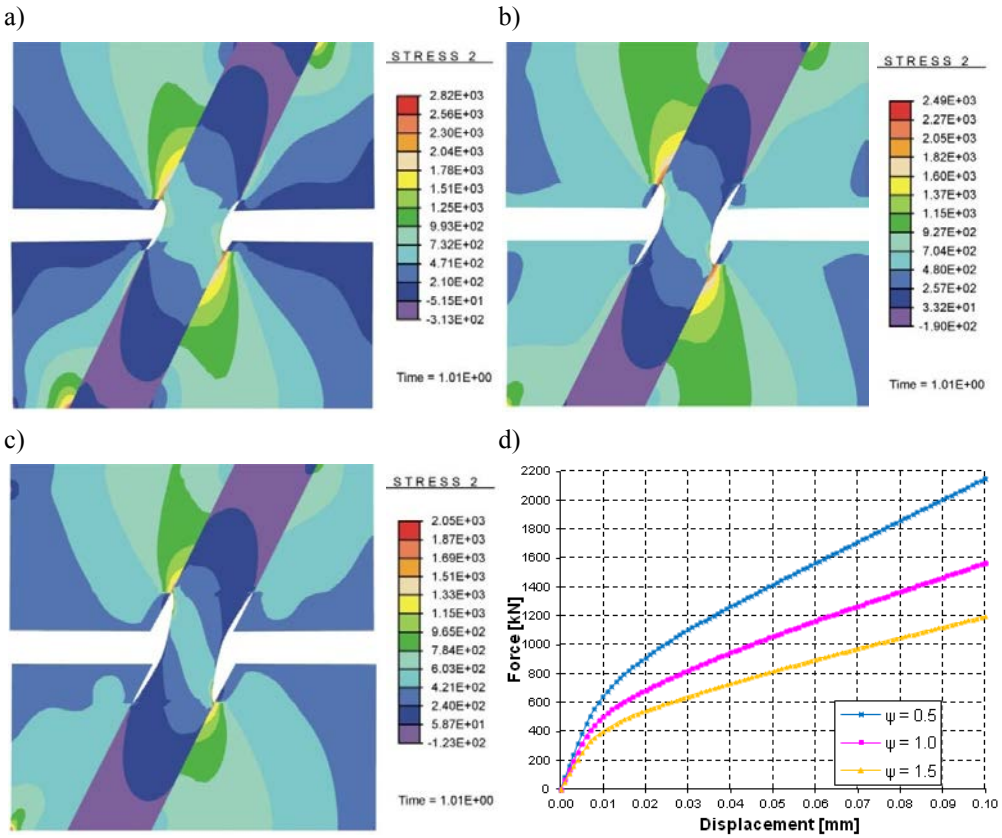

Figure 6.11. Influence of nondimensional debonding parameter ψ on normal-vertical stress distribution (parallel to the loading direction): a) ψ = 0.5, b) ψ = 1.0, c) ψ = 1.5; d) effect of nondimensional debonding parameter ψ on composite's load-displacement behaviour.

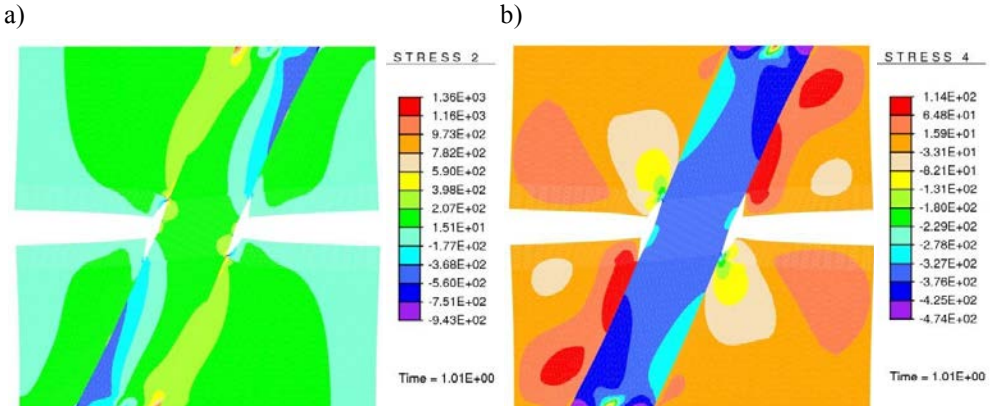

Figure 6.12. Stress distributions for elastic fibre in elastic-plastic matrix: a) normal stresses in vertical direction b) shear stresses.

From the stress distributions shown in Fig. 6.10(a-c), the regions of stress concentrations near the interfaces between fibre and matrix, may be identified. From the stress distributions shown in Fig. 6.11(a-c) it can be seen that the stresses near the matrix-fibre interface decrease with the increasing debonding size. Thus, the debonding increase has an amplifying effect on stresses between the fibre and the matrix. However, from Fig. 6.11(d) it can be noted that increase in debonding causes a reduction in the composite's stiffness and a significant effect on the composite's characteristics.

Also the case of elastic fibre in elastic-plastic matrix was considered. Exemplary results of the numerical calculations are shown in Fig. 6.12.

From the comparison of the normal vertical stress distributions in Figs 6.10(b,c) and 6.12(a,b), respectively, it may be seen that the peak stress values are larger for the case of elastic-plastic reinforcing fibre in an elastic matrix than for the opposite case. This can be due to the plastically deformable matrix in which the stresses are relaxed.

Axisymmetric single reinforcing fibre model with fixed debonding lengths

In this Subsection a numerical model for an axisymmetric problem of the uniaxial tension of two disconnected blocks of ceramic matrix reinforced with a metal fibre will be presented assuming elastic-plastic model for the Cu or Al fibre and linear elastic model for the Al_2O_3 matrix.

The geometrical assumptions of the model represent in a simplified way a macrocrack which is reinforced with a single metal ligament (*cf.* [89]). The tip of a crack and the corresponding stress concentrations are not modelled. Axial symmetry assumption made the calculations considerably simpler while furnishing information on the most important deformation and failure mechanisms.

The fibre undergoes large plastic deformations leading to necking and debonding from the matrix (Fig. 6.13). As in the previous case, the evolution of debonding is not yet modelled but its effect is analyzed using few fixed values of the debonding length. The nondimensional debonding parameter ψ defined by Eq. 6.3 is the ratio of the debonding length l_d to the initial fibre radius r_f^0.

The calculations were performed for three values of the debonding parameter $\psi = 0.4$, 0.6 and 2.0.

The interface between fibre and matrix is modelled as fully bonded. The materials of fibre and matrix are assumed to be isotropic. The alumina matrix

material is assumed to be elastic, the copper or aluminum fibre materials are assumed to be elastic-plastic. The geometrical and mechanical properties of fibre and matrix materials are shown in Table 6.3.

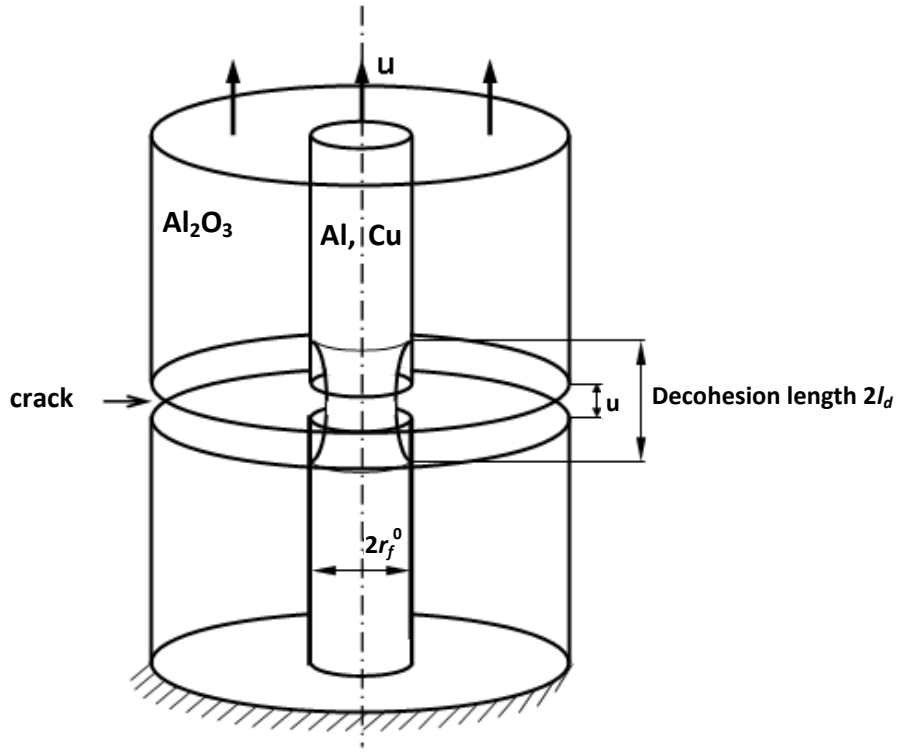

Figure 6.13. Scheme of axisymmetric model of uniaxial tension of two elastic blocks with reinforcing elastic-plastic fibre at fixed debonding lengths (reproduced with permission of *International Journal of Damage Mechanics*).

The elastic-plastic model described in detail in [89], based on elastic and isotropic hardening plasticity model implemented in ABAQUS [144] is applied here for a copper fibre. The material of the fibre is described by the J_2 flow plasticity. Large strains that can locally occur in the necking zone, are determined with an incremental algorithm. Spectral decomposition allows the use of the return mapping procedure for models with an isotropic yield function. The stress update algorithm is used for the integration of the J_2 plasticity constitutive equations.

Table 6.3. Material and geometrical parameters used in axisymmetric reinforcing fibre model with fixed debonding lengths, E_f, E_m, ν_f and ν_m denote Young's moduli and Poisson's ratios of fibre and matrix, respectively.

	Al_2O_3	Cu	Al
E_m, E_f [GPa]	390.0	110.0	69.0
ν_m, ν_f	0.2	0.35	0.33
σ_0 [MPa]	-	50.0	270.0
n	-	5.8	15.0
r_f^0 [μm]	-	175.0	175.0

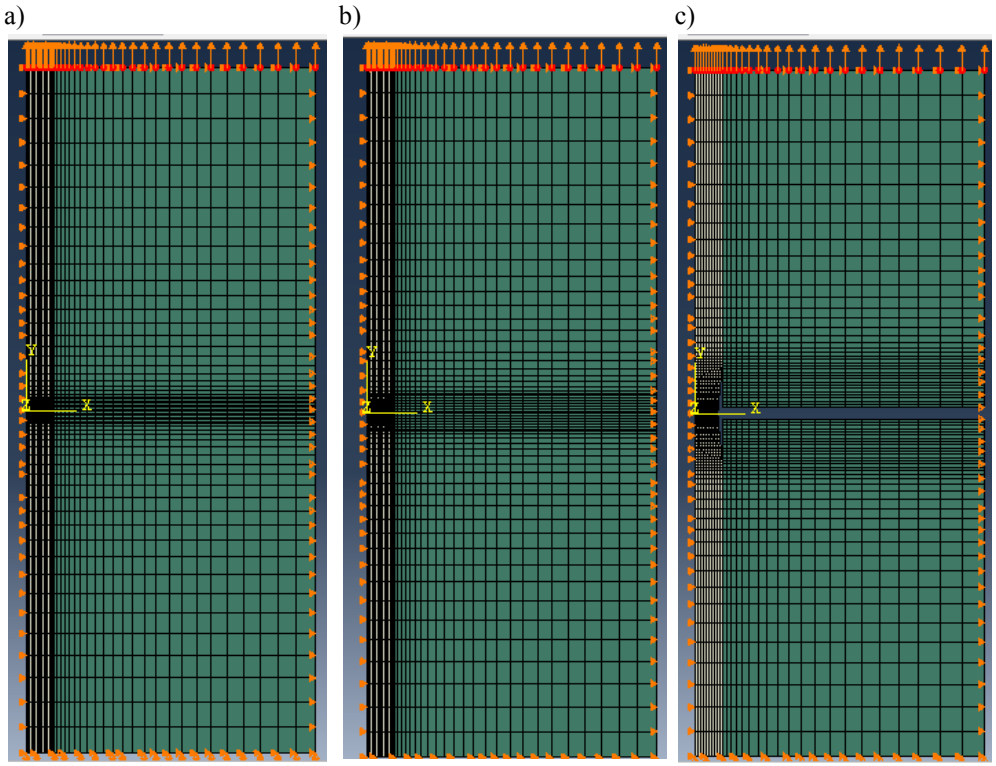

Figure 6.14. FEM model (FEM mesh created with FEAP); displacement loading and boundary conditions for three values of nondimensional debonding parameter ψ: a)ψ=0.4, b) ψ=0.6 and c) ψ=2.0.

The FEM meshes for this case were prepared with the FEAP [156] package. The axial and horizontal displacements at the bottom surface of the fibre and the matrix are blocked. The displacement loading is applied to the top surface of both fibre and matrix. This is done to mimic the behaviour of the ligament as an element of an interconnected network of metallic reinforcements in a real composite with interpenetrating microstructure. The calculations were performed with ABAQUS [144], with the use of four node bilinear axisymmetric CAX4 elements. The full finite elements model consisted of 2,691 nodes and 2,544 elements for the case of ψ=0.4, 2,809 nodes and 2,656 elements for ψ=0.6, and 2,623 nodes and 2,440 elements for ψ=2.0. Two material systems were used: alumina-copper (Al_2O_3/Cu) and alumina-aluminum (Al_2O_3/Al). However, the results will be presented mainly for the alumina-copper case. The FEM meshes for three nondimensional debonding parameters ψ are presented in Fig. 6.14. The obtained distributions of axial stresses and equivalent plastic strains are shown in Figs 6.15 and 6.16.

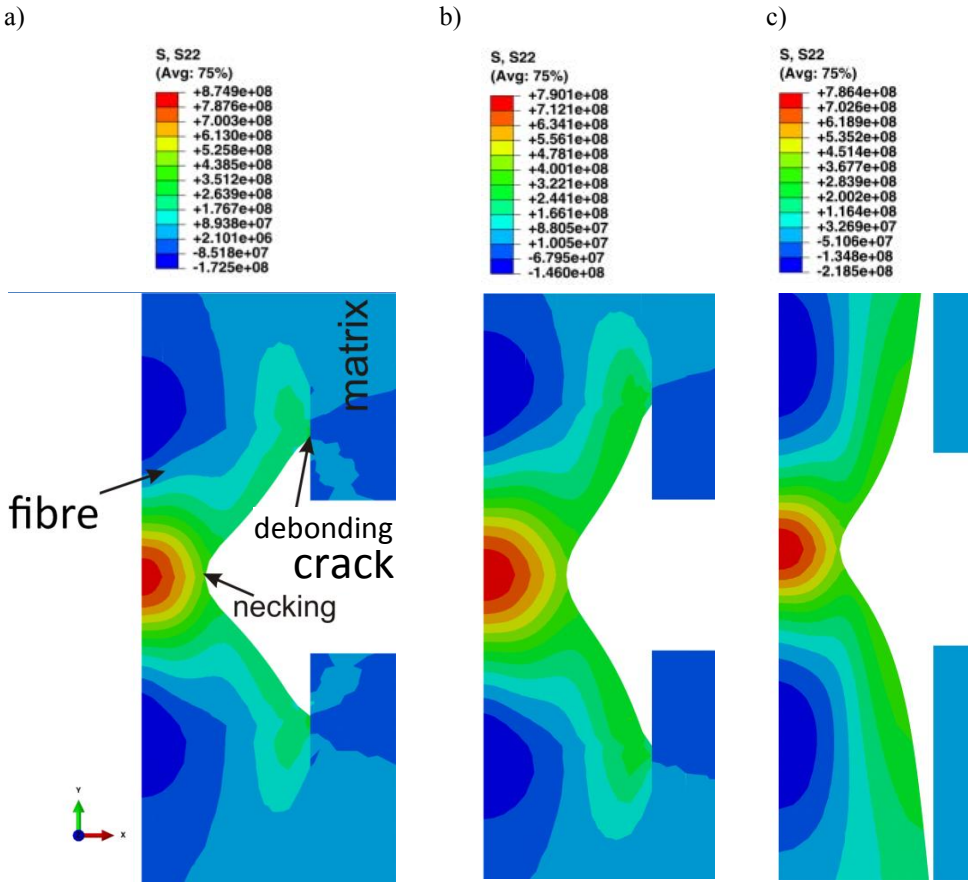

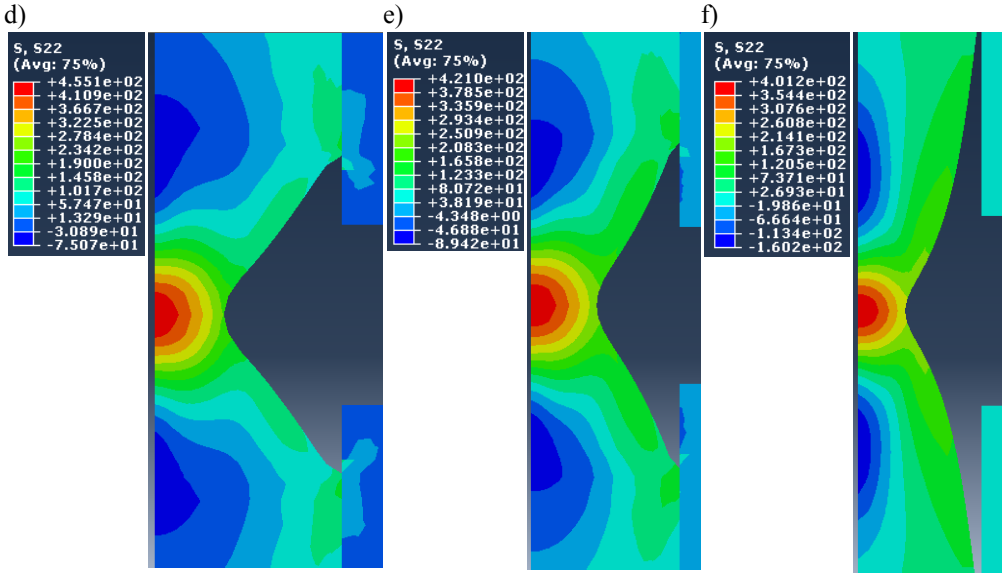

Figure 6.15. Axisymmetric model of uniaxial tension of cracked elastic matrix with reinforcing elastic-plastic fibre at fixed debonding lengths. ABAQUS results: (a-c) for Al_2O_3/Al, in Pa, (d-f) for Al_2O_3/Cu, in MPa, at loadings u_2: (d) 0.16 mm, (e) 0.175 mm, (f) 0.2 mm. Distributions of axial stresses σ_{22}: (a, d) ψ=0.4, (b, e) ψ=0.6, (c, f) ψ=2.0 (images not in the same scale).

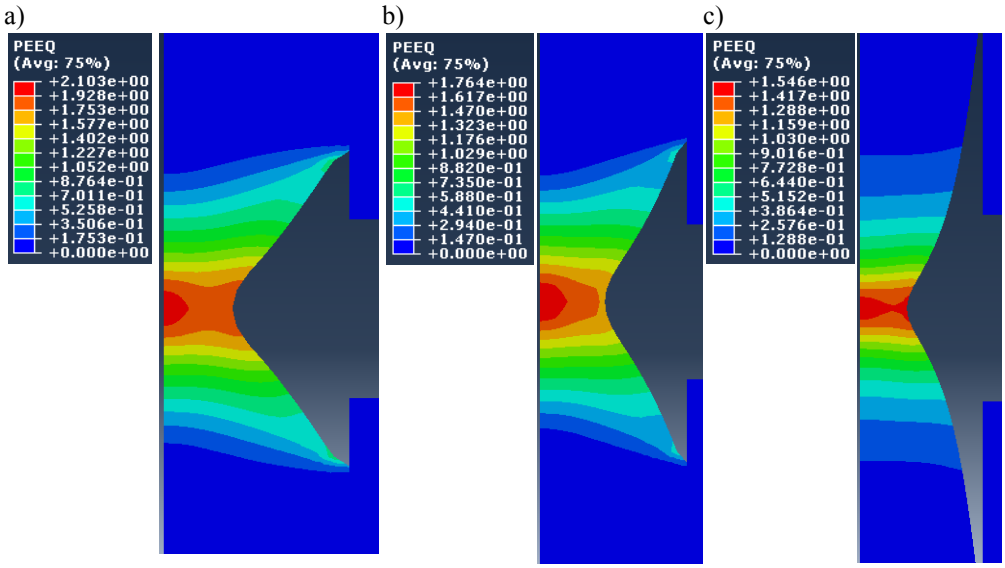

Figure 6.16. Axisymmetric model of uniaxial tension of cracked elastic matrix with reinforcing elastic-plastic fibre at fixed debonding lengths. Distributions of equivalent plastic

strains ε_{pl}^{EQ} (for different loadings u_2), for Al_2O_3/Cu: (a) ψ=0.4, u_2=0.16 mm, (b) ψ=0.6, u_2=0.175 mm, (c), ψ=2.0, u_2=0.2 mm (images not in the same scale).

In Fig. 6.17 the stress-displacement relationships $\sigma(u)$ in the reinforcing fibre are compared with the analytical solutions of [93] for both considered material systems and for three values of the debonding parameter ψ = 0.4, 0.6 and 2.0.

A softening part of the $\sigma(u)$ relationship due to necking of the ligament can be observed for all three values of the debonding parameter and for both material systems. The normalized stresses obtained with the present numerical model are for both material systems slightly higher than the normalized stresses furnished by the analytical model of Mataga for ψ = 0.4 and 0.6, with greater difference for the ψ = 0.4 case. For ψ = 2.0, however, normalized stresses from the analytical Mataga model are visibly higher than the stresses obtained from the present FEM model. For such a high value of ψ this could be due to a significant difference between the assumed shape of the necking ligament in the model of [93], which is a paraboloid of rotation, and the shape of the necking ligament resulting from the present numerical model. Mataga *et al*. [93] did not consider ψ*'s* greater than 1.0, hence it is difficult to say if his model is applicable for such high values of ψ.

The peak of the $\sigma(u)$ relationship shifts to lower σ/σ_0 values as ψ increases. This observation holds for both material systems, for the analytical model of [93], and for the present numerical model alike.

It can also be observed for both Al_2O_3/Al and Al_2O_3/Cu composites, that the softening behaviour becomes less steep with the increasing ψ. This could be interpreted that for lower values of ψ more intensive necking is needed to make the ligament elongate at the applied displacement.

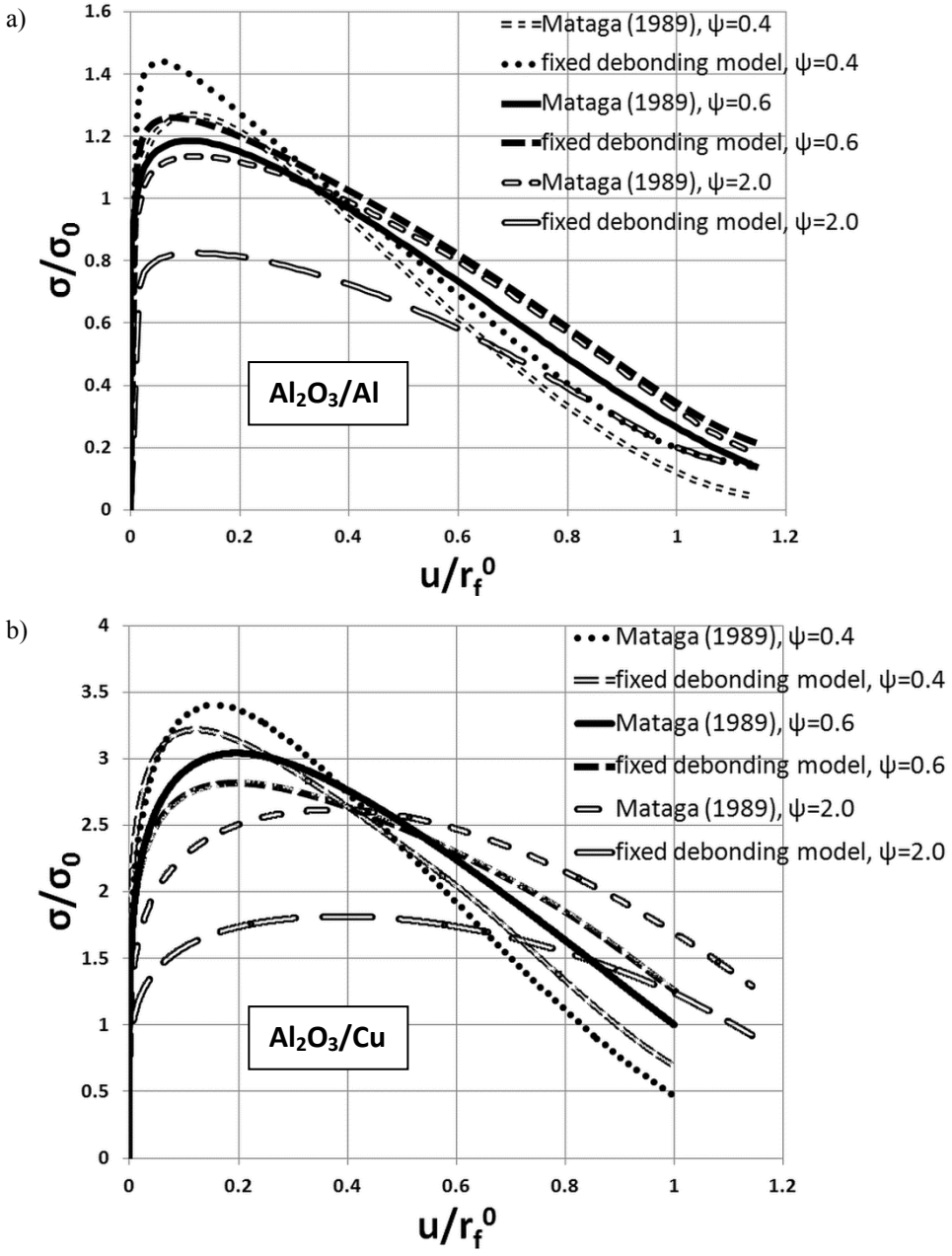

Figure 6.17. Normalized stress-displacement relationships in the reinforcing fibre from the numerical model with fixed debonding lengths, compared with the analytical solutions of [93] for different values of debonding parameter ψ: a) Al_2O_3/Al, b) Al_2O_3/Cu.

Pullout problem model with debonding evolution

In this Subsection a FEM model for the fibre pullout with account of fibre-matrix debonding evolution will be presented and applied to predict stress-displacement relationships for Cu and Al fibres embedded in Al_2O_3 matrix. The main parts of this model and its implementation for Al_2O_3/Al composites were published in [89]. The results concerning Al_2O_3/Cu composites shown herein have not been published yet.

The model of pullout problem is one of the prerequisites for modelling of crack bridging in real IPC materials as the pullout mechanism occurs in IPCs and it is, thus, necessary to know how the reinforcing fibre behaves. The pullout model presented below is an extension of the model of [82] by using elastic-plastic material model for the fibre. Bheemreddy *et al*. [82] investigated an axisymmetric elastic silicon-carbide (SiC_f) fibre which was embedded in an axisymmetric elastic silicon-carbide (SiC) matrix. The free end of the fibre was loaded with homogeneous displacements field to find the load-displacement characteristics. It was assumed that the load-displacement behaviour was not influenced by the matrix.

Consider the axisymmetric problem of an isotropic elastic-plastic metal fibre that undergoes debonding from the surrounding ceramic matrix modelled as isotropic elastic (Fig. 6.18). In the numerical model of this problem developed in [89] with ABAQUS [144] software the cohesive surface formulation was used to model contact at the interface between the fibre and matrix. Local large strains were admitted in the debonded and free parts of the fibre.

The geometry of the problem, FEM mesh and boundary conditions are depicted in Fig. 6.18 where r_m denotes the outer radius of the matrix, r_f^0 - initial radius of the fibre, r_f - actual fibre radius, l_m - length of the embedded part of the fibre, $l_m + l_0$ - total fibre length. The pullout displacement was applied uniformly as a quasi-static loading in the axial direction on the top surface of the fibre. The contact friction at the interface is activated after the fibre/matrix interface has debonded on a distance l_d. Friction was assumed to be spatially uniform and independent of time and rate. To eliminate the influence of the surrounding body on the results, a high value for the ratio of matrix to fibre radii was assumed $r_m / r_f^0 = 71.43$ (*cf*. Table 6.5). The displacements were blocked in both radial and axial directions at the bottom of the matrix, while the side belonging to the symmetry axis was constrained only in the radial direction.

a) b)

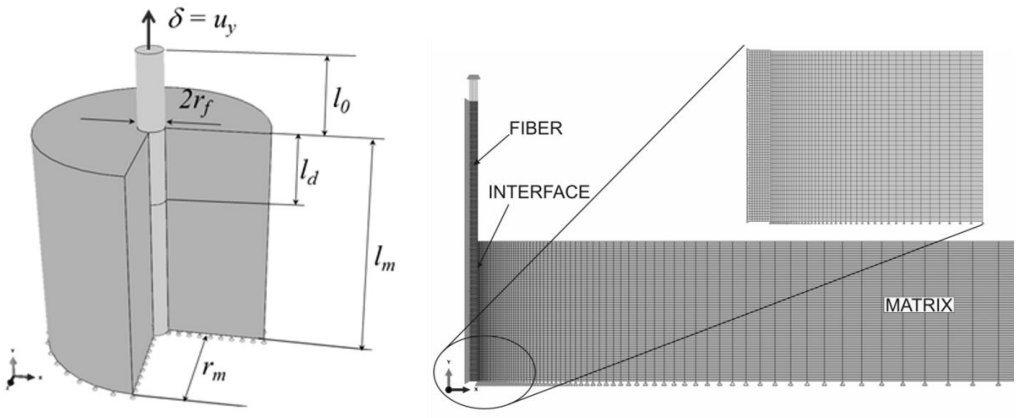

Figure 6.18. Pullout model: a) geometry, b) FEM mesh and boundary conditions (reproduced with permission of *International Journal of Damage Mechanics*).

The mesh with element size of approx. 0.02 mm × 0.02 mm was used in the vicinity of the interface between the fibre and matrix. The model consisted of 2205 nodes and 2360 elements in total. Four-node bilinear axisymmetric elements CAX4 modelled the fibre and matrix parts. The cohesive zone surface at the interface between fibre and matrix was applied to model the contact behaviour. The zero thickness cohesive zone was defined with four-node, two integration points, axisymmetric cohesive elements COHAX4. The geometrical and mechanical properties of the fibre and matrix materials and the interface are collected in Tables 6.4 and 6.5.

It was assumed that the J_2 flow plasticity describes the behaviour of the fibre material. Large strains that can locally occur in free segments of the fibre and may reach 50-100% were determined with an incremental algorithm. The unloading can also take place locally. It was further assumed that the strain rate tensor $\dot{\boldsymbol{\varepsilon}}$ can be decomposed into elastic $\dot{\boldsymbol{\varepsilon}}^e$ and plastic $\dot{\boldsymbol{\varepsilon}}^p$ parts

$$\dot{\boldsymbol{\varepsilon}} = \dot{\boldsymbol{\varepsilon}}^e + \dot{\boldsymbol{\varepsilon}}^p. \tag{6.4}$$

The elastic part obeys isotropic Hooke's law

$$\dot{\boldsymbol{\sigma}} = \mathbf{C}\colon(\dot{\boldsymbol{\varepsilon}} - \dot{\boldsymbol{\varepsilon}}^{\mathrm{p}}), \tag{6.5}$$

with

$$\mathbf{C} = 2G\mathbf{I} + K\mathbf{1}\otimes\mathbf{1}, \tag{6.6}$$

where G is the shear modulus, K is the bulk modulus. The plastic part $\dot{\boldsymbol{\varepsilon}}^p$ obeys associated flow rule: $\dot{\boldsymbol{\varepsilon}}^p = \dot{\lambda}\frac{\partial f}{\partial \boldsymbol{\sigma}}$, where $\dot{\lambda}$ is a non-negative plastic scalar. Loading and unloading conditions can be expressed in the Kuhn-Tucker form: $\dot{\lambda} \geq 0,\ f \leq 0,$ $\dot{\lambda} f = 0.$

The general yield criterion $F(\boldsymbol{\sigma}, \bar{\varepsilon}) = 0$ is satisfied by the stress tensor $\boldsymbol{\sigma}$, where $\bar{\varepsilon}$ is the equivalent plastic strain depending on the plastic loading history.

The quasi-static pullout process with an elastic-plastic fibre was modelled with ABAQUS/Standard [144] for Huber-Mises-Hencky yield condition and isotropic hardening law. A power law was adopted for the uniaxial stress-strain response of the metal material, which is often used in the literature for aluminum and copper [64,133,175]

$$\frac{\sigma}{\sigma_0} = \left(\frac{\bar{\varepsilon}}{\bar{\varepsilon}_0}\right)^{\frac{1}{n}}, \tag{6.7}$$

where: $\bar{\varepsilon} = \sqrt{\boldsymbol{\varepsilon}^p : \boldsymbol{\varepsilon}^p}$ is the equivalent plastic strain, σ_0 - initial yield stress equal 50 MPa, $\bar{\varepsilon}_0 = \frac{\sigma_0}{E} = 0.00045$, is the corresponding strain, n = 5.8 for copper.

The traction-separation model implemented in ABAQUS [144] first shows linear elastic behaviour followed by initiation and evolution of fibre debonding. For the elastic behaviour, elastic stiffness tensor relates nominal stresses to nominal strains across the fibre/matrix interface. The cohesive law can be expressed in the following general vector form

$$\boldsymbol{\tau} = \boldsymbol{f}(\boldsymbol{\delta}) \text{ , where } \boldsymbol{\tau} = \tau_n \boldsymbol{e}_n + \tau_t \boldsymbol{e}_t \text{ and } \boldsymbol{\delta} = \delta_n \boldsymbol{e}_n + \delta_t \boldsymbol{e}_t, \tag{6.8}$$

with: $\boldsymbol{\tau}$ - the cohesive stress vector, $\boldsymbol{\delta}$ - vector of the opening displacement, $\boldsymbol{f}(\boldsymbol{\delta})$ - local constitutive traction-separation relationship in the cohesive zone, $\boldsymbol{e}$ - unit vector, n, t - components normal and tangential to the separation plane, respectively.

The general loading case can be simplified to the mode II cracking due to the assumption of axial symmetry. The debonding propagation direction along the fibre-matrix interface is parallel to the fibre axis. Following the model implemented in ABAQUS [144], damage initiation in the cohesive zone is defined by the following criterion for the maximum nominal stress ratio

$$\left\{\frac{\langle\tau_n\rangle}{\left(\tau_{max,0}\right)_n}, \frac{\tau_s}{\left(\tau_{max,0}\right)_s}, \frac{\tau_t}{\left(\tau_{max,0}\right)_t}\right\} = 1, \tag{6.9}$$

where $\left(\tau_{max,0}\right)_i$ denote peak nominal stress in the respective direction and the Macaulay brackets applied on the nominal stresses $\langle\tau_n\rangle$ means that pure compressive stress or deformation state would not initiate damage. Similar approach in modelling of damage initiation can be found in [99].

Damage evolution in the cohesive zone is based on the fracture energy of the interface defined by the area under traction-separation curve. The normal and shear deformations in the cohesive zone are interrelated through the mode-mix based on energies. The work respectively in the normal and shear directions is described by

$$\begin{aligned} G_n &= \int_{\partial A} \tau_n \cdot \tilde{\delta}_n ds, \qquad G_s = \int_{\partial A} \tau_s \cdot \tilde{\delta}_s ds, \\ G_t &= \int_{\partial A} \tau_t \cdot \tilde{\delta}_t ds, \qquad G_T = G_n + G_s + G_t, \end{aligned} \tag{6.10}$$

where $\boldsymbol{\tau_n}$, $\boldsymbol{\tau_s}$, $\boldsymbol{\tau_t}$ are tractions in the respective normal and both shear directions and $\widetilde{\boldsymbol{\delta}}_{\boldsymbol{n}}$, $\widetilde{\boldsymbol{\delta}}_{\boldsymbol{s}}$, $\widetilde{\boldsymbol{\delta}}_{\boldsymbol{t}}$ are their respective conjugate relative displacements.

The mode mix formulations are denoted as

$$m_1 = \frac{G_n}{G_T}, \qquad m_2 = \frac{G_s}{G_T}, \qquad m_3 = \frac{G_t}{G_T}. \tag{6.11}$$

The condition for failure is formulated in a power law form (*cf.* [99])

$$\left(\frac{G_n}{G_n^C}\right)^\alpha + \left(\frac{G_s}{G_s^C}\right)^\alpha + \left(\frac{G_t}{G_t^C}\right)^\alpha = 1 \tag{6.12}$$

where G_n^C, G_s^C, G_t^C denote critical fracture energies in respective directions, with applied $\alpha = 1$.

Due to the limited available literature data for Cu/Al_2O_3 interfaces, material parameters of the interface for the present modelling purposes have been estimated based on observations from experiments (*cf.* Subsec. 6.1) and from few reference sources. Jarząbek *et al*. [177] reported tensile strength of Cu/Al_2O_3 bond of 68 and 74 MPa, depending on the alumina grain size. Juvé *et al.* [178] reported shear strength of copper-alumina bonds in the range of 10÷50 MPa, depending on manufacturing process parameters such as temperature, pressure, or solid state

bonding time. An interesting effect was observed in [178] for changing alumina roughness: up to R_a= 0.2 μm the shear strength of copper-alumina bonds made by solid state was almost constant (around 40 MPa), then increased above 50 MPa at ca. 0.4 μm to experience a drastic drop at around 0.5 μm down to 20 MPa followed by a decrease to less than 10 MPa at 2.0 μm.

In the present work relatively low interface strength values are assumed. This is due to the fact that in the above mentioned papers specifically prepared small-scale Cu/Al_2O_3 bonds were measured, while in the macroscopic Cu/Al_2O_3 composites samples investigated in this thesis imperfect bonds are likely to occur causing inferior interface strength. The material parameters of the Cu/Al_2O_3 interface used for the present modelling purposes are shown in Table 6.4.

Table 6.4. Material parameters for Cu/Al_2O_3 surface-based cohesive bond used for calculations in FE simulations.

Bond Component	Description	Constant	Value
Tangential behaviour	Coefficient of friction	μ	0.1
Normal behaviour	"Hard" contact		
Cohesive behaviour	Stiffness in normal Stiffness in shear 1 Stiffness in shear 2	K_{it} [N/m^3]	1.2×10^{11}
Damage initiation	Failure stress	$\tau_{max,0}$ [MPa]	10.0
Damage evolution	Damage parameter Fracture energy	D G_{IIc} [J/m^2]	0.9 10

A detailed description of the cohesive zone (CZ) modelling with a literature review, explanation of the ABAQUS [144] procedures and identification of the material parameters of the Al/Al_2O_3 interface are given in [89].

Selected results of the numerical calculations in ABAQUS [144] for the Cu/Al_2O_3 case are depicted in Figs. 6.19 - 6.20. In Figure 6.19 the distributions of

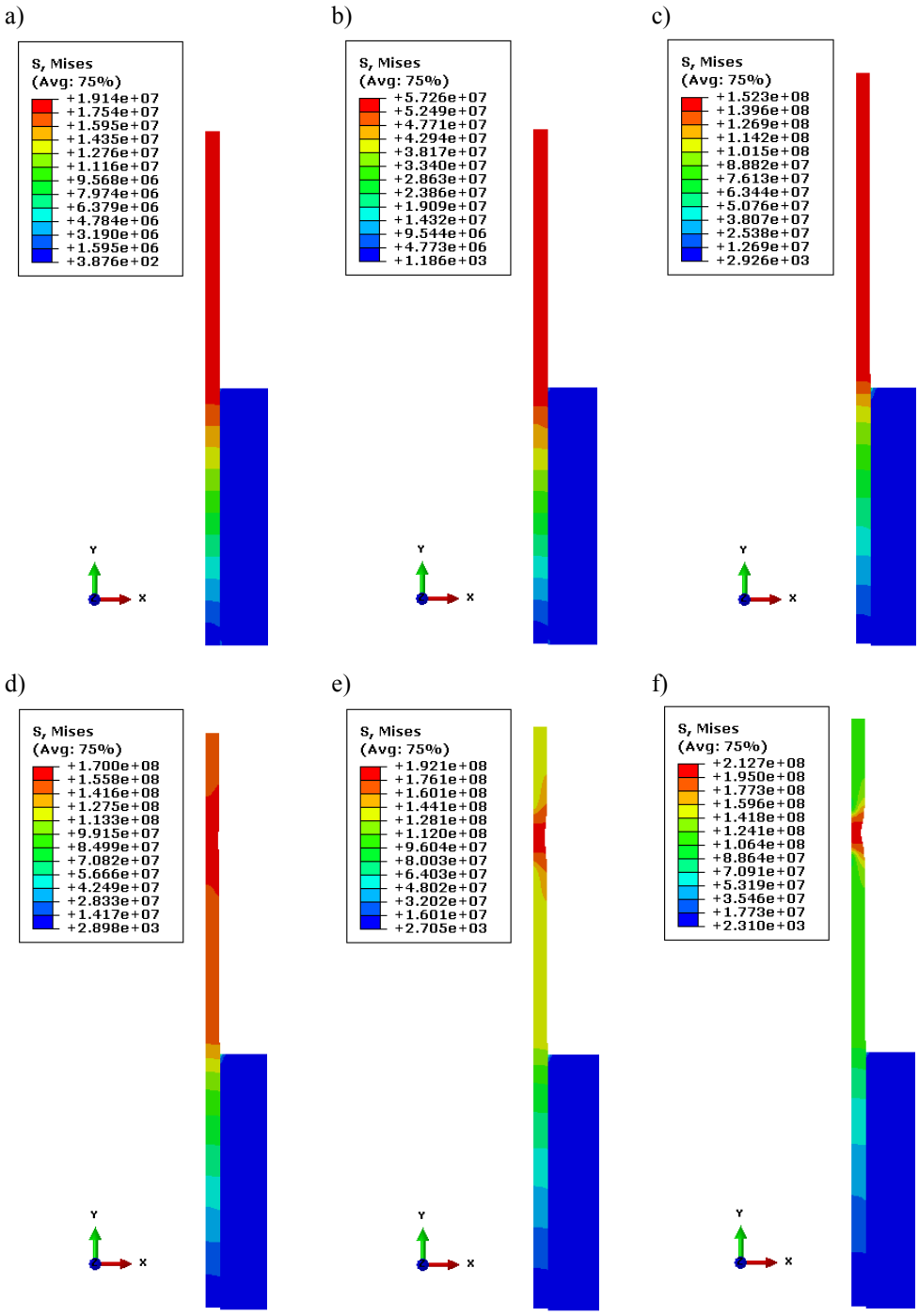

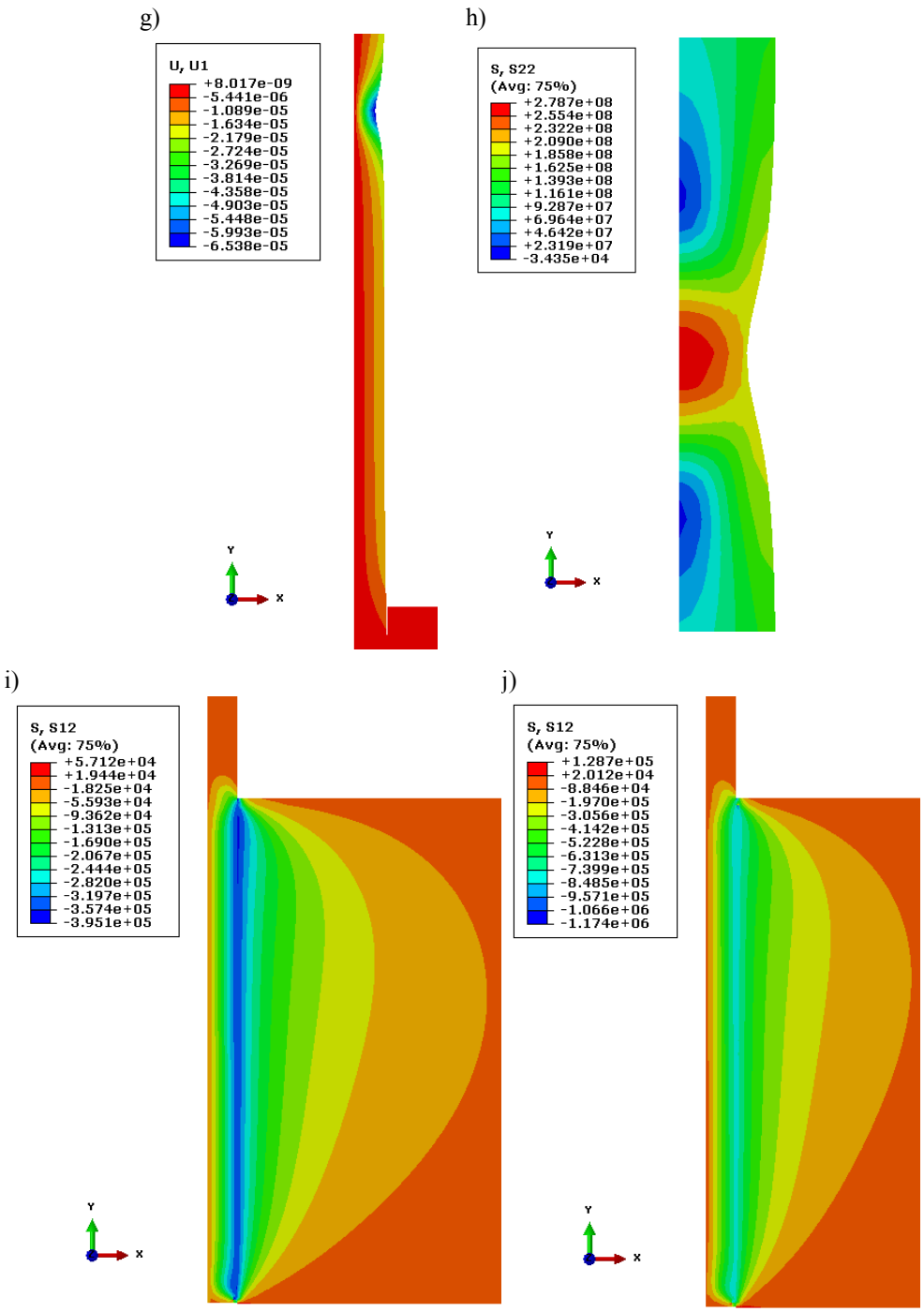

Figure 6.19. (a) – (f): Distributions of von Mises stresses (in Pa) at pullout stages for Cu/Al_2O_3: a) elastic deformation of the fibre, b) after initiation of yielding, c) thinning of the

fibre visible on the entire pulled out length, d) maximum stresses start to localize, e-f) neck formation; g) Radial displacements u_1 distributed in the pulled out fibre; h) Axial stresses σ_{22} in the necking zone; (i) –(j): Distributions of shear stresses τ_{12}: (i) before initiation of the interfacial crack, (j) after initiation of the interfacial crack. The debonding shear stress in the interface $\tau_{max,0} = 10.0$ MPa.

von Mises stresses, radial displacements, axial and shear stresses for the chosen set of parameters are shown for different pullout stages. It may be observed that due to applied displacement loading large plastic deformations occur in the fibre, preventing it from being pulled out from the matrix. Initially the fibre undergoes plastic deformations and thinning on the entire pulled out length. Then, the localization of the plastic strains occurs and formation of the necking zone takes place.

The stress-displacement relationships, which are the main result of this model of the fibre pullout, are presented in Fig. 6.20 for two sets of interfacial parameters. It may be seen that at the initial stage of the loading process curves are nearly linear, which corresponds to a steady response of the interface to the static load. Progressive interface failure that occurs with the increasing load results in a gradual reduction in stiffness. Plastic deformation elongates the fibre while keeping the stresses in the fibre nearly constant. The final fall in the load value occurs due to catastrophic failure.

The stress-displacement relationships, which are the main result of this model of the fibre pullout, are presented in Fig. 6.20 for two sets of interfacial parameters. It may be seen that at the initial stage of the loading process curves are nearly linear, which corresponds to a steady response of the interface to the static load. Progressive interface failure that occurs with the increasing load results in a gradual reduction in stiffness. Plastic deformation elongates the fibre while keeping the stresses in the fibre nearly constant. The final fall in the load value occurs due to catastrophic failure.

It is to be noted that Bheemreddy *et al*. [82] model was implemented for a ceramic-matrix composite made of SiC fibre embedded in SiC matrix (CMC). Hence, a direct comparison with the present results for Cu/Al_2O_3 system is not feasible. Nevertheless, the phases of the pullout process identified in [82], described also in [89] with regard to elastic-plastic behaviour of the fibre, are clearly recognizable in Fig. 6.20(a): elastic elongation of the protruding fibre part before the onset of debonding (O-A), elastic and possibly plastic elongation and thinning of the debonded and protruding parts of the fibre (A-B) till debonding completion at

a)

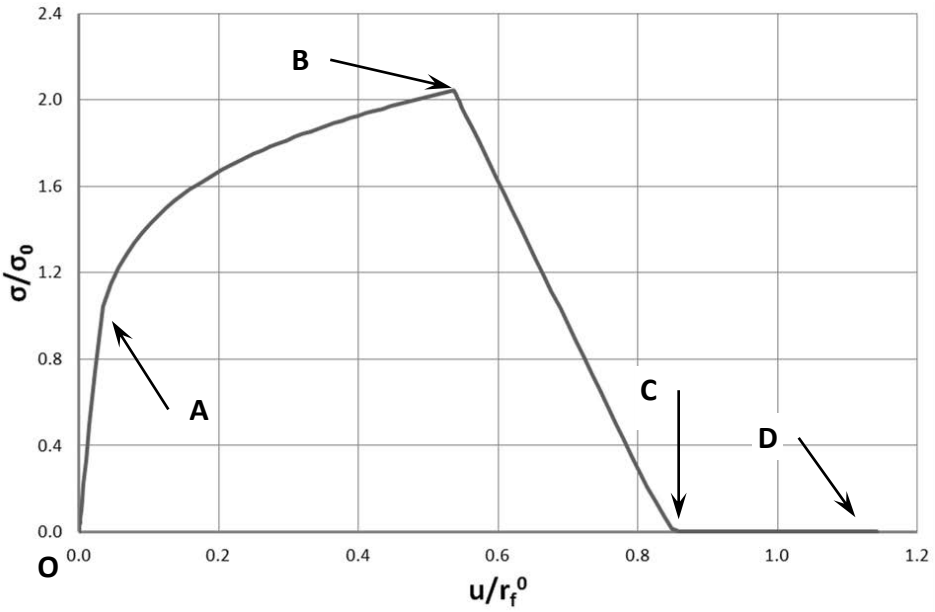

b)

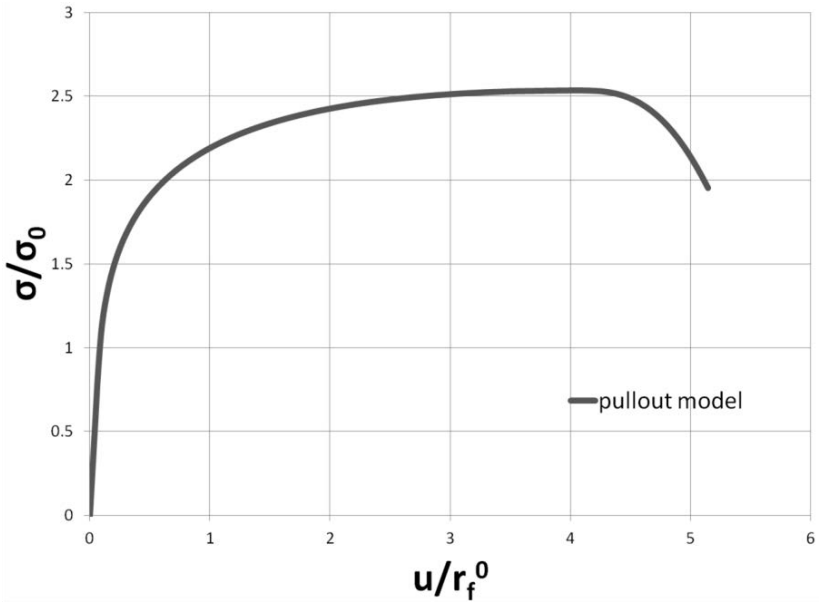

Figure 6.20. Normalised stress-displacement relationships obtained from present numerical model of the pullout problem; a) at debonding shear stress in the interface $\tau_{max,0}$ = 3.0 MPa with the main stages of the pullout process marked with letters **O** ÷ **D**, b) at parameters from Table 6.4.

maximum overall stress (B), load drop with rapid growth of deboding with interface undergoing shear, elastic and possibly plastic elongation accompanied by thinning of the debonded and protruding parts of the fibre (B-C), and unrestricted frictional pull out of the fibre completely separated from the matrix, with elastic strains recovery stalled by frictional matrix/fibre contact (C-D). Due to friction, the fall in the load value takes place at limited displacement, in contrary to the immediate drop in frictionless model of [82].

The pullout problem is regarded as one of the most important tests to find the expected behaviour of a fibre-matrix material system. If the interface in such a system is sufficiently weak, the fibre debonding from the matrix will occur when a crack growing through the matrix meets the fibre. The identification of the fibre/matrix interface mechanical properties is very important for the proper estimation of the mechanical behaviour of the whole composite. The bond between fibre and matrix has an important role in the ability of the fibres to stabilize the microcracks created during loading. The pullout of the reinforcing fibres also influences the total energy needed for the cracking process. It is then important to have a reliable pullout model capable to correctly identify the material parameters and cover the complete pullout process.

Axisymmetric single reinforcing fibre model with debonding evolution

A FEM model for the axisymmetric case of a single fibre reinforcing crack faces with account of the effect of debonding evolution will be analyzed in this Subsection as another prerequisite model to better understand the crack bridging mechanism in real IPC materials. The model itself and the results of numerical simulations for Al fibre reinforcing Al_2O_3 matrix were published in [89]. The results for an elastic-plastic Cu fibre reinforcing two separate blocks of elastic Al_2O_3 alumina matrix have not been published yet. Evolution of debonding between fibre and matrix is modelled using ABAQUS [144]. The interface between fibre and matrix is modelled with cohesive elements. Three debonding regions in the matrix-fibre interface can be distinguished: full bond, frictional slip and radial detachment as shown in Fig. 6.21. As before, the debonding length may be characterized with the nondimensional debonding parameter ψ, defined by Eq. (6.3) as the ratio of the debonding length l_d to the initial fibre radius r_f^0.

The model was calibrated with parameters given in Table 6.5. Similarly as in the pullout case the matrix/fibre radii ratio was taken as $r_m/r_f^0 = 71.43$ (*cf.* Table 6.5) to avoid the effect of the surrounding medium on the numerical results.

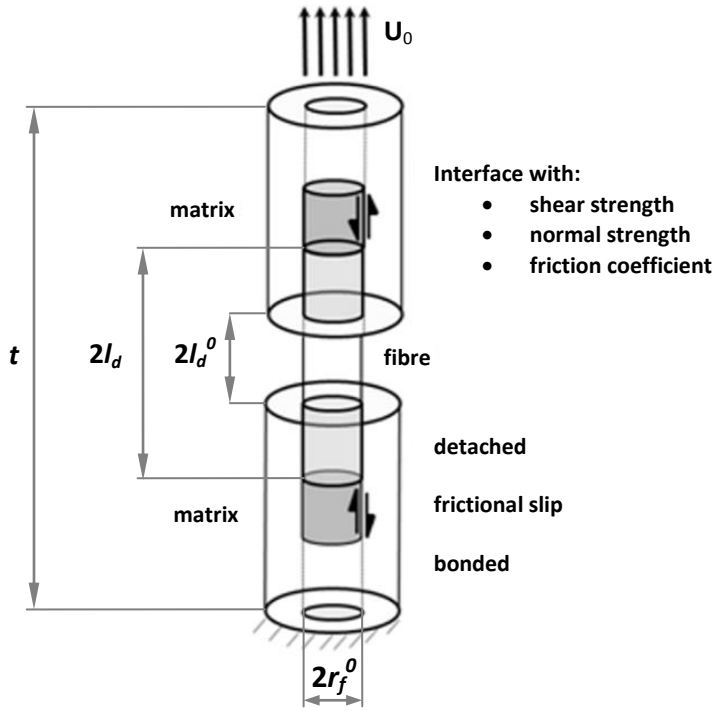

Figure 6.21. Single fibre reinforcing two blocks of elastic matrix separated by a crack with interface and debonding regions under tensile loading: full bonding, sliding against friction and radial detachment (reproduced with permission from *International Journal of Damage Mechanics*).

This case is similar to the second prerequisite model (*cf*. Fig. 6.13) considered in Subsec. 6.2.1. However, the main difference is that the effect of fibre/matrix debonding is not simulated by a series of fixed values of debonding parameter ψ but the debonding evolution is included in the overall model. The elastic-plastic model with J_2 flow plasticity and isotropic hardening was implemented in ABAQUS [144] to model the copper fibre bahaviour. Large strains that could locally occur in the necking zone, were determined with an incremental algorithm. Spectral decomposition allowed the use of the return mapping procedure for models with an isotropic yield function. The stress update algorithm was used for the integration of the J_2 plasticity constitutive equations. The traction-separation was modelled with cohesive elements as described in detail by [89].

The assumed boundary conditions (*cf*. Fig. 6.22) represent the situation in a real IPC material where the reinforcing ligament is interconnected at its ends with the metal phase network. Consequently, both axial and horizontal displacements are blocked at the bottom surface of the fibre and matrix. At the top surface of the fibre and matrix the displacement loading is applied.

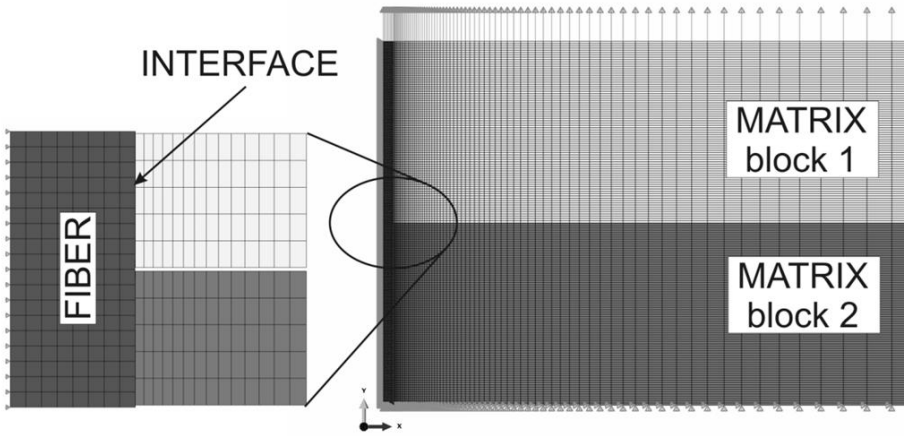

Figure 6.22. FEM mesh with boundary conditions for axisymmetric single fibre reinforcing two disconnected matrix blocks with evolution of fibre/matrix debonding; fibre-matrix interface modelled with cohesive elements (reproduced with permission from *International Journal of Damage Mechanics*).

The FEM mesh and boundary conditions are depicted in Fig. 6.22. The fibre and matrix were modelled with four-node bilinear axisymmetric elements CAX4. The whole FEM model consisted of 9652 nodes and 8921 elements. Geometrical and material parameters used for calculations are presented in Tables 6.4 and 6.5.

The results of numerical simulations for selected displacement, stress and strain components are shown in Fig. 6.23. The main outcome of the model, *i.e*. the stress-displacement relationship in the reinforcing fibre under progressive fibre/matrix debonding is graphically depicted in Fig. 6.24.

Table 6.5. Material and geometrical parameters used in the models of fibre pullout and axisymmetric reinforcing fibre with debonding evolution. E_f , E_m, ν_f and ν_m denote Young's moduli and Poisson's ratios of the fibre and matrix, respectively.

	Pullout model		Bridging fibre model	
	Al_2O_3	Cu	Al_2O_3	Cu
E_m, E_f, E [GPa]	390.0	110.0	390.0	110.0
ν_m, ν_f, ν	0.2	0.35	0.2	0.35
σ_0 [MPa]	-	50.0	-	50.0
n	-	5.8	-	5.8
r_f^0 [μm]	-	175.0	-	175.0
r_m [mm]	12.5	-	12.5	-
l_0 [mm]	-	3.0	-	-
l_m [mm]	3.0	6.0	-	-
l_d [mm]	-	0.0 ÷ 3.0	-	-
t [mm]	-	-	6.0	6.0

It can be noticed in Figs 6.23 - 6.24 that a relatively small necking in the reinforcing fibre results from extensive debonding. Only a smaller part of the stresses is supported by the interface, the main part being carried with the actual fibre cross section. It is also reflected in Fig. 6.24, where the stresses in the reinforcing fibre on the curve of the evolution of debonding model are only slightly declining. In other words at large displacements the axial stress in the fibre is still not far from the maximum value.

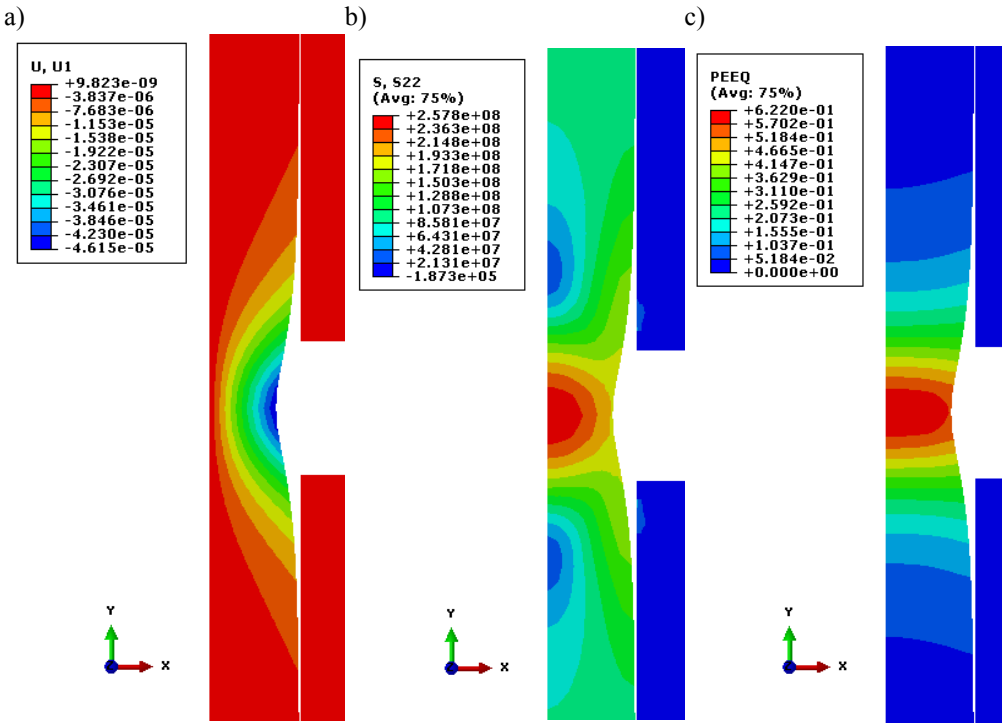

Figure 6.23. Distributions of radial displacements (a), axial stresses (b), and equivalent plastic strains $\bar{\varepsilon}$ (c) at axial displacement $u_2 = 0.25$mm.

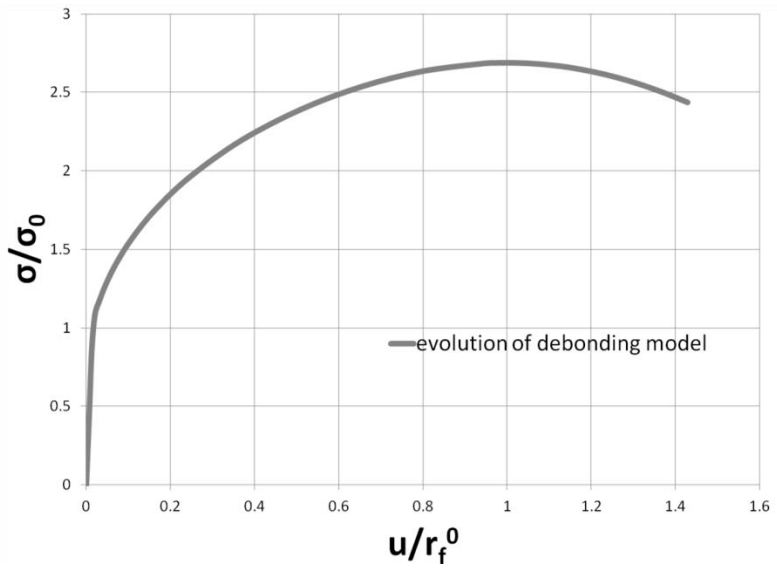

Figure 6.24. Stress-displacement relationship in the reinforcing fibre obtained with the FEM model accounting for the fibre/matrix debonding evolution.

Comparison of the prerequisite models with the Mataga model

The stress-displacement characteristics obtained from the pullout problem model and, the axisymmetric reinforcing fibre model with and without debonding evolution were compared with the analytical results of [93]. The respective curves are shown in Fig. 6.25 divided into two diagrams (a,b) for visual clarity. The fracture parameters used in numerical simulations regarding evolution of debonding were taken as G_{IIC} =10.0 Jm^{-2}, $\tau_{max,0}$ = 10.0 MPa.

It can be seen in Fig. 6.25(a) that according to the fixed debonding model the maximum stresses sustained by the reinforcing ligament for ψ = 0.4, 0.6 or 2.0 occur at very small displacements (corresponding to crack openings, COD), whereas for the model with debonding evolution the maximum stresses are reached at much larger displacement (and, thus, COD). The model with debonding evolution shows smooth stress-displacement behaviour and only a slight drop in stresses supported by the bridging ligament, in contrast to the fixed debonding model. The model with debonding evolution yields the results that are in accordance with observations of [97], who reported extensive delamination of copper from the alumina on fracture surfaces of wool felt PFA based IPCs. It could be then supposed that the model with debonding evolution yields results that are more reliable and closer to the behaviour of the real material. It can also be seen that for the fixed debonding model, stresses supported by the bridging fibre rapidly fall to nearly zero with the increasing displacement. For the model with debonding evolution, however, the stress decrease is much slower and relatively high stresses supported by the bridging fibre remain even for large displacements.

It can be seen from Fig. 6.25(b) that Mataga [93] results differ from the results obtained with the numerical model of the bridging fibre with debonding evolution. Similarly as for the model with fixed debonding lengths, this is due to the dissimilarities between the paraboloid of rotation shape of the necking ligament assumed in the model of Mataga [93], and necking ligament shape resulting from the present numerical model. For the numerical model with debonding evolution, relatively large displacements reflecting the crack opening COD are needed to reach the maximum stresses. For the numerical model of the bridging fibre with debonding evolution the stresses inside the fibre decline slowly and smoothly. Compared with observations of [97], it could be presumed that the results of this model may be the closest to the behaviour of the real material.

a)

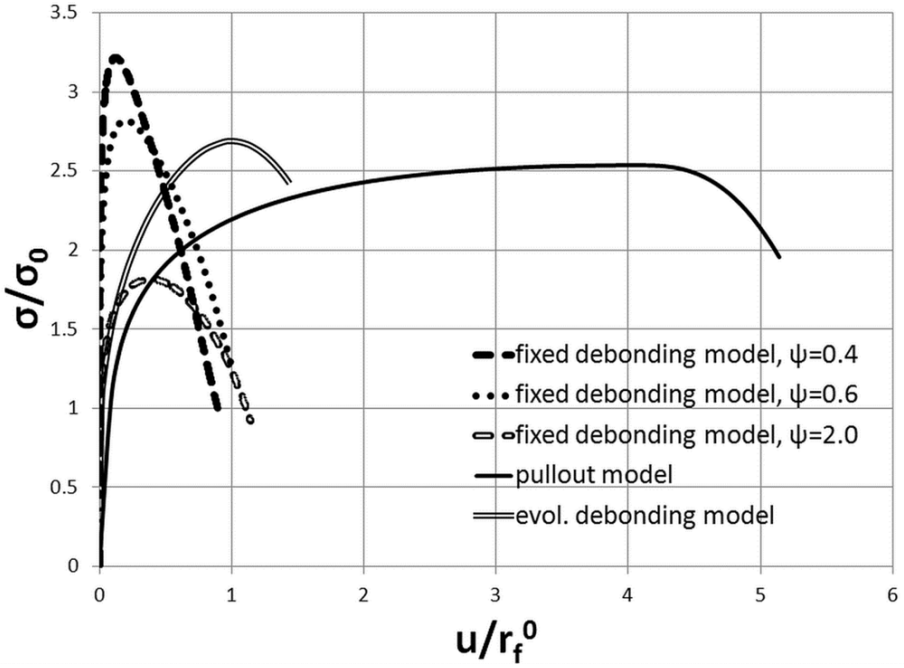

b)

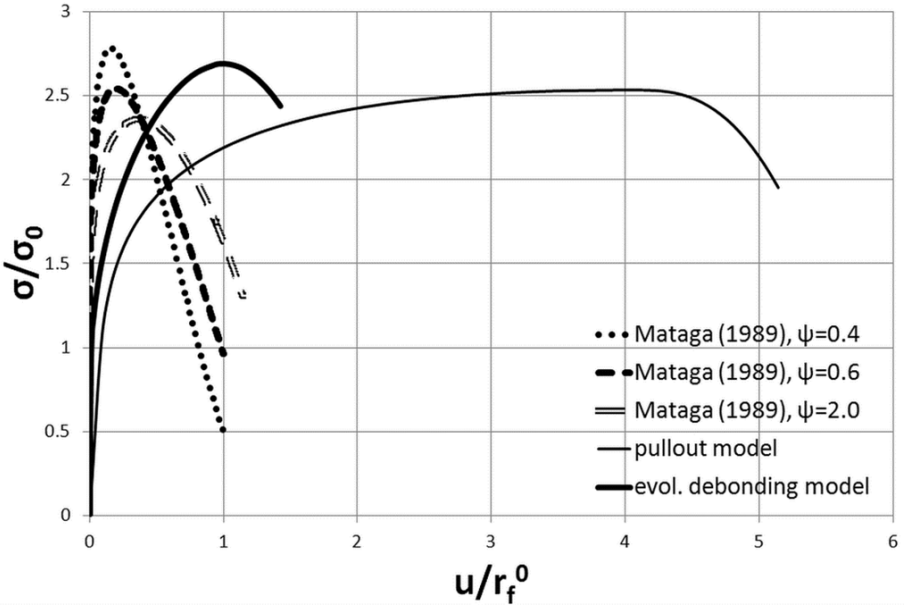

Figure 6.25. Comparison of the stress-displacement relationships in Cu fibre obtained according to the "pullout" and "evolving debonding" models with (a) fixed debonding model, and (b) Mataga [93] model (for different values of ψ).

6.2.2. FEM model of Compact Tension test

As it was mentioned in Subsection 6.1, the Compact Tension (C-T) test when used for fracture toughness determination in novel composite materials like IPCs is experimentally rather challenging because of the lack of well-established standards and technical protocols. Thus, the main aim of modelling presented in this work is to support experimental measurements of IPC's fracture toughness by a numerical approach taking into account real composite microstructure and the crack bridging mechanism.

Before the FEM calculations for a real IPC microstructure were finally possible, many attempts were needed to arrive at a model with all the necessary features. Initially a set of models with simplified fibrous microstructure, both in 2D and 3D, was investigated. Only then the final model of the C-T test of the real IPC with microstructure obtained from computed micro-tomography (micro-CT) scans could be developed.

In the numerical models of the C-T test described in the following Subsections the dimensions of C-T specimens were adjusted to the ASTM [179] standard.

Two-dimensional C-T model with single reinforcing skew fibre

The first of the 2D models was devised for a pre-cracked alumina specimen with crack faces reinforced with a single copper fibre. This model can be seen as an illustrative example of calculating the *J*-integral based on the potential energy approach described by [121].

The fibre was either perpendicular or inclined to the crack plane. The test specimen made of monolithic ceramic was also considered for comparison. The Al_2O_3 ceramic phase was modelled as isotropic elastic, the metallic Cu fibre as isotropic elastic-plastic, using the plasticity model implemented in FEAP [156] described in Subsec. 6.2.1 for the 2D model of skew reinforcing fibre. Material data of ceramics and fibre is given in Table 6.2. The boundary conditions were applied at the geometrical centres of the pins. The point displacement was applied as a load. FEAP [156] logarithmic stretch model was used to model the deformation. The model is schematically presented in Fig. 6.26(a-b) for unreinforced C-T specimen with pre-crack and in Fig. 6.26(c-d) for a single skew fibre bridging the crack developing from the notch.

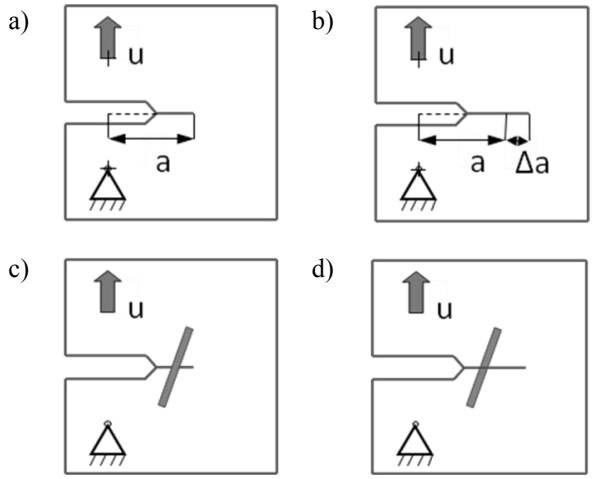

Figure 6.26. Scheme of C-T test to determine energy release rate and fracture toughness increase due to bridging: (a), (b) specimens from monolithic ceramic material, (c), (d) ceramic specimens with metallic reinforcements; (a), (c) – initial state, (b), (d) – state at infinitesimally increased crack length.

The *J*-integral was calculated based on the potential energy increase $\Delta\Pi$ for the infinitesimal increase of crack length Δa [44,121]. The energy release rate, or the crack extension force G can be defined in the following form

$$G = -\frac{d\Pi}{dA}, \tag{6.13}_1$$

where: dA is the infinitesimal crack surface increase, $d\Pi$ – potential energy increase, $\Pi = \Pi^{int} + \Pi^{ext}$ denotes the potential of external and internal forces, Π^{int} - strain energy representing internal energy: $\Pi^{\text{int}} = \int_V W dV$, W- strain energy, V - body volume, Π^{ext} - potential of the external loads $\mathbf{F}$: $\Pi^{ext} = -\int_{\partial V} \mathbf{F} \cdot \mathbf{u}\, dS$, $\mathbf{u}$ - displacements, ∂V - boundary surface of the body volume V, dS - area element.

In two-dimensional case, where $d\Pi$ is linked with the unit thickness as

$$G = -\frac{d\Pi}{da}, \tag{6.13}_2$$

the energy release rate G is associated with infinitesimally small crack length increase da. The energy release rate is related to the stress intensity factors K as in Eq. (3.5), namely

$$G = -\frac{d\Pi}{da} = f(K). \tag{6.14}$$

The *J*-integral introduced in Sec. 3 for an elastic material is equivalent to the energy release rate *G* (Eq. 3.4). Thus, for determination of the *J*-integral the increase of the potential energy for infinitesimally small crack length increase Δa is to be found (*cf.* [121])

$$J = \lim_{\Delta a \to 0} \left(-\frac{\Delta \Pi}{\Delta a} \right). \tag{6.15}$$

Calculating the difference $-\Delta\Pi = \Pi_2 - \Pi_1$, where Π_1 denotes the potential energy in the initial state at crack length a_1, and Π_2 in the final state at infinitesimally elongated crack of length $a_2 = a_1 + \Delta a$, $\Delta a \to 0$ one obtains the energy release due to the crack length increase Δa (*cf.* [121]). The energy release due to the crack length increase $a_2 - a_1$ was used in the present model to estimate the *J*-integral

$$J \approx -\frac{\Pi_2 - \Pi_1}{a_2 - a_1}. \tag{6.16}$$

This model of calculating the energy release ($-\Delta\Pi$) was applied to the case of unreinforced pre-cracked ceramic C-T specimen (Fig. 6.26(a,b)) and the C-T specimen with metal reinforcement spanning the crack faces (Fig. 6.26(c,d)). Two inclination angles of the reinforcing fibre to the crack plane were considered: 60° and 90°.

The energy release rate increase ΔG due to the presence of reinforcement was obtained comparing the results for the ceramic matrix with fibre-reinforced crack with the results for the homogeneous material with no crack-bridging fibre for the two inclination angles considered.

The calculations were made with FEAP [156] programme. The FE mesh in the vicinity of the crack is shown in Fig. 6.27 for the cases of monolithic Al_2O_3 ceramic (a, b) and Al_2O_3 ceramic reinforced with Cu fibre at two inclination angles to the crack plane: 90° (c, d) and 60° (e, f). Due to the mesh geometry the radii of the crack tip are equal to zero. The meshes in the crack tip vicinity for crack lengths $a_1 = a$ are presented in Figs. 6.27 (a), (c) and (e), the meshes for crack lengths $a_2 = a + \Delta a$ are presented in Figs. 6.27 (b), (d) and (f).

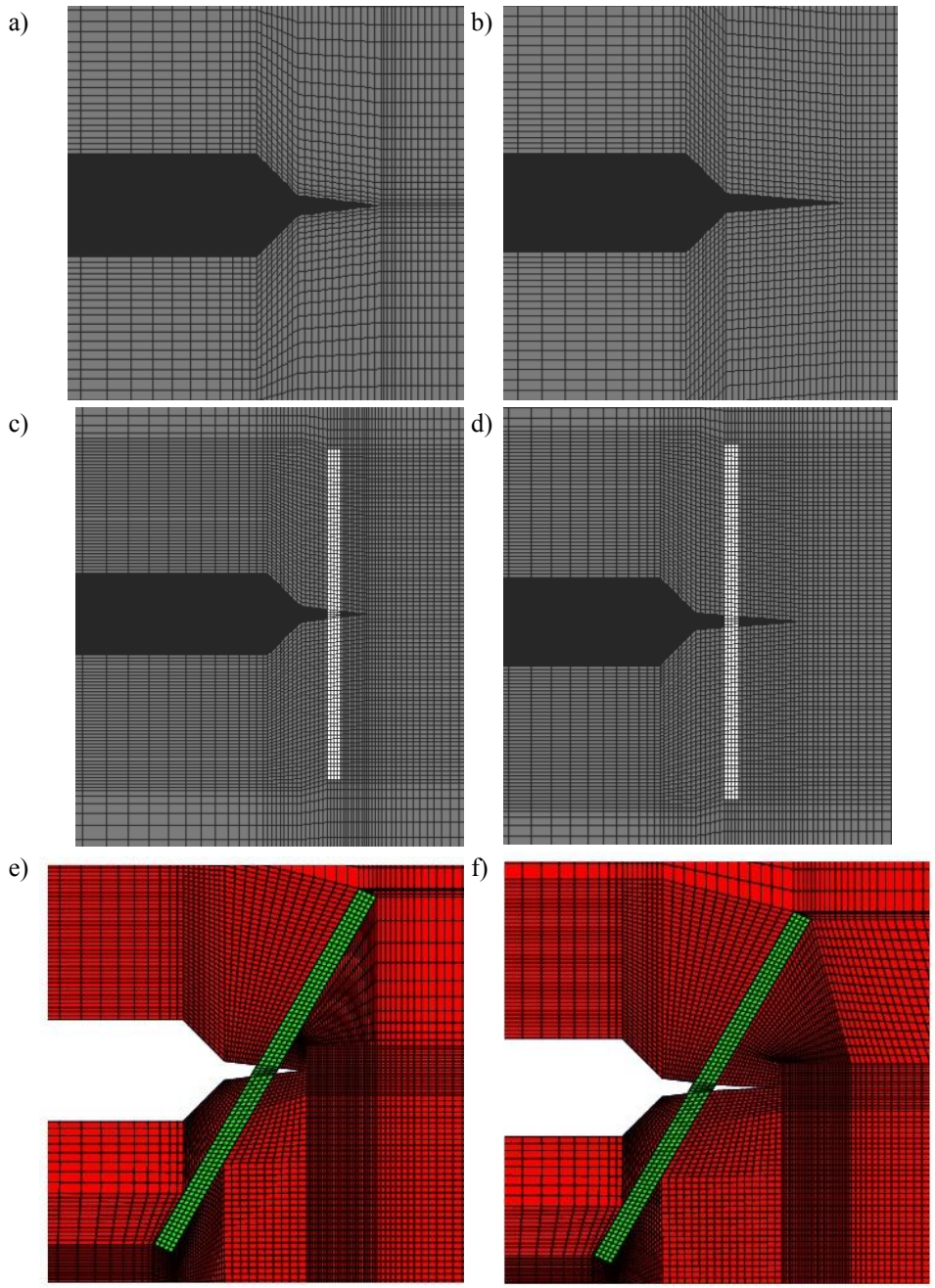

Figure 6.27. Pre-cracked C-T specimen model in FEAP [156] – FE mesh in the vicinity of the crack tip (dark grey (c,d) or red (e,f) colour – ceramics, light grey (c,d) or green (e,f) colour – metal): (a), (b) monolithic ceramics; (c), (d) with reinforcement inclined 90° to the

crack plane; (e), (f) with reinforcement inclined 60° to the crack plane; (a), (c), (e) – before, and (b), (d), (f) – after the crack length increase (images are not in the same scale).

The potential energies Π_i in the above cases were calculated from the reaction forces and displacements at the nodes along contours surrounding the crack tip. The 3rd contour from the crack tip was taken for the calculations (*cf*. Fig. 6.28). The *J*-integral values were then obtained according to Eq. 6.16.

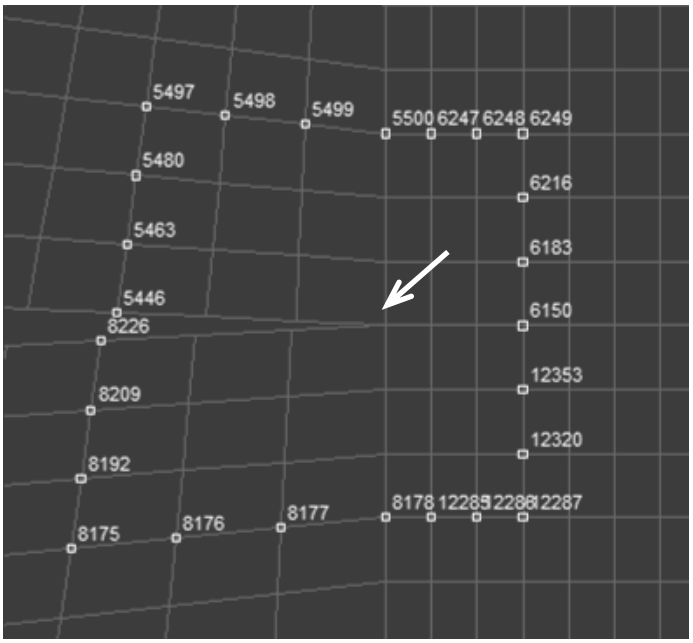

Figure 6.28. Nodes forming the 3rd contour for the *J*-integral (white arrow indicates crack tip).

In Fig. 6.29 the stress distributions obtained for the initial and elongated crack lengths are compared.

The calculated *J*-integrals for the cases of (i) unreinforced ceramic C-T specimens and (ii) C-T specimens with reinforcing fibres inclined at 60° and 90° to the crack plane, along with the corresponding energy release rate increase ΔG, are collected in Table 6.6.

From Table 6.6. it can be seen that the presence of the fibre reinforcing crack faces causes an increase in the energy release rate, thus, will enhance the material fracture energy. This increase is higher for the fibre perpendicular to the crack plane

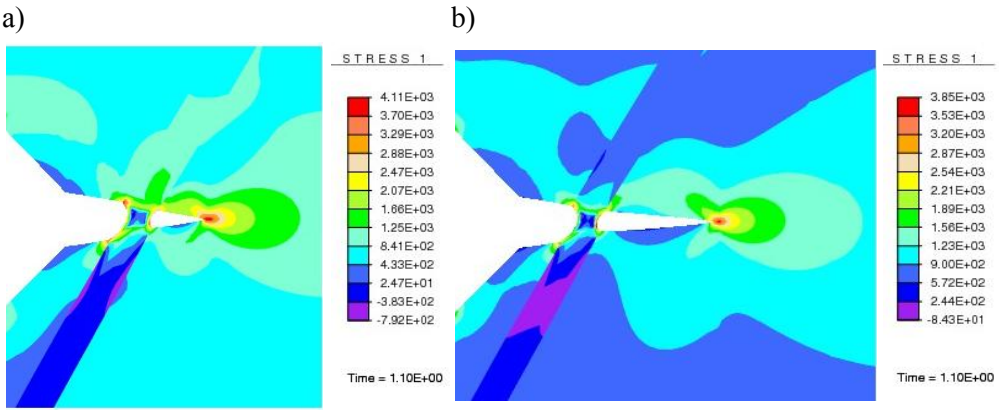

Figure 6.29. Horizontal stress distributions for fibre inclined at 60°to the crack plane for: (a) initial and (b) increased crack length.

than for the fibre inclined at the angle of 60°. This is due to the active (projected on the crack surface) fibre cross section, which is the largest for the fibre perpendicular to crack plane. Also, the influence of mode II loading, which was not considered in the theoretical model, reduces the fracture energy in the inclined fibre case.

Table 6.6. Numerical values of J-integral and ΔG for alumina C-T specimens with crack reinforcing copper fibre obtained for contour no. 3.

Unreinforced Al_2O_3 sample	Fibre reinforced sample, Al_2O_3 –Cu, fibre inclination 60°	Fibre reinforced sample, Al_2O_3 –Cu, fibre inclination 90°	ΔG for fibre inclination of 60°	ΔG for fibre inclination of 90°
J_C [$\times 10^3$ N/m]	J_{60} [$\times 10^3$ N/m]	J_{90} [$\times 10^3$ N/m]	$\Delta G_{60} = J_C - J_{60}$	$\Delta G_{90} = J_C - J_{90}$
2.038	0.821	0.145	1.217	1.893

Two-dimensional model with multiple reinforcements

The second 2D FEM model of the Compact Tension test is the model with multiple reinforcing fibres. The linear elastic Al_2O_3 ceramic was taken as the matrix material. The elastic-plastic constitutive model was assumed for the Cu fibre. The material and geometrical details of the fibre are listed in Table 6.3. The plasticity in the fibre was modelled using the $\sigma(u)$ relationship yielded by the model of the reinforcing fibre for the delamination parameter $\psi = 0.4$ and applying these data via UMAT procedure in ABAQUS [144]. The FEM mesh for the ceramic matrix prepared in ABAQUS [144] with the boundary conditions and force loading are presented in Fig. 6.30.

The *J*-integral was calculated according to the procedure in ABAQUS [144] along the contour *C*:

$$J = \int_{C} \left(U dy - t_i u_{i,x} dc \right), \tag{6.17}$$

where U is the strain energy density given by

$$U = \int_{0}^{\varepsilon} \sigma_{ij} d\varepsilon_{ij}, \quad \boldsymbol{\sigma}, \boldsymbol{\varepsilon} \text{ – stress and strain tensors,} \tag{6.18}$$

and **t** is the stress vector defined as

$$t_i = \sigma_{i\beta} n_\beta, \tag{6.19}$$

n – unit vector normal to the contour, **u** – vector of displacements ($u_{i,x}$ denotes derivative in x direction: $\frac{\partial u_i}{\partial x}$).

It was impossible to obtain some of the above stress components with FEAP [156], thus the calculations were made with ABAQUS [144].

The bridging fibres were modelled in ABAQUS [144] as plane strain elements connecting crack faces. Material model of the fibre remained the same as in the previous case. Calculations were made for quasi-static crack propagation. The FEM mesh with bridging fibres modelled as plane strain elements, the boundary conditions and displacement loading are presented in Fig. 6.30.

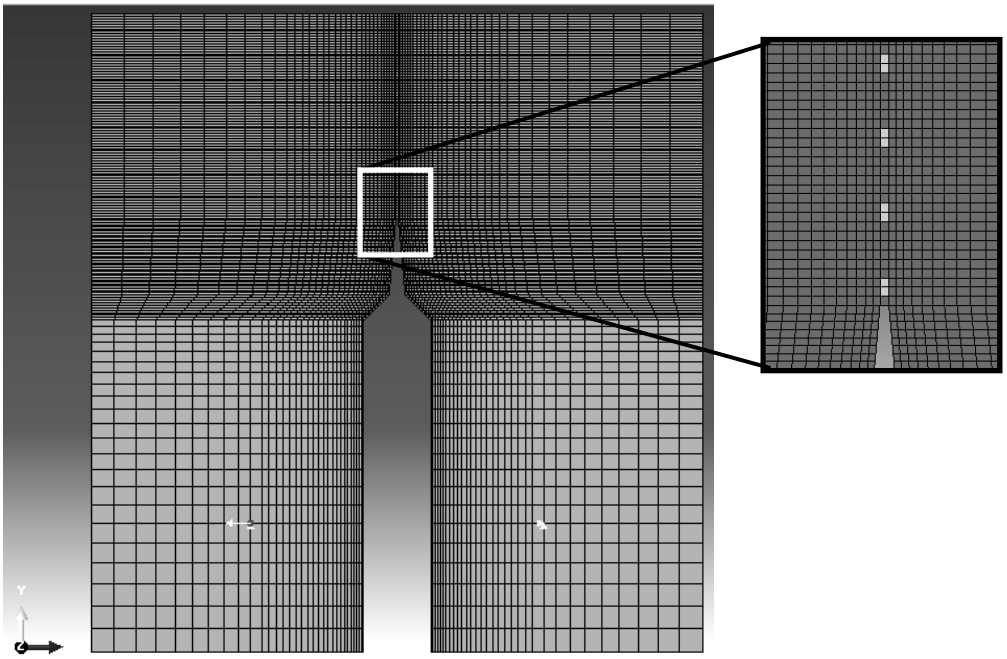

Figure 6.30. Compact-Tension (C-T) test model in ABAQUS [144] (mesh created with FEAP [156]) with bridging fibres modelled as plane strain elements (light colour), boundary conditions and displacement loading.

The resulting distributions of horizontal stresses for increasing crack length are presented in Fig. 6.31. For the plane strain quasi-static crack propagation model, *J*-integral was determined numerically using ABAQUS [144] procedures taking 42 contours for four different crack lengths. The resulting relation of *J*-integral vs. crack length increase Δa for an exemplary material is presented in Figure 6.32. It can be seen that the *J*-integral increases with the increasing crack length of the growing crack.

It is to be emphasized that the proposed plane model of the C-T test for pre-cracked ceramic material reinforced with multiple ductile fibres accounts for the delamination, large deformations and necking of the reinforcing fibres. The σ-u characteristics of the individual elastic-plastic fibre were obtained with separately developed model accounting for the same phenomena.

a)

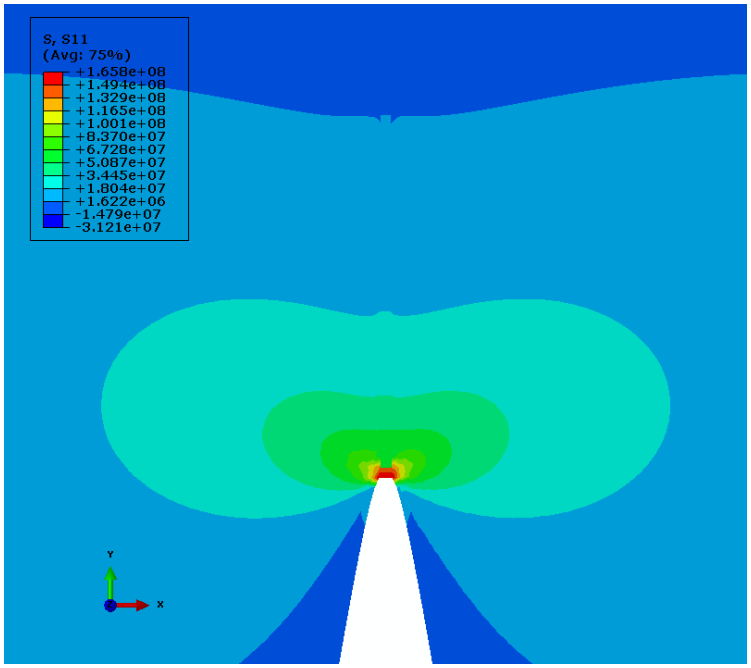

b)

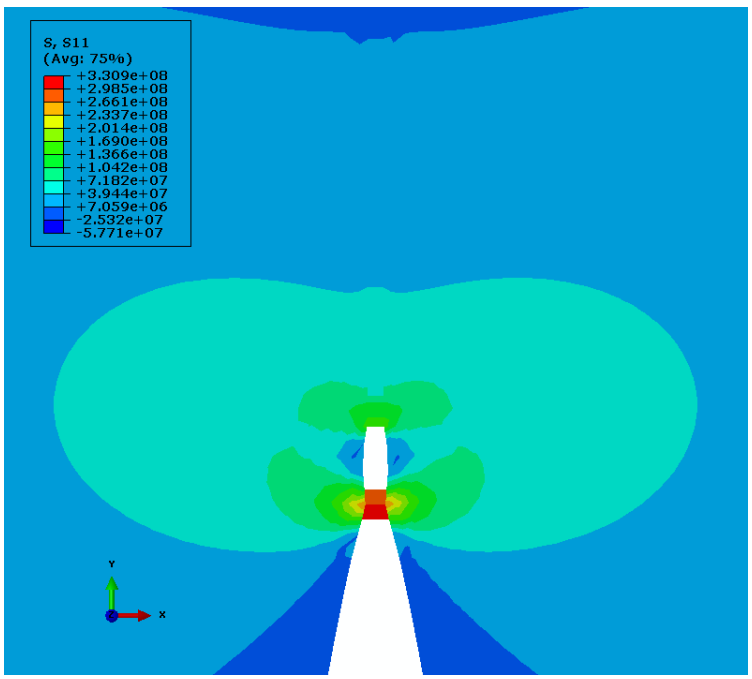

c)

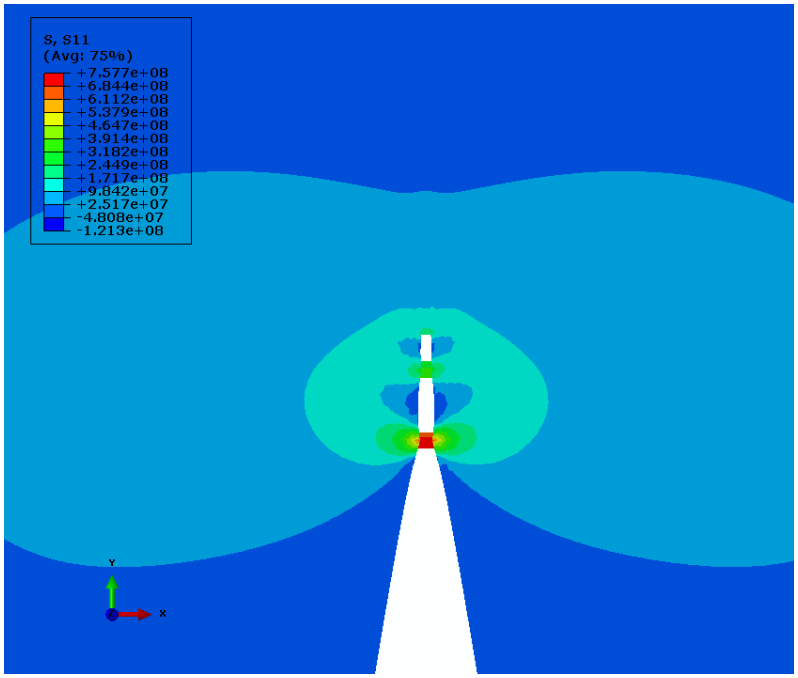

d)

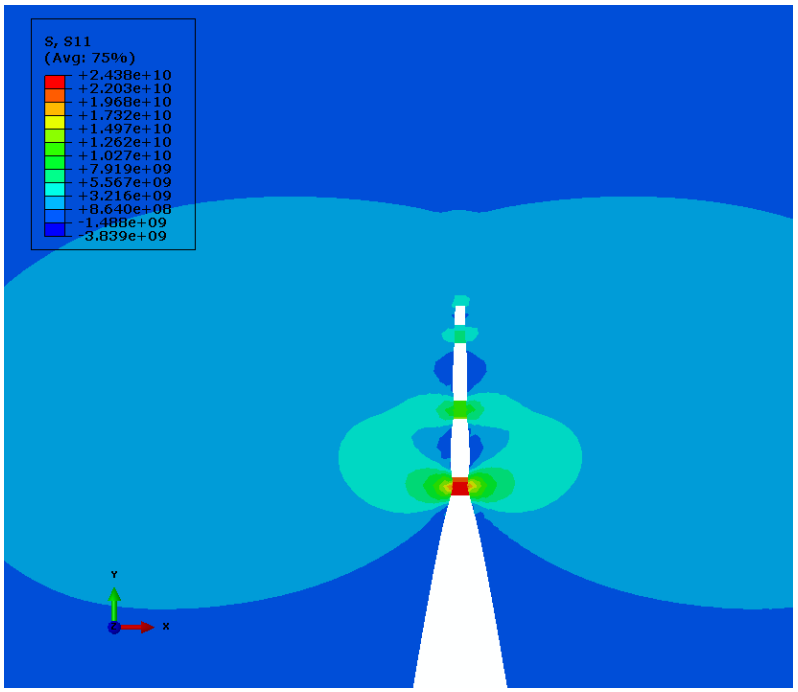

Figure 6.31. Distributions of horizontal stresses for increasing crack length in plane strain C-T model with multiple fibres.

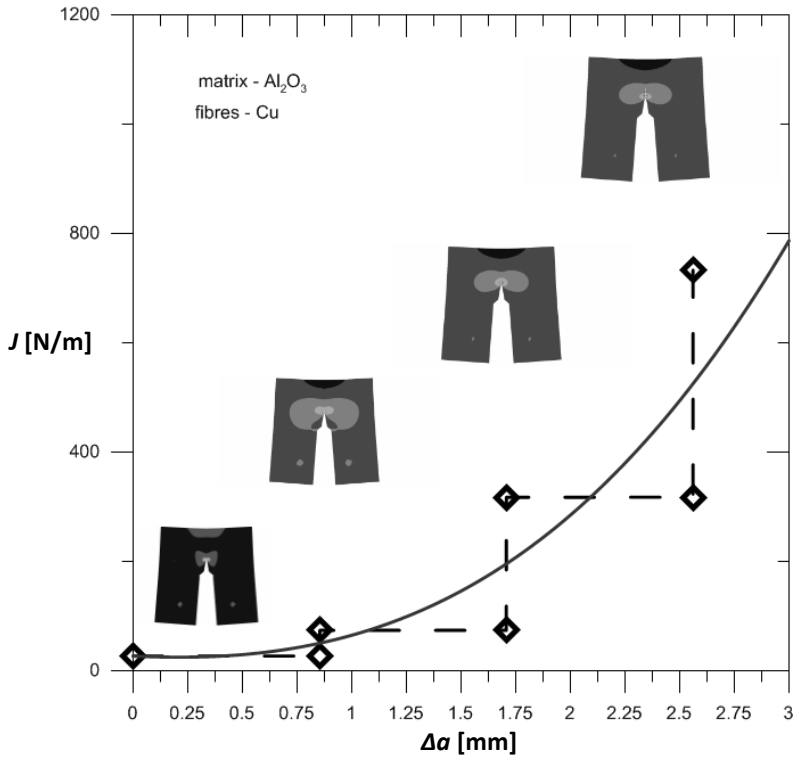

Figure 6.32. Illustrative example of *J*-integral vs. crack length increase *Δa* curve for plane strain C-T of alumina specimen toughened with copper fibres - results from ABAQUS [144]**.**

Three-dimensional model for simplified composite microstructure with fibres

In this model the Al_2O_3/Cu IPC material is modelled as the effective material in which a cuboid containing bridging fibres perpendicular to the predicted crack plane is placed in the vicinity of the crack tip. The fibres' locations and dimensions were taken according to Hoffmann *et al*. [94] experiments. The surrounding material is modelled as elastic with the effective elastic properties calculated using the extended *V-R-V* model developed in Section 5. The dimensions of the C-T specimen comply with the ASTM [179] standard. The material and geometrical data of the fibre are given in Table 6.3. In Fig. 6.33 an overall scheme of this Compact-Tension test model is presented.

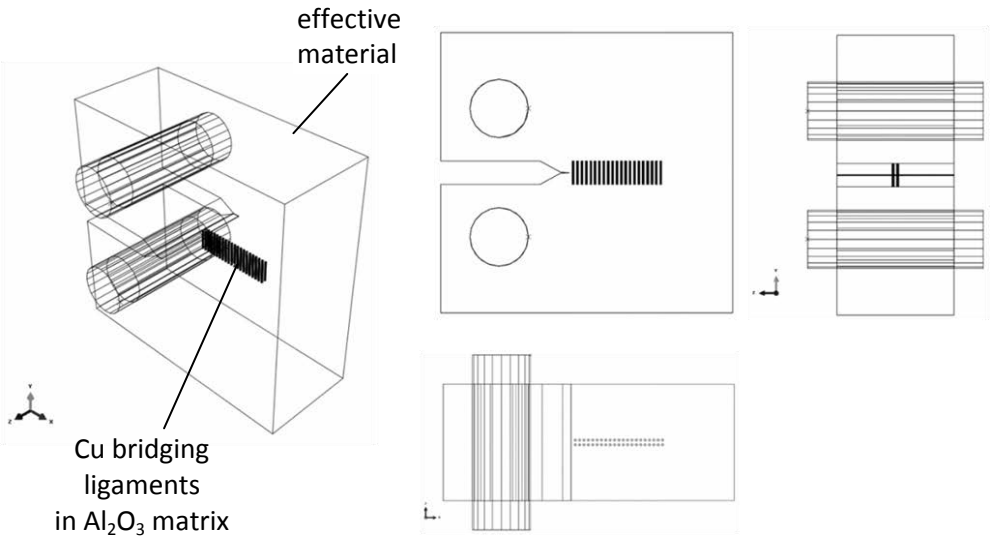

Figure 6.33. Scheme of three-dimensional Compact-Tension model for composite with multiple crack reinforcing parallel fibres, with perspective view and orthogonal projections from ABAQUS [144].

The overall view of the model in ABAQUS [144] with one of FE meshes and boundary conditions is shown in Fig. 6.34. The details of the crack tip vicinity with fibres are shown in Fig. 6.35. Selected stress and strain distributions in the reinforcing fibres obtained with this model are presented in Figs 6.36 and 6.37.

The crack propagation and the *J*-integral were not analysed with this simplified C-T model. It served merely as a necessary step towards a more accurate C-T model where a cuboid with prescribed topology of perpendicular cylindrical fibres would be replaced by micro-CT images of the interpenetrating microstructure with ductile ligaments in front of the growing crack. The rationale behind using such a material insert with a specific composite microstructure near the crack tip was to prepare the numerical ground in ABAQUS for the more complex FEM model when the growing crack encounters real microstructure of an IPC.

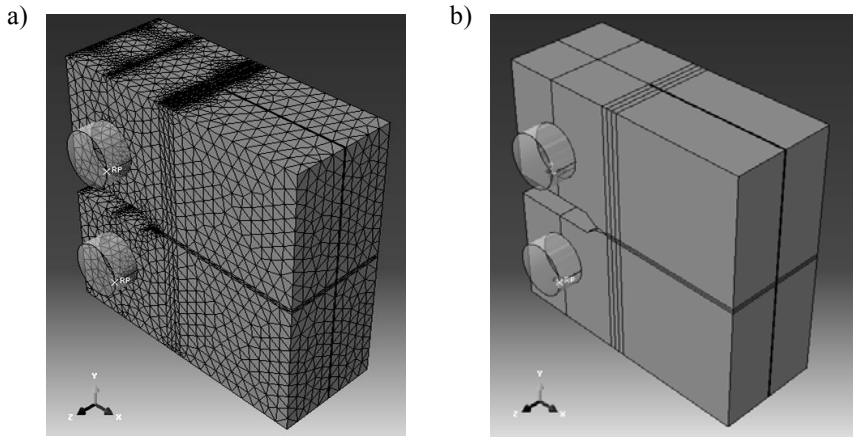

Figure 6.34. Simplified 3D model in ABAQUS [144] of Compact-Tension test with parallel fibres near the crack tip: a) sample FE mesh, b) boundary conditions.

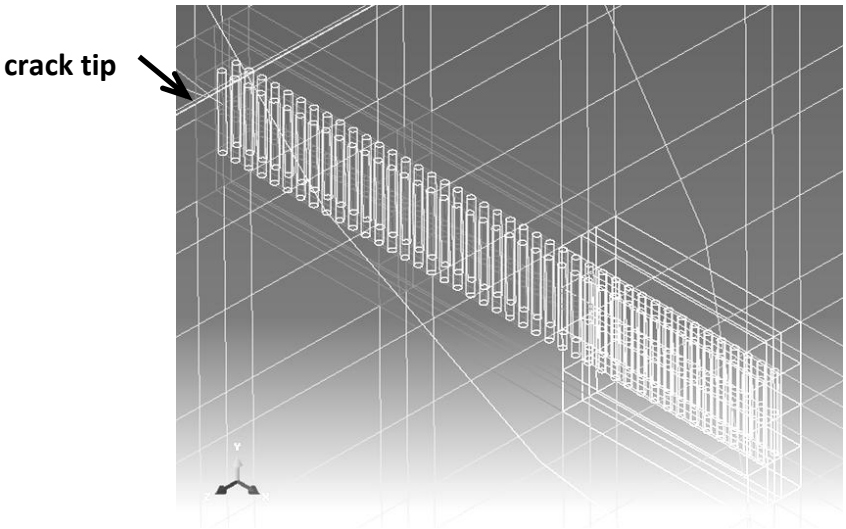

Figure 6.35. Detailed view of the crack tip neighbourhood with family of parallel reinforcing fibres.

a)

b)

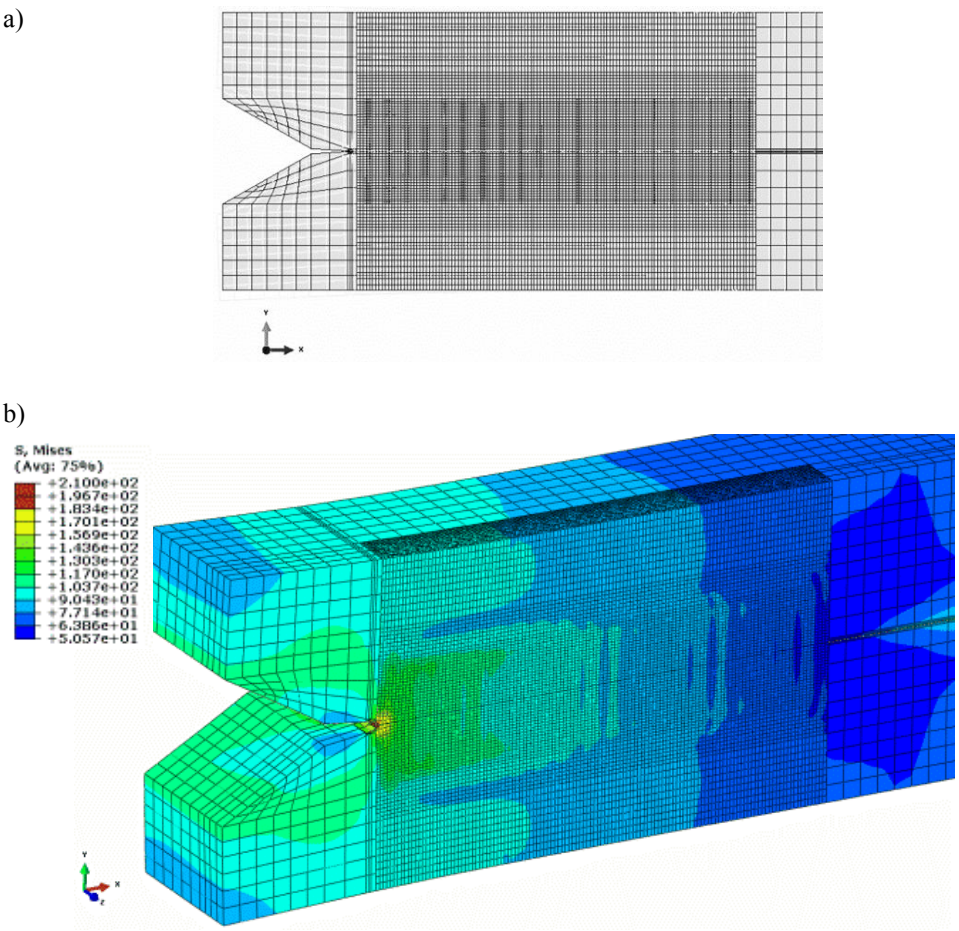

Figure 6.36. Numerical model and results from ABAQUS [144]: a) FEM mesh, b) von Mises stress distributions for a chosen increment of loading.

a)

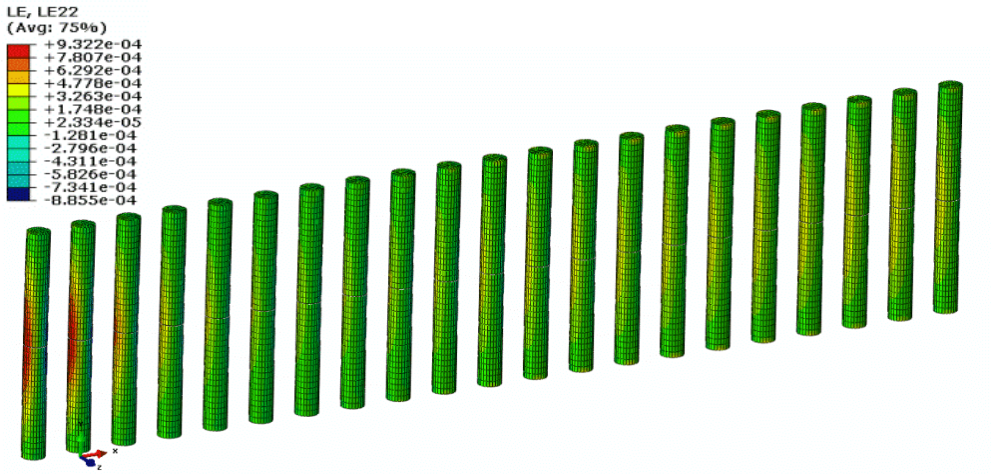

b)

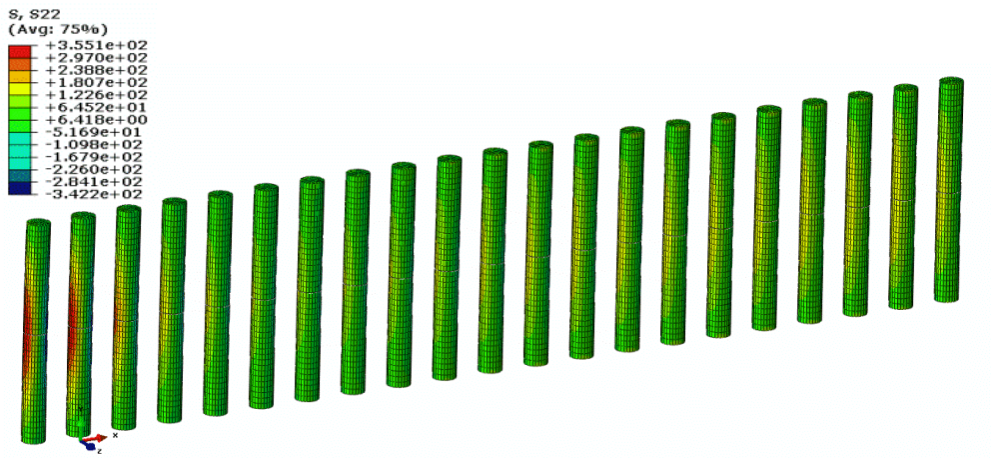

Figure 6.37. Numerical model and results from ABAQUS [144]: a) vertical logarithmic strain distribution in reinforcing fibres, b) vertical stress distribution in reinforcing fibres. Results are influenced by the three-dimensional state of deformation and strain inside the C-T specimen.

Numerical model with real IPC microstructure

In this Subsection the energy release rate increase will be determined for an IPC material in Compact-Tension (C-T) with account of a real interpenetrating microstructure obtained with *computed microtomography* (micro-CT). A solution of such a complex problem requires the use of special software and high performance computer (total number of elements = 946322, total number of degrees of freedom = 3583413). However, the analysis of this problem is possible with the use of the ABAQUS [144] software package carrying out the computations in two steps: (i) solving of the Compact Tension problem with homogenized material properties, followed by (ii) a "submodelling" approach for the chosen smaller volume of the material in the region of interest. The idea of the proposed model is depicted in Fig. 6.38.

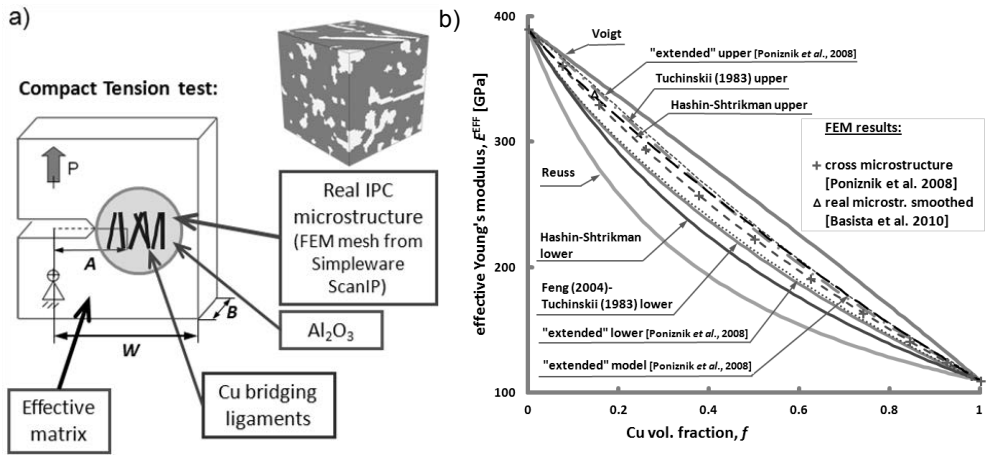

Figure 6.38. Scheme of the Compact-Tension test model of the IPC with real material microstructure obtained from micro-CT: (a) FE mesh in the vicinity of the crack based on the micro-CT data, (b) analytical and numerical models for effective elastic properties used for the remaining part of the C-T specimen (based on [7,139,147], with the permission of publishers).

The composite material under consideration is an Al_2O_3/Cu IPC with 25% Cu content. It was manufactured within the KMM-NoE[1] FP6 project by Jami Winzer at the Institute of Materials Science of Darmstadt University of Technology in Germany. The gas pressure-assisted infiltration of a molten copper into a ceramic

[1] Network of Excellence "Knowledge-based Multicomponent Materials for Durable and Safe Performance" (contract no. 502243-2)

preform was performed at the temperature of 1200°C and pressure of 100 bar. The interconnected pore network in the ceramic preform was obtained using a natural wool felt as the sacrificial pore forming agent, PFA ([97], see also Appendix).

A three-dimensional representation of the Al_2O_3/Cu IPC microstructure was obtained with micro-CT by Georg Geier at the Österreichisches Gießerei-Institut (Austrian Casting Institute) in Leoben. Volumetric micro-CT images of the IPC microstructure were obtained for a cylindrical specimen cut in two smaller pieces. The obtained micro-CT images were transformed into FE meshes with Simpleware ScanIP/FE [8] commercial software according to the procedure described in [139]: first, the image was imported into ScanIP [8] programme, then a representative volume of the 3D microstructure was chosen for further processing. For the chosen volume the segmentation into separate phases was done to distinguish the composite phases, *i.e*. alumina and copper. Then the FE mesh was obtained with ScanFE [8] programme. In view of the expected singularities such as the crack tip, and intended *J*-integral calculations necessitating the use of quadrilateral and not tetrahedral elements, smoothing of the FE mesh could not be applied and the mesh of voxels was created instead. The finite element 3D model was created and analysed with ABAQUS [144].

Due to the presence of dense metallic phase the dimensions of the Al_2O_3/Cu composite samples that could successfully be replicated with X-Ray micro-CT were very small compared to standard Compact Tension (C-T) test specimens. Therefore, it was decided to model the whole C-T composite specimen using the effective material properties model *V*-*R*-*V* developed in Sec. 5 (*cf*. Fig. 6.38(b)) and inserting a piece of the real composite interpenetrating microstructure in the vicinity of the expected crack growth trajectory, as illustrated in Figs. 6.38 and 6.39. The longer side of the real material piece was positioned along the predicted crack tip front, *i.e*. along the width of the C-T specimen.

The dimensions of the C-T specimen were taken according to the ASTM [179] standard. A cuboid image was cut out of the micro-CT image of cylindrical IPC specimen using the Simpleware ScanIP [8] software. The specimen dimensions were then adjusted to the dimensions of the cuboid image.

The characteristic dimensions of the C-T test specimen resulted from the resolution of the micro-CT device and the voxel size of 9.12 μm, and were as follows: W = 14.7 mm, A = 7.12 mm, width of the C-T test specimen: B = 7.35 mm (see Fig. 6.38(a)). The real composite cuboid piece in the vicinity of the crack tip was composed of two cuboids cut out from the same composite piece. The

composite piece had to be divided into two parts because of the size limitations of the micro-CT equipment. Consequently, two separate micro-CT images of these two pieces were obtained. From each of these images a cuboid of the dimensions of 60×60×403 voxels (0.547 × 0.547 × 3.67 mm) was extracted. Both cuboid pieces originated from the material parts separated with the distance of approx. 0.5 mm. Finally, from these two cuboids one cuboid piece of IPC was composed by shifting them next to each other. The dimensions of the resulting cuboid IPC piece were: 60×60×806 voxels (0.547 × 0.547 × 7.35 mm).

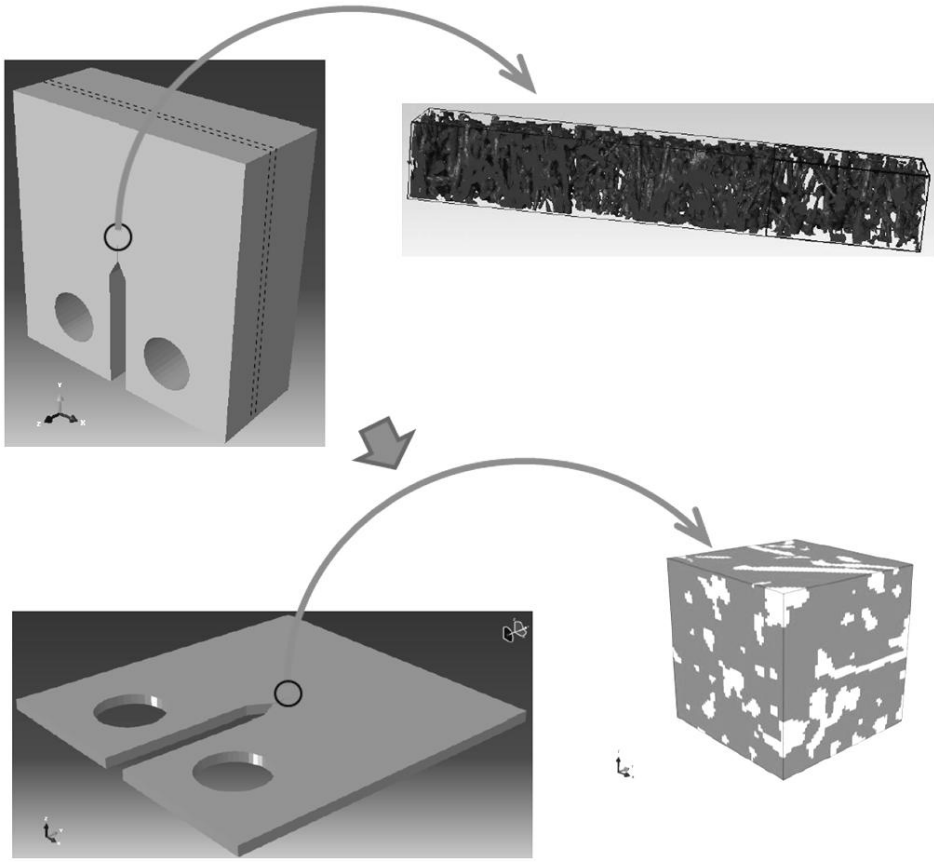

Figure 6.39. Schematic diagram of the real IPC microstructure model with submodelling applied to reduce the problem size.

In numerical simulations due to a large number of elements in the C-T test model with IPC microstructure, a submodelling had to be applied with a global model of the effective material and the real composite microstructure in the crack tip vicinity. The idea of submodelling is presented in Fig. 6.39. The displacement field

was taken from the surface of the boundary of real microstructure piece in the global model, and applied as the boundary conditions on the real material piece (*cf*. Fig. 6.41). Since the model is huge it was impossible to be solved with the available hardware capabilities. As a way out a slice of 60 voxels wide was cut out of the whole C-T test specimen and taken for calculations, as depicted in Fig. 6.39.

The slice cut out of the whole C-T test specimen had the outer dimensions (W and A) of the global C-T test model, with width of the diminished C-T test specimen: B^{slice} = 0.547 mm. The cube with real microstructure had the dimensions of 60×60×60 voxels (0.547 × 0.547 × 0.547 mm). The size of the microstructure volume taken for the analysis was limited by the available computational resources, which did not allow to perform the analysis of the representative volume element (RVE), as described in Subsec. 5.2.3.

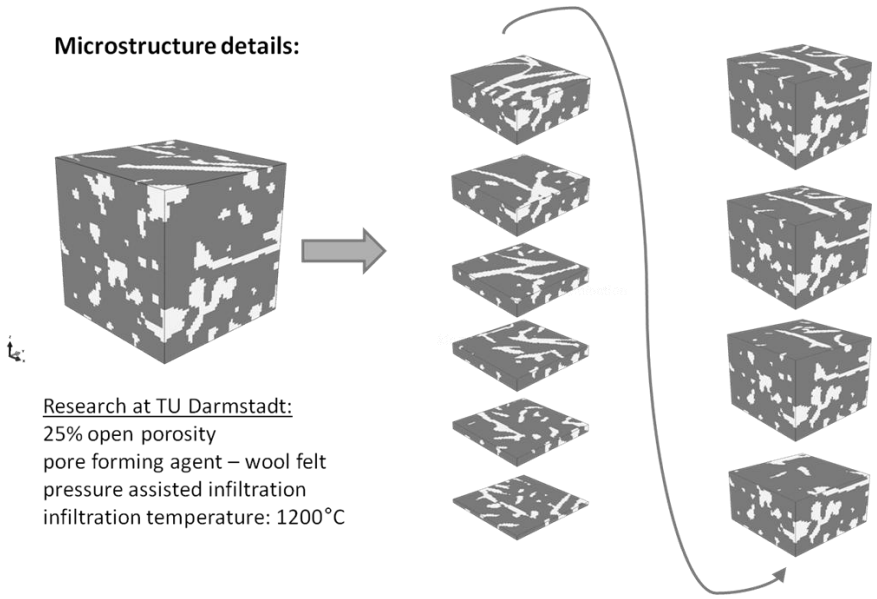

Figure 6.40. Details of the microstructure of real IPC [97] cube - horizontal cuts through the piece from bottom to top, with visible bridging ligaments and interconnections between fibres.

The FE mesh of the outer, global model part of the Compact Tension test specimen had to be fine-tuned to the size of the elements of the submodel. This caused large difficulties in the FE mesh design, compromising between the necessary very fine element size in the regions near the real material piece and near the loading and the boundary conditions application surfaces (pin holes), and the

need to optimize the mesh size in the less important areas. The FEM model for the global model part of the Compact-Tension "sliced" specimen had 778746 nodes, 730322 solid 8-node C3D8 elements, and 2282964 variables. The FEM model of the real microstructure cube part of the Compact Tension test "sliced" specimen had 433483 nodes, 216000 solid 8-node C3D8 elements, and 1300449 degrees of freedom. The details of the real microstructure cube are shown in Fig. 6.40, in which the horizontal cuts through the piece from bottom to top with bridging ligaments and interconnections between fibres, are visible.

The material models of the composite phases were described in [89] and also in the previous Subsections treating the single axisymmetric fibre pullout/reinforcing fibre with debonding evolution. The ceramic Al_2O_3 phase was modelled as isotropic elastic, the metallic Cu phase was modelled as isotropic elastic-plastic undergoing large plastic deformations. In the elastic-plastic model applied for the copper phase the J_2 flow plasticity and isotropic hardening model was used and implemented in ABAQUS [144]. The J_2 plasticity constitutive equations were integrated with the stress update algorithm. Large strains that might locally take place, were determined with an incremental algorithm. For the models with isotropic yield function, the spectral decomposition made possible the use of the return mapping procedure. Material parameters used for calculations are shown in Table 6.7.

Table 6.7. Material parameters used in calculations.

	Al_2O_3	Cu
E_m, E_f [GPa]	390.0	110.0
ν_m, ν_f	0.2	0.35
σ_0 [MPa]	-	50.0
n	-	5.8

In order to model the material discontinuities represented in finite elements as the embedded discontinuities, the Extended Finite Element Method (XFEM), introduced by [141] and developed further among others by [142] was used (*cf.* Subsec. 3.4). The XFEM was employed to model crack propagation in the elastic ceramic phase. At this stage of the model development it was assumed that copper ligaments may deform plastically but their damage and final rupture was not included in the analysis.

Using ABAQUS [144] it is possible to model damage initiation and damage evolution. The damage initiation criterion can be expressed in terms of maximum nominal stress MAXS or maximum principal stress, maximum nominal or principal strain, maximum separation displacements, or with their quadratic interaction functions. In the present numerical model the MAXS criterion is used for damage initiation in ceramic elements and at cohesive interfaces. According to [14] or [180], the value of flexural strength of dense alumina at room temperature varies between 330-430 MPa. For present modelling purposes the damage initiation stress in alumina was assumed to be 300 MPa. The ENERGY criterion for the damage evolution in ceramic elements is defined in terms of the fracture energy that is required for the element total failure. The energy required for fracture in the mixed mode is expressed as a power law.

A displacement-controlled quasi-static loading was applied to make the crack growing. During laboratory C-T tests the boundary conditions and the loading were applied at roller pins. In the present model the boundary conditions and the loading were applied to the C-T test specimen as a pressure on the pin holes surfaces. One of the pin holes was kept fixed to simulate real C-T test conditions. The displacement u from 0.0 to 0.25 mm was applied at the other pin hole. The boundary conditions and the loading are depicted in Figs. 6.41 and 6.43a.

The model with FE mesh is depicted in Fig. 6.41. The pre-crack tip was assumed as sharp (with zero radius). The crack tip angle was of the order of 0.03 rad (Fig. 6.42). The initial opening angle of the simulated crack developing in the real material piece was 0.0 rad (there was no pre-crack in the real material). The applied displacements were small, hence the opening angle in the real material piece did not grow substantially.

The results obtained with the global model of the C-T test are presented in Fig. 6.43 for selected displacement, stress and strain fields. The results for the submodel with the real IPC microstructure in both ceramic and metal phases are shown in Fig. 6.44.

The calculations were made with ABAQUS [144] software using multiprocessor computer cluster GRAFEN at the Institute of Fundamental Technological Research of the Polish Academy of Sciences. Supplementary calculations were performed at High Power Computers Centre of Interdisciplinary Centre for Mathematical and Computational Modelling (ICM KDM) of the University of Warsaw. The calculations of both models: global model and submodel, due to their large sizes, needed considerable computation time.

a) b)

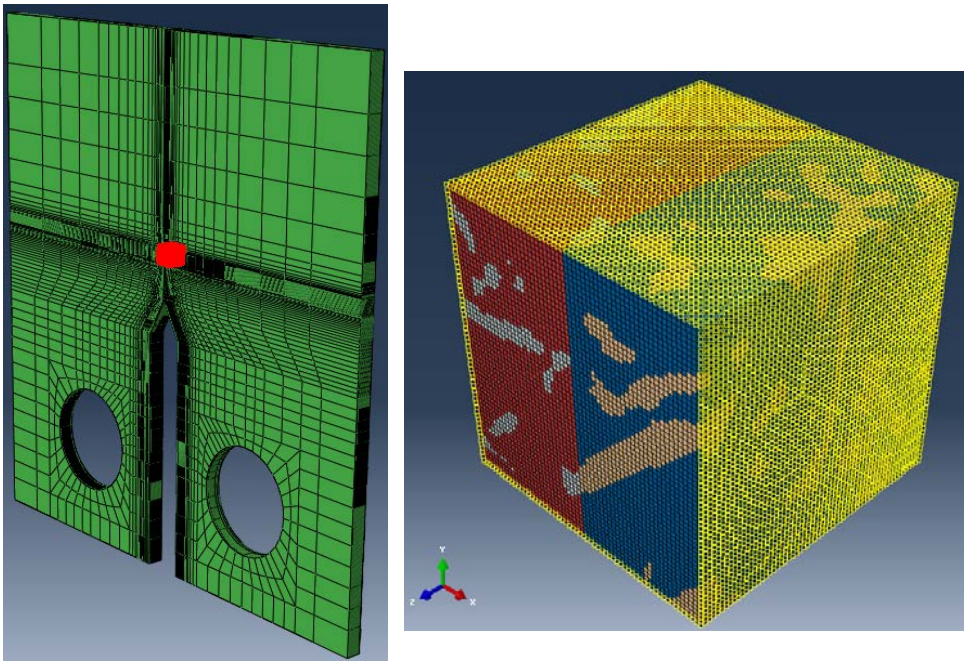

Figure 6.41. The FEM model for C-T test with account of real IPC microstructure developed in ABAQUS [144]: (a) outer, global model of C-T specimen with effective elastic properties, node set from which displacements are taken for the submodel marked in red, (b) submodel of real Al_2O_3/Cu IPC microstructure obtained with micro-CT imaging (displacement boundary conditions marked in yellow).

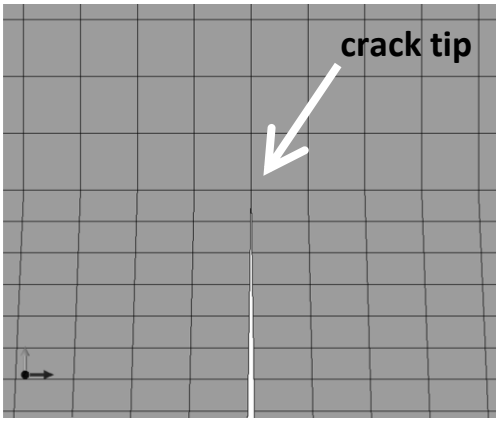

Figure 6.42. The shape of pre-crack tip.

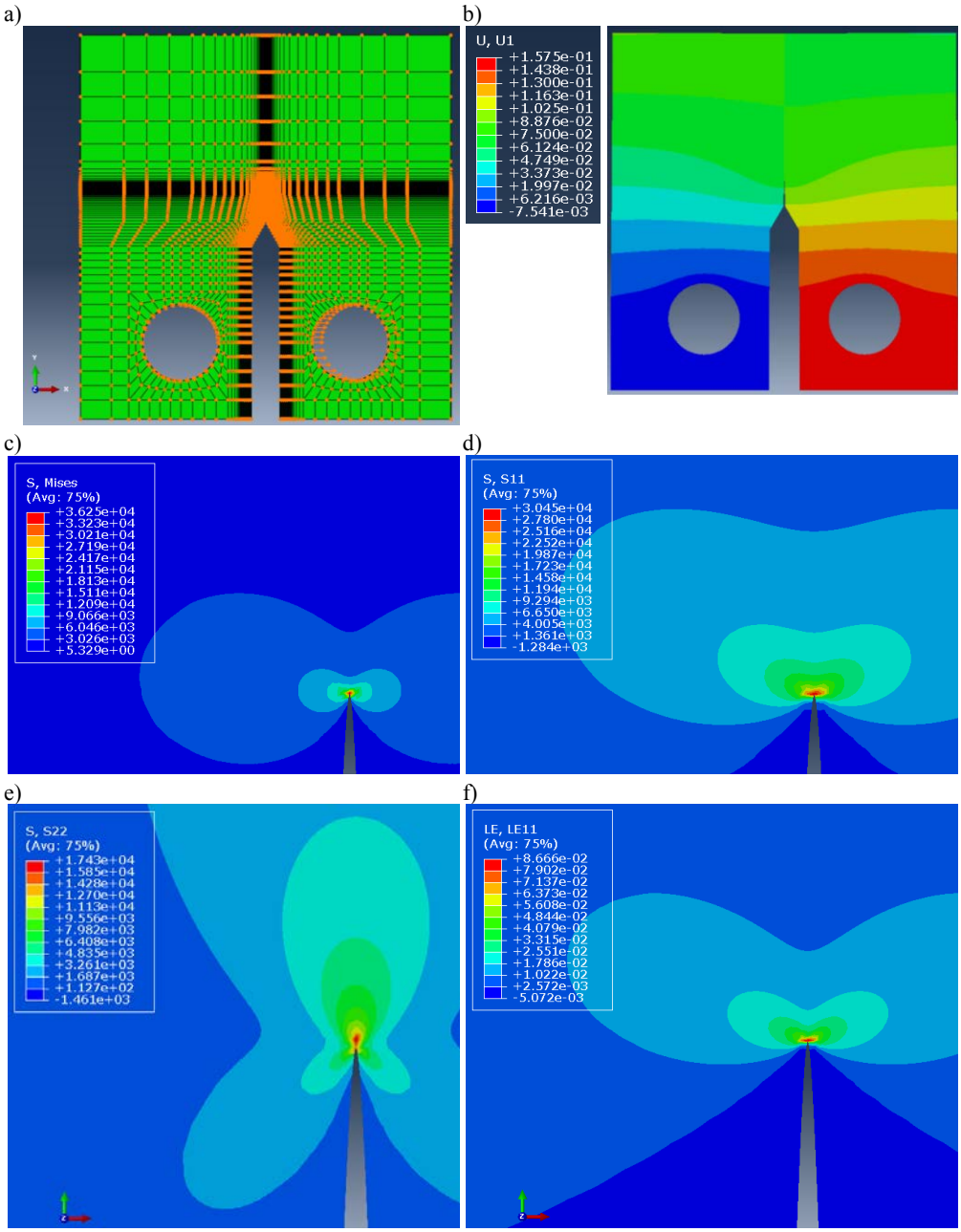

Figure 6.43. (a) Boundary conditions and (b-f) selected results from the global model of the C-T test at applied $u_1 = 0.157$ mm: (b) displacements in the loading (horizontal) direction u_1, (c) von Mises stresses in the crack tip vicinity, (d) stresses in the loading (horizontal) direction in the crack tip vicinity, (e) vertical stresses in the crack tip vicinity (all stresses in MPa), (f) logarithmic strains in the loading (horizontal) direction in the crack tip vicinity.

a)

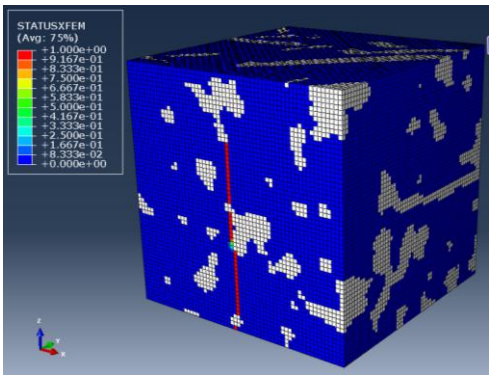

b)

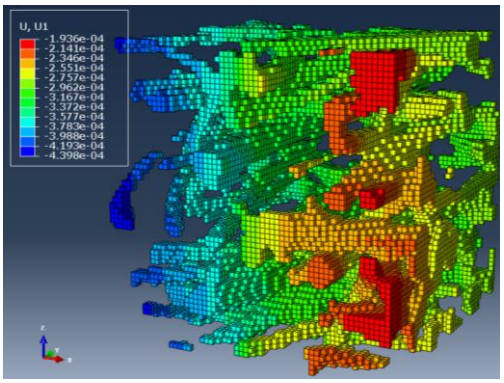

c)

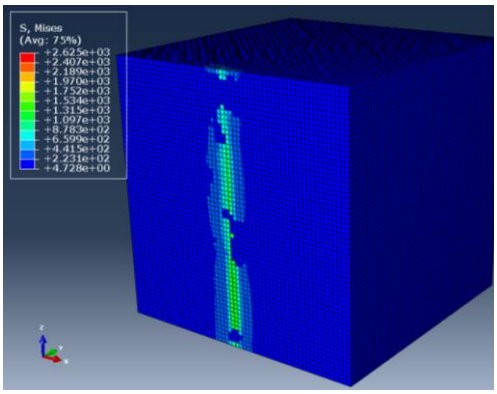

d)

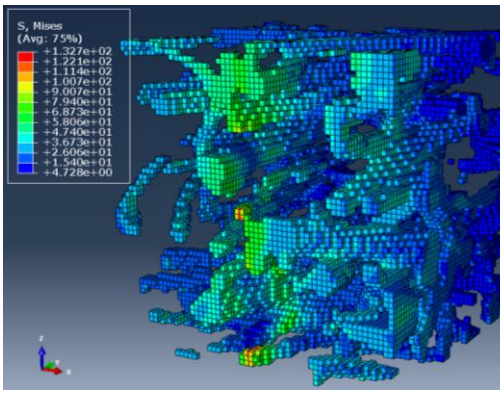

e)

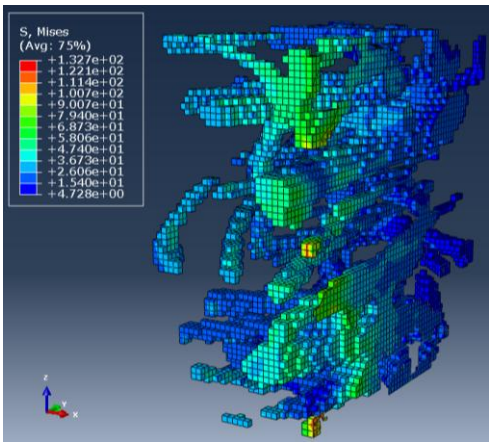

f)

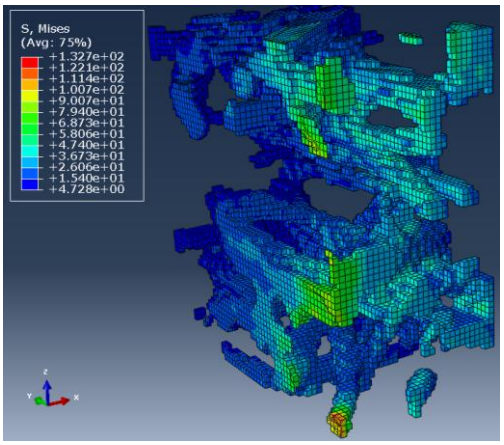

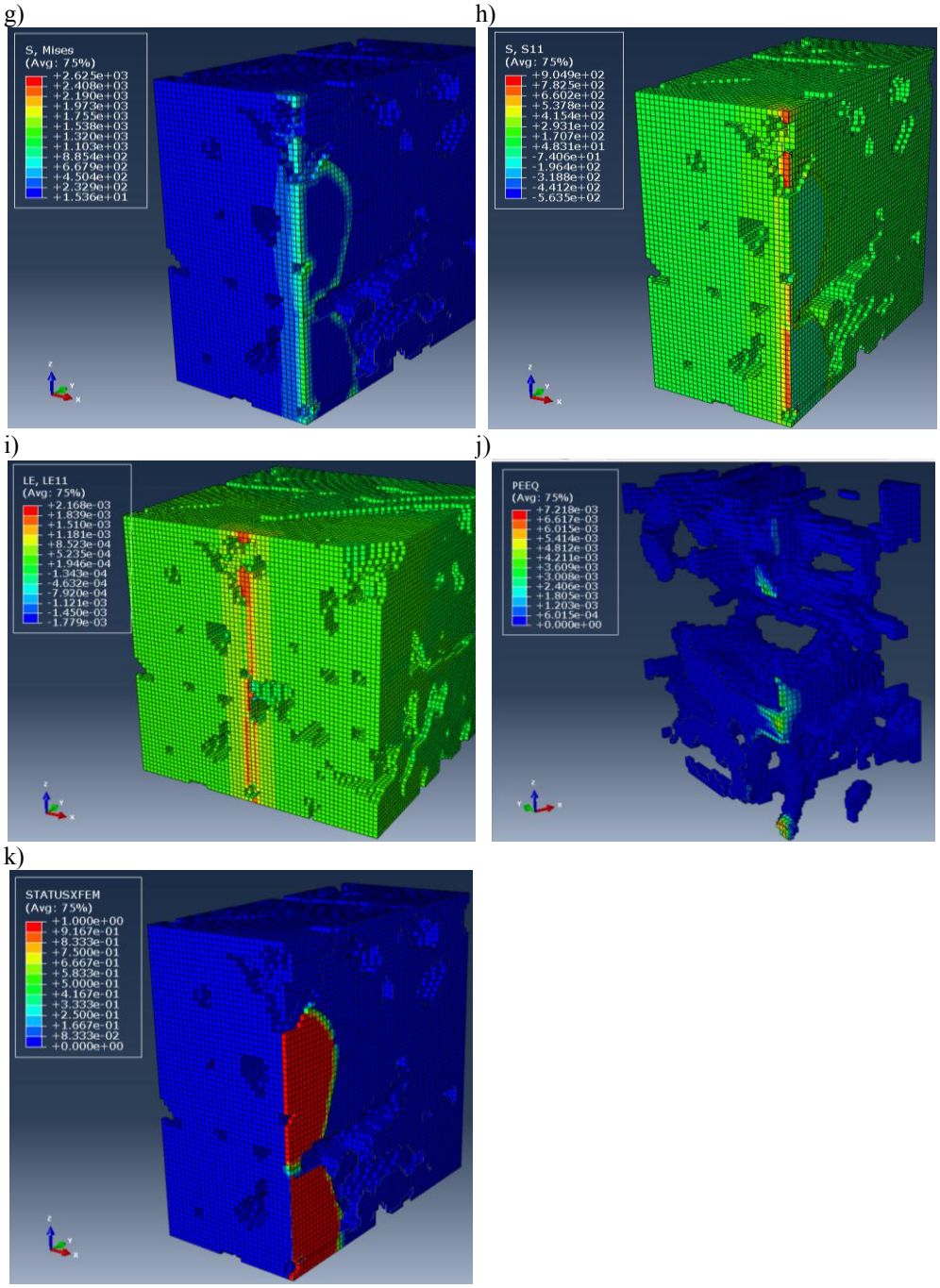

Figure 6.44. Selected model results obtained for the real IPC piece: (a) propagated crack marked with red (white – copper phase), (b) displacements in the loading direction in the

copper phase, (c-g) von Mises stresses, (d-f) - in the copper phase, (e) – left half, (f) – right half, (g) –left half of the ceramic phase, (h) stresses in the loading direction in the ceramic phase (all stresses in MPa), (i) logarithmic strains in the loading direction in the ceramic phase, (j) plastic equivalent strains in the copper phase (right half), (k) propagated crack marked with red in the ceramic phase (left half).

The *J*-integral was calculated along the crack front at 25 contours using ABAQUS [144] procedure. The *J*-integral values were taken for contours contained within the ceramic phase. These values rose gradually to saturate at the 11^{th} contour, which was then chosen for calculations. The calculated *J*-integrals vs. crack length increase Δa are presented in Fig. 6.45.

From the numerical results depicted in Fig. 6.44 it can be seen that the applied displacement loading caused stresses in the middle plane of the IPC piece initiating crack propagation in the ceramic phase and plastic yielding in the copper phase. The calculations were stopped when the time increment was lower than the minimum allowed. The propagated crack length reached approximately 0.1 mm.

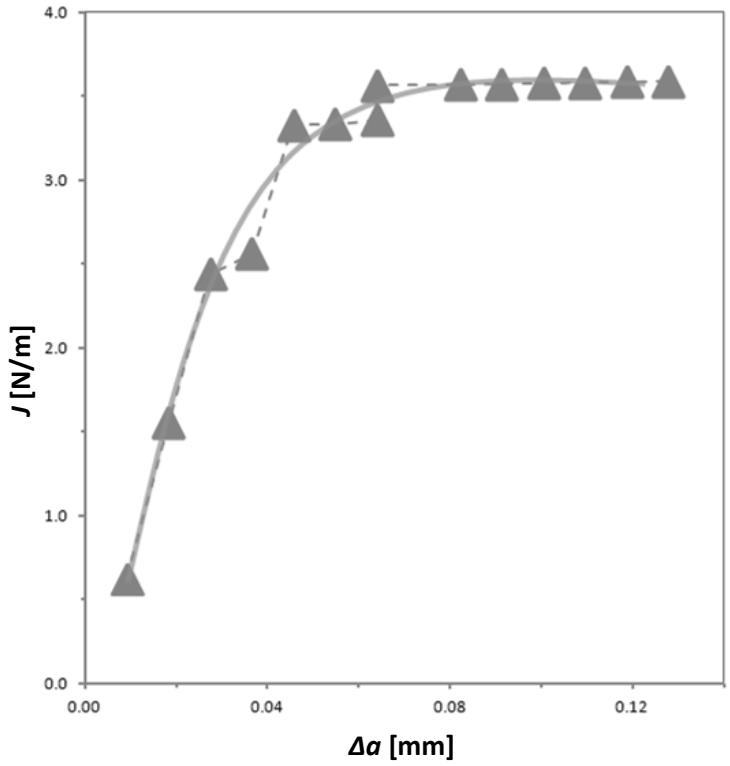

Figure 6.45. *J*-integral vs. crack length extension (reprinted with permission of *Advanced Engineering Materials)*

The results of *J*-integral calculations for the 3D case, recently published in [139], are presented in Fig. 6.45. They represent the very beginning of the crack propagation process as the crack has grown up to 0.1 mm, only. The convex shape of $J(\Delta a)$ curve for the 3D case (Fig. 6.45) is different than the concave shape obtained for the 2D case (Fig. 6.32). On the other hand since the 3D crack front has grown only by a small size increment, the plateau reached in Fig. 6.45 may correspond to the initial part of the $J(\Delta a)$ curve in the 2D case, which assumes a concave shape as the crack keeps growing. A more plausible interpretation of different characters of $J(\Delta a)$ curves may be attributed to the effect of three-dimensionality that favours less steep increase of the *J*-integral and its tendency to reaching a plateau.

The numerical predictions of the *J*-integral in the 3D case are in qualitative agreement with the experimental results reported by [181] for gas pressure infiltrated α-Al_2O_3 preforms with liquid high purity Al and Al/Cu2% alloy, measured in the Compact Tension test. Even though the microstructure of their composites differs from the interpenetrating microstructure considered in the present model the crack behaviour represented by the *J*-integral vs. crack extension curves is very much the same in shape. An explanation for this observation can be sought in similar crack toughening mechanisms. However, this statement needs further studies to be claimed true.

7

Summary, conclusions and future research

The objectives of the research presented in this dissertation were twofold: (i) to propose analytical and numerical models for estimation of the macroscopic mechanical properties, and (ii) to propose numerical models for deformation and fracture capable of determination of the fracture parameters of novel metal-ceramic composites with interpenetrating microstructure (*interpenetrating phase composites*, IPCs).

A number of different analytical and numerical models have been developed for the effective material properties and the fracture related parameters of the IPCs. In what follows a concise account of these models will be given with the **original elements highlighted**, wherever relevant.

Mishnaevsky [42,140,153] codes were used to model in two dimensions the effective elastic properties of a particle-like microstructure and of a cross-like microstructure. The particle-like microstructure was compact in shape, while the cross-like microstructure was branched. The results were compared to the Voigt and Reuss estimates in order to examine the influence of the microstructure on the macroscopic properties of IPC materials.

The effective elastic constants: Young's modulus, Poisson's ratio, bulk and shear moduli, related to the volume fraction of the phases, were estimated on the examples of Al_2O_3/Cu and Al_2O_3/Al interpenetrating phase composites, using models based on the decomposition of the cross unit cell mimicking an interpenetrating microstructure. The analytical models of Voigt, Reuss, [17,18] and [22] were applied. Extensions of [17,18] and [22] models were proposed, as derived from the eigenmoduli of the stiffness tensor (bulk and shear moduli), which is a **novel approach**. A third way of unit cell division was implemented, which is also an **original contribution** to the IPCs' effective properties estimation. Young's

modulus, bulk modulus, shear modulus and Poisson's ratio were predicted with the novel extended models.

Three **new analytical models**, based on three directions of decomposition of the cross unit cell, derived from the eigenmoduli of the stiffness tensor, were developed for estimation of the overall coefficient of thermal expansion (CTE) of IPCs.

Two **original numerical methods** were developed for estimation of the effective elastic constants of IPC materials: (i) method for the simplified microstructure of three-dimensional cross, and (ii) generic method for real IPC microstructures based on three-dimensional microstructure images obtained with computed microtomography (micro-CT). For two-phase three-dimensional cross microstructure model, the whole range of phases' volume fractions were addressed. For the generic method for real microstructure, two different Al_2O_3/Cu IPCs of different microstructures and copper volume fractions were modelled. Two kinds of finite element meshes were created for this method: a voxel type mesh and a mesh with smoothed boundaries between phases containing both hexagonal and tetragonal elements.

The analytical and numerical modelling of the effective elastic properties and fracture of IPCs was enriched with experimental investigations of IPCs of different microstructures. Preparation of IPC samples together with analysis of the influence of different processing parameters on the resulting materials' microstructure and properties, measurements of the elastic properties in RT and in thermal cycles, and observations and measurements of fracture in IPCs, were performed. The results of experimental measurements were further compared with the results of analytical and numerical models of the effective elastic properties and fracture of IPCs. They also served as a basis of modelling assumptions and necessary simplifications.

The modelling of fracture parameters and crack evolution in IPCs, which constitutes the second main part of this thesis, was preceded by experimental observations of crack propagation and fracture surfaces, and measurements of fracture toughness. A set of models were explored in order to finally determine the increase of the fracture toughness that occurs in IPC composites due to crack bridging. The prerequisite models of a single elastic-plastic fibre reinforcing elastic matrix were developed in order to determine the stress-displacement characteristics in the reinforcing ligament, necessary for the determination of the *J*-integral in the whole composite. Numerical models of the Compact-Tension tests were developed in two and three dimensions. The Compact-Tension test was modelled in three

dimensions for the real IPC microstructure obtained from micro-CT images. The *J*-integral was calculated for two- and three dimensional cases.

The deformation mechanisms of IPCs including large plastic deformations and necking of metal ligaments, delamination of reinforcements from the matrix, and crack bridging was determined using the **finite element models originally developed** within this thesis. The 2D model of a skew reinforcing fibre, inspired by the experimental investigations of [94], enabled analysis of the deformation of either elastic-plastic copper reinforcement embedded in elastic alumina matrix, or conversely, of elastic reinforcement in elastic-plastic matrix. The influence of the nondimensional debonding parameter on the force – displacement characteristics was examined in detail.

The stress – displacement curves for elastic-plastic reinforcing fibres were obtained for Al_2O_3/Al and Al_2O_3/Cu composite systems with the finite element model of an axisymmetric elastic-plastic metallic fibre in an elastic alumina matrix, undergoing large plastic deformation and necking. The influence of fibre-matrix debonding on the σ-u characteristics was also analysed with this model.

A finite element model of the fibre pullout, being an **original extension** of the model of [82] by introducing the elastic-plastic model for the fibre, was proposed. The model accounted for the large plastic deformation and necking in the fibre and for the evolution of fibre debonding from the matrix. The purpose of the fibre pullout model was the identification of the interfacial material properties which could subsequently be used in the numerical determination of *J*-integral for IPCs. This systematic approach to model parameters identification in numerical modelling of *J*-integral in IPCs can be seen as another original element of the thesis.

A **novel finite element model** was developed for an axisymmetric reinforcing fibre with the evolution of fibre-matrix debonding. The model was intended to help understand the mechanism of crack bridging in real IPC materials. The material parameters used for Al_2O_3/Cu composite, including those of the cohesive interface, were assumed the same as for the pullout model. The stress – displacement characteristics obtained from this model were compared with the results of pullout model and with analytical results of [93], reflecting well the behaviour of the reinforcing fibres in Al_2O_3/Cu IPC observed in experiments by [182].

Numerical models were proposed for the determination of the energy release rate increase ΔG due to crack bridging mechanism in IPCs. Two-dimensional numerical models for the Compact-Tension (C-T) test were developed in several variants. Different techniques of modelling of the reinforcing fibres and propagation

of the crack were used to determine the *J*-integrals. The two-dimensional original models include the C-T test model with a skew reinforcing elastic-plastic copper fibre embedded in an elastic alumina matrix and the C-T test model with multiple elastic-plastic copper fibres embedded in an elastic alumina matrix. For the case with multiple bridging fibres and quasi-static crack propagation, the *J*-integral related to the crack length increase Δa was numerically determined.

The **original three-dimensional finite element models of the Compact-Tension** (C-T) test included the model for a simplified composite microstructure with cylindrical fibres and the model of a real composite microstructure obtained from microtomography (micro-CT) experiments. Submodelling was applied in the case of the real IPC microstructure due to the large size of the problem. Additionally, it was necessary to cut out a slice from the model of the C-T specimen. The submodel of a vicinity of the crack tip was made of the cube of voxels with real Al_2O_3/Cu IPC microstructure obtained from micro-CT scans, according to the original modelling scheme (*cf.* Sec. 5). The alumina ceramic phase was modelled as elastic with possibility of initiation and evolution of damage using the Extended Finite Element Method (XFEM). The copper metallic phase was modelled as elastic-plastic undergoing large plastic deformations. The global model consisted of the linear elastic material with effective properties of the investigated Al_2O_3/Cu IPC estimated with the **newly developed methods described in Sec. 5.** The global model was subjected to quasi-static loading and the resulting displacement field from the area bounding the submodel was applied at the submodel as the boundary conditions. Under the applied quasi-static loading, the crack propagation was modelled in the ceramic phase of the submodel. The *J*-integral was calculated in function of the crack length Δa.

The main objectives of this dissertation have been achieved with the mentioned above analytical and numerical models of metal-ceramic IPCs, aiming at prediction of the overall elastic properties, deformation mechanism with account of large plastic deformations of the metal phase, debonding of the reinforcement from the matrix and crack bridging, as well as the macroscopic fracture parameters and crack evolution in real IPCs with microstructure modelled by means of micro-CT images. The results of the analytical and numerical models were compared not only with the existing results from the literature, but also with the experimental results obtained within this work during research stays abroad. The analytical models estimating the overall elastic properties of IPCs, compared with the experimental measurements, enabled fast finding of a microstructure with the optimum properties. The main phenomena occurring in real IPC materials, such as interconnections between fibres,

debonding, skew fibres, contact between delaminated fibre and matrix, or interaction between bridging fibres, were addressed.

The main theses of this dissertation formulated in Sec. 4 have been verified and confirmed. The influence of the composite microstructure on the effective elastic properties was shown using Mishnaevsky [42,140,153] codes and significant differences between the effective elastic properties for different microstructures in planar case were disclosed. The results obtained for particle-like microstructure were closer to the upper Voigt estimate, while the results for cross-like microstructure had lower values, closer to the Reuss estimate, confirming the strong influence of the microstructure on the macroscopic properties of IPC materials. The microstructure influence on the effective elastic properties was visible also when the experimental results of Young's modulus measurements were compared for different IPC microstructures (*cf*. Appendix).

The analytical models of the effective elastic constants (*i.e*. the extensions of the [17,18] and [22] models and the model based on the third way of unit cell division), for both Al_2O_3/Cu and Al_2O_3/Al IPC composites, together with the numerical models based on the three-dimensional cross-like microstructure and of the real Al_2O_3/Cu microstructure obtained from micro-CT experiments fit between the Voigt and Reuss bounds. Two Al_2O_3/Cu IPCs of different microstructures and copper volume fractions were modelled using the **newly developed generic numerical methods** for estimation of the effective elastic and thermal constants of real IPC composites, with the use of 3D microstructure images obtained from the computed microtomography (micro-CT). These numerical procedures enabled analyses of different actual microstructures and their influence on the macroscopic IPC properties. The main difficulty when modelling the real IPC microstructure obtained from micro-CT was the large size of finite element meshes requiring long computational time and the necessity to divide the real material piece into a number of smaller parts, and then performing calculations for each of them separately. However, the latter task was partially automated with a FORTRAN code.

The overall coefficients of thermal expansion (CTE), calculated according to the proposed models for Al_2O_3/Cu and Al_2O_3/Al IPC composites, were contained within the Rosen and Hashin [38] bounds.

By comparison of the results of analytical and numerical modelling of the overall elastic constants and of experimental measurements at room temperature, fast identification of a microstructure providing optimum properties is possible.

The proposed numerical models accounting for large plastic deformations and necking of metal ligaments, delamination of reinforcements from the matrix, and crack bridging toughening mechanism have proven their capability of reflecting the phenomena that may occur in real IPC materials. The difficulties with these models included the lack of necessary material properties of the interfaces, large size of the models causing long computational times and numerical instabilities that might occur due to damage in the cohesive interface.

Numerical models using micro-CT scans of real IPC microstructures and a commercial software to automatically generate FE mesh were proposed as a **ready to use computational tool** for the investigation of crack propagation in IPCs. As compared with the results for the two-dimensional case, the resulting *J*-integrals were obtained for the initial stage of the crack propagation process, thus different shapes of the characteristics were obtained in 2D and 3D cases. In particular, for the three-dimensional case a less steep increase of the *J*-integral was noted. Excessive computational time was needed to perform calculations for the real microstructure model. The use of high power computers was necessary and even then the computations of the single calculation process (global model and submodel) for only a slice cut out of the C-T specimen, required a very long time. Moreover, due to specifics of the crack propagation and *J*-integral calculations, it was impossible to perform calculations in parallel on multiple processors to speed them up. Nevertheless, the obtained results were in qualitative agreement with the results obtained by [181] for similar composite materials.

The use of computed micro-tomography images in the proposed numerical models makes them a versatile modelling tool for different microstructures with no need to make any simplifying assumption as to the geometry of reinforcements that are usually made in micromechanical models of composite materials. With the analytical and numerical models developed in this thesis the overall elastic properties, deformation and fracture parameters of IPCs may be predicted supporting complicated and costly experimental measurements, at the same time reflecting the most important characteristics of the IPC microstructure and providing reliable results.

Directions of future research shall include analytical and numerical estimation of the effective elastic constants of IPCs taking into account a material anisotropy using definitions of the directional stiffness constants given by [146], expansion of the numerical models for other material phases like porosity, impurities or interfaces, or incorporation of plasticity and large deformations in metallic phase in modelling of the overall mechanical properties of IPCs. The IPCs with

microstructures based on corn or rice starch PFA, which had shown promising characteristics in laboratory measurements in thermal cycles with almost no microcracking upon cooling and good shape stability, should be further investigated experimentally in elevated temperatures. Unforeseen behaviour of IPCs with microstructures based on natural wool PFA observed during high temperature cycles, also renders these composites valuable for further examinations.

The pullout tests and Ashby *et al*. [133] tests of a single reinforcing fibre, would be highly recommended to experimentally determine the alumina-copper interface properties during crack bridging and pullout, and to apply these results in the respective numerical models.

As for the models of the determination of the energy release rate increase due to bridging in the compact tension test, introduction and calculation of the configurational crack tip forces according to the theoretical basis described by [121], would be important. Also further effort should be invested in (i) performing calculations for the global model with crack propagation that yield more realistic displacement fields for the submodel, (ii) performing calculations for the whole C-T specimen and for the larger real material piece enabling longer crack propagation, or (iii) introduction of the cohesive interface. Analyses of the computations paralleling for the Compact Tension test model would also be necessary, as well as the experimental characterization of the fracture parameters to validate the numerical models.

A

Appendix. Experimental background for the models developed in the thesis

This Appendix provides a concise overview of the manufacturing methods of interpenetrating phase composites (IPCs). It also contains results of own experimental work on IPCs manufacturing and characterization that are beyond the main theme of thesis, which is modelling, but contribute to a better understanding of the material properties and fracture mechanisms considered in the main text.

A1. Manufacturing of interpenetrating phase composites: an overview

The commonly used methods of IPC manufacturing are based on pressure-assisted or pressure-less infiltration of molten metals into ceramic preforms (*cf.* [3,15,97]). Preform preparation techniques including sintering of coarse powders, foam based methods, or methods using sacrificial pore forming agents are described in [183] followed by a detailed parametrical analysis of the infiltration process. The gas pressure infiltration of liquid metallic phase into a porous ceramic perform is a commonly used fabrication technique of IPCs. The ceramic preform may form a random porous network of a sintered aluminum oxide or contain hollow parallel channels or regular grids if special processing techniques are applied [20]. In what follows a set of representative works with different processing techniques of IPCs will be briefly discussed and examples of IPCs' essential mechanical properties will be given.

Clarke [184] investigated processing and properties of interpenetrating phase composites defined as multiphase with each phase topologically interconnected throughout the microstructure. Manufacturing and characterization of titanium trialuminide (Al_3Ti) / aluminium (Al) metal-intermetallic interpenetrating composites was presented by [185]. Processing techniques of glass-containing IPCs

were reviewed in [83]. Scherm *et al*. [86] manufactured interpenetrating lightweight metal matrix composites, based on porous Al_2O_3 ceramics infiltrated with aluminum alloy AlSi9Cu3. The ceramic preforms were produced by cold pressing of fine grained ceramic alumina powders with pyrolysable pore formers, followed by burnout and partial sintering. Porous preforms were die casted with Al alloy. Both metal and ceramic phases were distributed isotropically. Mechanical characterization was performed in tensile and compression tests. Thermal properties such as thermal diffusivity (conductivity), coefficient of thermal expansion and specific heat capacity were also measured. The strengthening mechanisms such as stress transfer from metal matrix to the ceramic reinforcements, dislocation strengthening, and refinement of the metal grain size, were identified. The composites showed enhanced mechanical properties compared to the matrix alloy: ultimate tensile strength and Young's modulus but were slightly less ductile. Strong bonding between ceramic and metal was observed on fracture surfaces of tensile specimens.

Hemrick *et al*. [186] investigated low and high temperature fabrication methods of nano-scale IPCs. Infiltration of metal (Cu, Al or alloy) into a nanoporous ceramic matrix (alumina, silica or titania) was one of the routes for low temperature processes. Low temperature co-sintering of mixed ceramic and metallic nanopowders, infiltration of metal into nanoporous cellular ceramicss or ceramic nano-foams, and co-formation of bi-continuous block copolymer microphases with ceramic and metal precursors were also evaluated as methods to produce improved nano-scale IPCs. The influence of the composition on the mechanical strength was examined.

Hein [187] used the powder injection moulding method to fabricate metal ceramic interpenetrating composites. Different material combinations were tested and the produced materials were characterised in terms of density, mechanical properties and microstructures. The advantage of the powder injection moulding method is the ability to produce near-net shape parts in large quantities.

Sun *et al*. [84] developed an Mg-based metallic-glass/titanium IPC exhibiting enhanced mechanical performance: high fracture strength of 1783 MPa and large fracture strain of 31%. The composite was manufactured with pressure assisted infiltration of a Mg-based metallic glass alloy into a porous titanium with a pore size of 30-200 μm and nominal porosity of 30%. The composite samples were tested in quasistatic compression test. The IPC fractured at 1783 MPa, compared to 800 MPa for porous titanium and 825 MPa for BMG alloy. The microstructure of the manufactured IPC materials was examined using different microscopy techniques. Shear bands in the specimens that underwent compression to the preset strains were

observed. It was concluded that the interpenetrating microstructure had a highly positive influence on the mechanical properties of the composite. The interpenetrating microstructure ensured throughout constraint of the shear bands propagation, promoted homogeneously distributed local shear deformations and decentralized the deformation of the composite, and also introduced a mutual reinforcement between metallic glass and titanium.

Roy *et al*. [87] investigated internal load transfer and compressive damage evolution in an interpenetrating $Al_2O_3/AlSi_{12}$ composite. The composites fabricated by squeeze-casting of eutectic aluminium–silicon alloy melt in a porous alumina preform, were investigated in micromechanical load partitioning between the three phases of the composite. The failure of the composite occurred by propagation of cracks in the regions rich with the ceramic phase.

In the work of Kailash [188] interpenetrating polymer networks were investigated, with particular emphasis on fracture behaviour in tensile, quasi-static and dynamic tests. Both quasi-static and dynamic tests showed decrease of fracture toughness with the decrease of the volume fraction of the stiffer PMMA phase. In quasi-static tests the stability of the crack and fracture toughness depended on the volume fractions of the components. The quasi-static fracture toughness had an optimum for higher volume fractions of PMMA.

Moro and Solomon [189] designed and manufactured IPCs for vibration damping. The novel shape memory alloy-ceramic composites using reactive metal penetration technique, were produced. Mu *et al*. [190] developed a Ti/Ti-based-metallic-glass interpenetrating phase composite (IPC) by infiltrating $Ti_{34.3}Zr_{31.5}Ni_{5.5}Cu_5Be_{23.7}$ melt alloy into porous Ti preform. A mutual reinforcement effect, for both amorphous and crystalline phases was observed during characterization of the composite.

Chang H. *et al*. [85] investigated the effects of the dynamic impact load at high velocities on Al-Mg/Al_2O_3 IPC coatings of Al backing. The coatings were manufactured using pressureless infiltration of Al_2O_3 foams of densities in the range of 15-30% and of approximately 25-75 μm cell radii. Split Hopkinson's Pressure Bar (SHPB) and Depth of Penetration (DoP) methods were used to acquire ballistic properties of IPCs. The tests showed that IPCs themselves cannot sustain the impact of high velocity armour piercing rounds. On the other hand, when covered with the dense Al_2O_3 front layer of 4 mm thickness, no penetration into Al backing was observed and the specimen remained unbroken. Moreover, there was no delamination between ceramic front and IPC. The bridging of the crack with the

metal phase was observed, which must have contributed to the structural integrity and composite performance. The authors concluded that IPCs, whilst inappropriate to use as a front face to resist dynamic impact load, backed dense Al_2O_3 front very effectively and provided well-performing and impact-protecting interlayer phase between Al_2O_3 front and Al backing. That could be due to the reduction in the acoustic impedance mismatch between Al_2O_3 and Al, provided by the IPC layer.

A2. Fabrication of IPCs by pressure assisted infiltration: results of own research work

The aim of this Subsection is to show experimental investigations and comparison of the influence of different parameters of manufacturing on the resulting microstructure, mechanical and thermal characterisation of Al_2O_3/Cu composites.

A process of pressure assisted metal infiltration of ceramic preforms will be presented which was carried out at the Institute of Materials Science, TU Darmstadt, Germany during the research stay of the author at the TUD in the framework of KMM-NoE[1] project, as supervised by Dr Jami Winzer, Dr Ludwig Weiler and Prof. Jürgen Rödel.

The gas pressure infiltration technique was used to obtain dense interpenetrating phase composites Al_2O_3/Cu. The pore networks were obtained using different types of starch as the pore forming agents. Microscopic analyses showed that a rice starch based composite microstructure is finer and more uniform than the microstructure based on a corn starch. Composite samples were made out of 30%, 50% and 60% porosity preforms. The complete manufacturing process comprised (i) preparations of slurries from alumina powder and starch, (ii) preparations of porous alumina bodies from cast slurries, (iii) sintering of alumina bodies to obtain porous ceramic preforms, and finally, (iv) fabrication of the composite by gas pressure infiltration of alumina preforms with molten copper [182].

[1] KMM-NoE was a Network of Excellence in the 6th EU Framework Programme entitled „Knowledge-based Multicomponent Materials for Durable and Safe Performance" coordinated by IPPT PAN.

A2.1. Preparation of the slurry

The samples were made from water-based slurries of Almatis GmbH CT3000 powder alumina of grain 0.7 μm and starch as a pore forming agent (PFA). There were two kinds of starch used: corn and rice. To improve the properties of the slurry Dolapix (dispersant) and Contraspum (to remove air bubbles) were added. There slurries contained 35%, 40% and 45% volume fraction of solid phase, as bases for composites of 60%, 50% and 30% starch/porosity/copper contents, respectively.

The components were mixed and de-agglomerated with magnet stirrer and ultrasonic Dr Hielscher GmbH stirrer. After mixing the slurries were evacuated to remove the air. Before using slurries were homogenized on roller mixer for at least 24 hours and evacuated. The scheme of the preparation of the slurry is depicted in Fig. A1.

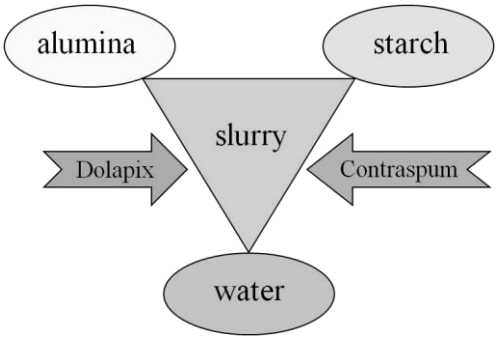

Figure A1. The scheme of the preparation of the slurry.

A2.2. Drying process

After preparing the slurries, the samples were slip cast into the forms with frames and plaster base. Then the samples were dried in controlled ambient conditions to remove the largest possible amount of humidity from the samples in order to avoid damage of the samples due to excessive drying. The drying process was controlled by mass measurements. During each step the ambient temperature and humidity were kept constant. Each step of the drying process was regarded as finished when the mass of the sample stopped to decrease and reached constant value for at least two subsequent measurements. As long as the sample was in a liquid state, mass estimations were made with regard to the mass of empty form and the total mass of the slurry together with the form. During drying the temperature and humidity were controlled. After casting into the forms, one set of the samples was put into the Binder humidity cupboard under controlled temperature and

humidity. The initial parameters were set to 20ºC and 80% or 90% of relative humidity. The other samples were kept under the cover in the room temperature and humidity. After the samples of both sets have dried in these conditions they were moved to the Memmert furnace and gradually heated up to 95ºC. It was observed that too rapid changes in temperature and humidity conditions caused cracking of the samples.

The rate of mass decrease was usually highest in the initial step of drying, while the samples were in the forms. After removal from the form, the drying rate gradually decreased. When the mass of the sample remained constant for at least two subsequent measurements, the drying conditions were changed to lower the humidity and rise the temperature. The drying rate then increased and remained constant for some measurements. The drying step was then repeated. The drying process is presented as drying curves in Fig. A2. It may be seen that the mass loss related to the initial sample mass was proportional to the starch content. Samples were taken out for sintering when their masses remained constant while being kept in 95ºC. For some of the samples evacuation at 40 mbar was additionally carried out, giving yet more mass losses. Five green alumina-PFA samples were manufactured, with: 30%, 50% and 60% corn starch PFA contents, and 30% and 50% rice starch PFA contents.

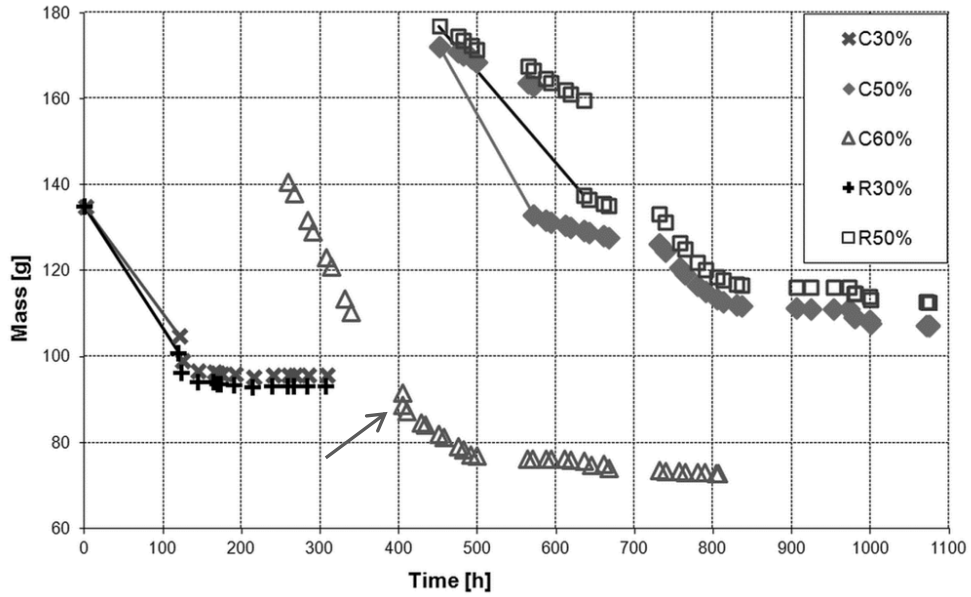

Figure A2. Drying curves for green alumina-PFA samples. Except for C60% sample, all curves start at the moment of casting the slurries into forms. The lines connect these points

with points after removing samples from frames, from where the direct mass of the sample was measured. Arrow indicates point after removing the sample C60% from frames, as it was not possible for this sample to indicate the value of the mass of just poured slurry.

A2.3. Sintering of the porous preforms

Before sintering the samples were ground to remove any flaws and notches that could initiate cracks during sintering. The samples were then sintered in the Arnold Schroeder Nabertherm oven. The sintering programme was as follows: first, slow heating at the rate of 0.5ºC/min up to 650ºC – the temperature higher of the temperature of burning out of starch, the slow rate was used to enable air removal during starch burnout; then faster heating rate of 2ºC/min up to 900ºC; heating rate increased to 10ºC/min up to 1550ºC - the sintering temperature; 2h hold at the sintering temperature; cooling down to the room temperature. The scheme of the sintering process is presented in the Fig. A3.

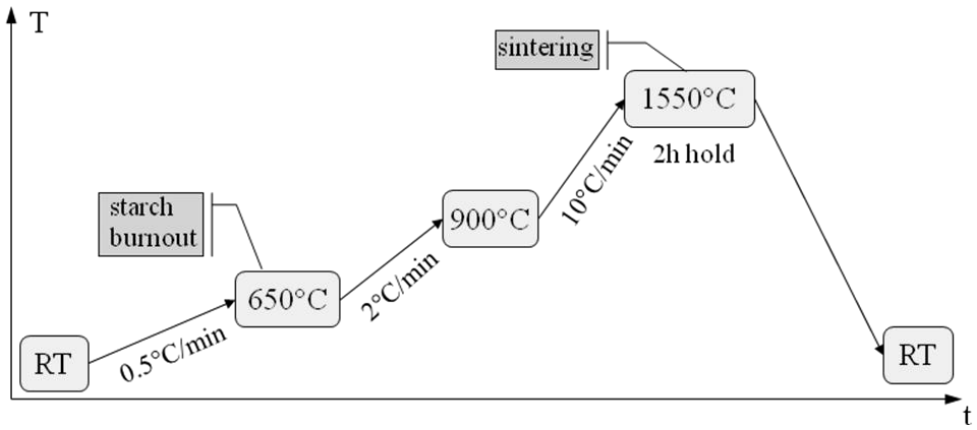

Figure A3. Scheme of preform burnout and sintering process

A2.4. Metal infiltration

After sintering, the samples were prepared for pressure assisted infiltration with pure copper (99.999%). The dimensions of porous samples for infiltration were of 50×50×8 mm. Before infiltration the alumina samples and pieces of copper were cleaned in acetone and isopropanol.

Prepared and assembled samples were infiltrated in the Fine Ceramics Technologies F8028 FPW furnace. The samples in a holder were put over the crucible with pieces of copper. The infiltration programme started with applying vacuum. Then the temperature was increasd to 1200ºC to melt the copper. The crucible was moved up so porous alumina samples were immersed in the molten copper. The argon pressure was applied to facilitate infiltration and to ensure inert atmosphere. After infiltration the crucible was moved down to take infiltrated samples out of the molten copper. The argon pressure was kept constant until the solidification of copper to avoid copper leakage from the preforms. The temperature was then lowered to the room temperature. The scheme of infiltration process is shown in Fig. A4.

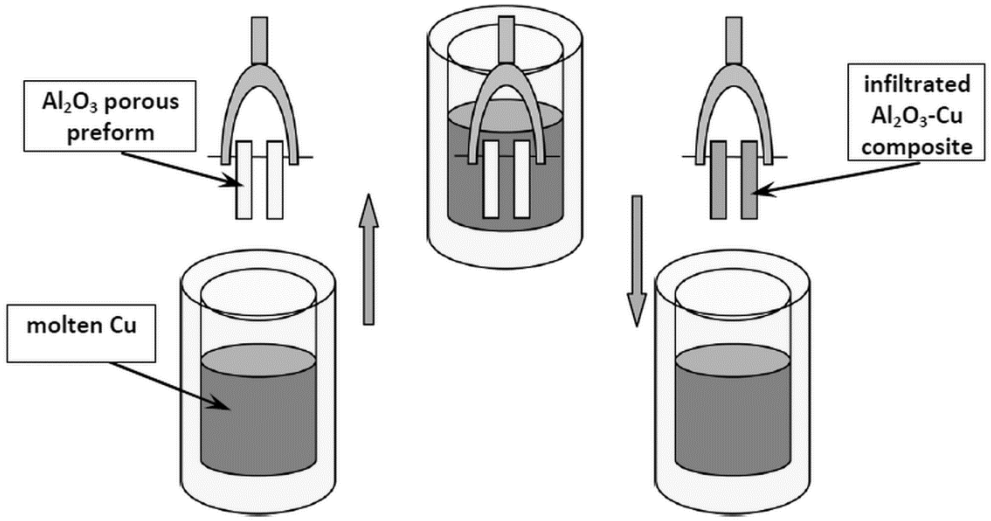

Figure A4. Scheme of infiltration process.

The structural and process parameters such as the pore forming agents, porosity, temperature, pressure and humidity have significant effect on the quality of the manufactured composites [182].

A3. Characterization of material properties of Al_2O_3/Cu IPC

The experiments described below were conducted in order to collect information for modelling purposes, in particular for comparison with the results of analytical and numerical modelling. The influence of copper fraction and composite microstructure on Young's modulus was investigated. The characterization of Al_2O_3/Cu composites was performed during research stays within KMM-NoE Project at the Institute of Materials Science, TU Darmstadt, Germany under scientific guidance and supervision of Dr Ludwig Weiler (TUD).

A3.1. Description of specimens and their microstructures

The measurements were made on prismatic specimens of infiltrated Al_2O_3/Cu composites with different microstructures and different copper contents. The interpenetrating microstructures were based on the following pore forming agents (PFA): polypropylene wool felt (composite with 25vol.% Cu), natural wool felt (composites with 25 and 50 vol.% Cu), and also corn and rice starch (composites with 40 vol.% Cu).

The specimens were labelled according to the PFA used and the porosity/metal content: P - polypropylene wool felt, W - natural wool felt, R - rice starch, M - corn starch, Mp - porous preform based on corn starch PFA. The numbers denote percentage of volume porosity/copper fraction in a preform/composite.

In Fig. A5 the microstructure of Al_2O_3/Cu composites is presented as micro-CT images. It may be seen that the microstructure of the rice starch based IPC (Fig. A5b) is very fine and falls below the resolution level. The IPCs based on natural wool felt (W) were analyzed under optical microscope (Fig. A6). Those based on corn starch and rice starch are depicted in Figs A6a-b and c-d, respectively.

It can be seen that the microstructure based on corn starch is more coarse. In this case the copper struts have rounded shapes, replicating corn starch grains. Inside many of the grain-shaped struts ceramic agglomerates can be observed, created due to starch swelling. This phenomenon and its importance for the resulting composite is explained in [183]. Rice starch-based microstructure is finer and different in shape than the microstructure based on corn starch. The copper struts are more elongated and the shape of the grains is more diffused (elongated ligaments of the thickness

near to the grains diameters often occur, making the microstructure more similar to fibrous one). In Figs. A6(e-f), IPCs with two felt-based microstructures, polypropylene (e) and natural (f) wool felt, can be compared. In the IPC based on the polypropylene wool felt the surfaces of copper struts are smooth, whereas in the IPC with microstructure based on the natural wool felt the copper struts keep the details of natural wool fibres microstructure, replicating tiny hooks that cover wool fibres.

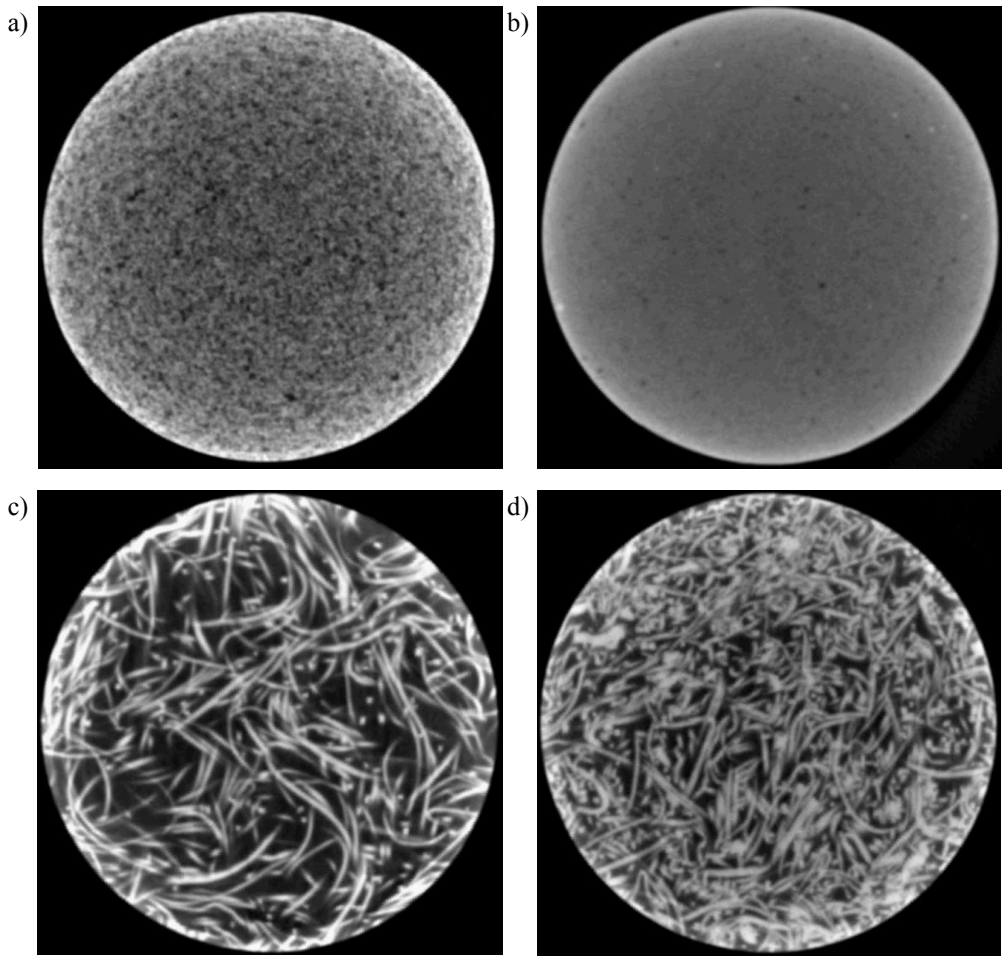

e)

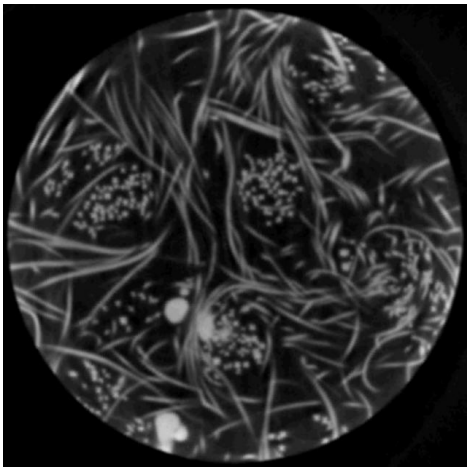

Figure A5. Microstructure of the infiltrated Al_2O_3/Cu IPC composites (micro-CT images, courtesy of G. Geier, Leoben): a) corn starch PFA, 30% Cu (M30), b) rice starch PFA, 30% Cu (R30) (very fine microstructure below resolution level), c) natural wool felt PFA, 25% Cu (W25), d) natural wool felt PFA, 50% Cu (W50), e) polypropylene wool felt PFA, 25% Cu (P25). Light grey – copper, dark grey - alumina

a)

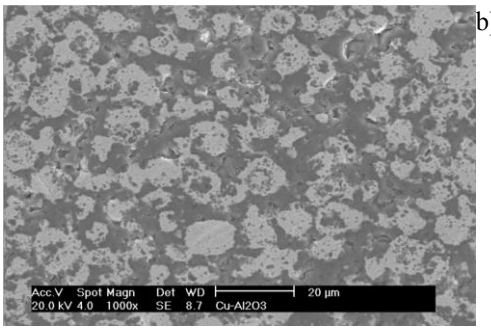

b)

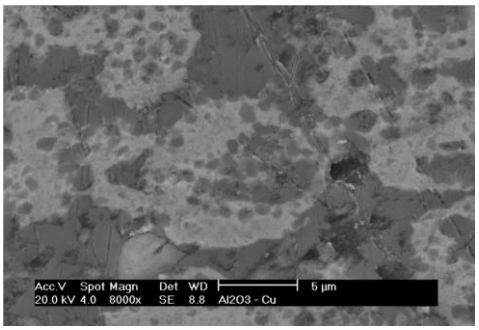

c)

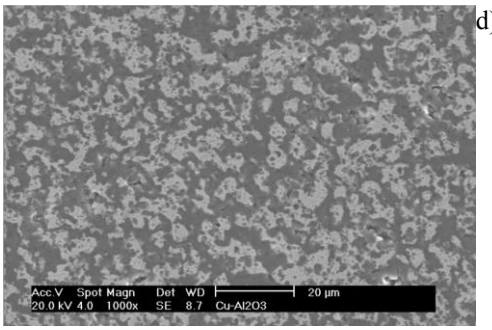

d)

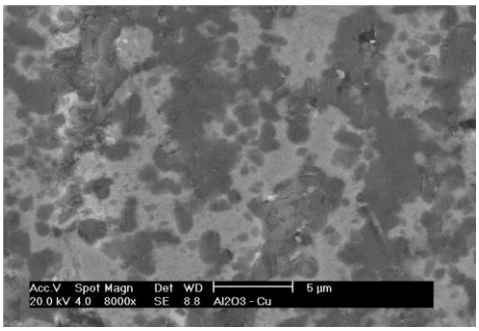

e) f)

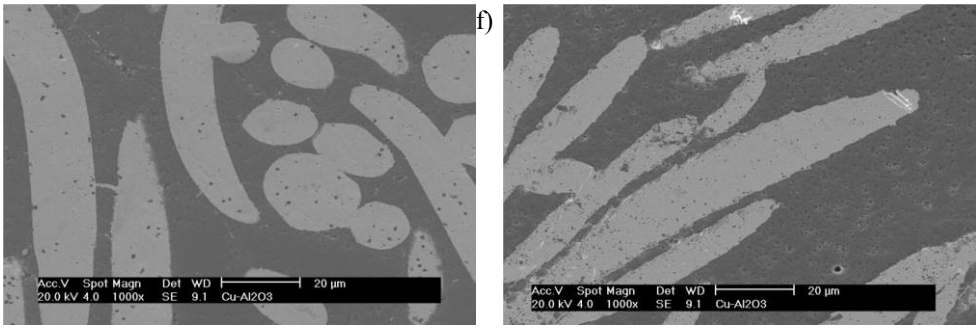

Figure A6. Microstructures of infiltrated Al_2O_3/Cu composites (microscopic images, courtesy of J. Winzer, L. Weiler, J. Rödel, TUD): a) corn starch PFA, 40% Cu (M40), magnification 1000x, b) corn starch PFA, 40% Cu (M40), magnification 8000x, c) rice starch PFA, 40% Cu (R40), magnification 1000x, d) rice starch PFA, 40% Cu (R40), magnification 8000x, e) polypropylene wool felt PFA, 45% Cu, magnification 1000x, f) natural wool felt PFA, 30% Cu, magnification 1000x. Light grey – copper, dark grey - alumina

A3.2. Porosity measurements

To determine the actual amount of copper in the infiltrated Al_2O_3/Cu composite samples, porosity measurements were made. First, the Archimedes method was used to find the density of the composite

$$\rho = \frac{m_{dry} * \rho_{H_2O}}{m_{satd} - m_{suspend}}, \tag{A3.1}$$

where: m_{dry} – mass of the dry specimen, ρ_{H2O} – water density, m_{satd} – mass of the specimen infiltrated with water, $m_{suspend}$ – mass of the specimen suspended in water.

The apparent specific gravity was calculated according to the formula

$$SG_{apparent} = \frac{\rho_{dry}}{\rho_{H_2O}} = \frac{m_{dry}}{V_{specimen}} \frac{V_{specimen}}{m_{H_2O}} = \frac{m_{dry}}{m_{H_2O}} = \quad = \quad = \frac{m_{dry}}{m_{dry} - m_{suspend}}, \tag{A3.2}$$

where m_{H_2O} - mass of the volume of water equal to the volume of the specimen. Then the amount of copper in the composite was calculated using densities of pure copper and alumina according to the formula

$$C_{Cu} = \frac{SG_{apparent} - \rho_{Al_2O_3}}{\varrho_{Cu} - \rho_{Al_2O_3}} \cdot 100\%. \tag{A3.3}$$

The density of copper was taken as 8.94 g/cm^3, the density of monolithic alumina as 3.96 g/cm^3.

The density was measured for composite samples where corn starch and rice starch PFAs were used to obtain open porosity. The density measurements were obtained with two different methods: (i) calculating density from the dimensions and mass of the specimen, and with (ii) the Archimedes method. It can be seen in Table A.1 that the results obtained with both methods do not differ more than 1%. From the results in Table A.1 it can also be seen that there is a residual porosity, which does not exceed 0.5%. The presence of residual porosity means that the infiltration process was not fully completed as some pores might not be accessible for infiltrating metal. For this and other microstructural reasons the actual copper content was, thus, less by approximately 3% than the nominal value of 40% for the measured samples.

Table A.1. Measurements of density and copper content of Al_2O_3/Cu composites.

Specimen	Density of composite			Residual Porosity	Cu content	Al_2O_3 content
	from dimensions	from Archimedes method				
	[g/cm^3]	[g/cm^3]	[%]	[%]	[%]	[%]
R40	5.775	5.774	99.52	0.48	37.00	63.00
M40	5.818	5.855	99.74	0.26	38.36	61.64

A3.3. Measurements of Young's modulus at room temperature

The mechanical and physical characteristics of the phase materials of metal-ceramic composites may differ radically from each other according to the composite material design. These differences in properties may, however, cause problems during manufacturing. Since IPCs combine ceramics and metals, materials with dissimilar mechanical and thermal properties, during manufacturing at high temperatures and cooling to room temperature different thermal expansion coefficients of both phases may cause delamination and large residual stresses. In brittle materials like ceramics, large residual stresses may lead to microcracking. It is, thus, important to know the material data of phase materials of the composite. One of the simplest methods of identification of the presence of microcracks and other impurities that may weaken the material, is measurement of the Young modulus. The impulse excitation of vibration method was used by [191,192] to

measure Young's moduli as a function of temperature for alumina ceramics with different average grain sizes. The description and comparison of available mechanical and non-destructive methods of measurements of Young's modulus used for metal-ceramic composites that may also be applied to IPCs was given by [102]. Three-point bending test, resonance frequency damping analysis, ultrasonic pulse-echo technique and scanning acoustic microscopy tests are described in detail and compared therein.

The method of Young's modulus measurement used for the purpose of this thesis was the impulse excitation of vibration. The measurements at room temperature were made with Grindosonic - the Impulse Excitation Technique J. W. Lemmens equipment, and, at the beginning of a thermal cycle, with the Integrated Material Control Engineering (IMCE) N. V. Resonant Frequency and Damping Analyser (RFDA) HT 1750, Diepenbeek, Belgium. Both types of equipment use the method of detecting the fundamental mode I (flexural) resonant frequency f_f of a freely vibrating material, according to ASTM [193] standard. The specimen was put on the supports at a distance L, and at 0.224 L from each end to fit onto flexural vibration node lines (see Fig. A7), where for mode I of vibrations zero displacements occur. The microphone was put over the antinode, where the maximum amplitude of mode I vibrations occurs, either in the middle or at specimen's end. Then, the specimen was singularly hit with the impulser rod at another antinode to induce the elastic vibrations. The microphone collected the signal of vibrations. The fundamental frequency of this signal was identified via by the signal analyser and recorded.

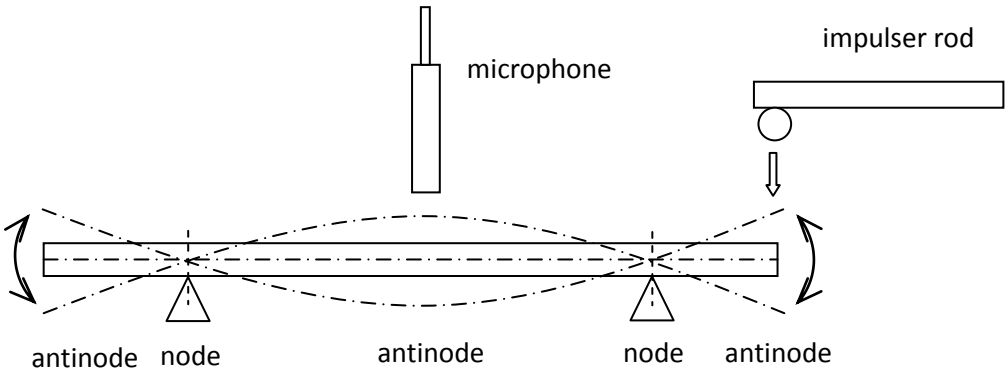

Figure A7. Detection of fundamental flexural resonant frequency of a vibrating specimen.

Resonant frequency of a freely vibrating material depends on its mass, dimensions and elastic modulus. Thus, Young's modulus can be calculated from the measured resonant frequency. In ASTM [193] standard, dynamic Young's modulus E is related to the fundamental resonant frequency f_f according to the following formula

$$E(f_f) = 0.9465\left(\frac{mf_f^2}{B}\right)\left(\frac{L^3}{H^3}\right)T_1 \tag{A3.4}$$

where: m – mass of the specimen, L – length of the specimen, B – width of the specimen, H – thickness of the specimen, T_1 – correction factor defined as

$$T_1 = 1 + 6.585(1 + 0.0752\nu + 0.8109\nu^2)(H/L)^2 - \\ - 0.868(H/L)^4 - \\ -\left[\frac{8.340(1 + 0.2023\nu + 2.173\nu^2)(H/L)^4}{1.000 + 6.338(1 + 0.1408\nu + 1.536\nu^2)(H/L)^2}\right] \tag{A3.5}$$

where ν is the Poisson's ratio.

The results of Young's modulus measurements made with both devices are given in Table A2.

Table A2. Measurements of Young's modulus of IPC composites and porous performs made with impulse excitation technique at room temperature using Grindosonic and IMCE RFDA test equipment. E_1 and E_2 denote Young's moduli measured in out-of-plane flexure and in-plane flexure, respectively.

Specimen	E_1, Out-Of-Plane Flexure [GPa]		E_2, In-Plane Flexure [GPa]
	Measuring equipment		
	Grindosonic	IMCE RFDA	Grindosonic
Composite samples:			
W25	244.26	-	246.63
W50	182.54	183.93	173.99
P25	274.10	274.34	272.77
M40	266.46	267.05	267.39
R40	254.45	254.71	253.85
Porous preforms:			
Mp15	253.60	-	256.08
Mp30	155.53	-	-

In Table A2 the Young's moduli for IPC composites and porous preforms measured with the impulse excitation technique at room temperature are shown. For

the out-of-plane flexure the measurements were made with both Grindosonic and IMCE RFDA impulse excitation equipment. It can be seen that both devices gave similar results and the differences between measured Young's moduli did not exceed 1%. The in-plane flexure measurements were made to check anisotropy of the investigated IPC microstructures. From the results in Table A2 it is clear that the out-of-plane flexure and in-plane flexure measurements gave similar results, not exceeding 1%, with the only exception being the specimen W50 for which the results did not exceed 5%. It can be interpreted that anisotropy of the investigated IPCs is not significant, an they can, thus, be regarded as isotropic. The differences between Young's moduli in out-of-plane flexure and in-plane flexure measurements occur due to locally non-uniform dispersions of the composite's phases. The difference between Young's moduli in both directions was smallest for both IPCs with microstructures based on starch PFAs (M and R), and larger for fibruous PFAs (P and W) and porous alumina (Mp) specimens. This occurred probably due to finer and more uniform microstructures of starch PFA-based composites. Fibrous PFA-based composites were less uniform showing local anisotropy due to specific placement of the fibres. This effect was most significant for the specimen W50.

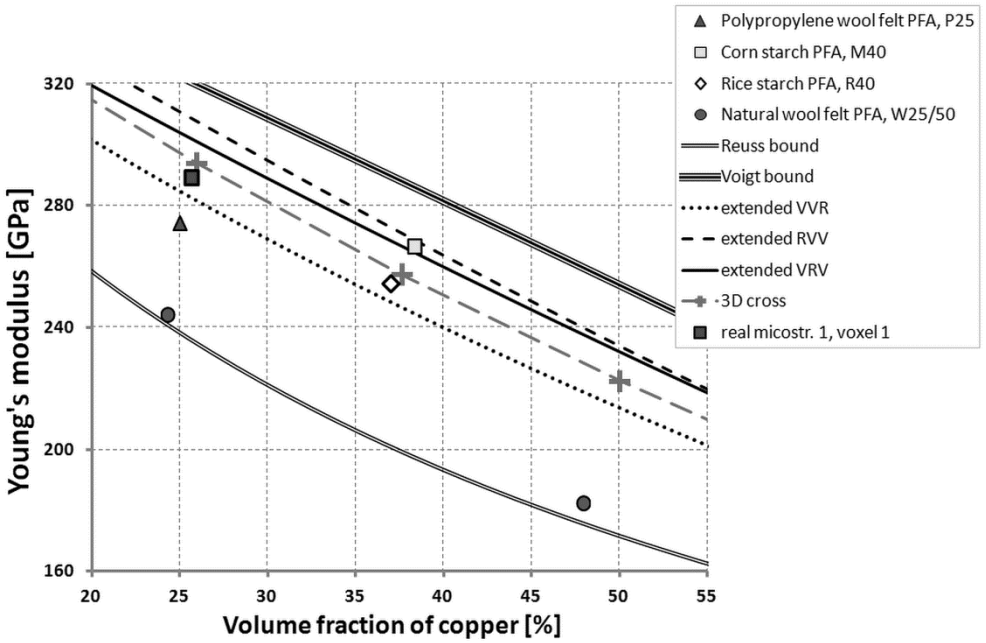

Figure A8. Effect of microstructure and copper content on Al_2O_3/Cu composites Young's moduli. Measurements done with Grindosonic impulse excitation of vibration equipment and compared with Voigt and Reuss bounds, extended *V-V-R*, *R-V-V* and *V-R-V* models and

numerical models of 3D cross and of real microstructure for alumina-copper composites at room temperature.

In Figure A8 the influence of the copper content and composite microstructure on Young's modulus is shown. It can be seen that the Young's modulus values for all the IPCs fit between the Reuss and Voigt bounds and are below the extended *R-V-V* model. With the exception of corn starch PFA-based composite all measured Young's modulus values for IPCs are also below the results for D -cross numerical model. On the example of natural wool PFA based composite, it may be observed that for IPC of the same kind of microstructure Young's modulus decreases with increasing volume fraction of copper in the material. Accordingly, the same relationship may be observed for porous Al_2O_3 preforms when porosity was increasing (see Table A.2).

For the composites with the same copper volume fraction, the microstructure influence on the elastic modulus of IPC composites can be analyzed on two examples of 25% and 40% of Cu content. For the IPC with 25vol.% Cu, the composite with microstructure based on polypropylene felt PFA showed higher Young's modulus. For IPCs with 40% Cu, the specimen with microstructure based on the rice starch PFA had finer and more uniform microstructure than the IPC with microstructure based on the corn starch PFA. However, corn starch PFA-based IPC shows approximately 4. % higher Young's modulus than IPC with microstructure based on rice starch PFA.

The Young's moduli for natural wool PF s based IPCs are lower than for other microstructures, and closest to the Reuss bound for the effective Young's modulus. The Young's moduli for polypropylene and starch PF s based IPCs are closer to the Voigt bound, what indicates IPCs with these microstructures are relatively stronger than IPCs with microstructures based on natural wool. The closest to the Voigt bound, and thus the best related to copper contents, appears to be the corn starch PFA-based composite. However, it should be noted that microscopic observations [182] showed that the rice starch based IPCs have finer and more uniform microstructure than corn starch based IPCs. The differences in Fig 8 in Young's moduli measured for different composite microstructures depicted in Figs. A5 and A6, can be due to different parameters characterizing phase geometries, especially *tortuosity* parameter investigated *e.g*. by [194]. In fact, Young's moduli are closest to upper estimations of Voigt and *R-V-V* for IPCs with microstructures based on corn starch, which seem to have the highest tortuosity from all investigated microstructures. IPCs with microstructures based on rice starch do not have such

high toruosity and their Young's moduli are closer to *V-V-R* model than for corn starch based IPCs. Wool felt based IPCs have lower tortuosity compared to starch based IPCs and, consequently, their Young's moduli are closer to *V-V-R* model, with higher Young's moduli values for polypropylene wool felt and larger tortuosity than natural wool felt.

A3.4. Measurements of Young's modulus in thermal cycles

Measurements of Young's modulus in thermal cycles were carried out to examine the behaviour of IPC composites in elevated temperatures. Measurements were made for different composite microstructures and copper volume fractions and temperatures up to 800°C. As described by [191,192], for poly-phase materials Young's modulus measurements in temperature cycles may indicate microcracking due to the thermal expansion coefficients mismatch between phases. Thus the Young's modulus measurements in thermal cycles may provide evidence if the material is resistant to high temperatures. The composites with microstructures based on polypropylene wool felt (25% Cu), natural wool felt (25% and 50% Cu) and corn and rice starch (40% Cu) were investigated in this series of experiments.

The measurements of Young's modulus in temperature cycles were made with Integrated Material Control Engineering (IMCE) N. V. Resonant Frequency and Damping Analyser (RFDA) HT 1750, Diepenbeek, Belgium. The idea of measurements of Young's modulus with impulse excitation of vibration technique, is explained in the previous Subsec. A3.3. The detailed description of IMCE RFDA equipment may be found in [191]. The idea of thermal measurements with this equipment is described in [192].

The Young's modulus was determined according to ASTM [193] formula (Eq. A3.4), from the measured fundamental flexural resonant frequencies of the vibrating material, in a similar manner than for measurements at RT. Resonant frequencies were measured in time intervals during temperature cycle. For each measurement the Young's modulus was calculated. The specimen was positioned on the Pt-Rh wire supports inside the heating chamber. The position of the flexural nodes at which the measured specimens were to be supported, was calculated by the measuring unit based on the specimen's length L, and equal to 0.224 L from each end of the specimen. For each measurement the specimen was excited with an impulse from a rod hitting at an antinode (for the fundamental flexural resonance placed at both ends and in the middle of the specimen), where the maximum amplitude of fundamental flexural vibrations occurs. Then a microphone placed

above the sample at another antinode collects the sample vibration signal. The Fast Fourier Transform (FFT) of the signal was calculated and analysed by the measuring unit to find the fundamental resonant frequency. The Young's modulus based on this resonant frequency was calculated within the measuring unit. The frequencies of up to 20^{th} order were additionally recorded by the system. For some measurements, FFTs were recorded to check if the resonant frequency of the specimen was chosen correctly by the system for that measurement point.

The temperature inside the chamber was measured with two independent thermocouples. The temperature of the sample was assumed to be equal to the indicated with the thermocouple. There were two thermal programmes applied: one up to 400ºC, with heating ratio of 2ºC/min and dwell time of 15 min at the maximum temperature, and the second up to 800ºC with heating ratio of 5ºC/min and dwell time of 15 min at the maximum temperature. The measurements were taken at each 30 seconds.

The low temperature cycle up to 400°C was carried out to check the behaviour of the P25, W25 and R40 composites in elevated temperatures before exposition to higher temperatures. The results of measurements in thermal cycles in both temperature ranges, from RT to 400°C and from RT to 800°C, are presented collectively in Fig. A9 and, only for starch based IPCs, in Fig. A10. The graphs were made from the results of the Young's moduli calculated by the IMCE RFDA. Additionally, in Fig. A10 the resonant frequencies were chosen from the recorded FFTs and the Young's moduli calculated for them were added to the graph. It was done to check the resonant frequencies taken by the measurement unit and thus, the correctness of measured Young's moduli.

The relationship between the Young and temperature can be used as an indicator if the material microstructure remained intact upon cooling. The Young modulus of an undamaged material increases linearly during cooling (*cf.* [191]), while the presence of hysteresis indicates microcracking. For alumina-copper composites microcracking during cooling can occur due to high contrast between thermal expansion coefficients of both composite constituents. To compare the deviations from the linear Young's modulus vs. temperature relationship regardless of composite microstructure or volume fraction of phases, a graph was prepared in Fig. A11, analogously to the graphs in [191,192]. Young's moduli for each measurement (*i.e.* temperature point) were related to the theoretical value that would result for the same temperature in case of no microcracking. In this way, a graph of drop downs of Young's moduli $-\Delta E$ from linear Young's modulus – temperature relationship, related to temperature decrements $-\Delta T$ from the highest value reached during the

cycle, was prepared. The linear Young's modulus vs. temperature relationship was obtained taking Young's moduli values measured in RT shown in Table A2 (IMCE readings; for sample W25 Grindosonic measurement of out-of-plane flexure instead), and Young's moduli values measured at the highest temperature reached during thermal cycle. A scheme explaining described above procedure was added to the Fig. A9 on the example of W50 specimen.

The copper oxidation in elevated temperatures can cause an increase in specimen's mass and volume, and may lead to microcracking. The dimensions and masses of the specimens were measured after thermal cycles. Young's moduli were recalculated with masses that were measured after the cycles. Only the final values of Young's moduli were recalculated, because it could not be exactly stated from which temperature the change of the mass occurred (it is impossible to measure the dimensions of the specimen inside the closed furnace chamber during thermal cycles). The resulting points are added in Fig. A10. It can be seen that for both IPCs with microstructures based on starch, the recalculated Young's moduli are nearly equal to the Young's moduli that were based on initial masses, thus the increase of dimensions and masses for these microstructures was insignificant.

As it was observed for composites made with different PFA (Figs. A9 and A11), the microstructure influences the microcracking. For the IPC with microstructure based on polypropylene wool felt (P25), after a thermal cycle of up to 400ºC extensive microcracking occurred. Almost no microcracking was observed for IPCs with microstructures based on both kinds of starch. For IPCs based on natural wool as the PFA a very interesting behaviour was observed in temperature cycle of up to 400°C, namely a quite strong microcracking occurred lowering the Young modulus for about 30GPa for W25 IPC and almost 45GPa for W50 IPC (13% and 24% of the initial value before thermal cycle for the samples W25 and W50, respectively).

However, after thermal cycling of the same specimens for up to 800°C, Young's modulus decrease in W25 was very small (of the order of 10GPa) the same as for the starch based IPCs, indicating almost no microcracking. Also for W50 IPC the decrease in Young's modulus was not large (less than 20 GPa). Additionally, in Fig. A9 it can be seen that the final values of Young's moduli for W2 and W 0 IPCs were noticeably higher than in the previous cycle. Compared with the initial values before thermal cycles, after the 800ºC cycle Young's modulus decreased: 12.4 GPa (%) for W2 IPC, and 19.0 GPa (10%) for W 0 IPC. The decrease in Young's modulus for these IPCs after 800ºC cycle is much less than the decrease in the 400ºC cycle, and indicates that both natural wool based composites improved their properties in the high temperature cycle. This could be due to the microstructure of

the natural wool fibres, which are covered with tiny hooks as observed by J. Winzer and L. Weiler (see Fig. A6f). Such microstructure enables penetration of copper and reduces thermal stresses in the ceramics, preventing microcracking.

After two thermal cycles, RT - 400ºC and RT - 800ºC, the composites with microstructures based on both kinds of starch showed no microcracking and only slight decrease of Young's modulus, compared to Young's modulus before thermal cycles: 13.06 GPa (5%) for corn starch based composite, and 10.1 GPa (4%) for rice starch based composite. It can be seen in Figs. A9 and A10 that the cooling curves for these composites are almost linear for both thermal cycles which indicates that no microcracking occurred due to elevated temperature within the measured range. For 800 ºC cycles for both composites, their cooling curves are almost parallel, however, rice starch based IPC appears to be slightly less deviated from linear shape. This can be interpreted as a higher resistance to high temperatures of the IPCs with microstructure based on rice starch.

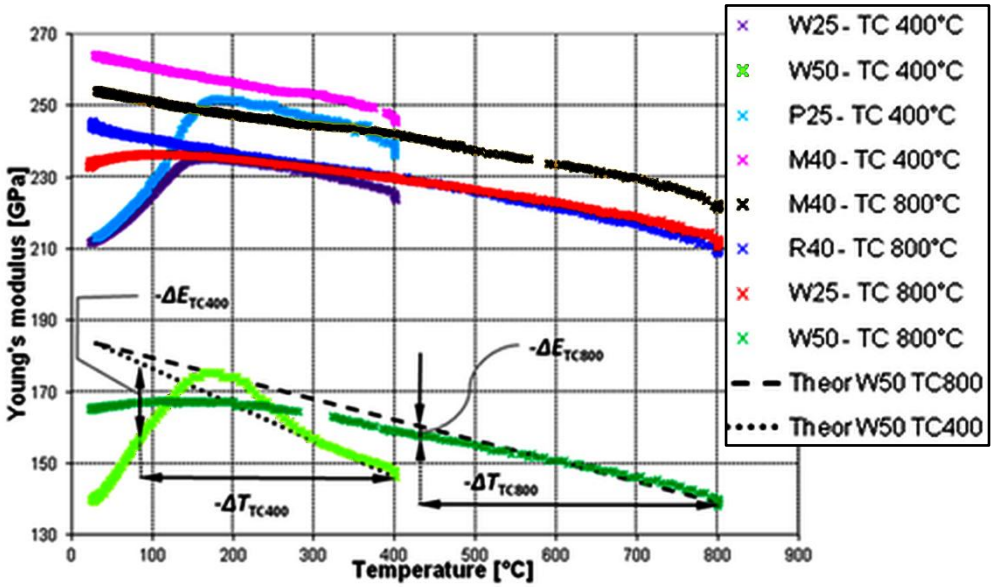

Figure A9. Young's moduli in temperature cycles RT-400°C and RT-800°C for Al_2O_3/Cu composites with different microstructures and copper contents. On the example of W50 IPC specimen, the idea of [191,192] is presented how to obtain curves showing differences between theoretical and real Young's moduli decrease upon cooling for two thermal cycles RT- 400°C and RT-800°C.

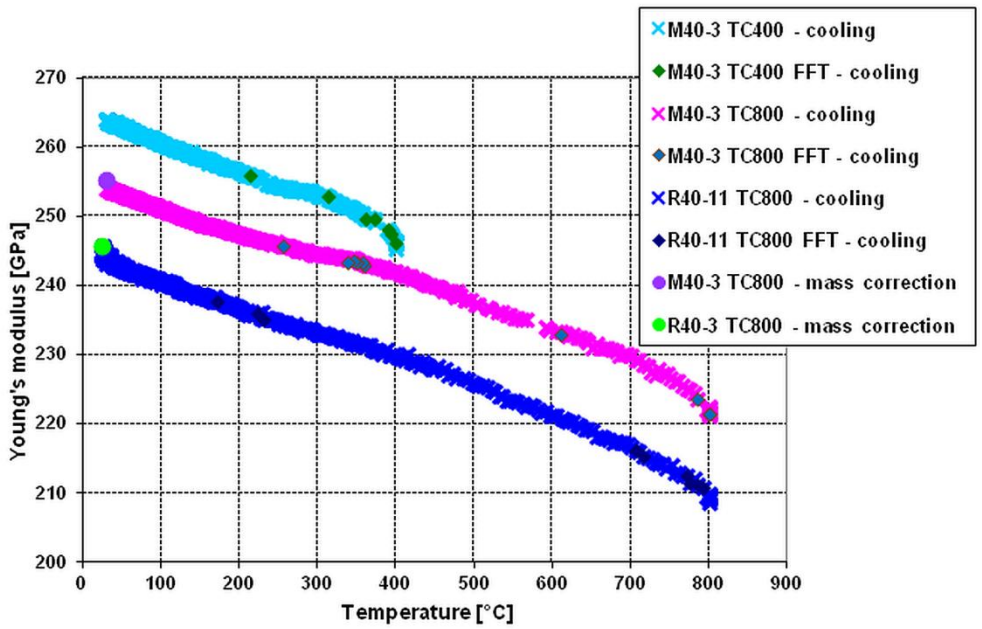

Figure A10. Young's modulus in temperature cycles for l_2O_3/Cu IPCs based on corn and rice starch

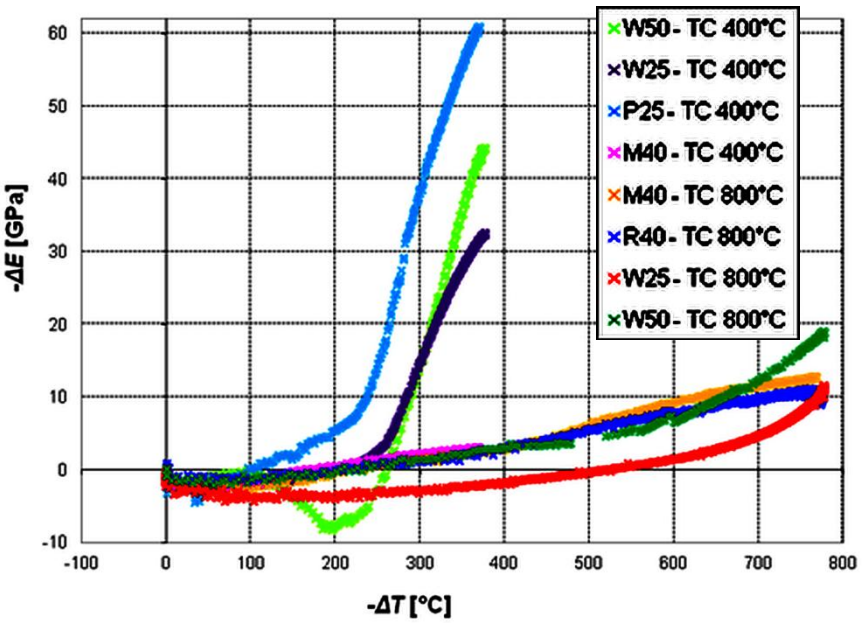

Figure A11. Reduction of Young's modulus vs. temperature decrease in cooling, temperature cycles up to 400°C and 800°C for Al_2O_3/Cu IPC composites with different microstructures and copper contents (the idea of the graph is explained in Figure A9).

A4. Closing remarks on IPCs characterization

The measurements of the Young modulus of Al_2O_3/Cu IPCs with microstructures based on PFAs of polypropylene wool felt (25% Cu), natural wool felt (25% Cu and 50% Cu), and also corn and rice starch (40% Cu) have shown the influence of copper fraction and composite microstructure on Young's modulus in RT and in thermal cycles of up to 800ºC. The results of Young's modulus in RT were compared with the Voigt and Reuss bounds. Obviously, an increase of softer copper fraction in a composite of the same microstructure decreases Young's modulus, as it can be seen on the example of W25 and W50 IPCs. However, the results have also shown that the microstructure of the interpenetrating networks has significant effect on its properties, especially during thermal cycles. The tortuosity paramemter (*cf*. [194]) seems to have particular influence which should be carefully investigated with regard to phases orientation. Also other microstructural parameters such as interfacial area fraction or characteristic dimension (*i.e*. length or diameter) of the metallic phase ligaments, should be determined and their influence on composites' properties should be carefully analysed. Partially this task was achieved in the thesis thankful to indirect relationship of these parameters with the cross-sectional dimension of the phases in the numerical three-dimensional cross model described in Subsec. 5.2.2.

The Young's modulus measurements in room temperature were made in two perpendicular directions and showed no significant anisotropy of the investigated composites, regardless of the microstructure. The composites could thus, be regarded as isotropic, which facilitated the models created in this thesis.

From measurements in temperature cycles it was clear that for the microstructure based on corn and rice starch PFAs, the Young's modulus relationship with temperature is almost linear and does not show microcracking, even in temperature range of up to 800 ºC. The Young's moduli calculated for dimensions and weight measured after thermal cycles were nearly equal to the Young's moduli calculated for initial dimensions and weight before thermal cycles. This is a clear evidence that preforms manufactured with the starch-based PFA preserve well the IPC samples shape under thermal loading.

Another observation from the reported experiments is that while the copper content increase in IPC generally decreases Young's modulus in RT, its influence on thermal behaviour is not so obvious. During thermal cycles the microstructure appeared to be the most influencing factor on the IPC's behaviour. The smoother

and less complicated geometry microstructure of the phases, such as polypropylene wool felt based IPC (*cf*. Figs. A5(e) and A6(e)), the stronger microcracking and deeper decrease in Young's modulus after thermal cycles. The microstructures that had rougher interfacial surfaces between phases (natural wool felt based IPCs and starch based IPCs) showed much less or nearly no microcracking after thermal cycles. The IPCs with finer and more complicated microstructures showed less microcracking – beginning with relatively coarse microstructure of natural wool based IPCs that showed quite strong microcracking in lower temperature cycles, but after higher temperature cycles showed an improvement in properties and almost no microcracking (*cf*. Fig. A9 and A11).

Higher microcracking after lower and higher temperature cycles was observed (*cf*. Fig. A11) for the microstructure with higher copper content and, thus, more prone to contain coarse agglomerates of copper (*cf*. Fig. A5(c) and (d)). For much finer microstructure based on corn starch (*cf*. Figs. A5(a) and Figs. A6(a,b)), almost no microcracking occurred during cooling either in lower or in higher temperature cycles (*cf*. Figs. A10 and A11). For an IPC with the finest microstructure based on rice starch (*cf*. Fig. A6(c,d)), where both phases are dispersed to the most extent, the relationship of Young's modulus with temperature during cooling is nearly linear (*cf*. Fig. A10). The explanation of such a behaviour may be that the finer and more rough the microstructure, the better and more efficiently can softened copper fill pores and microcracks in alumina at elevated temperatures.

The IPC microstructures based on either corn or rice starch PFA showed almost no microcracking upon cooling from elevated temperatures down to RT and good shape stability. This is an encouragement for further investigations of IPCs with these microstructures in view of their potential applications as structural materials in high temperature regimes. Also, further research of natural wool based composites and explanation of interesting behaviour of their Young moduli observed in high temperature cycles is worth pursuing.

References

1. Broutman L. J. and Krock R. H. *Composite Materials*. *Vol. 1*, *Interfaces in Metal Matrix Composites*, *ed*.: *A. Metcalfe*, Academic Press, *New York*, *London*, 1974.
2. Pietrzak K. *Formowanie się warstw pośrednich w kompozytach metalowo-ceramicznych i ich złączach*, Oficyna Wydawnicza Politechniki Warszawskiej, *Warszawa*, 1998.
3. Basista M. and Węglewski W. Modelling of damage and fracture in ceramic matrix composites, *Journal of Theoretical and Applied Mechanics*, 44, 455–484, 2006.
4. Felten F., Schneider G. A., Sadowski T. Estimation of *R*-curve in WC/Co cermet by CT test, *International Journal of Refractory Metals and Hard Materials*, 26, 55-60, 2008.
5. Léger A., Calderon N. R., Charvet R., Dufour W., Bacciarini C., Weber L., Mortensen A. Capillarity in pressure infiltration: improvements in characterization for high-temperature systems, *Journal of Materials Science*, 47 (24), 8419-8430, 2012.
6. Skirl S. *Mechanische Eigenschaften und Thermisches Verhalten von Al_2O_3/Al und Al_2O_3/Ni_3Al Verbundwerkstoffen mit Durchdringungsgefüge, Dr.-Ing. Dissertation*, Fachbereich der Materialwissenschaft, Technische Universität Darmstadt, VDI Verlag GmbH, *Düsseldorf*, 1998.
7. Poniznik Z., Salit V., Basista M. and Gross D. Effective elastic properties of interpenetrating phase composites, *Computational Materials Science*, 44, 813-820, 2008.
8. Simpleware ScanIP/FE v.4.3 Simpleware Ltd., *Exeter*, *UK*, 2011.
9. Daehn G. S., Starck B., Xu L., Elfishawy K. F., Ringnalda J., Fraser H. L. Elastic and plastic behavior of a co-continuous alumina/aluminum composite, *Acta Materialia*, 44 (1), 249-261, 1996.

10. Agrawal P., Conlon K., Bowman K. J., Sun C. T., Cichocki F. R. Jr., Trumble K. P. Thermal residual stresses in co-continuous composites, *Acta Materialia*, 51, 1143–1156, 2003.
11. Park J. S., Sun C. T., Trumble K. P. Effect of contiguity on the mechanical behavior of co-continuous ceramic metal composites, *in: Proceedings of the American Society for Composites: Twentieth Technical Conference, eds.: F. K. Ko, G. R. Palmese, Y. Gogotsi, A. S. D. Wang,* DEStech Publications, Inc., 2005
12. Del Rio E., Nash J. M., Williams J. C., Breslin M. C., Daehn G. S. Co-continuous composites for high-temperature applications, *Materials Science & Engineering A, Structural Materials: Properties, Microstructure and Processing*, 463, 115-121, 2007.
13. Rödel J., Prielipp H., Claussen N., Sternitzke M., Alexander K. B., Becher P. F., Schneibel J. H. Ni_3Al/Al_2O_3 composites with interpenetrating networks, *Scripta Metallurgica et Materialia*, 33, 843-848, 1995.
14. Prielipp H., Knechtel M., Claussen N., Streiffer S. K., Müllejans H., Rühle M., Rödel J. Strength and fracture toughness of aluminum/alumina composites with interpenetrating networks, *Materials Science and Engineering A*, 197, 19–30, 1995.
15. Skirl S., Krause R., Wiederhorn S. M., Rödel J. Processing and Mechanical Properties of Al_2O_3/Ni_3Al Composites with Inerpenetrating Network Microstructure, *Journal of the American Ceramics Society*, 84, 2034–2040, 2001.
16. Torquato S., Yeong C. L. Y., Rintoul M. D., Milius D. L., Aksay I. A. Elastic properties and structure of interpenetrating boron carbide/aluminum multiphase composites, *Journal of the American Ceramics Society*, 82, 1263–68, 1999.
17. Feng X., Mai Y. and Qin Q. A micromechanical model for interpenetrating multiphase composites, *Computational Materials Science*, 28, 486-493, 2003.
18. Feng X., Tian Z., Liu Y. and Yu S. Effective elastic and plastic properties of interpenetrating multiphase composites, *Applied Composite Materials*, 11, 33-55, 2004.
19. Hoffman M., Skirl S., Pompe W., Rödel J. Thermal residual strains and stresses in Al_2O_3/Al composites with interpenetrating networks, *Acta Materialia*, 47, 565–577, 1999.
20. Raddatz O., Schneider A., Claussen N. Modelling of *R*-curve behaviour in ceramic/metal composites, *Acta Materialia*, 46, 18, 6381–6395, 1998.
21. Frey G.S. son. Über die Elektrische Leitfähigkeit Binärer Aggregate, *Zeitschrift für Elektrochemie* 38, 260–274, 1932.

22. Tuchinskii L. I. Elastic constants of pseudoalloys with a skeletal structure, *Powder Metallurgy and Metal Ceramics*, 22 (7), 588-595, 1983.
23. Sharma N.K., Pandit S. N., Vaish R. Microstructural modeling of Ni-Al_2O_3 composites using object-oriented finite-element method, *International Scholarly Research Network, ISRN Ceramics*, 2012, Article ID 972054, 6 pages, 2012.
24. Agarwal A., Singh I. V., Mishra B.K. Evaluation of elastic properties of interpenetrating phase composites by mesh-free method, *Journal of Composite Materials,* 47, 1407-1423, 2013a.
25. Agarwal A., Singh I. V., Mishra B.K. Numerical prediction of elasto-plastic behaviour of interpenetrating phase composites by EFGM, *Composites,*51*,* 327-336, 2013b.
26. Gao J., Rayes N. Modeling of the Mechanical Properties of a Polymer-Metal Foam Interpenetrating Phase Composite, Mechanics of Solids, Structures and Fluids, *ASME 2014 International Mechanical Engineering Congress and Exposition*, *Montreal*, *Quebec*, *Canada*, 9, IMECE2014-37608, V009T12A048; 6 pages, doi: 10.1115/IMECE2014-37608, 2014.
27. Xie F., Lu Z., Yuan Z. Numerical analysis of elastic and elastoplastic behavior of interpenetrating phase composites, *Computational Materials Science*, 97, 94–101, 2015.
28. Ai L., Gao X.-L. Evaluation of effective elastic properties of 3-D printable interpenetrating phase composites using the meshfree radial point interpolation method, *Mechanics of Advanced Materials and Structures*, *published online*: *25 Jan 2016*, 11 pages, DOI:10.1080/15376494.2016.1143990, 2016.
29. Nemat-Nasser S. and Hori M. *Micromechanics: Overall Properties of Heterogeneous Materials*, Elsevier, *Amsterdam*, 1999.
30. Aboudi J. *Mechanics of Composite Materials*, Elsevier, 1991.
31. Mura T. *Micromechanics of Defects in Solids*, Martinus Nijhoff Publication, *The Hague*, 1987.
32. Janus-Michalska M. and Pęcherski R. B. Macroscopic properties of open-cell foams based on micromechanical modelling, *Technische Mechanik*, 23, 234–244, 2003.
33. Moon R., Tilbrook M., Hoffman M. and Neubrand A. Al–Al_2O_3 composites with interpenetrating network structures: composite modulus estimation, *Journal of the American Ceramics Society*, 88, 3, 666-74, 2005.
34. Jhaver R. Compression response and modeling of interpenetrating phase composites and foam-filled honeycombs, *M. Sc. Thesis*, Auburn University, *Auburn*, *Alabama*, 2009a.

35. He Y. Computational modeling of interpenetrating phase composites, *M. Sc. Thesis*, The University of Texas at Dallas, *Dallas*, 2013.
36. Cheng F., Kim S. M., Reddy J. N., Abu-Al-Rub R. K. Modeling of elastoplastic behavior of stainless-steel/bronze interpenetrating phase composites with damage evolution, *International Journal of Plasticity*, 61, 94–111, 2014.
37. Tippur H. Processing, Failure Characterization and Modeling of Lightweight Interpenetrating Network Composites, *Final Report, Auburn University*, *AL*, 2012.
38. Rosen B. W., Hashin Z. Effective thermal expansion coefficients and specific heats of composite materials, *International Journal of Engineering Science*, 8, 157-173, 1970.
39. Levin V. M. On the coefficients of thermal expansion of heterogeneous materials, English translation: *Mechanics of Solids*, 2 (1), 58-61, 1967.
40. Hashin Z. and Shtrikman S. A Variational Approach to the Theory of the Elastic Behaviour of Multiphase Materials, *Journal of the Mechanics and Physics of Solids*, 11, 127-140, 1963.
41. Mishnaevsky L. Jr Automatic voxel-based generation of 3D microstructural FE models and its application to the damage analysis of composites**,** *Materials Science and Engineering A*, 407, 11-23, 2005.
42. Mishnaevsky L. Jr A simple method and program for the analysis of the microstructure-stiffness interrelations of composite materials, *Journal of Composite Materials*, 41 (1), 73-87, 2007a.
43. Milton G. *The Theory of Composites*, Cambridge University Press, 2002.
44. Gross D. and Seelig T. *Fracture Mechanics with an Introduction to Micromechanics*, Springer, *Berlin*, *Heidelberg*, *New York*, 2006.
45. Leßle P., Dong M., Schmauder S. Self-consistent matricity model to simulate the mechanical behaviour of interpenetrating microstructures, *Computational Materials Science*, 15, 455–465, 1999.
46. Jhaver R. and Tippur H. Processing, compression response and finite element modeling of syntactic foam based interpenetrating phase composite (IPC), *Materials Science and Engineering A,* 499, 507–517, 2009b.
47. Wejrzanowski T. Spychalski W., Różniatowski K., Kurzydlowski K. J. Image based analysis of complex microstructures of engineering materials, *International Journal of Applied Mathematics and Computer Science*, 18 (1), 33–39, 2008.
48. Nowak M., Nowak Z., Pęcherski R. B., Potoczek M., Śliwa R. E. On the reconstruction method of ceramic foam structures and the methodology of

Young modulus determination, *Archives of Metallurgy and Materials*, 58 (4), 1219–1222, 2013.
49. Nowak Z., Nowak M., Pęcherski R. B., Potoczek M., Śliwa R. E. Mechanical properties of the ceramic open-cell foams of variable cell sizes, *Archives of Metallurgy and Materials*, 60 (3), 1957–1963, 2015.
50. Wejrzanowski T., Skibinski J., Madej L., Kurzydlowski K. J. Modeling structures of cellular materials for application at various length – scales, *Computer Methods in Materials Science*, 13 (4), 493–500, 2013a.
51. Wejrzanowski T., Skibinski J., Szumbarski J., Kurzydlowski K. J. Structure of foams modeled by Laguerre–Voronoi tessellations, *Computational Materials Science*, 67, 216–221, 2013b.
52. Michailidis N., Stergioudi F., Omar H., Tsipas D. N**.** An image-based reconstruction of the 3D geometry of an Al open-cell foam and FEM modeling of the material response, *Mechanics of Materials*, 42, 142–147, 2010.
53. Jaganathan S., Tafreshi H. V*.,* Pourdeyhimi B. A realistic approach for modeling permeability of fibruous media: 3-D imaging coupled with CFD simulation, *Chemical Engineering Science*, 63, 244-252, 2008a.
54. Jaganathan S., Tafreshi H. V*.,* Pourdeyhimi B. Two-Scale Modeling Approach to Predict Permeability of Fibrous Media, *Journal of Engineered Fibers and Fabrics, SPECIAL ISSUE 2008 – FILTRATION*, 13-18, 2008b.
55. Kenesei P**.**, Biermann H. and Borbély A. Estimation of Elastic Properties of Particle Reinforced Metal-Matrix Composites Based on Tomographic Images, *Advanced Engineering Materials*, 8 (6), 500-506, 2006a.
56. Kenesei P**.**, Klohn A**.**, Biermann H. and Borbély A. Mean Field and Multiscale Modeling of a Particle Reinforced Metal-Matrix Composite Based on Microtomographic Investigations, *Advanced Engineering Materials*, 8 (6), 506-510, 2006b.
57. Doroszko M. and Seweryn A. A new numerical modelling method for deformation behaviour of metallic porous materials using X-ray computed microtomography, *Materials Science & Engineering A*, 689, 142-156, 2017.
58. Roux S., Hild F., Viot P., Bernard D. Three-dimensional image correlation from X-ray computed tomography of solid foam, *Composites Part A*, 39, 1253–1265, 2008.
59. Li G., Zhang X., Fan Q., Wang L., Zhang H., Wang F., Wang Y. Simulation of damage and failure processes of interpenetrating SiC/Al composites subjected to dynamic compressive loading, *Acta Materialia*, 78, 190–202, 2014.

60. Heggli M., Etter T., Wyss P., Uggowitzer P. J. and Gusev A. Approaching representative volume element size in interpenetrating phase composites, *Advanced Engineering Materials*, 7 (4), 225–229, 2005.
61. Seweryn A. *Metody numeryczne w mechanice pękania, in: Biblioteka Mechaniki Stosowanej, Seria A. Monografie, eds.: Z. Mróz, M. Kleiber, H. Petryk, K. Sobczyk,* Instytut Podstawowych Problemów Techniki PAN, *Warszawa*, 2003.
62. de Borst R., Pamin J., Schellekens J. C. J. and Sluys L. J. Continuum Methods for Localized Failure, in: *Fracture of Brittle Disordered Materials: Concrete, Rock and Ceramics*, *eds.*: *G. Baker and B. L. Karihaloo*, CRC Press, Taylor & Francis, 2004.
63. de Borst R. and Pamin J. Gradient plasticity in numerical simulation of concrete cracking, *European Journal of Mechanics - A/Solids*, 15 (2), 295-320, 1996.
64. Emmel T. *Untersuchung des Bruchverhaltens von Metall-Keramik-Verbundverkstoffen*, *MSc Thesis*, Technische Hochschule Darmstadt, *Darmstadt*, 1995.
65. Rödel J. Mechanics of bulk ceramics, *in: Mechanics of Advanced Materials, AMAS Course – MAM'2001, ed*.: *Z. Mróz,* Institute of Fundamental Technological Research, Polish Academy of Sciences*, Warsaw*, October 8-12, 369-445, 2001.
66. Grassi M., Zhang X. Finite element analyses of mode I interlaminar delamination in z-fibre reinforced composite laminates, *Composites Science & Technology*, 63, 1815-1832, 2003.
67. Kruzic J. J., Nalla R. K., Kinney J. H., Ritchie R. O. Crack blunting, crack bridging and resistance-curve fracture mechanics in dentin: effect of hydration, *Biomaterials*, 24 (28), 5209–5221, 2003.
68. Cartie D. D. R., Cox B. N., Fleck N. A. Mechanisms of crack bridging by composite and metallic rods, *Composites Part A*, **35**, 1325–1336, 2004.
69. Fünfschilling S., Fett T., Hoffmann M. J., Oberacker R., Schwind T., Wippler J., Böhlke T., Özcoban H., Schneider G. A., Becher P. F., Kruzic J. J. Mechanisms of toughening in silicon nitrides: The roles of crack bridging and microstructure. *Acta Materialia*, 59, 3978-3989, 2011.
70. Shao Y., Zhao H.-P., Feng X.-Q., Gao H. Discontinuous crack-bridging model for fracture toughness analysis of nacre, *Journal of Mechanics and Physics of Solids*, 60 (8), 1400–1419, 2012.
71. Cotterell B., Rice J. R. Slightly curved or kinked cracks, *International Journal of Fracture,* 16 (2), 155-169, 1980.
72. Gilbert R. I. Shrinkage, cracking and deflection - the serviceability of concrete structures, *Electronic Journal of Structural Engineering* 1 (1), 2-14, 2001.

73. Evans A. G., Dagleish B. J., He M. and Hutchinson J. W. On crack path selection and the interface fracture energy in bimaterial systems, *Acta Metallurgica*, 37 (12), 3249–3254, 1989.
74. Shum D. K. M. and Hutchinson J. W. On toughening by microcracks, *Mechanics of Materials*, 9, 83-91, 1990.
75. Kobayashi A., Ramulu M. A dynamic fracture analysis of crack curving and branching, *Journal de Physique Colloques*, 46 (C5), C5-197-C5-206, 1985.
76. Ha Y. D. H., Bobaru F. Studies of dynamic crack propagation and crack branching with peridynamics, *International Journal of Fracture*, 162, 229–244, 2010.
77. Hutchinson J. W., Jensen H. M. Models of fiber debonding and pullout in brittle composites with friction, *Mechanics of Materials*, 9 (2), 139–163, 1990.
78. Stang H., Li Z., Shah S. P. Pullout problem: stress versus fracture mechanical approach, *Journal of Engineering Mechanics*, 116, 2136-2150, 1990.
79. Nairn J. A., Liu C.-H., Mendels D.-A., Zhandarov S. Fracture Mechanics Analysis of the Single-Fiber Pull-Out Test and the Microbond Test Including The Effects of Friction and Thermal Stresses, *in*: *Proceedings of the* 16*th Ann. Technical Conference of the American Society of Composites*, American Society for Composites, VPI, *Blacksburg VA*, September 9-12, 2001.
80. Jia Y. Y., Yan W., Liu H.-Y. Numerical study on carbon fiber pullout using a cohesive zone model, *in*: *Proceeding of 18th International Conference on Composite Materials*, International Committee on Composite Materials (ICCM), *Jeju Island, South Korea*, August 21-26, 2011.
81. Jia Y. Y., Yan W., Liu H.-Y. Numerical study on residual thermal stresses in carbon fiber pullout, *in*: *Proceeding of 28th International Congress of the Aeronautical Sciences*, International Council on The Aeronautical Sciences (ICAS), *Brisbane, Australia*, September 23-28, 1855-1860, 2012.
82. Bheemreddy V., Chandrashekhara K., Dharani L. R., Hilmas G. E. Modeling of fiber pull-out in continuous fiber reinforced ceramic composites using finite element method and artificial neural networks, *Computational Materials Science,* 79, 663–673, 2013.
83. Bansal N. P. *Handbook of Ceramic Composites*, Springer Science & Business Media, 2006.
84. Sun Y., Zhang H. F., Wang A. M., Fu H. M., Hu Z. Q., Wen C. E., and Hodgson P. D. Mg-based metallic glass/titanium interpenetrating phase composite with high mechanical performance, *Applied Physics Letters*, 95, 171910, 2009.
85. Chang H., Binner J. and Higginson R. Ballistic evaluation and damage characterization of metal-ceramic interpenetrating composites for light armor

applications, in: *Advances in Ceramic Armor VI: Ceramic Engineering and Science Proceedings*, *ed*.: *J. J. Swab*, John Wiley & Sons, 97- 104, 2010.
86. Scherm F., Völkl R., Neubrand A., Bosbach F., Glatzel U. Mechanical characterisation of interpenetrating network metal–ceramic composites, *Materials Science and Engineering A*, 527, 1260–1265, 2010.
87. Roy S., Gibmeier J., Kostov V., Weidenmann K. A., Nagel A., Wanner A. Internal load transfer and damage evolution in a 3D interpenetrating metal/ceramic composite, *Materials Science and Engineering A*, 551, 272– 279, 2012.
88. Wang L., Fan Q., Li G., Zhang H., Wang F. Experimental observation and numerical simulation of SiC3D/Al interpenetrating phase composite material subjected to a three-point bending load, *Computational Materials Science*, 95, 408–413, 2014.
89. Poniżnik Z., Nowak Z. and Basista M. Numerical modeling of deformation and fracture of reinforcing fibers in ceramic-metal composites, *International Journal of Damage Mechanics*, ISSN: 1056-7895, DOI: 10.1177/1056789515611945, 26 (5), 711-734, 2017.
90. Budiansky B., Amazigo J. C., Evans A. G. Small-scale crack bridging and the fracture toughness of particulate-reinforced ceramics, *Journal of the Mechanics and Physics of Solids,* 36 (2), 167-187, 1988.
91. Sigl L. S.**,** Mataga P. A.**,** Dagleish B. J., McMeeking R. M. and Evans A. G. On the toughness of brittle materials reinforced with a ductile phase, *Acta Metallurgica*, 36 (4), 945-953, 1988.
92. Beldica C. and Botsis J. Experimental and numerical studies in model composites Part II: Numerical results, *International Journal of Fracture*, 82 (2), 175–192, 1996.
93. Mataga P. A. Deformation of crack bridging ductile reinforcements in toughened brittle materials, *Acta Metallurgica*, 37, 3349-3359, 1989.
94. Hoffman M., Fiedler B., Emmel T., Prielipp H., Claussen N., Gross D., Rödel J. Fracture behaviour in metal fibre reinforced ceramics, *Acta Materialia*, 45 **(**9), 3609–3623, 1997.
95. Lapczyk I., Hurtado J. A. Progressive damage modeling in fiber-reinforced materials, *Composites Part A*, 38, 2333–2341, 2007.
96. Bobiński J. and Tejchman J. Simulations of fracture in concrete elements using continuous and discontinuous models, *Mechanics and Control*, 30 (4), 183–193, 2011.
97. Winzer J. S. *Production and Characterisation of Alumina-Copper Interpenetrating Composites*, *Ph. D. thesis*, Material- und Geowissenschaften,

Nichtmetallisch-Anorganische Werkstoffe, Technische Universität Darmstadt, *Darmstadt*, 2011.

98. Ju J. W. and Ko Y. F. Micromechanical elastoplastic damage modeling of progressive interfacial arc debonding for fiber reinforced composites, *International Journal of Damage Mechanics*, 17 (4), 307-356, 2008.
99. Sadowski T., Balawender T., Śliwa R., Golewski P., Kneć M. Modern hybrid joints in aerospace: modelling and testing, *Archives of Metallurgy and Materials*, 58 (1), 163–169, 2013a.
100. Sadowski T., Golewski P. Numerical study of the prestressed connectors and their distribution on the strength of a single lap, a double lap and hybrid joints subjected to uniaxial tensile test, *Archives of Metallurgy and Materials*, 58 (2), 579–585, 2013b.
101. Postek E. and Sadowski T. Cracks in interfaces and around their junctions in WC/Co composite, *Engineering Transactions*, 64 (4), 589–596, 2016.
102. Węglewski W., Bochenek K., Basista M., Schubert Th., Jehring U., Litniewski J., Mackiewicz S. Comparative assessment of Young's modulus measurements of metal–ceramic composites using mechanical and non-destructive tests and micro-CT based computational modeling, *Computational Materials Science*, 77, 19–30, 2013.
103. Węglewski W., Basista M., Manescu A., Chmielewski M., Pietrzak K., Schubert Th. Effect of grain size on thermal residual stresses and damage in sintered chromium–alumina composites: Measurement and modeling, *Composites Part B*, 67, 119–124, 2014.
104. Dandekar C. R., Shin Y. C. Effect of porosity on the interface behavior of an Al_2O_3–aluminum composite: A molecular dynamics study, *Composites Science and Technology*, 71, 350–356, 2011.
105. Zhong W. and Pan N. A computer simulation of single fiber pull out process in a composite, *Journal of Composite Materials*, *37*, 1951-1969, 2003.
106. Tsai J. H., Patra A. and Wetherhold R. Finite element simulation of shaped ductile fiber pullout using a mixed cohesive zone/friction interface model, *Composites Part A*, 36, 827-838, 2005.
107. Zhang G. Q., Suwatnodom P. and Ju J. W. Micromechanics of crack bridging stress-displacement and fracture energy in steel hooked-end fiber-reinforced cementitious composites, *International Journal of Damage Mechanics*, 22, 6, 829-859, 2012.
108. Skarżyński Ł. and Tejchman J. Experimental investigations of fracture process in concrete by means of X-ray micro-computed tomography, *Strain*, 52, 26–45, 2016.

109. Kozicki J. and Tejchman J. Simulation of fracture process in concrete elements with steel fibres using discrete lattice model, *in: Selected Topics of Contemporary Solid Mechanics, eds.: Z. Kotulski, P. Kowalczyk, W. Sosnowski, Proceedings of the 36th Solid Mechanics Conference, Gdańsk, Poland,* September 9-12*, Prace IPPT-IFTR Reports 2/2008,* Instytut Podstawowych Problemów Techniki PAN*, Warszawa*, 2008.
110. Emmel T. *Theoretische und numerische Untersuchung von Versagensmechanismen in Metall-Keramik-Verbundverkstoffen*, *Dr.-Ing. Dissertation*, Institut für Mechanik, Technische Universität Darmstadt, *Darmstadt*, 2002.
111. Rice J. A path independent integral and the approximate analysis of strain concentration by notches and cracks*, Journal of Applied Mechanics*, 35, 379–386, 1968.
112. Cherepanov G. P. Crack propagation in continuous media, *Journal of Applied Mathematics and Mechanics (Engl. transl. of PMM, 31 (3), 476–488)*, 31 (3), 503–512, 1967.
113. Broek D. *Elementary Engineering Fracture Mechanics*, Noordhoff International Publishing, *Leyden*, *The Netherlands*, 1974.
114. Eshelby J. D. The Force on an Elastic Singularity, *Philosophical Transactions of the Royal Society A, Mathematical, Physical and Engineering Sciences*, https://doi.org/10.1098/rsta.1951.0016, 1951.
115. Maugin G. A. *Material Inhomogeneities in Elasticity*, Chapman & Hall, *London*, 1993.
116. Maugin G. A. Configurational Forces, *in*: *UNESCO Encyclopedia of Life Support Systems (EOLSS)*, *Volume: Continuum Mechanics*, Article 6.161.18, 40 pages, *eds*.: *J. Merodio and G. Saccomandi*, Developed under the Auspices of the UNESCO, Eolss Publishers, *Paris*, *France*, [http://www.eolss.net], 2009.
117. Miehe C. and Gürses E. A robust algorithm for configurational-force-driven brittle crack propagation with *R*-adaptive mesh alignment, *International Journal For Numerical Methods In Engineering*, 72, 127–155, 1999.
118. Müller R., Gross D., Maugin G. A. Use of material forces in adaptive finite element methods, *Computational Mechanics*, 33, 421–434, 2004.
119. Gross D., Müller R., Kolling S. Configurational forces – morphology evolution and finite elements, *Mechanics Research Communications*, 29, 529–536, 2002.
120. Gross D., Kolling S., Müller R., Schmidt I. Configurational forces and their applications in solid mechanics, *European Journal of Mechanics A/Solids*, 22, 669–692, 2003.

121. Plate C. *Fracture Mechanical Analysis of Failure Processes in Antarctic Ice Shelves*, *Ph. D. thesis*, Lehrstuhl für Technische Mechanik, Technische Universität Kaiserslautern, *Kaiserslautern*, 2015.
122. Irwin G. R. Analysis of Stresses and Strains Near the End of a Crack Traversing a Plate, *Journal of Applied Mechanics*, 24, 361–364, 1957.
123. Eischen J. W. Fracture of nonhomogeneous materials, *International Journal of Fracture*, 34, 3-22, 1987.
124. Honein T. and Herrmann G. Conservation laws in nonhomogeneous plane elastostatics, *Journal of Mechanics and Physics of Solids*, 45, 789-805, 1997.
125. Anlas G., Santare M. H., Lambros J. Numerical calculation of stress intensity factors in functionally graded materials, *International Journal of Fracture*, 104, 131-143, 2000.
126. Kim J. H. and Paulino G. H. Mixed-mode *J*-integral formulation and implementation using graded elements for fracture analysis of nonhomogeneous orthotropic materials, *Mechanics of Materials*, 35, 107–128, 2003.
127. Simha M. K**.**, Fisher F. D., Kolednik O. and Chen C. R. Inhomogeneity effects on the crack driving force in elastic and elastic-plastic materials, *Journal of Mechanics and Physics of Solids*, 51, 209-240, 2003.
128. Marshall D. B and Cox B. N. A *J*-integral method foor calculating steady-state matrix cracking stresses in composites, *Mechanics of Materials*, 7 (2), 127-133, 1988.
129. Wang P. C. and Yang J. M. Simulation of fatigue cracking and life distribution of SCS-6 fiber-reinforced orthorombic titanium aluminide composites, *Materials Science and Engineering*, A222, 101-108, 1997.
130. Yang E. and Li V. C. Numerical study on steady-state cracking of composites, *Composites Science and Technology*, 67, 151-156, 2007.
131. Gross D. and Seelig T. *Fracture Mechanics with an Introduction to Micromechanics*, Second Edition, Springer, *Berlin*, *Heidelberg*, *Dordrecht*, *London*, *New York*, 2011.
132. Bridgman P. W. *Studies of Large Plastic Flow and Fracture*, Harvard University Press, *Cambridge*, 1964.
133. Ashby M. F., Blunt F. J. and Bannister M. Flow characteristics of highly constrained metal wires, *Acta Metallurgica*, 37 (7), 1847-1857, 1989.
134. Gurson A. L. Continuum Theory of Ductile Rupture by Void Nucleation and Growth: Part I—Yield Criteria and Flow Rules for Porous Ductile Media, *Journal of Engineering Materials and Technology*, The American Society of Mechanical Engineers ASME, 99 (1), 2-15, 1977.

135. Launey M. E. and Ritchie R. O. On the Fracture Toughness of Advanced Materials, *Advanced Materials*, 21, 2103–2110, 2009.
136. Argon A. S. Fracture of Composites, in: *Treatise on Materials Science and Technology: Materials Science Series*, *ed*.: *H. Herman*, Elsevier, 1, 2013.
137. Schmauder S. and Mishnaevsky L. Jr *Micromechanics and Nanosimulation of Metals and Composites. Advanced Methods and Theoretical Concepts*, Springer, *Berlin*, *Heidelberg*, 2009.
138. Węglewski W., Basista M. Modelling of thermal stresses and damage in Cu/Al_2O_3 interpenetrating phase composites, *European Congress on Computational Methods in Applied Sciences and Engineering (ECCOMAS 2012)*, *eds*.: *J. Eberhardsteiner et.al*., *Vienna*, *Austria*, 2012.
139. Basista M., Węglewski W., Bochenek K., Poniżnik Z. and Nowak Z. Micro-CT finite element analysis of thermal residual stresses and fracture in metal-ceramic composites, *Advanced Engineering Materials*, ISSN: 1438-1656, DOI: 10.1002/adem.201600725, 19 (8), 1600725-1-9, 2017.
140. Mishnaevsky L. Jr *Computational Mesomechanics of Composites*, Wiley-Interscience, 2007b.
141. Belytschko T. and Black T. Elastic crack growth in finite elements with minimal remeshing, *International Journal for Numerical Methods in Engineering*, 45, 601-620, 1999.
142. Dumstorff P. and Meschke G. Crack propagation criteria in the framework of X-FEM-based structural analyses, *International Journal for Numerical and Analytical Methods in Geomechanics*, 31, 239-259, 2007.
143. Zangmeister T. *On the XFEM for the Elasto-Plastic Deformation of Heterogeneous Materials*, *Ph. D. thesis*, Lehrstuhl für Technische Mechanik, Technische Universität Kaiserslautern, *Kaiserslautern*, 2015.
144. ABAQUS. SIMULIA *ABAQUS 6.10 Documentation,* Dassault Systems, Simulia Corp., *Providence, RI, USA*, 2010.
145. Dobrzański L. A. *Podstawy nauki o materiałach i metaloznawstwo. Materiały inżynierskie z podstawami projektowania materiałowego*, Wydawnictwa Naukowo-Techniczne, *Gliwice – Warszawa*, 2002.
146. Ostrowska-Maciejewska J. and Kowalczyk-Gajewska K. *Rachunek tensorowy w mechanice ośrodków ciągłych*, Wydawnictwo Instytutu Podstawowych Problemów Techniki PAN, *Warszawa*, 2013.
147. Basista M. and Poniżnik Z. Modelling of effective elastic properties and crack bridging in metal-ceramic interpenetrating phase composites, *World Journal of Engineering*, 7 (3), 95-96, 2010.

148. Ostrowska-Maciejewska J. *Mechanika Ciał Odkształcalnych*, Wydawnictwo Naukowe PWN, *Warszawa*, 1994.
149. Werkstoffdatenblatt des Deutsches Kupferinstitut Cu-ETP, www.kupferinstitut.de, 2005.
150. Lipka J. *Wytrzymałość materiałów*, Wydawnictwa Politechniki Warszawskiej, *Warszawa*, 1990.
151. Zimmermann A., Hoffmann M., Emmel T., Gross D., Rödel J. Failure of metal-ceramic composites with spherical inclusions, *Acta Materialia*, 49, 3177-87, 2001.
152. Christensen R. M. *Mechanics of Composite Materials*, John Wiley & Sons, *New York*, 1979.
153. Mishnaevsky L. Jr *Private communication*, 2006.
154. Schmauder S., Weber U., Hofinger I. and Neubrand A. Modelling the deformation behaviour of W/Cu composites by a self-consistent matricity model, *Technische Mechanik*, 19 (4), 313–320, 1999.
155. Torquato S. Modeling of physical properties of composite materials, *International Journal of Solids and Structures*, 37, 411-422, 2000.
156. Taylor R. L. *FEAP - A Finite Element Analysis Program, Version 7.5 User/Theory Manual*, Department of Civil and Environmental Engineering, University of California, *Berkeley*, 2005.
157. Huet Ch. Coupled size and boundary-condition effects in viscoelastic heterogeneous and composite bodies, *Mechanics of Materials*, 31, 787–829, 1999.
158. ASTM E111-97. Standard test method for Young's modulus, Tangent modulus, and Chord modulus, *Annual Book of ASTM Standards*, American Society for Testing and Materials, *West Conshohocken*, *PA*, 03.01, 230-236, 1999.
159. ASTM E132-97. Standard test method for Poisson' ratio at Room Tempeature, *Annual Book of ASTM Standards*, American Society for Testing and Materials, *West Conshohocken*, *PA*, 03.01, 260-262, 1999.
160. Ruud J. A., Josell D., Spaepen F. and Greer A. L. A new method for tensile testing of thin films, *Journal of Materials Research*, 8 (1), 112-117, 1993.
161. Benito, J.A., Manero, J.M., Jorba, J., Roca A. Change of Young's modulus of cold-deformed pure iron in a tensile test, *Metallurgical and Materials Transactions A*, 36A, 3317-3324, 2005.
162. Ogden R. W. *Non-Linear Elastic Deformations*, Dover Publications, Inc., *Mineola*, *New York*, 1997.

163. Petryk H. *Podstawy Mechaniki Materiałów*, *lecture note*s, Instytut Podstawowych Problemów Techniki PAN, *Warszawa*, 2006.
164. Naruse K. Estimation of shear moduli of wood by quasi-simple shear tests, *Journal of Wood Sci*ence, 49, 479–484, 2003.
165. Hußnätter W. and Merklein M. Characterization of material behavior under pure shear condition, *International Journal of Material Forming*, 1, Suppl. 1, 233, 2008.
166. Nunes L. C. S. Mechanical characterization of hyperelastic polydimethylsiloxane by simple shear test, *Materials Science and Engineering A*, 528, 1799–1804, 2011.
167. Nunes L. C. S. and Moreira D. C. Simple shear under large deformation: Experimental and theoretical analyses, *European Journal of Mechanics A/Solids*, 42, 315-322, 2013.
168. Timoshenko S. *Strength of Materials, Part 1: Elementary Theory and Problems*, D. Van Nostrand Company, Inc., *Toronto*, *New York*, *London*, 1953.
169. Destrade M., Murphy J. G., Saccomandi G. Simple shear is not so simple, *International Journal of Non-Linear Mechanics*, 47, 210–214, 2012.
170. Moreira D. C. and Nunes L. C. S. Test method: Comparison of simple and pure shear for an incompressible isotropic hyperelastic material under large deformation, *Polymer Testing*, 32, 240-248, 2013.
171. Gitman I. M., Askes H. and Sluys L. J. Representative volume: Existence and size determination, *Engineering Fracture Mechanics*, 74, 2518-2534, 2007.
172. ISO 23146. First edition 2008-06-01 *Fine ceramics (advanced ceramics, advanced technical ceramics) — Test methods for fracture toughness of monolithic ceramics* — Single-edge V-notch beam (SEVNB) method, 2008.
173. Ashby M. F. *GRANTA – The CES 2009 EduPack Resource Booklet, Part 2: Material and Process Selection Charts*, *downloaded from*: www.grantadesign.com/education/, 2009.
174. Marciniak Z., Mróz Z., Olszak W., Perzyna P., Rychlewski J., Sawczuk A., Szczepiński W., Urbanowski W. and Życzkowski M. *Teoria Plastyczności*, *eds.: Olszak W., Perzyna P. and Sawczuk A.,* Instytut Podstawowych Problemów Techniki Polskiej Akademii Nauk, Państwowe Wydawnictwo Naukowe, *Warszawa*, 1965.
175. Życzkowski M. *Combined Loadings in the Theory of Plasticity,* PWN - Polish Scientific Publishers, *Warsaw*, 1981.
176. Lubliner J. *Plasticity Theory*, Macmillan Publishing Company, *New York*, 1990.

177. Jarząbek D. M., Chmielewski M., Dulnik J. and Strojny-Nędza A. The influence of the particle size on the adhesion between ceramic particles and metal matrix in MMC composites, *Journal of Materials Engineering and Performance*, doi: 10.1007/s11665-016-2107-3, 2016.
178. Juvé D., Courbière M. and Tréheux D. Bonding of the Cu-Al_2O_3 interfaces. Mechanisms, structure and mechanical properties, *in*: *Metal-Ceramic Interfaces: Proceedings of an International Workshop, Acta-Scripta Metallurgica proceedings series*, *eds.: M. Rühle, A. G. Evans, J. P. Hirth, M. F. Ashby, Elsevier,* 4, 152-158, https://books.google.pl/books?id=AGchBQAAQBAJ, 2013
179. ASTM E399. Standard test method for plane-strain fracture toughness of metallic materials, *Annual Book of ASTM Standards*, American Society for Testing and Materials, *West Conshohocken*, *PA*, 03.01, 422-452, 1999.
180. Munro R. G. Evaluated material properties for a sintered α-alumina, *Journal of the American Ceramic Society*, NIST Structural Ceramics Database, SRD Database Number 30, 80 (8), 1919–28, 1997.
181. Miserez A., Rossol A. and Mortensen A. Investigation of crack-tip plasticity in high volume fraction particulate metal matrix composites, *Engineering Fracture Mechanics*, 71, 2385-2406, 2004.
182. Winzer J. S., Weiler L., Poniznik Z., Salit V., Gross D., Basista M., Dusza J., Rödel J. Mechanical properties of copper-alumina interpenetrating network composites, *33rd International Conference and Exposition on Advanced Ceramics and Composites*, January 18-23, *Daytona Beach*, *Florida*, *USA*, www.ceramics.org/daytona2009, ICACC-S1-050-2009, 2009.
183. Mattern A., Huchler B., Staudenecker D., Oberacker R., Nagel A., Hoffmann M. J. Preparation of interpenetrating ceramic-metal composites, *Journal of the European Ceramic Society*, 24, 3399-3408, 2004.
184. Clarke D. R. Interpenetrating Phase Composites, *Journal of the American Ceramic Society*, 75 (4), 739 – 758, 1992.
185. Wang S., Wang L., Li C., Chi Q., Fei Z. The dry sliding wear behavior of interpenetrating titanium trialuminide/aluminium composites, *Applied Composite Materials*, 14, 129–144, 2007.
186. Hemrick J. G, Hu M. Z., Peters K. M., Hetzel B. Nano-Scale Interpenetrating Phase Composites (IPC'S) for Industrial and Vehicle Applications, *Final Technical Report,* Oak Ridge National Laboratory, *Oak Ridge*, *Tennessee*, 2010.
187. Hein S. B. Powder injection moulding of metal ceramic interpenetrating phase composites, *Powder Metallurgy*, DOI: http://dx.doi.org/10.1179/1743290114Y.0000000116, 2014.

188. Kailash C. J. *Fracture Behavior of Particulate Polymer Composites (PPCs) and Interpenetrating Polymer Networks (IPNs): Study of Filler Size, Filler Stiffness and Loading Rate Effects*, *PhD Thesis*, Auburn University, *Auburn*, *Alabama*, 2013.
189. Moro M. and Solomon V. C. Design and manufacturing of interpenetrating phase composites for vibration damping applications, *Proceedings of the 2012 American Society for Engineering Education ASEE North-Central Section Conference*, 2012.
190. Mu J., Zhu Z. W., Zhang H. F., Zhang H. W., Fu H. M., Li H., Wang A. M., Hu Z. Q. A Ti/Ti-Based-Metallic-Glass Interpenetrating Phase Composite with Remarkable Mutual Reinforcement Effect, *Advances in Materials Science and Engineering*, Hindawi Publishing Corporation, Article ID 127172, 6 pages, 2014.
191. Galal-Yousef S. *Mikrorissbildung durch anisotrope thermische Ausdehnung: Experiment und numerische Simulation*, *Dr.-Ing. Dissertation*, Fachbereich Material- und Geowissenschaften, Technische Universität Darmstadt, Shaker Verlag, *Aachen*, 2004.
192. Galal-Yousef S., Rödel J., Fuller Jr. E. R., Zimmermann A. and El-Dasher B. S. Microcrack evolution in alumina ceramics: experiment and simulation, *Journal of the American Ceramic Society*, 88 (10), 2809-2816, 2005.
193. ASTM E1876-99. Standard test method for dynamic Young's modulus, shear modulus, and Poisson's ratio by Impulse Excitation of Vibration, *Annual Book of ASTM Standards*, American Society for Testing and Materials, *West Conshohocken*, *PA*, 03.01, 1046-1054, 1999.
194. Haj Ibrahim S., Neumann M., Klingner F., Schmidt V. and Wejrzanowski T. Analysis of the 3D microstructure of tape-cast open-porous materials via a combination of experiments and modeling, *Materials and Design*, 133, 216-223, 2017.